UNIVERSITY OF COPENHAGEN

Multispecies Dynamics in Weakly Ionized Dusty Protoplanetary Disks

Leonardo Krapp

Supervisors:

Oliver Gressel, Pablo Benítez-Llambay and Martin E. Pessah

PhD Thesis in Theoretical and Computational Astrophysics

The Niels Bohr Institute

This thesis has been submitted to the PhD School of The Faculty of Science, University of Copenhagen

Multispecies Dynamics in Weakly Ionized Dusty Protoplanetary Disks

PhD Thesis in Theoretical and Computational Astrophysics

Krapp Leonardo

Supervisors:

Oliver Gressel, Pablo Benítez-Llambay and Martin E. Pessah.

The Niels Bohr International Academy

The Niels Bohr Institute

Faculty of Science

University of Copenhagen

July 8, 2019

Abstract

Understanding the dynamical evolution of protoplanetary disks is of vital importance in modern astrophysics because many of these environments are deemed to evolve into planetary systems like our own. In recent years, ALMA observations of the dust component and CO emission unveiled the presence of substructures such as spiral arms, rings, and gaps, and indicated that protoplanetary disks have a very rich dynamical activity. However, it is not clear yet whether the observed features are signatures of planets in formation, given the complexity of the astrophysical processes taking place at each of the different disk scales.

In this thesis, we focus our efforts on studying the momentum transfer between different species and its effect on the disks evolution. Despite disks being poorly ionized, charged species can transfer energy and momentum from the magnetic field to the neutrals due to collisions, significantly affecting the dynamics. In addition, the aerodynamical coupling between dust particles and the gaseous component has significant consequences for the dust dynamics and evolution. Thus, collisions play an important role in affecting different processes related to accretion mechanisms, the growth of dust particles, and the planetesimal formation. We base our discussion on three publications that define the core of this research. We first introduce a framework to solve the momentum exchange between multiple species with particular emphasis on dust dynamics. We then use this framework to study the impact of the self-organization induced by the Hall effect on the dust evolution, and the linear and non-linear phase of the streaming instability.

More specifically, we present an asymptotically and unconditionally stable numerical method to account for the momentum transfer between multiple species. We show that the scheme conserves momentum to machine precision and that its implementation in the publicly available code FARGO3D converges to the correct equilibrium solution. Aiming at studying dust dynamics, we use the implementation to address problems such as damping, damped sound waves, local and global gas-dust radial drift in a disk and linear streaming instability. We furthermore provide analytical or exact solutions to each of these problems considering an arbitrary number of species. We successfully validate our implementation by recovering the solutions from the different test problems to second- and first-order accuracy in space and time, respectively. From this, we conclude that our scheme is suitable, and very robust, to study the self-consistent dynamics of several fluids.

In the field of non-ideal magnetohydrodynamics, we investigate the evolution of turbulence triggered by the magneto-rotational instability, including the Hall effect and considering vertically unstratified

cylindrical disk models. In the regime of a dominant Hall effect, we robustly obtain large-scale self-organized concentrations in the vertical magnetic field that remain stable for hundreds of orbits. For disks with initially only vertical net flux alone, we confirm the presence of zonal flows and vortices that introduce regions of super-Keplerian gas flow. Including a moderately strong net-azimuthal magnetic flux can significantly alter the dynamics, partially preventing the self-organization of zonal flows. For plasma beta-parameters smaller than 50, large-scale, near-axisymmetric structures develop in the vertical magnetic flux. In all cases, we demonstrate that the emerging features are capable of accumulating dust grains for a range of Stokes numbers.

Finally, we study the linear and non-linear phase of the streaming instability. This instability is thought to play a central role in the early stages of planet formation by enabling the efficient bypass of several barriers hindering the formation of planetesimals. We recover linear and non-linear results from previous works considering only one-dust species, validating our developed framework to study dust dynamics. Treating dust as a pressureless fluid, we run non-linear shearing-box simulations of the streaming instability and compare our results with two different setups previously obtained with Lagrangian particles. Simulations with Stokes number of unity show an excellent agreement with those performed with particles. However, in the other test case, which has a ten times smaller Stokes number, convergence with resolution is not found. We conclude that further studies are required in other to address whether the pressureless fluid approach is suitable for studying the non-linear phase of the streaming instability. We furthermore present the first study exploring the efficiency of the linear streaming instability when a particle-size distribution is considered. We find that, for a given dust-to-gas mass ratio, the multi-species streaming instability grows on timescales much longer than those expected when only one dust species is involved. In particular, distributions that contain dust-to-gas density ratios close to unity lead to unstable modes that can grow on timescales comparable to, or larger than those of secular instabilities. We anticipate that processes leading to particle segregation and/or concentration can create favorable conditions for the instability to grow fast. Our findings may have important implications for a large number of processes in protoplanetary disks that rely on the streaming instability as usually envisioned for a unique dust species. Our results suggest that the growth rates of other resonant-drag-instabilities may also decrease considerably when multiple species are considered.

Resumé

Forståelsen af den dynamiske udvikling af protoplanetare tilvækstskiver er af centralt betydning indenfor den moderne astrofysik. Ikke mindst fordi mange af disse miljøer vil endeligt udvikle sig til planetariske systemer som vores egen. I de sidste år har ALMA observeringer af støvkomponenten og CO emissionen i disse skiver afsløret substrukturer som spiralarme, ringer, og huler, hvilket viser deres bred dynamisk aktivitet. Dog er det ikke klart endnu, om de observerede egenskaber er signaturerne af planeter under dannelse eller ej, specielt hvis man ser på kompleksiteten af de astrofysiske processer som foregår på skivens forskellige længdeskalaer.

I denne her afhandling fokuserer vi på at studere impulstransferen imellem forskellige specier og dens effekt på skiveudviklingen. På trods af skivens lav ioniseringsgrad kan elektrisk ladete specier transferere energi og impuls fra magnetfeltet til neutrale partikler via kollisioner, hvilket kan markant påvirke dynamikken. Desuden har den aerodynamiske kobling mellem støvpartikler og gassen en signifikant betydning før støvens dynamiske udvikling. Således spiller kollisionerne en vigtig rolle i at påvirke forskellige processer relateret til massetransport, vækst af støvpartikler og ikke mindst planetdannelse. Vores diskussion er baseret på tre publiceringer som definerer kernen af disse afhandling. Vi introducerer en framework for at løse impulstransferen bland forskellige specier, med specielt fokus på støvdynamik. Denne framework bruger vi så for at studere indflydelsen af selvorganisation introduceret på grund af Hall effekten på støvdynamikken, såvel som den lineare og ikke-lineare fase af streaming instabiliteten.

Mere specifik præsenterer vi en asymptotisk og betingelsesløst stabil numerisk metode som beskriver impulstransferen mellem forskellige specier. Vi beviser at skemaet bevarer impulsen præcist og at dens implementering i den offentlig tilgængelige code FARGO3D konvergerer til den korrekte ligevægtsløsning. Med formålet at studere støvdynamikken, bruger vi implementeringen til at henvende os problemer som dæmpning, dæmpede lydbølger, lokalt og globalt gas-støv drift i en tilvækstskive, såvel som linear streaming-instabiliteten. Derudover giver vi analytiske eller eksakte løsninger til enhver af disse problemer, under betragtning af en vilkårligt antal af specier. Vi validerer vores implementering ved at genvinde løsningerne af de forskellige testproblemer med anden- henholdsvis første-ordre nøjagtighed i rummet og tiden. Herfra konkluderer vi at vores skema er velegnet og robust til at studere den selvkonsistente dynamik af multiple fluids.

I sammenhang med ikke-ideale magnetohydrodynamik udforsker vi udviklingen af turbulens, som

udløses af magnet-rotations-instabiliteten, under inklusion af Hall-effekten og under betragtning af vertikalt ulagdelte cylindriske skivemodeller. I regimet af dominant Hall-effekt får vi reproducerbart stor-anlagte selv-organiserede koncentrationer af vertikalt magnetfelt, som forbliver stabilt over hundrede omdrejninger. For skiver med udelukkende vertikalt flux, konfirmerer vi optræden af zone-strømminger og hvirvler som bevirker regioner af super-Keplersk gas strømming. Inklusionen af en azimutal flux af moderat styrke kan betydeligt påvirke gasens dynamik og delvist forhindre selv-organisationen af zone-strømmingerne. For en plasma beta parameter mindre end 50 opstår der næsten-aksesymmetriske strukturer i den vertikale magnetfelt. I alle tilfælde demonstrerer vi at de opstående strukturer kan akkumulere støv af en række af Stokes-taller.

Endelig studerer vi den lineare og ikke-lineare fase af streaming-instabiliteten. Instabiliteten, tror man, spiller en centralt rolle i de tidlige stadier af planetdannelse, ved at etablere en virkningsfuld bypass af forskellige barrierer, som forhindrer dannelsen af planetesimaler. Vi bekræfter lineare og ikke-lineare resultater af tidligere arbejder som betragtede kun en enkel støvkomponent, hvilket validerer vores udviklet framework for støvdynamik. Med behandling af støvet som trykløst fluid udfører vi ikke-lineare shearing-boks simuleringer af streaming-instabiliteten og sammenligner vores resultater med to forskellige opsætninger som har tidligere været behandlet med Lagrange-partikler. Vores simuleringer med Stokes-tal af ét viser en udmærket overensstemmelse med simuleringerne som brugte partikler. Til gengæld finder vi ingen konvergens med opløsning i andre testfald med mindre Stokes-tal. Vi konkluderer at yderlige studier er påkrævet for at afgøre om vores trykløst-fluid tilgang er passende for at studere den ikke-lineare fase af streaming-instabiliteten. Endvidere præsenterer vi den første studie som udforsker virkningsgraden af den lineare streaming-instabilitet under betragtning af en størrelsesfordeling af støvpartikler. For en fastholdt ratio mellem støv og gas finder vi at den multi-sepcies version af instabiliteten vokser på tidsskalaer som er meget længere end dem hvor en enkel støvkomponent er inkluderet. Især fordelinger som indeholder støv-gas ratioer tæt på ét medfører ustabile moder som vokser på en tidsskala som er lige så stor eller større end den af en sekulær instabilitet. Vi forventer at processer, som medfører segregation af partikler og/eller koncentration, kan dog skabe fordelagtige konditioner for instabiliteten at vokse hurtigt. Vores optagelser kunne have vigtige implikationer for en række af processer i protoplanetare tilvækstskiver som bygger på streaming-instabiliteten med en enkel støvkomponent, dvs som den vanligvis bliver behandlet. Vores resultater tyder i øvrigt på, at vækstraterne af andre såkaldte resonant-drag-instabilities kunne også blive formindsket dramatisk, når man betragter en størrelsesfordeling.

Publications

This thesis is based on the following publications:

Dust Segregation in Hall-dominated Turbulent Protoplanetary Disks.
Krapp, L., Gressel, O., Benítez-Llambay, P., Downes, T. P., Mohandas, G., and Pessah, M. E. (2018).
The Astrophysical Journal, 865:105.

Asymptotically Stable Numerical Method for Multispecies Momentum Transfer: Gas and Multifluid Dust Test Suite and Implementation in FARGO3D.
Benítez-Llambay, P., Krapp, L., and Pessah, M. E. (2019).
The Astrophysical Journal Supplement, 241:25.

Streaming Instability for Particle-size Distributions.
Krapp, L., Benítez-Llambay, P., Gressel, O., and Pessah, M. E. (2019).
The Astrophysical Journal Letters, 878(2):L30.

Acknowledgements

This thesis would not be possible without the tremendous dedication of my three mentors, Prof. Oliver Gressel, Dr. Pablo Benítez-Llambay, and Prof. Martin Pessah. I am pleased to say that it was a great and rewarding experience working together with them within these three years.

Firstly, I would like to express my sincere gratitude to my PhD advisor Prof. Oliver Gressel for his continuous support and patience. His help and generosity gave me the opportunity to come to Copenhagen and conduct a PhD in Astrophysics. I am very grateful for the many discussions and insightful comments, but also for the hard questions which incented me to widen my research from various perspectives. I greatly appreciate his motivation and encouragement for the dissemination of the work and all of the opportunities I was given to conduct my research.

I would like to thank and express my sincere admiration to Dr. Pablo Benítez-Llambay, who selflessly offered his collaboration and has been a truly dedicated mentor. Besides the daily useful discussions in the blackboard, it has been an amazing experience working side by side with him in two of the publications that support this thesis and in the development of the multi-fluid version of the code FARGO3D. I would like to recognize his talent for identifying the relevant questions and his generosity for always sharing his expertise and skills so willingly. He has also provided many of the tools needed to complete this thesis successfully. His guidance and immense knowledge helped me at every step.

I would like to express my special appreciation and thanks to Prof. Martin Pessah for his crucial contributions to this thesis and the long stimulating discussions. He has been a model for his dedicated teaching and exceptional leadership of the Theoretical Astrophysical Group at the Niels Bohr Institute. His advice on both research as well as on my career have been invaluable. Without his precious support, it would not have been possible to conduct this thesis.

I would also like to thank my fellow mate Philipp Weber, for his friendship and valuable discussions during these years. Throughout the writing of this thesis, I have received a great deal of support and assistance from him.

I would like to acknowledge the valuable input and contributions of Prof. Turlough Downes, who provided me multispecies steady-state shocks solutions to validate the numerical scheme for the Hall effect implemented in FARGO3D, in addition to several meaningful discussions. I would also like to thank Dr. Gopakumar Mohandas, who provided me analytical solutions in cylindrical coordinates

utilized to the test the linear growth of the Hall-modified magneto-rotational instability with the codes FARGO3D and NIRVANA-III.

Additional acknowledgments are for: Prof. Frédéric Masset for inspiring discussions that motivated the multifluid project. Prof. Andrew Youdin for suggesting us adding up densities when computing cumulative density distributions in order to ease the comparison between the fluid approach and Lagrangian particles. Prof. Troels Haugbølle for useful discussions and helpful suggestions.

Finally, but by no means least, I would like to thank my family and friends, my parents, my sister and my beloved wife for supporting me emotionally throughout the three years of research so far away from home.

Funding and Computational Resources

The research leading to these thesis has received funding from the European Research Council under the European Union's Horizon 2020 research and innovation programme (grant agreement No 638596). This research was also supported in part by the National Science Foundation under Grant No. NSF PHY17-48958 and by the Munich Institute for Astro- and Particle Physics (MIAPP) of the DFG cluster of excellence "Origin and Structure of the Universe". We acknowledge that the results of this research have been achieved using the PRACE Research Infrastructure resource MareNostrum-4 based in Spain at the Barcelona Supercomputing Center (BSC). Computations were performed on the `astro_gpu` partition of the Steno cluster at the University of Copenhagen HPC center.

Contents

List of Figures

List of Tables

1 Introduction

1.1 Evidence for Protoplanetary Disks

The formation of planets remains as one of the major mysteries in the modern Astrophysics. The origin of life may well be inherent to the formation of the Earth together with the entire Solar System. Since the nebular hypothesis posted by Kant (1755) substantial theoretical progress has been achieved in the last century to build-up the scenario of Planet Formation. Such a process is believed to be a consequence of the star formation where the rotating cloud surrounding the protostar collapses into a disk giving birth to a protoplanetary disk (PPD) consisting of gas and dust (see Lissauer (1993) and references therein). Understanding the building blocks of planet formation became more challenging since the discovery of the first exoplanet in 1995 (Mayor and Queloz, 1995) due to the vast diversity of properties among the ~ 4000 confirmed detection to the date (e.g., Schneider et al., 2011).

Observations around star-forming regions as Taurus (Torres et al., 2012), Lupus (Ansdell et al., 2016) and Orion (Kounkel et al., 2017) provided substantial constraints on the gas and dust components as well as the disks sizes and information on the chemical composition of PPDs. Furthermore, recent high-resolution observations of the continuum confirmed the presence of substructure in the dust component such as gaps, rings and spiral arms (ALMA Partnership et al., 2015; Andrews et al., 2016; Andrews et al., 2018). Many of these observations indicate that the dust component constitutes $\sim 1\%$ of the total mass of the PPD and is settled-out to the disk midplane with a scale-height of $1\mathrm{AU}$ at an orbital location of $100\mathrm{AU}$ (see e.g., Pinte et al., 2016).

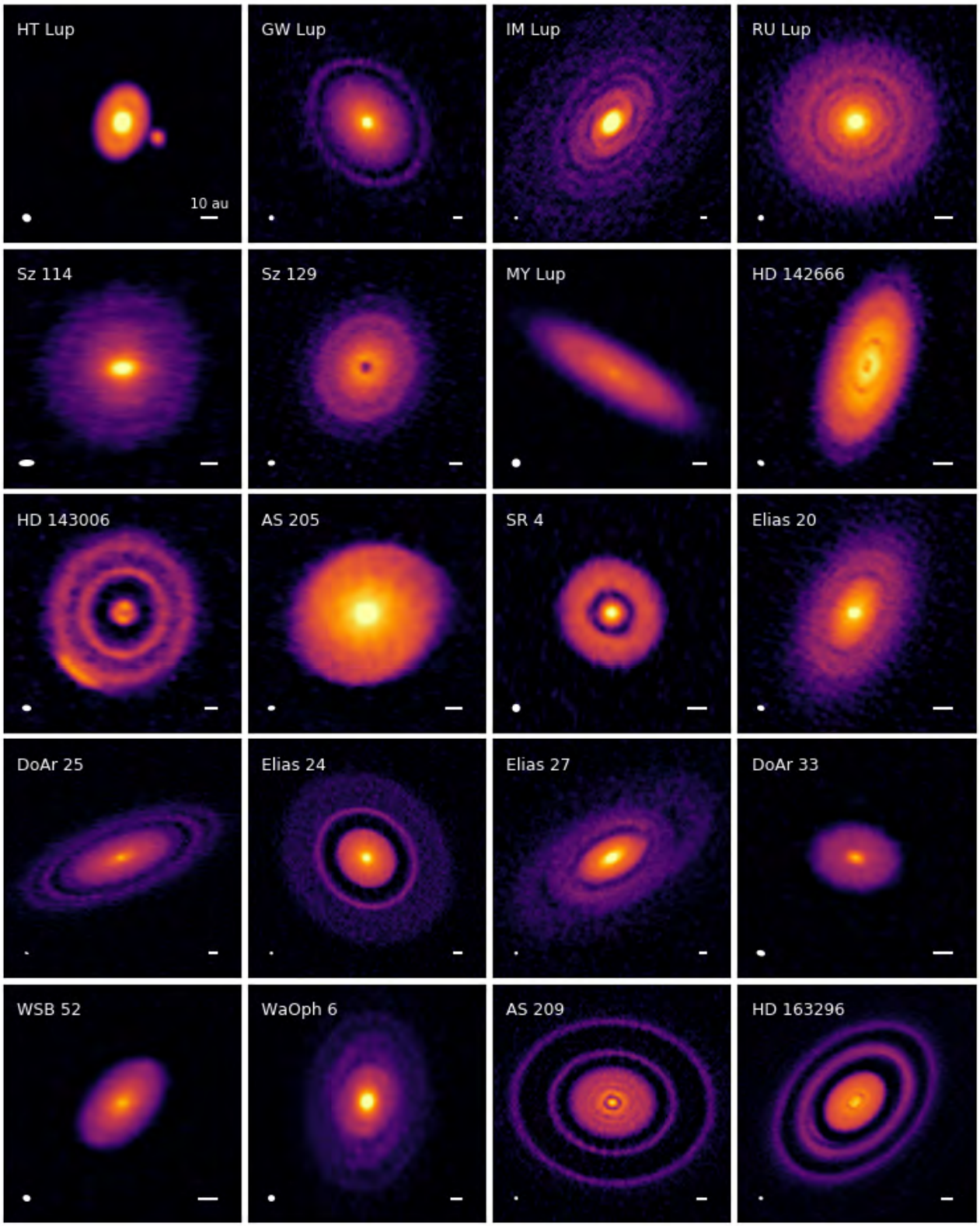

Figure 1.1.1: Gallery adopted from Andrews et al. (2018) corresponding to the Disk Substructures at High Angular Resolution Project (DSHARP). It shows the 1.25 mm emission of 20 PPDs.

1.2 Ionization processes in protoplanetary disks

The presence of magnetic fields in PPDs has been suggested from the observed outflows in the form of collimated protostellar jets and wide-angle disk winds (e.g., Arce et al., 2007; Bjerkeli et al., 2016). Taken at face value that disks are magnetized, a clear interest exists on determining the strength of the magnetic field together with the ionization fraction.

PPDs are subject to different ionization processes that shape the electron and ions density distributions from the surface layers to the midplane. The estimated temperatures of PPDs suggest that the gas is generally too cold for thermal ionization to be relevant, except in regions located at $r < 1\mathrm{AU}$ (e.g., Fromang et al., 2002). Far-ultraviolet (FUV) radiation can ionize the surface density layers of PPDs creating favorable conditions for the magneto-rotational instability (MRI) active layer (e.g., Perez-Becker and Chiang, 2011). In addition, ionization beyond the surface layer can be sustained by the stellar X-ray luminosity, typically assumed to be in the range of $L_X \sim 10^{29} - 10^{32}\mathrm{erg\ s}^2$ (e.g., Igea and Glassgold, 1999; Turner et al., 2010; Ercolano and Glassgold, 2013). Cosmic rays (CR) provide another important contribution to the ionization fraction (e.g., Umebayashi and Nakano, 1981; McCall et al., 2003) together with radioactive decay (e.g., Turner and Drake, 2009) (primarily the decay of $^{26}\mathrm{Al}$), because they can ionize the medium at the very inner regions of PPDs.

Charged grains can also modify the conductivity of the poorly ionized plasma by adsorbing free electrons, or through charge exchange due to collisions (e.g., Bai and Goodman, 2009). Recombination processes are also crucial in PPDs. Positive charges can capture electrons due to different reactions. The dominant reactions correspond to the dissociative recombination, radiative recombination with metal ions and reactions that transfer charge from molecular to metal ions (see e.g., Armitage, 2011).

All the estimates indicate that PPDs are poorly ionized and therefore, the coupling between the bulk of the fluid and the magnetic field might be reduced compared to the fully ionized regime. However, charged species transfer momentum and energy from the magnetic field onto the neutrals due to collisions. A rather simple framework to account for the system's coupled dynamics is the non-ideal magnetohydrodynamics (MHD) approximation, including the Ohmic and ambipolar diffusions and the Hall effect (Cowling, 1956; Nakano and Umebayashi, 1986a). These effects strongly depend on the ionization fraction as well as on the strength of the magnetic field (see e.g., Wardle, 1999; Bai, 2011b). The importance of self-consistent non-ideal MHD models including chemical reaction networks (for instance based on Ilgner and Nelson (2006)), has been enhanced by many authors in the last decade

(e.g. Bai and Stone, 2013; Simon et al., 2015; Gressel et al., 2015; Bai, 2017; Béthune et al., 2017). Contrary to the classical turbulent flow driven by the magneto-rotational instability (MRI) (Balbus and Hawley, 1991), all the mentioned works point towards a laminar accretion scenario dominated by magneto-centrifugal (Blandford and Payne, 1982; Gressel et al., 2015) or magneto-thermal winds (Lynden-Bell, 1996; Bai et al., 2016).

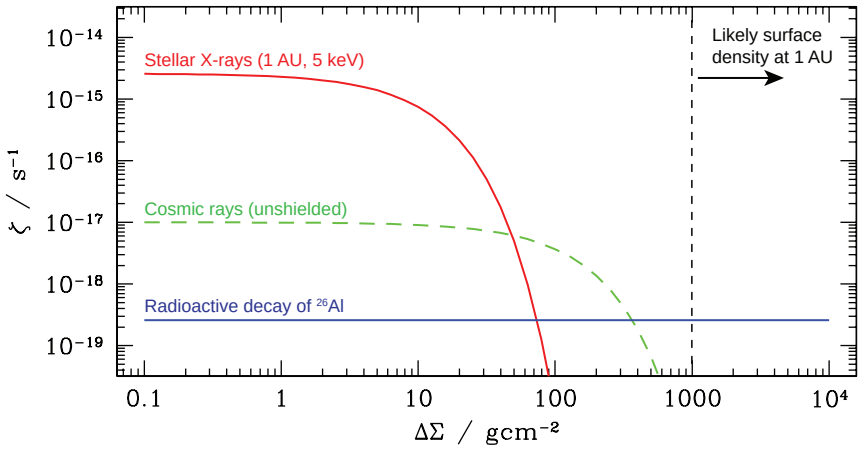

Figure 1.2.1: Figure adopted from Armitage (2011). Ionization rate of different sources (X-rays, cosmic rays and radioactive decay of ^{26}Al) as a function of the column density $\Delta\Sigma$, measured from the disk surface.

1.3 Accretion processes in protoplanetary disks

The average lifetime of PPDs is approximately $1 - 10\,\mathrm{Myr}$, with typical gas accretion rates of $\dot{M} \sim 10^{-8\pm1} M_\odot/\mathrm{yr}$ (Hartmann et al., 1998; Sicilia-Aguilar et al., 2006). The complex astrophysical scenario of PPDs permits different mechanisms for the radial and vertical transport of angular momentum. The classical accretion disk model from Lynden-Bell and Pringle (1974) requires a certain amount of viscosity to remove the angular momentum. Turbulence is usually an efficient source of viscosity in PPDS. For instance, Maxwell stress can be generated from the MRI (Balbus and Hawley, 1991) in highly ionized magnetized regions. However, the non-ideal effects as the Ohmic and ambipolar diffusion can reduce the level of Maxwell stress significantly, and suppress the MRI (Wardle, 1999; Balbus and Terquem, 2001) due to the low ionization level beyond $\gtrsim 1\,\mathrm{AU}$. Thus, the gas dynamics becomes laminar in the absence of any source of Reynolds stress when non-ideal MHD effects dominate the magnetic field evolution (Bai and Stone, 2013).

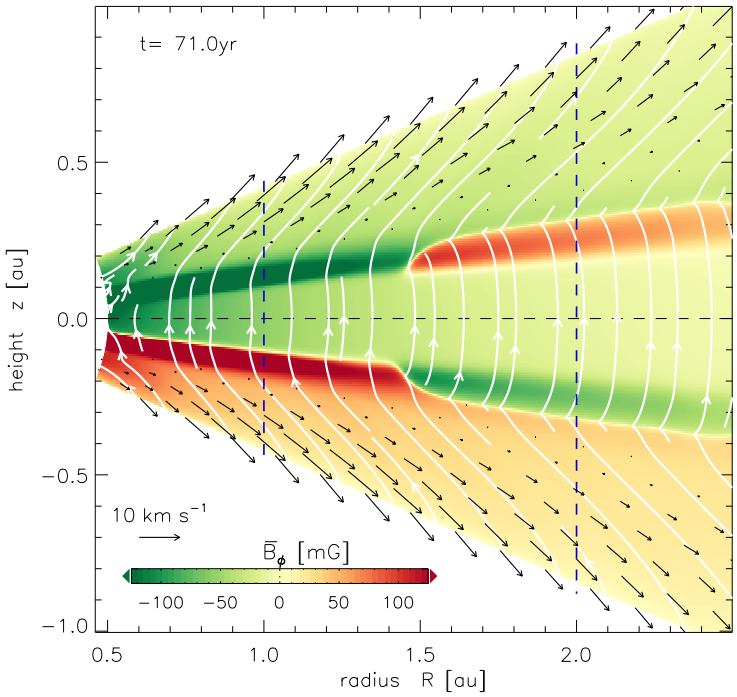

Figure 1.3.1: Figure adopted from Gressel et al. (2015) shows an example where the accretion and mass loss is driven by a magneto-centrifugal wind, including Ohmic and ambipolar diffusion. The color correspond to the azimuthal field, withe solid lines are the projected vertical and radial magnetic field while the black arrows shows the velocity field. The simulations were performed with the code NIRVANA-III (see Section 1.5.2).

Hydrodynamical instabilities in regions of large Ohmic and ambipolar diffusion might provide a source of turbulence and thus viscous transport. Candidates to produce significant Reynolds stress are the subcritical baroclinic instability (Lesur and Papaloizou, 2010), the vertical shear instability (Nelson et al., 2013), the convective overstability (Klahr and Hubbard, 2014) and the zombie vortex instability (Marcus et al., 2015). Regions with a high concentration of dust might also be suitable for the streaming instability (Youdin and Goodman, 2005) as will be discussed in Chapter 5.

Besides turbulent transport, winds may also play a vital role in shortening the lifetime of the disk by partially removing its mass. Photoevaporation has been proposed as an effective mechanism through which disks are believed to lose mass (see e.g., Williams and Cieza, 2011; Alexander et al., 2014). For instance, the rapid disk dispersal measured in the observations of T Tauri stars has been reproduced by photoevaporative viscous models (Alexander et al., 2006). In the context of magnetized disks, the local shearing box simulations of Bai and Stone (2013), and later the global numerical models of Gressel et al. (2015) indicate that the upper layers of the PPD are suitable for launching magneto-centrifugal winds when ambipolar diffusion becomes dominant. More recently, consistent thermochemistry and ray tracing have been added to the simulations providing a more accurate treatment of the microphysics

and the external heating. These models point towards the presence of magneto-thermal winds where the flow is driven by pressure gradients instead of tension forces (e.g., Bai et al., 2016; Béthune et al., 2017; Wang et al., 2019).

1.4 The dust component

Observations of protoplanetary disks indicate a wide range of values for the dust-to-gas ratio from 1% up to 100% (e.g., Ansdell et al., 2016). The evolution of dust particles depends on transport and collisional processes (e.g., Testi et al., 2014) continuously affecting the grain sizes. Such processes include coagulation and sticking which may be effective mechanisms to grow μm sized particles into $\sim$ cm sized grains (e.g., Blum, 2018). However, large particles eventually reach high impact velocities, and, depending on their intrinsic properties, are prone to fragment. Thus, fragmentation sets a barrier that prevents particles from growing beyond a certain size (Windmark et al., 2012; Birnstiel et al., 2016). Besides, the aerodynamical coupling to the gas molecules can induce fast inward (or outward e.g., Benítez-Llambay et al., 2019) drift of the solids, and thus efficiently remove large particles in timescales much shorter than the disk lifetime (Whipple, 1972a; Weidenschilling, 1977). How grains overcome such fragmentation and radial-drift barriers to form km-size bodies has become an enormous challenge for the current theoretical understanding of PPDs. It is worth mentioning that we will address a potential mechanism in Chapter to stall the dust radial-drift in 4.

1.5 Review on the codes FARGO3D and NIRVANA-III

1.5.1 FARGO3D

FARGO3D[1] is an 3D Eulerian MHD code, with particular emphasis on solving PPDs dynamics and planet-disk interaction. A comprehensive review of the code is presented in (Benítez-Llambay and Masset, 2016) and, as a consequence of this work, a new public version is available which includes the multispecies momentum transfer (Benítez-Llambay et al., 2019). We dedicate a discussion to the major improvements and new capabilities in Chapter 3 and in this section we summarize the main features.

[1] https://fargo3d.bitbucket.io — http://fargo.in2p3.fr

The code belongs to the family of the so-called ZEUS-type codes, which are based on finite-difference upwind, dimensionally split methods (Stone and Norman, 1992). Mass and momentum are strictly conserved, and shock-jump conditions are satisfied in barotropic systems (e.g., isothermal systems). The code has been developed to exploit High-Performance-Computing (HPC) facilities, and it is capable of running in CPU- and/or GPU-clusters, with shared or distributed memory. It is written in C with additional Python scripts and uses a parser to convert C into CUDA language, removing the need of having CUDA programming skills to modify the code.

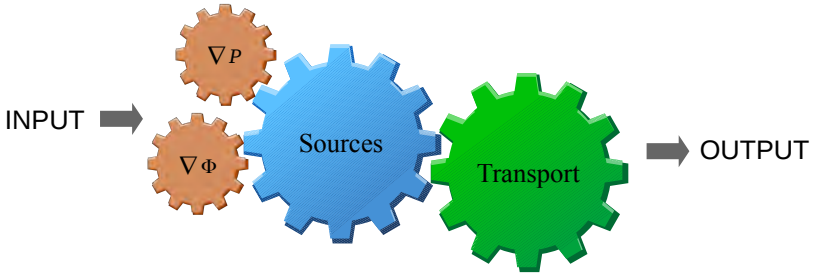

Figure 1.5.1: Operator splitting scheme in FARGO3D.

It solves the MHD equations in Cartesian, cylindrical and spherical coordinates on a static and staggered[2] mesh. Non-uniform meshes can be defined, except in the x-direction (φ in cylindrical or spherical coordinates) which under the current development is always uniform with periodic boundary conditions. Time integration is first-order while second-order is achieved in the spatial integration. The code solves the internal energy equation with two possible equations of state implemented, namely locally isothermal and adiabatic.

A full timestep in the code is divided into two substeps (at least), labeled as the Source and Transport steps. (i) The Source step solves the momentum and internal energy equations in a non-conservative form without the advection term. For the momentum, the contribution of the pressure (gas and magnetic), gravity, and viscosity are included. The work done by the pressure forces is added to the internal energy (in a non-isothermal case when energy is updated). (ii) The Transport step updates the density, energy and momentum by solving the advective term, all three using a conservative form of the Euler equations. The fluxes, defined at the cell-center, are interpolated into the cell-faces using a zone-wise linear reconstruction with a van Leer's slope (van Leer, 1977). The transport is done using dimensional

[2]Pressure, density and internal energy are cell-centered while the velocities (and magnetic field) components are face-centered.

splitting, first in the z-direction, then in the y-direction and finally in the x-direction.

Defining Q as a generic quantity that follows a transport equation of the form

$$\partial_t Q + \nabla \cdot (\mathbf{v}Q) = \mathcal{S}(Q), \tag{1.5.1}$$

the splitting technique can be written as

$$\partial_t Q_1 = \mathcal{S}(Q_0) \qquad \text{source step} \tag{1.5.2}$$

$$\partial_t \int_V Q_2 \mathrm{dV} = -\int_{\partial V} Q_1 \mathbf{v} \cdot \mathrm{d}\mathbf{S} \qquad \text{transport step} \tag{1.5.3}$$

where V defines a volume and ∂V its boundary. The quantity Q advances a full timestep from an initial state $Q_0 \rightarrow Q_1$ and again a full timestep from $Q_1 \rightarrow Q_2$. A comprehensive explanation of the numerical procedure that solves the discretized form of these two equations can be found in Benítez-Llambay and Masset (2016).

The induction equation is solved with the constrained transport (CT) scheme, which guarantees $\partial_t (\nabla \cdot \mathbf{B}) = 0$ to machine precision (Evans and Hawley, 1988). To integrate the induction equation, and compute the magnetic tension in the momentum equations, FARGO3D uses the method of characteristics (MOC) (Stone and Norman, 1992).

1.5.2 NIRVANA-III

NIRVANA-III solves the compressible MHD equations describing a time-dependent multi-physics non-relativistic system (Ziegler, 2004, 2011, 2016). The code is written in C and works in Cartesian, cylindrical and spherical geometries. NIRVANA-III is MPI parallelized with HPC capabilities for clusters of CPUs. It includes a block-structured adaptive mesh refinement (AMR) that consist of a set of nested blocks of size 4^3 cells. The code solves the conservative fluids equations with isothermal, adiabatic and polytropic equations of state and a flux conservative total energy formulation. A dual-energy formalism for high-Mach-number/low-plasma-beta flows is also available.

The spatial integration is done utilizing a semi-discrete (i.e., no time discretization) second-order finite-volume Godunov scheme. High precision (up to third order in time) is obtained by enabling the 2nd or 3rd Runge-Kutta time integration. NIRVANA-III includes three different Riemann solvers to integrate

the MHD equations. A two-dimensional HLL MHD-Riemann solver (Ziegler, 2004; Londrillo and del Zanna, 2004), and one-dimensional HLL/HLLD MHD-Riemann solver with upwind-interpolated electric fields (Gardiner and Stone, 2008).

The induction equation is solved using the CT scheme, where for the Hall effect a flux-type HLL prescription (Lesur et al., 2014) or an operator-split method (O'Sullivan and Downes, 2006) can be used. Parabolic terms, for instance the Ohmic and ambipolar diffusions, are updated via Strang-split second-order Runge-Kutta-Legendre super-time-stepping method (Meyer et al., 2012).

Simulations of disks may include the orbital advection scheme that follows from Stone et al. (2008) and Mignone et al. (2012).

1.6 The objectives of this Thesis

In this Thesis, we address some of the most crucial problems of the current theoretical understanding of PPDs. Furthermore, we believe that the obtained results may serve as a guideline for future work given their impact on disk dynamics and planetesimal formation.

In the following we shortly outline the structure of this work and introduce our major goals. A detailed description and subsequent discussion will then be presented in chapters 3, 4 and 5.

Objective I: Create a multifluid framework accounting for the momentum transfer between charged species, dust-grains and a gaseous fluid with particular focus on the development of new numerical schemes to correctly solve the equations describing the dynamics of protoplanetary disks.

Such a framework has been proposed before by several authors. However, the groundbreaking result of our work — related to this goal — is the presentation of a numerical method that always converges to the correct solution, that is, the solution obtained by an analytical method as the time goes to infinity. This result is complemented with general analytical solutions for a diversity of problems, including an arbitrary number of species. We additionally address the validity of the fluid approach for dust species recovering linear and non-linear solutions that have been already studied using Lagrangian particles. The simplicity and efficiency of our numerical method opens new possibilities to study dust dynamics in PPDs, and potentially other fields. Moreover, we discuss and implement different numerical techniques

to solve the Hall effect and Ohmic diffusion. This implies that we do not explicitly solve collisions between charged and neutral species and instead adopt the non-ideal MHD approximation. We offer a comparison between different numerical schemes which provides solid grounds to determine whether the solutions of the non-linear fluid equations are affected by the different numerical approximations.

Objective II: Study the impact of magnetic fields on the dynamics of protoplanetary disks, adopting the non-ideal magnetohydrodynamics approximation with particular emphasis in the Hall effect and its role in the evolution of magneto-rotational instability and the self-organization of turbulent flows.

Non-ideal MHD effects introduce a variety of theoretical and numerical challenges because of their dependency on the ionization fraction and the strength and direction of the magnetic field, which is still poorly constrained by observations. Thus, parameter explorations with a self-consistent treatment of the thermodynamics are required, imposing a high computational cost. Besides, a numerical method to properly solve the Hall effect, that is accurate and stable, is yet to be found. Partially overcoming these challenges, recent results suggest that self-organized structures, induced by the Hall effect in turbulent flows, can serve as a bypass for the drift-barrier problem in dust evolution. The pressure gradient affected by the zonal flows locally modifies the rotational equilibrium from sub-Keplerian to super-Keplerian azimuthal velocities, stopping the radial-drift of particles as they reach a Keplerian rotation. Moreover, the local accumulation of dust may favor the formation of planetesimal, which casts special interest on this issue. Starting from the results of previous authors, we confirm the presence of self-organized structures induced by the Hall effect as a result of the non-linear dynamics using different numerical methods. We extend these results by including dust and simulating radially varying disk models. We find that self-organization is an efficient mechanism for the segregation and accumulation of dust particles, even in regimes dominated by a strong azimuthal magnetic flux.

Objective III: Determine the linear growth of the streaming instability in local regions of protoplanetary disks considering multiple dust species that can be described by a particle-size distribution.

The streaming instability is thought to play a central role in the early stages of planet formation by enabling the efficient bypass of several barriers hindering the formation of planetesimals. However, a study of the linear phase of this instability has never been done including more that one particle size. Taking that as a motivation, we present the first study exploring the efficiency of the linear streaming

instability when a particle-size distribution is considered and arrive at some remarkable conclusions: We find that the multi-species streaming instability grows on timescales much longer than those expected when only one dust species is involved. In particular, distributions that contain dust-to-gas density ratios that are close to order unity lead to unstable modes that can grow on timescales comparable, or larger, than those of secular instabilities. Our findings may have important implications for a large number of processes in protoplanetary disks that rely on the streaming instability as usually envisioned for a single dust species. in addition, our results suggest that the growth rates of other resonant-drag-instabilities may also decrease considerably when multiple species are considered.

The persisting uncertainty of key parameters for the dynamics of interest dissuades us from including the mentioned physical processes in a single study. Instead, to explore the most important questions, we adopt a rather conservative approach, setting-up a controlled framework with a set of well-defined and isolated problems for each of the stated objectives. The diversity of the problems discussed within this work will address particular aspects of the dynamics of the protoplanetary disk, and vary from analytical linear stability calculations to fully non-linear numerical simulations.

2 Protoplanetary Disk Dynamics

Protoplanetary disks are composed of a mixture of partially ionized gas and dust particles. In this work, we assume that the mixture can be modeled as a plasma in local thermal equilibrium; hence, the gas molecules, ions, and electrons follow a Maxwellian distribution. Thus, the dynamics of the system is fully described by the transport equations obtained after averaging the Boltzmann equation (e.g. Braginskii, 1965; Draine, 1986; Chernoff and Shapiro, 1987; Benilov, 1997). The charged species interact with the magnetic and electric fields, which evolve according to the Maxwell equations neglecting the displacement current. In addition, the species interchange momentum due to elastic collisions which significantly affects the conductivity of the plasma (e.g., Cowling, 1956; Norman and Heyvaerts, 1985; Wardle, 1999; Falle, 2003; Pandey and Wardle, 2008). In our framework, mass and energy transfers are neglected. Dust grains can also affect the conductivity of the plasma in PPDs (e.g., Bai, 2011b), but we adopt a more conservative approach considering dust particles to be neutral. In the strong coupling regime, the dust's interaction with the gas due to drag forces allows us to describe its dynamics as a pressureless fluid (e.g. Cuzzi et al., 1993; Garaud et al., 2004).

In this chapter, we present the equations that describe the dynamics of PPDs in the context of non-ideal MHD and set the framework of our work (see Section 2.1). We neglect radiative transfer, cooling, and viscous processes as well as self-gravity and chemical reactions. Also, we do not include a self-consistent ionization model. A brief discussion on the validity of the non-ideal MHD approximation is presented in Section 2.2.

2.1 Equations

The complete set of equations describing a system of a neutral gas coupled to the magnetic field due to collisions with ions and electrons, and $N-1$ dust-species reads as

$$\begin{aligned}
\partial_t \rho_{\rm g} + \nabla\cdot(\rho_{\rm g}\mathbf{v}_{\rm g}) &= 0\,, \\
\partial_t \rho_{{\rm d},j} + \nabla\cdot(\rho_{{\rm d},j}\mathbf{v}_{{\rm d},j}) &= 0\,, \\
\rho_{\rm g}(\partial_t \mathbf{v}_{\rm g} + \mathbf{v}_{\rm g}\cdot\nabla\mathbf{v}_{\rm g}) &= -\nabla P - \rho_{\rm g}\nabla\Phi + \mathbf{J}\times\mathbf{B} + \mathbf{F}_{\rm g}\,, \\
\rho_{{\rm d},j}(\partial_t \mathbf{v}_{{\rm d},j} + \mathbf{v}_{{\rm d},j}\cdot\nabla\mathbf{v}_{{\rm d},j}) &= -\rho_{{\rm d},j}\nabla\Phi + \mathbf{F}_{{\rm d},j}\,, \text{ with } j = 1,\ldots,N-1.
\end{aligned} \tag{2.1.1}$$

The density and velocity are defined as $\rho_{\rm g}$, $\mathbf{v}_{\rm g}$ and $\rho_{{\rm d}j}$, $\mathbf{v}_{{\rm d},j}$ for the gas and dust j-species, respectively. Importantly, both species are considered as neutral fluids, but as we will discuss in Section 2.2, a neutral fluid experiences a Lorentz force as a consequence of the collisions with the charged species.

The time evolution of the magnetic field is determined by the induction equation

$$\partial_t \mathbf{B} = \nabla\times(\mathbf{v}_{\rm g}\times\mathbf{B}) - \nabla\times\mathbf{E}\,, \tag{2.1.2}$$

where the electric field is obtained from the generalized Ohm's law,

$$\mathbf{E} = \eta_{\rm O}\mathbf{J} + \eta_{\rm H}\mathbf{J}\times\widehat{\mathbf{e}}_{\rm B} - \eta_{\rm A}\mathbf{J}\times\widehat{\mathbf{e}}_{\rm B}\times\widehat{\mathbf{e}}_{\rm B}, \tag{2.1.3}$$

with $\widehat{\mathbf{e}}_{\rm B}$ the unit vector along $\mathbf{B}$, and where the current density is $\mathbf{J}\equiv\mu_0^{-1}\nabla\times\mathbf{B}$. The three terms of Eq. (2.1.3) correspond to the Ohmic diffusion (O), the Hall effect (H) and the ambipolar diffusion (A). We discuss the validity of this equation together with the expressions for the diffusivities in Section 2.2.

We adopt a locally isothermal equation of state where the sound speed, $c_{\rm s}$, satisfies $c_{\rm s}^2 = P/\rho_{\rm g}$.

The drag force, $\mathbf{F}$, accounts only for the collisions between the gas and the dust species,

$$\begin{aligned}
\mathbf{F}_{\rm g} &= -\rho_{\rm g}\sum_{j=1}^{N-1}\alpha_{{\rm g}j}\left(\mathbf{v}_{\rm g} - \mathbf{v}_{{\rm d},j}\right)\,, \\
\mathbf{F}_{{\rm d},j} &= -\rho_{{\rm d},j}\alpha_{j{\rm g}}\left(\mathbf{v}_{{\rm d},j} - \mathbf{v}_{\rm g}\right)\,,
\end{aligned} \tag{2.1.4}$$

with α_{gj} the collision rate between the gas and the j-dust-species. This collision rate parameterizes the momentum transfer per unit time and is, in general, a function of the physical properties of the species and their mutual relative velocity. Momentum conservation implies

$$\rho_l \alpha_{lj} = \rho_j \alpha_{jl} \,. \tag{2.1.5}$$

In the following chapters we will solve this set equations, or a subset, depending on the problem. In Section 2.2, we extend our discussion to provide some insight on the validity of the single-fluid induction equation.

2.1.1 Dust as a pressureless fluid

In the case of a system composed of gas and several dust species, dust can be modeled as a pressureless fluid. It is clear that this approximation fails in describing the dynamics of systems dominated by crossing trajectories, a regime prone to develop when gas and dust species are coupled very weakly.

In this work, we neglect collisions between dust species, and hence dust species only interact indirectly via their coupling with the gas. After using the condition (2.1.5), the collision rate, α_{lj}, can be written as

$$\alpha_{lj} \equiv \alpha_l \delta_{j\mathrm{g}} + \epsilon_j \alpha_j \delta_{\mathrm{g}l} \,, \tag{2.1.6}$$

with $\epsilon_j = \rho_j / \rho_{\mathrm{g}}$ and $\delta_{i\mathrm{g}}$ the Kronecker delta.

The inverse of the collision rate α_l is defined as the stopping time, $t_{\mathrm{s}l}$. In the context of PPDs, the stopping time is usually represented by the Stokes number, T_{s}, which is a dimensionless parameter that characterizes the stopping time in units of the inverse local rotation frequency[1], Ω^{-1}, such that

$$t_{\mathrm{s}l} = T_{\mathrm{s}l} \Omega^{-1} \,. \tag{2.1.7}$$

The Stokes number depends on the properties of the gas and the dust-grains. When the size of the dust particle is smaller than $9\lambda_{\mathrm{mfp}}/4$, with λ_{mfp} being the gas mean-free-path, the grains are in the Epstein regime, and the Stokes number can be written as (see e.g., Epstein, 1924; Safronov, 1972; Whipple,

[1] It can be adopted another relevant timescale instead of the one given by the rotation frequency

1972b; Draine and Salpeter, 1979; Takeuchi and Lin, 2002),

$$T_{\rm s} = \Omega \sqrt{\frac{\pi}{8}} \frac{\rho_{\rm p} a}{\rho_{\rm g} c_{\rm s}}, \tag{2.1.8}$$

where the dust grain is assumed to be spherical with radius a and a material density $\rho_{\rm p}$. In this work, we always assume $T_{\rm s}$ to be constant.

2.1.2 Particle-size distributions

The size distribution of solids in PPDs may extend from μm to several km. Dust evolution processes shape the distribution, and thus, it becomes a function of space and time. However, as an approximated initial distribution we consider a power-law of the form $n(a) \propto a^q$, which correspond to the interstellar medium particle-size distribution obtained from extinction measurements over the wavelength from $0.1\mu{\rm m} < \lambda < \mu{\rm m}$ (e.g., Dohnanyi, 1969; Mathis et al., 1977).

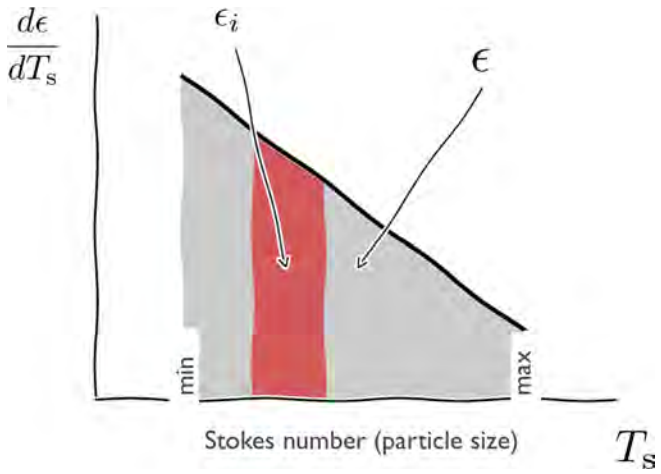

Figure 2.1.1: Schematic representation of a particle-size distribution where the particle size is proportional to the Stokes number.

In this work, we do not evolve the continuous particle-size distribution in time. We adopt a discrete approximation that is characterized by the total dust-to-gas density ratio, ϵ, a range of Stokes numbers properly bound by a minimum and a maximum, $\Delta T_{\rm s} = [T_{\rm s,min}, T_{\rm s,max}]$, and the total number of species N associated with a distinct Stokes number, $T_{{\rm s},j}$, with $j = 1, \ldots, N$. The total mass of the distribution remains constant when varying N, i.e., $\sum_{j=1}^{N} \epsilon_j = \epsilon$, where ϵ_j is the dust-to-gas density ratio associated with a given dust species.

Assuming that all the grains are spherical with radius a, we see that $\rho_{\rm d}(a) \propto a^{3+q}$. In addition, in a local approximation where Ω, $\rho_{\rm g}$ and $c_{\rm s}$ are constant, the size $a \propto T_{\rm s}$. Thus, the density ratio ϵ_j is obtained after integrating over a given Stokes number interval $[T_{{\rm s},j+1}, T_{{\rm s},j}]$ as

$$\frac{\epsilon_j}{\epsilon} = \begin{cases} \dfrac{T_{{\rm s},j+1}^{4+q} - T_{{\rm s},j}^{4+q}}{T_{\rm s,max}^{4+q} - T_{\rm s,min}^{4+q}} & \text{if } q \neq 4 \\ \\ \dfrac{\ln\left(T_{{\rm s},j+1}\right) / \ln\left(T_{{\rm s},j}\right)}{\ln\left(T_{\rm s,max}\right) / \ln\left(T_{\rm s,min}\right)} & \text{if } q = 4\,. \end{cases} \tag{2.1.9}$$

2.2 Non-Ideal Magnetohydrodynamics

The non-ideal MHD approximation has been extensively discussed in a general framework since Cowling (1956) and more recently applied to PPDs due to the low ionization fraction and the expected presence of magnetic fields (e.g., Wardle, 1999). A full derivation of Eqs. (2.1.1)-(2.1.3) (neglecting the dust species) can be found in Nakano and Umebayashi (1986a) and Nakano and Umebayashi (1986b). In the following, we briefly describe the important steps and assumptions.

We start by considering a set of N charged species that interchange momentum via collisions with a neutral species. We define the density and velocity of the neutral species as ρ_n and $\mathbf{v}_n$, while for each charged species, we use ρ_i and $\mathbf{v}_i$. Defining $\mathrm{d}/\mathrm{dt} = \partial_t + \mathbf{v}\cdot\nabla$, the momentum equations read as

$$\begin{aligned} \sum_{j=1}^{N} \rho_n \nu_{in}(\mathbf{v}_i - \mathbf{v}_n) - \nabla P_n - \rho_n \frac{\mathrm{d}\mathbf{v}_n}{\mathrm{d}t} = 0\,, \\ Z_i e n_i \left(\mathbf{E} + \mathbf{v}_i \times \mathbf{B}\right) - \rho_i \nu_{in}(\mathbf{v}_i - \mathbf{v}_n) - \nabla P_i - \rho_i \frac{\mathrm{d}\mathbf{v}_i}{\mathrm{d}t} = 0\,, \quad \text{for } i = 1, \ldots, N, \end{aligned} \tag{2.2.1}$$

where n_i, $Z_i e$ and m_i are the number density, charge and mass of the i-species, respectively, with e being the charge of the electron. The pressure for the i-species is defined as P_i, and we are assuming that the pressure tensor is isotropic for all the species. Collisions between charged species are neglected, thus the collision frequency, ν_{in}, is defined as

$$\nu_{in} = \rho_n \frac{\langle \sigma v_i \rangle}{m_i + m_n}, \tag{2.2.2}$$

where $\langle \sigma v_i \rangle$ is the rate coefficient for the momentum transfer between a neutral and a charged species,

with mass m_n and m_i, respectively (e.g., Draine, 1986). The viscous damping timescale is defined as

$$\tau_{in} = 1/\nu_{in}. \tag{2.2.3}$$

The main assumptions for the non-ideal MHD approximation are (i) charge neutrality, (ii) low ionization fraction and (iii) viscous damping much shorter than the dynamical timescale, i.e.,

$$\sum_{j=1}^{N} eZ_i n_i = 0, \quad \rho_i/\rho_n \ll 1, \quad \tau_{in} \ll t_{\rm dyn}. \tag{2.2.4}$$

2.2.1 Single-fluid momentum equation

Defining the density and velocity as ρ and $\mathbf{v}$ of total fluid mixture, we have

$$\rho = \rho_n + \sum_{j=1}^{N} \rho_j = \rho_n \left(1 + \sum_{j=1}^{N} \frac{\rho_j}{\rho_n}\right) \simeq \rho_n \,, \tag{2.2.5}$$

$$\mathbf{v} = \frac{1}{\rho}\left(\rho_n \mathbf{v}_n + \sum_{j=1}^{N} \rho_j \mathbf{v}_j\right) \simeq \mathbf{v}_n \,, \tag{2.2.6}$$

where we used condition (ii) of 2.2.4. Now, adding Eqs. (2.2.1) we obtain

$$\rho_n \frac{{\rm d}\mathbf{v}_n}{{\rm d}t} = -\nabla P + \mathbf{J} \times \mathbf{B} \,, \tag{2.2.7}$$

with $P = P_n + \sum_j P_j$ and $\mathbf{J} = \sum_j eZ_j n_j \mathbf{v}_j$. This explains why in Eq. (2.1.1) a neutral fluid experiences a Lorentz force.

2.2.2 Induction equation

The Maxwell equations determine the evolution of the electric and magnetic field. In PPDs, the velocities satisfy $v \ll c$, with c the speed of light, and we can safely neglect the displacement current, then the Faraday and Ampere's law read as

$$\frac{\partial \mathbf{B}}{\partial t} = -\nabla \times \mathbf{E}, \qquad \mathbf{J} = \frac{1}{\mu_0} \nabla \times \mathbf{B} \,. \tag{2.2.8}$$

The electric field, $\mathbf{E}$, can be obtained from the momentum equations of the charged species, which leads to a generalized Ohm's law. In the co-moving frame of the neutrals, the electric field read as

$$\tilde{\mathbf{E}} = \mathbf{E} + \mathbf{v}_n \times \mathbf{B}. \tag{2.2.9}$$

In addition, we recast the pressure and inertial terms of the charged species into a new variable $\mathbf{h}$:

$$\mathbf{h}_i = -\nabla P_i - \rho_i \frac{\mathrm{d}\mathbf{v}_i}{\mathrm{d}t}\,. \tag{2.2.10}$$

Defining relative velocity between the neutral fluid and the i-species as $\mathbf{v}_{ri} = \mathbf{v}_i - \mathbf{v}_n$, the momentum equation of the positive charged species, k, and the electron species, in the frame of the neutral fluid, reads as

$$Z_k e n_k \left(\tilde{\mathbf{E}} + \mathbf{v}_{rk} \times \mathbf{B}\right) - \frac{\rho_k}{\tau_k}\mathbf{v}_{rk} + \mathbf{h}_k = 0\,, \tag{2.2.11}$$

$$Z_e e n_e \left(\tilde{\mathbf{E}} + \mathbf{v}_{re} \times \mathbf{B}\right) - \frac{\rho_e}{\tau_e}\mathbf{v}_{re} + \mathbf{h}_e = 0\,. \tag{2.2.12}$$

Taking the electric field from the Eq. (2.2.11) into Eq. (2.2.12), subsequently solving the resulting equation for $\mathbf{v}_{rk}$, and using the condition $\mathbf{h}_n + \sum_j \rho_j/\tau_j \mathbf{v}_{rj} = 0$ in combination with Eq. (2.2.7), leads to[2]

$$\left(A_1 + \frac{A_2}{\tau_e \omega_e}\right)\mathbf{v}_{re} - \left(A_1 + \frac{A_2}{\tau_e \omega_e}\right)\mathbf{R}\mathbf{v}_{re} = \mathbf{J} \times \mathbf{B} + \mathcal{F}(\mathbf{h}_k, \mathbf{h}_e, A_1, A_2, \tau_k, \tau_e, \omega_k, \omega_e)\,, \tag{2.2.13}$$

where the matrix $\mathbf{R}$ defines a rotation in a plane orthogonal to $\mathbf{B}$ by an angle $-\pi/2$. The gyrofrequency, ω_j, is

$$\omega_j = Z_j \frac{e|\mathbf{B}|}{m_j c}, \tag{2.2.14}$$

and the coefficients, A_1, and, A_2, are defined as

$$A_1 = \sum_{j=1}^{N} \frac{\rho_j \omega_j^2}{\tau_j (1/\tau_j^2 + \omega_j^2)} \qquad A_2 = \sum_{j=1}^{N} \frac{\rho_j \omega_j}{\tau_j^2 (1/\tau_j^2 + \omega_j^2)}\,. \tag{2.2.15}$$

The conditions 2.2.4 imply that all the terms in the L.H.S of Eq. (2.2.15) which are represented by the function $\mathcal{F}$ are negligible with respect to $\mathbf{J} \times \mathbf{B}$ (Nakano and Umebayashi, 1986a). Thus, the electron

[2]This is done assuming a Cartesian coordinate system with $\mathbf{B}$ parallel to z.

velocity satisfies

$$\left(A_1 + \frac{A_2}{\tau_e \omega_e}\right) \mathbf{v}_{re} - \left(A_1 + \frac{A_2}{\tau_e \omega_e}\right) \mathbf{R}\mathbf{v}_{re} = \mathbf{J} \times \mathbf{B}. \tag{2.2.16}$$

Neglecting $\mathbf{h}_e$ in the electron momentum equation (2.2.12), the balance between the Lorentz force and the collisional force leads to a generalized Ohm's law, that is,

$$\tilde{\mathbf{E}} = \mathbf{v}_{re} \times \mathbf{B} - \frac{m_e}{e\tau_e} \mathbf{v}_{re}\,. \tag{2.2.17}$$

Replacing the solution of Eq. (2.2.16) and transforming back to the original reference frame we obtain

$$\mathbf{E} = -\mathbf{v}_n \times \mathbf{B} + \frac{1}{\sigma_1}\mathbf{J} + \frac{1}{\sigma_2}\mathbf{J} \times \mathbf{B} - \frac{1}{\sigma_3}(\mathbf{J} \times \mathbf{B}) \times \mathbf{B}\,, \tag{2.2.18}$$

with

$$\sigma_1 = \sum_{j=1}^{N} \frac{(Z_j e)^2 \tau_j n_j}{m_j}\,, \quad \sigma_2 = \frac{A_1^2 + A_2^2}{A_2 |\mathbf{B}|}\,, \quad \sigma_2 = \frac{1}{A_1/(A_1^2 + A_2^2) - 1/(\sigma_1 |\mathbf{B}|^2)}\,. \tag{2.2.19}$$

2.2.3 Diffusion coefficients

The inverse of the conductivities σ_1, σ_2 and σ_3 define the Ohmic ($\eta_{\rm O}$), Hall ($\eta_{\rm H}$) and ambipolar ($\eta_{\rm A}$) diffusion coefficients used to write the induction equation 2.1.2. These coefficients can be expressed in terms of the Hall and Pedersen conductivities defined as $\sigma_{\rm O}$, $\sigma_{\rm H}$ and $\sigma_{\rm P}$ (Wardle, 1999, 2007, see e.g.,) which depend on the Hall parameter, defined as

$$\beta_j = \frac{|Z_j| e}{m_j} \frac{|\mathbf{B}| \tau_j}{c \rho_n}\,. \tag{2.2.20}$$

Thus, we will adopt the following expressions for the diffusion coefficients

$$\eta_{\rm O} = \frac{c^2}{4\pi\sigma_{\rm O}}\,, \quad \eta_{\rm H} = \frac{c^2}{4\pi\sigma_\perp} \frac{\sigma_{\rm H}}{\sigma_\perp}\,, \quad \eta_{\rm A} = \frac{c^2}{4\pi\sigma_\perp} \frac{\sigma_{\rm P}}{\sigma_\perp} - \eta_{\rm O}\,, \tag{2.2.21}$$

where $\sigma_\perp = \sqrt{\sigma_{\rm H}^2 + \sigma_{\rm P}^2}$.

If charged particles other than ions and electrons are negligible, the diffusion coefficients simplify to (Wardle, 1999; Pandey and Wardle, 2008; Bai, 2011a)

$$\begin{aligned}
\eta_{\rm O} &= \frac{c^2\gamma_e m_e \rho_n}{4\pi e^2 n_e} \sim \frac{1}{x_e}\,, \\
\eta_{\rm H} &= \frac{c|\mathbf{B}|}{4\pi e n_e} \sim \frac{1}{x_e}\frac{|\mathbf{B}|}{\rho_n}\,, \\
\eta_{\rm A} &= \frac{|\mathbf{B}|^2}{4\pi\nu_{in}\rho_n\rho_i} \sim \frac{1}{x_e}\left(\frac{|\mathbf{B}|}{\rho_n}\right)^2\,,
\end{aligned} \tag{2.2.22}$$

where $x_e = n_e/n$ is the ionization fraction, ρ_i is the ion density, n_e is the electron number density and m_e is the electron mass. Under this approximation and in a weakly ionized medium, i.e., $\rho_e/\rho_n < \rho_i/\rho_n \ll 1$, Pandey and Wardle (2008) found that the non-ideal MHD equations are valid if the characteristic frequency of the system of interest, ω, satisfies

$$\omega \lesssim \sqrt{\frac{\rho_{\rm g}}{\rho_i}}\frac{\beta_e}{1+\beta_e}\nu_{in}\,, \tag{2.2.23}$$

with β_e and β_i being the Hall parameter of the electrons and ions, respectively. This approximation provides a simple way to characterize the importance of the three non-ideal MHD terms as a function of the Hall parameter. Thus, the ratio of the Hall term and Ohmic diffusion depends on the electron Hall parameter while the ratio between the Hall term and the ambipolar diffusion depends on the ion Hall parameter, that is

$$\frac{\rm H}{\rm O} \sim \beta_e\,, \qquad \frac{\rm A}{\rm H} \sim \beta_i. \tag{2.2.24}$$

The regime dominated by Ohmic diffusion corresponds to the case $\beta_i \ll \beta_e \ll 1$ while the ambipolar diffusion will dominate the evolution of the magnetic field in the case where $1 \ll \beta_i \ll \beta_e$. The Hall effect dominates the regime in between, that is $\beta_i \ll 1 \ll \beta_e$, this corresponds to a regime where ions are well coupled to the neutral fluid, but electrons can drift.

Figure 2.2.1 (from Armitage (2015)) shows the specific regions of a PPD in which of each of the non-ideal MHD effects dominates. This shows that the Hall effect is important in the inner regions of the protoplanetary disk $\lesssim 30\mathrm{AU}$ and close to the midplane. In these regions the Hall frequency $\omega_{\rm H}$ is smaller than the dynamical frequency and the Hall length, $L_{\rm H}$, is larger than the dynamical length scale.

Both quantities scale with the ion density as

$$\omega_{\rm H} \sim \frac{\rho_i}{\rho}\omega_{ci}\,, \qquad L_{\rm H} \sim \frac{\rho}{\rho_i}\frac{v_{\rm A}}{\nu_{in}}\beta_i^{-1}\,, \tag{2.2.25}$$

where ω_{ci} is the ion cyclotron frequency. The smaller the ionization fraction, the larger the Hall length, and thus the Hall effect becomes important at that scale. Typical values for the Hall frequency and the Hall length in PPDs can be found in Table 3 of Pandey and Wardle (2008), where, assuming a minimum mass solar nebula disk model (Hayashi, 1981) with a magnetic field of $B \sim 10^{-2}$G, the Hall length is the order of $L_{\rm H} \sim 10^5$km at $r = 5\,$AU.

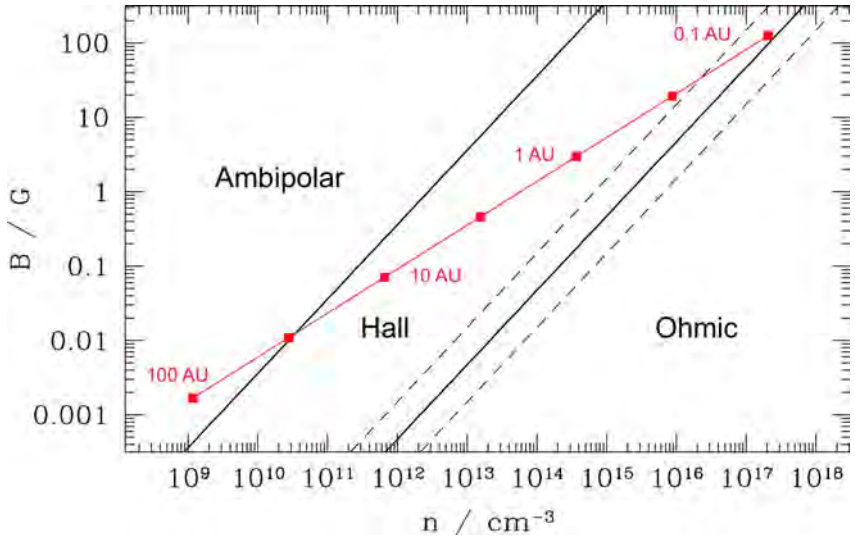

Figure 2.2.1: Figure adopted from Armitage (2015) that shows the importance of the non-ideal MHD effects in a PPD, depending on the magnetic field strength and the number density of neutral, n.

2.3 The Magneto-Rotational Instability (MRI)

In the last decade, the understanding of the accretion scenario of PPDs has moved from a turbulent viscosity induced by the MRI (Balbus and Hawley, 1998), to a laminar and almost inviscid flow relying on magneto-centrifugal (Bai and Stone, 2013; Gressel et al., 2015) and magneto-thermal (Bai et al., 2016) winds for angular momentum transport. Generally, one can argue that turbulent and laminar processes may coexist in the complex environment of PPDs. Thus, regardless the importance of the MRI for accretion, it can always affect the dynamics locally. For instance, it provides an efficient mechanism to stall the radial-drift of the dust, as we will show in this work (see Chapter 4). In the

following, we briefly describe the nature of the MRI and its evolution when considering a weakly ionized plasma.

Lets consider a differentially rotating disk with angular frequency $\Omega(r) = \Omega_0 r^q$, that is threaded by a vertical magnetic field, $\mathbf{B} = B\hat{z}$, and the fluid is frozen to the field lines, i.e., ideal MHD regime. Furthermore, lets assume that the flow is incompressible and waves propagate with the Alfvén speed, $v_{\rm A} = B/\sqrt{\mu_0 \rho}$. A locally perturbed fluid parcel that is removed from its orbital equilibrium to an inward position will rotate slightly faster than in its equilibrium state and furthermore will induce a displacement of the magnetic field lines. The magnetic tension will try to restore the field lines to the initial vertical equilibrium pulling the parcel to a new orbital position. If the magnetic tension is weak enough, a buckling of the field lines can occur, increasing the magnetic tensions and leading to runaway growth.

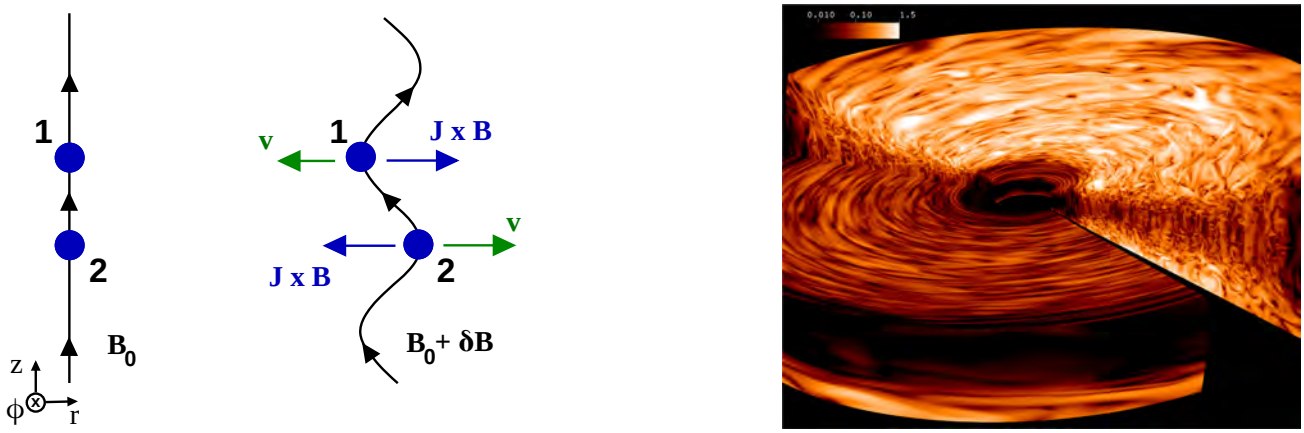

Figure 2.3.1: Left panel: Figure from Wardle and Salmeron (2012) that sketch the configuration adopted to illustrate the nature of MRI. The fluid perturbations represented by blue circles carry with them the vertical field line (black solid line), which will exert a tension force trying to restore the equilibrium state. Right panel: Figure from Flock et al. (2011) shows the non-linear evolution of the rms velocity in a global simulation of a PPD.

When the linear perturbation propagates along a periodic vertical direction, that is $\delta B = \mathrm{Re}\left(\sum_n \delta B_n e^{ik_n z - i\omega_n t}\right)$, the instability criteria (that gives a pure imaginary frequency ω_n) reads as

$$k_n^2 v_{\rm A}^2 + \frac{{\rm d}\Omega^2}{{\rm d}\ln r} < 0\,, \tag{2.3.1}$$

where k_n is a vertical wavenumber (Balbus and Hawley, 1991). For arbitrary small and real wavenumbers, this criterion imposes a necessary condition, $q < 0$, which is satisfied in PPDs that have a Keplerian rotation frequency, i.e., $q = -3/2$. After the linear phase, the instability saturates, giving a

turbulent self-regulated flow that dominates the dynamics (e.g., Balbus and Hawley, 1998).

In the case of a Keplerian disk, the maximum growth rate is given by $\omega = 3/4\Omega$ and the associated vertical wavenumber is $k_{\rm max} = \sqrt{15}\Omega/4v_{\rm A}$. The three non-ideal effects significantly affect the properties of the MRI (Wardle, 1999; Sano and Stone, 2002; Bai and Stone, 2013), for instance in a Hall dominated regime the wavenumber associated with the maximum growth is given by $k^2_{\rm max} = 2\Omega/\eta_{\rm H}$ (e.g., Mohandas and Pessah, 2017).

The coupling between the magnetic field and the neutral fluid at a length scale proportional to the characteristic wavelength of the MRI unstable modes is given by the Elsasser numbers (e.g. Wardle and Salmeron, 2012),

$$\Lambda_{\rm O} \equiv \frac{v_A^2}{\eta_{\rm O}\Omega}\,, \qquad \Lambda_{\rm A} \equiv \frac{v_A^2}{\eta_{\rm A}\Omega}\,, \qquad \Lambda_{\rm H} \equiv \frac{v_A^2}{\eta_{\rm H}\Omega}\,, \tag{2.3.2}$$

which are dimensionless parameter commonly used to describe the importance of the non-ideal effects at different locations of the PPDs. Moreover, the relative importance of the Hall term can, in general, be defined via the Hall length that was introduced in Section 2.2 and is redefined here as,

$$L_{\rm H} \equiv \eta_{\rm H}\, v_{\rm A}^{-1}\,, \tag{2.3.3}$$

(Pandey and Wardle, 2008; Kunz and Lesur, 2013). This definition will be adopted within this work when addressing the strength of the Hall diffusion in our disk models. This is motivated by the work of Kunz and Lesur (2013), where, employing a an incompressible non-stratified shearing box disk model, they found that if $L_{\rm H}/H \gtrsim 0.2$ the MRI saturates to a new regime where the self-organization mechanism starts to be operative. The typical length, H, can be adopted as the hydrostatic scale height of a vertical stratified disk. Thus, $L_{\rm H}/H$ provides a dimensionless control parameter for this new saturation regime of the MRI.

3

Numerical Scheme for Multispecies Momentum Transfer

In this chapter we will focus on the momentum transfer between multiple species. First, we present an asymptotically and unconditionally stable numerical scheme to solve the collisions between an arbitrary number of species.

Aimed at studying dust dynamics, we implement this numerical method in the publicly available code FARGO3D. To validate our implementation, we develop a test suite for an arbitrary number of species, based on analytical or exact solutions of problems related to perfect damping, damped sound waves and global gas-dust radial drift in a disk. In particular, we obtain first-order, steady-state solutions for the radial drift of multiple dust species in protoplanetary disks, in which the pressure gradient is not necessarily small.

We show that the implementation in the MHD code FARGO3D will always converge to the correct analytical asymptotic equilibrium solution. We then conclude that our scheme is suitable, and very robust, to study the self-consistent dynamics of several fluids. In particular, it can be used for solving the collisions between gas and dust in protoplanetary disks, with any degree of coupling. To our knowledge, such a complete assessment of the numerical scheme has never been done, so it constitutes one of the major achievements of the present work.

3.1 Implicit update

In this section we will focus on the numerical solution of the velocity for a set of colliding species. The method assumes a linear drag force in the velocity[1] and all the collision frequencies satisfy the symmetry relation defined in Eq. (2.1.5). After introducing the implicit update, we show that it conserves momentum to machine precision. In addition, we demonstrate several properties of the numerical scheme in order to show that it is asymptotically stable, that is, the numerical error is always bound and converges to zero as the timestep, or the number of integration steps, increases.

Considering only the collision term in the momentum equation (see Eq. (2.1.1)) the acceleration of the i-species reads as

$$\frac{\mathrm{d}\mathbf{v}_i}{\mathrm{d}t} = -\frac{1}{\rho_i}\sum_{j=1}^{N}\alpha_{ij}\left(\mathbf{v}_i - \mathbf{v}_j\right) . \tag{3.1.1}$$

Note that Eq. (3.1.1) is a first-order differential equation, and can be solved by:

(i) *Analytical methods*: Such a linear system defines a regular eigenvalue problem. This method is probably the best choice if the problem is isolated because there is no need of any discretization, i.e., no truncation error. The system is non-symmetric, and a transformation is needed in other to use an efficient eigenvalue solver. As a result, two matrix transformations are required, plus the eigenvalue solver, to obtain a full update of the velocity, which makes this approach numerically expensive as the number of species increases. Furthermore, if the equation is combined with numerical integrators (for example in an MHD code), the numerical errors of the solution will be dominated by the step with lowest precision. Thus, it might be redundant to use an such an exact method for solving the collisions. Finally, if the collision rate depends on the velocity, the system becomes non-linear and, as we will show, this is not a limitation for our implicit method.

(ii) *Time-explicit method*: Explicit methods may provide a rather fast convergence to the equilibrium solution in comparison to the implicit integration. However, large collision rates in an explicit update impose a very restrictive stability condition when solving for a mixture of multiple fluids (see e.g. Vorobyov et al., 2018; Stoyanovskaya et al., 2018). This makes the computation slower, significantly affecting the performance of a code.

(iii) *Time-implicit method*: This is the adopted method in this work and it will be discussed in this

[1] In Section 3.2.4.5 we show that the method recover solutions in non linear drag force regimes.

section.

The most straightforward formula for an implicit update is obtained by expressing Eq.3.1.1 in finite differences and evaluating the velocities on the R.H.S. in the advanced time (backward Euler method), i.e.,

$$\frac{\mathbf{v}_i^{n+1} - \mathbf{v}_i^n}{\Delta t} = -\sum_{j \neq i} \alpha_{ij}^n \left(\mathbf{v}_i^{n+1} - \mathbf{v}_j^{n+1} \right) . \tag{3.1.2}$$

Eq. (3.1.2) corresponds to a set of $3N$ linear algebraic equations for the unknown $\mathbf{v}^{n+1}$ velocities, which can be written in a more convenient way as

$$\mathbf{v}_i^{n+1} \left[1 + \Delta t \sum_{j \neq i} \alpha_{ij}^n \right] - \Delta t \sum_{j \neq i} \alpha_{ij}^n \mathbf{v}_j^{n+1} = \mathbf{v}_i^n . \tag{3.1.3}$$

A more compact form of Eq. (3.1.3) is obtained by defining the column vectors

$$\mathbf{V}_k = \left[\mathbf{v}_1 \cdot \mathbf{e}_k , \ \ldots \ , \ \mathbf{v}_N \cdot \mathbf{e}_k \right]^{\mathsf{T}} , \tag{3.1.4}$$

that is, $\mathbf{V}_k$ is formed by the projection of the velocity of each species along the direction of the unit vector $\mathbf{e}_k$, with $k = 1, 2, 3$. The superscript T stands for transpose. With this, Eq. (3.1.3) can be written as a matrix equation

$$\mathbf{T}\mathbf{V}_k^{n+1} = \mathbf{V}_k^n , \tag{3.1.5}$$

where

$$\mathbf{T} = \mathbf{I} + \Delta t \mathbf{M} , \tag{3.1.6}$$

is an $N \times N$ matrix, $\mathbf{I}$ is the identity matrix, and the (i, j)-element of the matrix $\mathbf{M}$ is

$$\mathbf{M}_{ij} \equiv \sum_{k \neq i}^{N} \alpha_{ik}^n \delta_{ij} - \alpha_{ij}^n \left(1 - \delta_{ij} \right) . \tag{3.1.7}$$

The first and second terms in Eq. (3.1.7) set the diagonal and non-diagonal elements of $\mathbf{M}$, respectively. Because $\mathbf{T}$ is nonsingular (see Section 3.2.2.1), the solution of Eq. (3.1.5) exists.

Stone (1997) showed a simple solution of Eq. (3.1.5) for two fluids. However, the complexity of these solutions rapidly increases with N, making them impractical. Thus, we prefer to solve Eq. (3.1.5) numerically by means of Gaussian elimination with partial pivoting (see e.g. Press et al., 2007, Chapter 2).

As an example we show a 4×4 version of the matrix $\mathbf{M}$,

$$\mathbf{M} = \begin{pmatrix} \alpha_{12}+\alpha_{13}+\alpha_{14} & -\alpha_{12} & -\alpha_{13} & -\alpha_{14} \\ -\alpha_{21} & \alpha_{21}+\alpha_{23}+\alpha_{24} & -\alpha_{23} & -\alpha_{24} \\ -\alpha_{31} & -\alpha_{32} & \alpha_{31}+\alpha_{32}+\alpha_{34} & -\alpha_{34} \\ -\alpha_{41} & -\alpha_{42} & -\alpha_{43} & \alpha_{41}+\alpha_{42}+\alpha_{43} \end{pmatrix} . \tag{3.1.8}$$

3.2 Properties of the implicit scheme

Two important properties of the method arise from Eq. (3.1.5). These are momentum conservation to machine precision and asymptotic stability for any Δt.

3.2.1 Momentum conservation to machine precision

The implicit scheme, defined by Eq. (3.1.5), conserves total momentum to machine precision. This property can be demonstrated by comparing the momentum before and after the application of the operator $\mathbf{T}$.

We first calculate the momentum of the system at time t_n, and write the old velocities in terms of the new ones via Eq. (3.1.5). Defining $a_{ij} = \Delta t \alpha_{ij}^n$, it follows that

$$\begin{aligned}
&\sum_i \rho_i \mathbf{v}_i^n \\
&= \sum_i \rho_i \sum_j \left[\left(1 + \sum_{k \neq i} a_{ik} \right) \delta_{ij} - a_{ij} \left(1 - \delta_{ij} \right) \right] \mathbf{v}_j^{n+1} \\
&= \sum_j \mathbf{v}_j^{n+1} \sum_i \rho_i \left[\left(1 + \sum_{k \neq i} a_{ik} \right) \delta_{ij} - a_{ij} \left(1 - \delta_{ij} \right) \right] \\
&= \sum_j \mathbf{v}_j^{n+1} \left[\rho_j + \rho_j \sum_{k \neq i} a_{jk} - \sum_{i \neq j} \rho_i \frac{\rho_j}{\rho_i} a_{ji} \right] \\
&= \sum_j \mathbf{v}_j^{n+1} \rho_j \left[1 + \sum_{k \neq i} \left(a_{jk} - a_{jk} \right) \right] \\
&= \sum_j \rho_j \mathbf{v}_j^{n+1} ,
\end{aligned} \tag{3.2.1}$$

where we have used the Condition (2.1.5) and replaced i by k in the last step. In this calculation, the densities are evaluated at time t_n because the collision step does not modify them. We thus conclude that,

$$\sum_i \rho_i \mathbf{v}_i^{n+1} = \sum_i \rho_i \mathbf{v}_i^{n} = \cdots = \sum_i \rho_i \mathbf{v}_i^{0} \,, \tag{3.2.2}$$

implying that the implicit scheme conserves momentum to machine precision.

3.2.2 Stability and convergence of the implicit scheme

In this section, we first demonstrate that $\mathbf{T}^{-1}$ exists, is diagonalizable with one as an eigenvalue, strictly positive, and right stochastic. We then use these properties to address the stability and convergence of the implicit scheme.

3.2.2.1 T is nonsingular

The demonstration of this property relies on the Geršgorin circle theorem (Geršgorin, 1931), which identifies a set of disks in the complex plane defined as $\{\mathcal{D}_i\}$ with $i = 1, \ldots, N$, where all the eigenvalues of a complex square matrix are contained. Each disk is centered at the diagonal matrix element $\mathbf{M}_{ii}$ and has a radius $R_i = \sum_{j=1, j\neq i}^{N} \mathbf{M}_{ij}$. Thus, each row of the matrix $\mathbf{M}$ defines a disk with radius equals to its center (each row of $\mathbf{M}$ sums to zero) and every eigenvalue lies within at least one of those disks.

To show that $\mathbf{T}$ is nonsingular, it is enough to prove that zero is not an eigenvalue of it. We first note that, if λ_T is an eigenvalue of $\mathbf{T} = \mathbf{I} + \Delta t \mathbf{M}$, then $\lambda_M = (\lambda_T - 1)/\Delta t$ is an eigenvalue of $\mathbf{M}$. Upper and lower bounds for λ_M can be found by means of the Geršgorin circle theorem which, from Eq. (3.1.7), implies

$$0 \leq \lambda_M \leq 2 \max_{k=1,\ldots,N} \left(\sum_{j\neq k}^{N} \alpha_{kj} \right) . \tag{3.2.3}$$

Hence, all the eigenvalues of $\mathbf{M}$ are real and non-negative. Because $\lambda_T = 1 + \Delta t \lambda_M$, the Condition 3.2.3 automatically implies that zero is not an eigenvalue of $\mathbf{T}^{-1}$, provided $\Delta t > 0$. This concludes our demonstration that $\mathbf{T}$ is nonsingular.

As a short note that will be useful for future references, we show that zero is an eigenvalue of $\mathbf{M}$ with

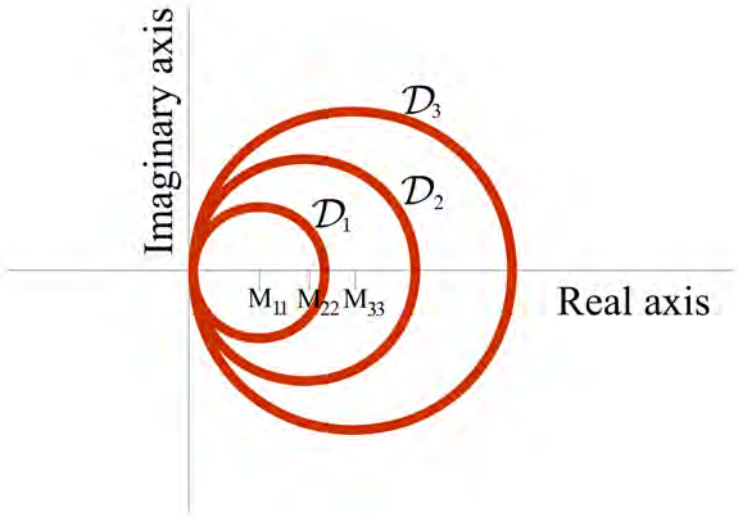

Figure 3.2.1: Schematic representation of the Gershgorin disks of the matrix $\mathbf{M}$ with dimension 3×3 .

an associated eigenvector $\mathbf{x}^{\mathsf{T}} = (1, .., 1) \equiv \mathbf{1}^{\mathsf{T}}$. Adding all the entries of any arbitrary i-row of $\mathbf{M}$ gives

$$\sum_{k=1}^{N} \mathbf{M}_{ik} = 0\,, \tag{3.2.4}$$

then,

$$\mathbf{M}\mathbf{x} = \left(\sum_{k=1}^{N} \mathbf{M}_{0k}, \ldots, \sum_{k=1}^{N} \mathbf{M}_{Nk} \right) = 0\mathbf{x}\,, \tag{3.2.5}$$

thus, $\lambda_M = 0$ is eigenvalue and $\mathbf{M}$ is singular.

3.2.2.2 $\mathbf{T}^{-1}$ is diagonalizable

First, we note that $\mathbf{M}$ and $\mathbf{T}$ commute because $\mathbf{MT} = \mathbf{M} + \Delta t \mathbf{M}^2 = \mathbf{TM}$, which implies that both matrices are diagonalizable under the same similarity transformation. Thus, to prove that $\mathbf{T}^{-1}$ is similar to a diagonal matrix, $\mathbf{\Lambda}$, it is enough to show that $\mathbf{M}$ is diagonalizable.

In the following we demonstrate that $\mathbf{M}$ is similar to a real symmetric matrix $\mathbf{S}$ under the transformation $\mathbf{M} = \mathbf{D}^{-1}\mathbf{S}\mathbf{D}$. Because $\mathbf{S}$ is a real symmetric matrix, it is similar to a diagonal form under an orthogonal transformation $\mathbf{Q}$, then it follows that $\mathbf{QD}$ defines the transformation that diagonalize $\mathbf{M}$.

To prove that $\mathbf{M}$ is similar to $\mathbf{S}$, we define the similar diagonal transformation

$$\mathbf{D}_{ij} \equiv \sqrt{\frac{\rho_0}{\rho_j}}\delta_{ij} = \eta_j \delta_{ij} \,, \tag{3.2.6}$$

for any arbitrary ρ_0, and show that $\mathbf{S} = \mathbf{D}^{-1}\mathbf{M}\mathbf{D}$ is symmetric. We first calculate

$$\begin{aligned}
\left(\mathbf{D}^{-1}\mathbf{M}\right)_{ij} &= \sum_k \mathbf{D}^{-1}_{ik}\mathbf{M}_{kj} \\
&= \sum_k \eta_k \delta_{ik} \left(\sum_{l\neq k} \alpha_{kl}\delta_{kj} - \alpha_{kj}\left(1-\delta_{kj}\right) \right) \\
&= \sum_k \eta_k \delta_{ik} \sum_{l\neq k} \alpha_{kl}\delta_{kj} - \sum_k \eta_k \delta_{ik}\alpha_{kj}\left(1-\delta_{kj}\right) \\
&= \sum_{l\neq j} \eta_j \alpha_{jl}\delta_{ij} - \eta_i \alpha_{ij}\left(1-\delta_{ij}\right) \,.
\end{aligned} \tag{3.2.7}$$

from which we can obtain $\mathbf{S}_{ij}$

$$\begin{aligned}
\mathbf{S}_{ij} = \left(\mathbf{D}^{-1}\mathbf{M}\mathbf{D}\right)_{ij} &= \sum_k \left(\mathbf{D}^{-1}\mathbf{M}\right)_{ik}\mathbf{D}_{kj} \\
&= \sum_k \left[\sum_{l\neq k} \eta_k \alpha_{kl}\delta_{ik} - \eta_i \alpha_{ik}\left(1-\delta_{ik}\right) \right] \eta_j^{-1}\delta_{kj} \\
&= \sum_k \eta_k \eta_j^{-1}\delta_{ik} \sum_{l\neq k} \alpha_{kl} - \sum_k \eta_i \eta_j^{-1}\alpha_{i,k}\left(1-\delta_{ik}\right)\delta_{kj} \\
&= \sum_{l\neq k} \alpha_{jl}\delta_{ij} - \alpha_{ij}\eta_i\eta_j^{-1}\left(1-\delta_{ij}\right) \,.
\end{aligned} \tag{3.2.8}$$

Finally, the symmetry of $\mathbf{S}$ is proven by using Eq. (2.1.5), i.e., $\alpha_{ij} = \alpha_{ji}\eta_j^2\eta_i^{-2}$.

$$\mathbf{S}_{ij} = -\alpha_{ij}\eta_i\eta_j^{-1}\left(1-\delta_{ij}\right) = -\alpha_{ji}\eta_j\eta_i^{-1}\left(1-\delta_{ij}\right) = \mathbf{S}_{ji} \,, \quad \text{for } i \neq j \,. \tag{3.2.9}$$

3.2.2.2.1 Alternative demonstration: Since $\mathbf{M}$ and $\mathbf{T}$ commute they are simultaneously diagonalizable. Therefore, to prove that $\mathbf{T}^{-1}$ is diagonalizable, it is enough to show that $\mathbf{M}$ is similar to a (real) symmetric matrix, i.e., $\mathbf{S} = \mathbf{D}^{-1}\mathbf{M}\mathbf{D}$ with $\mathbf{S} = \mathbf{S}^{\mathsf{T}}$. We demonstrate this as follows: Defining the diagonal matrix, $\mathbf{R}$, with elements $R_{ij} = \rho_i/\rho_0\delta_{ij}$, for any arbitrary ρ_0 and $i, j = 1, \ldots N$, Eq. (2.1.5) implies $R_{ik}M_{kj} = R_{jk}M_{ki}$, i.e., $\mathbf{R}\mathbf{M} = (\mathbf{R}\mathbf{M})^{\mathsf{T}}$ is symmetric. Because $\mathbf{R}$ is diagonal it follows that $\mathbf{R}\mathbf{M} = \mathbf{M}^{\mathsf{T}}\mathbf{R}$. Multiplying this last equality, to both left and right, by the matrix $\mathbf{R}^{-1/2}$,

we obtain $\mathbf{R}^{1/2}\mathbf{M}\mathbf{R}^{-1/2} = \mathbf{R}^{-1/2}\mathbf{M}^{\mathsf{T}}\mathbf{R}^{1/2} = (\mathbf{R}^{1/2}\mathbf{M}\mathbf{R}^{-1/2})^{\mathsf{T}}$. This demonstrates that the matrix $\mathbf{S} = \mathbf{D}^{-1}\mathbf{M}\mathbf{D}$ with $\mathbf{D} = \mathbf{R}^{-1/2}$ is symmetric.

3.2.2.2.2 Diagonal form of $\mathbf{T}^{-1}$: We define $\mathbf{P}$ as the matrix of which the columns are the eigenvectors of $\mathbf{M}$, thus

$$\mathbf{M} = \mathbf{P}\mathbf{J}\mathbf{P}^{-1}, \qquad \mathbf{T} = \mathbf{I} + \Delta t\mathbf{P}\mathbf{J}\mathbf{P}^{-1}. \tag{3.2.10}$$

with $\mathbf{J}$ the Jordan normal form of $\mathbf{M}$. Then, it follows that

$$\mathbf{P}\mathbf{T}^{-1}\mathbf{P}^{-1} = [\mathbf{I} + \Delta t\mathbf{J}]^{-1} \equiv \mathbf{\Lambda} \tag{3.2.11}$$

and each element of the diagonal form $\mathbf{\Lambda}$ is

$$\mathbf{\Lambda}_{ij} = \frac{1}{1 + \Delta t\lambda_{Mi}}\delta_{ij}\,, \tag{3.2.12}$$

with λ_{Mi} the ith eigenvalue of $\mathbf{M}$. Note that the similar transformation defined by $\mathbf{P}$ is independent of Δt because it diagonalizes $\mathbf{M}$ and it has one column with all the entries equal to one, because $\mathbf{1}^{\mathsf{T}}$ is an eigenvector of $\mathbf{M}$ (and $\mathbf{T}$) as we have shown in Section 3.2.2.1.

3.2.2.3 $\mathbf{T}^{-1}$ is right stochastic

A right stochastic matrix is defined as a matrix of which entries are non-negative and with each row summing to one.

First, we show that each ith row of $\mathbf{T}^{-1}$ satisfies $\sum_{j=1}^{N}\mathbf{T}^{-1}_{ij} = 1$. From Eq. (3.1.7), it is clear that all the rows of $\mathbf{T}$ sum to one, i.e.,

$$\sum_{j=1}^{N}\mathbf{T}_{ij} = 1 + \Delta t\sum_{j=1}^{N}\mathbf{M}_{ij} = 1\,, \tag{3.2.13}$$

and because,

$$1 = \sum_{j=1}^{N}\delta_{ij} = \sum_{j=1}^{N}\left(\sum_{k=1}^{N}\mathbf{T}^{-1}_{ik}\mathbf{T}_{kj}\right) = \sum_{j=1}^{N}\mathbf{T}^{-1}_{kj}\left(\sum_{k=1}^{N}\mathbf{T}_{jk}\right) = \sum_{j=1}^{N}\mathbf{T}^{-1}_{kj}\,. \tag{3.2.14}$$

Furthermore, for any $\Delta t > 0$

$$\mathbf{T}_{ij} < 0\,, \quad \text{for } i \neq j\,, \tag{3.2.15}$$

so $\mathbf{T}$ belongs to the group of matrices for which non-diagonal entries are all negative, $T \in \mathbb{Z}^{n\times n}$.

To prove that the inverse of $\mathbf{T}$ is non-negative we use a theorem from Berman and Plemmons (1979) (see Theorem 2.3, Chapter 6). The theorem states that any matrix that (i) belongs to the group of $\mathbb{Z}^{n\times n}$ matrices and (ii) its eigenvalues are all real and positive has a non-negative inverse. Such a matrix belongs to a very special type of matrices defined as the $\mathbb{M}$-matrices group. Condition (i) follows from the definition of $\mathbf{T}$ (as we mentioned before) and condition (ii) was demonstrated in Section 3.2.2.1 using the Geršgorin circle theorem. Thus we conclude that $\mathbf{T}^{-1}$ is a right stochastic matrix.

3.2.2.4 $\mathbf{T}^{-1}$ is strictly positive

In the previous section we show that $\mathbf{T}^{-1}$ is non-negative, and in this section we prove that none of its entries is zero, that is a strictly positive matrix.

Theorem 2.7 in chapter 6 from Berman and Plemmons (1979) states that the inverse, $\mathbf{T}^{-1}$, of an irreducible non-singular $\mathbb{M}$-matrix is strictly positive, i.e., $\mathbf{T}^{-1}_{ij} > 0$ for all $i, j \in 1 \ldots N$. Since we show in Section 3.2.2.3 that $\mathbf{T}$ is a nonsingular $\mathbb{M}$-matrix, it only remains to be demonstrated that $\mathbf{T}$ is irreducible.

Theorem 2.7 in chapter 2 from Berman and Plemmons (1979) states that a matrix $\mathbf{T}$ is irreducible if and only if its direct graph, $G(\mathbf{T})$, is strongly connected. $G(\mathbf{T})$ consists of n vertices $P_1, \ldots, P_n$, where an edge leads from P_i to P_j if and only if $\mathbf{T}_{ij} \neq 0$. Furthermore, it is strongly connected if for any ordered pair (P_i, P_j) of vertices, there exists a path that leads from P_i to P_j. Clearly, if all the species collide with each other, then $\mathbf{T}_{ij} \neq 0$ for all i, j and $G(\mathbf{T})$ is strongly connected. This statement holds, even when neglecting direct collisions between species i and j, provided that each species collides with another (proxy) species k. This is because the path from P_i to P_j is defined through P_k.

The idea behind the demonstration can be better understood via a simple example. We consider a case with 3 species where in (A) all the species collide against each other, (B) Species 1 collides with species 2 and 3 and vice versa, but species 2 and 3 do not collide, and (C) species 1 collides with species 2 and

3 but without a back reaction (no feedback).

$$\mathbf{T}_{\mathrm{A}} = \begin{pmatrix} 1+\Delta t\,(\alpha_{12}+\alpha_{13}) & -\Delta t\alpha_{12} & -\Delta t\alpha_{13} \\ -\Delta t\alpha_{21} & 1+\Delta t\,(\alpha_{21}+\alpha_{23}) & -\Delta t\alpha_{23} \\ -\Delta t\alpha_{31} & -\Delta t\alpha_{32} & 1+\Delta t\,(\alpha_{31}+\alpha_{32}) \end{pmatrix},$$

$$\mathbf{T}_{\mathrm{B}} = \begin{pmatrix} 1+\Delta t\,(\alpha_{12}+\alpha_{13}) & -\Delta t\alpha_{12} & -\Delta t\alpha_{13} \\ -\Delta t\alpha_{21} & 1+\Delta t\alpha_{21} & 0 \\ -\Delta t\alpha_{31} & 0 & 1+\Delta t\alpha_{31} \end{pmatrix},$$

$$\mathbf{T}_{\mathrm{C}} = \begin{pmatrix} 1+\Delta t\,(\alpha_{12}+\alpha_{13}) & -\Delta t\alpha_{12} & -\Delta t\alpha_{13} \\ -\Delta t\alpha_{21} & 1+\Delta t\alpha_{21} & 0 \\ 0 & 0 & 1 \end{pmatrix}. \tag{3.2.16}$$

Figure 3.2.2 shows the corresponding graphs for the cases (A), (B) and (C). In the case (A) all the vertices are connected because $T_{ij} \neq 0$ for all i, j. In the case (B), because there are no collisions between species-2 and species-3 the vertices P_2 and P_3 are not directly connected, but it is still possible to move from P_2 to P_3 through P_1, thus the graph of T_{B} is strongly connected. Removing the back reaction of species 1 onto species 3 from the case B makes it impossible to move from P_3 to P_1, thus the graph of T_{C} is not strongly connected and T_{C} is not irreducible.

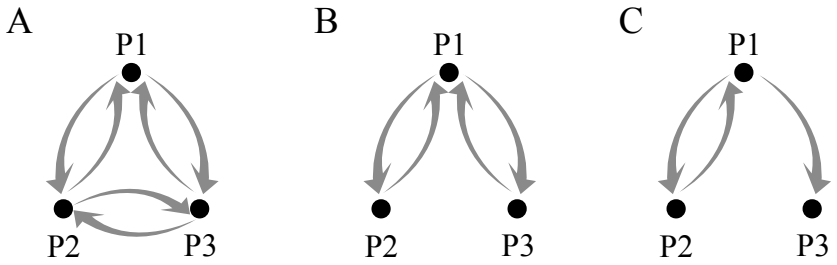

Figure 3.2.2: Graphs of the matrices $\mathbf{T}_{\mathrm{A}}$, $\mathbf{T}_{\mathrm{B}}$ and $\mathbf{T}_{\mathrm{C}}$

3.2.2.5 Asymptotic stability

The implicit scheme defined by Eq. (3.1.5) is asymptotically stable. This is,

$$\text{(a)} \lim_{\mathrm{n}\to\infty} \mathbf{T}^{-\mathrm{n}}\mathbf{V}_{\mathrm{k}}^{0} - \mathbf{c} = 0 \quad \text{and} \quad \text{(b)} \lim_{\Delta\mathrm{t}\to\infty} \mathbf{T}^{-1}\mathbf{V}_{\mathrm{k}}^{\mathrm{n}} - \mathbf{c} = 0\,, \tag{3.2.17}$$

for some constant vector $\mathbf{c}$ and any vector $\mathbf{V}_k^0$. The vector $\mathbf{c}$ defines the equilibrium state of the system and the Eqs. (3.2.17) imply that if we integrate for an arbitrary large (a) number of steps, or (b) time step, the system converges to the equilibrium state. In the following we demonstrate that these two limits exist and correspond to the velocity of the center of mass of the system.

3.2.2.5.1 Arbitrary large number of steps ($\lim n \to \infty$)**:** To prove this property we use that $\mathbf{T}^{-1}$ is a right stochastic and strictly positive matrix (see Sections 3.2.2.3 and 3.2.2.4). Hence, from the Perron-Frobenius Theorem (Perron, 1907), $\mathbf{T}^{-1}$ converges to a matrix with identical rows, i.e.,

$$\lim_{n\to\infty} \left(\mathbf{T}^{-n}\right)_{ij} = p_j \,, \tag{3.2.18}$$

where p_j is the j^{th} element of a vector $\mathbf{p}$. In the following, we only use that $\mathbf{p}$ is constant.

By definition, for any direction $\mathbf{e}_k$, the implicit scheme satisfies

$$\mathbf{V}_k^{n+1} = \mathbf{T}^{-1}\mathbf{V}_k^n = \cdots = \mathbf{T}^{-(n+1)}\mathbf{V}_k^0 \,. \tag{3.2.19}$$

It then follows that the asymptotic limit is

$$\lim_{n\to\infty} \mathbf{V}_k^{n+1} = \lim_{n\to\infty} \mathbf{T}^{-(n+1)}\mathbf{V}_k^0 \equiv V_{\mathrm{c},k}\mathbf{1}^{\mathsf{T}}. \tag{3.2.20}$$

where $\mathbf{1}^{\mathsf{T}}$ is a vector whose elements are all equal to one and $V_{\mathrm{c},k} = \mathbf{p}\cdot\mathbf{V}_k^0$. Since momentum is conserved, it follows that

$$V_{\mathrm{c},k}\sum_{j=1}^{N}\rho_j = \sum_{j=1}^{N}\rho_j V_{jk}^0 \,, \tag{3.2.21}$$

from which we prove that the asymptotic limit (3.2.20) corresponds to the velocity of the center of mass, $V_{\mathrm{CM},k}$, defined as

$$V_{\mathrm{CM},k} = \frac{\sum_{j=1}^{N}\rho_j V_{jk}^0}{\sum_{j=1}^{N}\rho_j} \,. \tag{3.2.22}$$

Thus, we conclude that the numerical method converges asymptotically to the velocity of the center of mass, and this is independent of the choice of Δt.

3.2.2.5.2 Arbitrary large time step ($\lim \Delta t \to \infty$)**:** Now, we address the problem of the stability and convergence for any sufficiently large time step. In Section 3.2.2.2, we have shown that $\mathbf{T}^{-1}$ is diagonalizable, with diagonal form

$$\mathbf{\Lambda}_{ij} = \frac{1}{1 + \Delta t \lambda_{Mi}} \delta_{ij} \,, \tag{3.2.23}$$

where λ_{Mi} are the eigenvalues of $\mathbf{M}$, with $\lambda_{Mj} = 0$ for some j.

Because $\mathbf{T}^{-1}$ is right stochastic, $\lambda_{Mj} = 0$ has algebraic multiplicity equal to one. Thus, for any sufficiently large time step, all the entries of $\mathbf{\Lambda}$ approach zero, except $\Lambda_{jj} = 1$. After applying the similar transformation that diagonalizes the system, Eq. (3.1.5) adopts the form

$$\hat{\mathbf{V}}_k^{n+1} = \mathbf{\Lambda} \hat{\mathbf{V}}_k^n \,, \tag{3.2.24}$$

where $\hat{\mathbf{V}}_k = \mathbf{P}^{-1}\mathbf{V}_k$, with $\mathbf{P}$ the matrix of which the columns are the eigenvectors of $\mathbf{T}^{-1}$. In the limit of large Δt, Eq. (3.2.24) reads

$$\lim_{\Delta t \to \infty} \left(\hat{\mathbf{V}}_k \right)_i^{n+1} = \hat{V}_{j,k}^n \delta_{ij} \,. \tag{3.2.25}$$

Because we set $\Lambda_{jj} = 1$ and $\mathbf{T}^{-1}$ is right stochastic, all the entries of the column $\mathbf{P}_j$ are equals to one, that is, $\mathbf{P}_j = \mathbf{1}^\mathsf{T}$. We thus obtain

$$\lim_{\Delta t \to \infty} \mathbf{V}_k^{n+1} = \lim_{\Delta t \to \infty} \mathbf{P} \hat{\mathbf{V}}_k^{n+1} = \hat{V}_{j,k}^n \mathbf{P}_j = \hat{V}_{j,k}^n \mathbf{1}^\mathsf{T} \,, \tag{3.2.26}$$

which is equivalent to Eq. (3.2.20) and we used the condition that $\mathbf{P}$ does not depend on Δt.

Eqs. (3.2.20) and (3.2.26) allow us to conclude

$$\lim_{n \to \infty} \mathbf{T}^{-n} \mathbf{V}_k^0 = \lim_{\Delta t \to \infty} \mathbf{T}^{-1} \mathbf{V}_k^n = V_{\mathrm{CM}} \mathbf{1}^\mathsf{T} \,, \tag{3.2.27}$$

and the implicit scheme is thus asymptotically and unconditionally stable.

3.2.3 Implementation in FARGO3D

We now describe the implementation of the implicit scheme in the code FARGO3D. We first note that the collision term, described by Eq. (3.1.1), is decoupled from the source and transport substeps.

Thus, aside from the collisions, we evolve every species according to the same algorithms described in Benítez-Llambay and Masset (2016).

The implicit scheme for solving the collision term involves an extra substep, in which the velocity of each species is partially updated according to the Eq. (3.1.5). There are three different options to place this additional partial update: (i) before the source step, (ii) after the source step and before the transport step or, (iii) after the transport step. Options (i) and (iii) are equivalent after the first time step, which we discard because the dust species do not reach the asymptotic limit in the presence of additional forces. In this case the relative velocity between the dust and gas asymptotes to its terminal velocity, where the additional forces are in balance with the drag forces. Since in options (i) and (iii) the drag forces are computed in the absence of additional forces, they cannot correctly reproduce this limit (Booth et al., 2015). Option (ii) reproduces this limit because evaluating the collision term after the source term is equivalent to a solution treating both terms together. While not strictly necessary, the

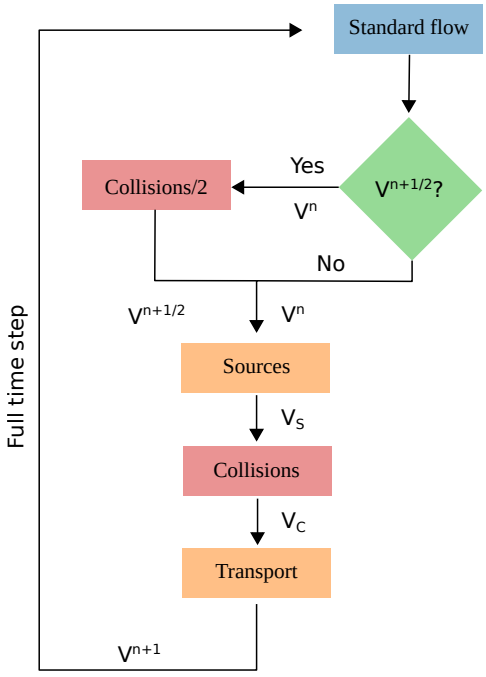

Figure 3.2.3: Figure 1 from Benítez-Llambay et al. (2019). Flowchart of our implementation. During a generic time step Δt, depending on whether the predictor step is required, we call the collision routine using a time step $\Delta t/2$, and obtain a partially updated velocity $V^{n+1/2}$. We then update the velocities by sources and use the output, $V_{\rm S}$, as input for the collision step. After this, we use the updated velocities, $V_{\rm C}$, as input for the transport step, from which we obtain the updated velocity, V^{n+1}. The flow then returns to the standard flow, from which a full update has been performed.

coupling between the source and collision steps can be improved by adding a predictor step before the

source step. The source step consists of a partial update of the form:

$$\frac{\partial \mathbf{v}}{\partial t} = \mathcal{S}(\mathbf{v}) \,, \tag{3.2.28}$$

where $\mathcal{S}$ are sources that depend on the velocities. In finite differences, the previous equation reads:

$$\mathbf{v}^{n+1} = \mathbf{v}^{n} + \Delta t \mathcal{S}(\mathbf{v}^{*}) \,. \tag{3.2.29}$$

In the standard implementation, we assume $\mathbf{v}^{*} = \mathbf{v}^{n}$. However, we can improve the coupling between collision and source steps by setting $\mathbf{v}^{*} = \mathbf{v}^{n+1/2}$, i.e., by estimating an advanced velocity from the collision step with a time step $\Delta t/2$. We then compute the source step using a full time step and finally calculate the collision step with a full time step.

For completeness, Figure 3.2.3 presents a flowchart of our implementation. During a generic time step, depending on whether the predictor step is required, the collision routine is called using a time step $\Delta t/2$ and calculates a partially updated velocity. Then, the codes updates the velocities of all the species by the standard source terms and uses the updated velocities as input for the collision step. During this step, the code solves Eq. (3.1.5) and then uses the updated velocities as input for the transport step. After the transport step, a full update has been performed.

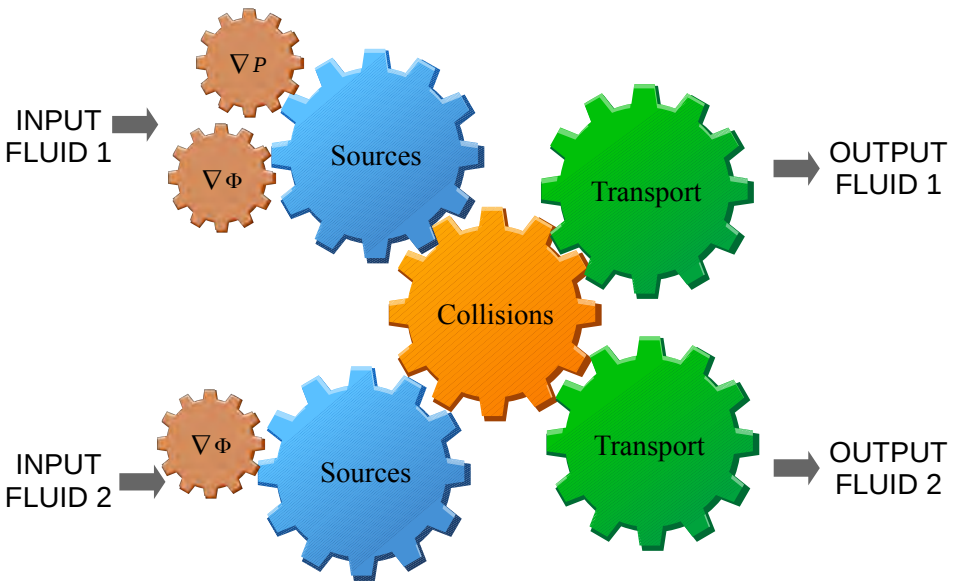

Figure 3.2.4: Schematic representation of the splitting in FARGO3D including the collision module.

3.2.3.1 Convergence to the correct asymptotic equilibrium

A system of multiple species that exchange momentum due to their velocity difference converges to an equilibrium state where, in absence of any external acceleration, the relative velocities are zero. To illustrate this property and to explain why the operator splitting satisfies this condition we consider a 1D system of N species, each of them experiencing an external acceleration, $\mathbf{a}$, that we assume ot be independent of the velocity as well as the collision rate, α_{ij}. Neglecting the advection term, the momentum equation of the species j reads as

$$\frac{\partial v_j}{\partial t} = -\frac{1}{\rho_i}\sum_{j=1}^{N}\alpha_{ij}(v_i - v_j) + a_j\,, \tag{3.2.30}$$

which is the analytical form of the equation that is solved between the source and collisions step.

The system can be arranged into a matrix form as

$$\partial_t \mathbf{V} + \mathbf{M}\mathbf{V} = \mathcal{A}\,, \tag{3.2.31}$$

with $\mathbf{V} = (v_1, \ldots, v_n)$ and $\mathcal{A} = (a_1, \ldots, a_n)$, and $\mathbf{M}$ being the matrix defined in Eq. (3.1.7). Because $\mathbf{M}$ is similar to a diagonal form, $\mathbf{J}$, (see Section 3.2.2.2) the system can be decoupled, and for each $\lambda_{Mj} \neq 0$ we have

$$\hat{v}_j = \frac{1}{\lambda_{Mj}}\left(\hat{a}_j + \hat{c}_j e^{-\lambda_{Mj}t}\right)\,, \tag{3.2.32}$$

with $\hat{v}_j$ and $\hat{a}_j$ being the j-component of the vectors $\mathbf{P}^{-1}\mathbf{V}$ and $\mathbf{P}^{-1}\mathcal{A}$, respectively. The unique case with $\lambda_{Mi} = 0$ gives

$$\hat{v}_i = \hat{a}_i t + \hat{c}_i. \tag{3.2.33}$$

The constants defined as $\hat{c}$ are determined by the initial condition. The solution in the diagonal space can be written as

$$\hat{\mathbf{V}} = \left(\frac{1}{\lambda_{M0}}\left(\hat{a}_0 + \hat{c}_0 e^{-\lambda_{M0}t}\right), \ldots, \hat{a}_i t + \hat{c}_i, \ldots, \frac{1}{\lambda_{MN}}\left(\hat{a}_N + \hat{c}_N e^{-\lambda_{MN}t}\right)\right). \tag{3.2.34}$$

After applying the transformation $\mathbf{V} = \mathbf{P}\hat{\mathbf{V}}$, and using the fact that the ith column of $\mathbf{P}$ is equal to $\mathbf{1}^{\mathsf{T}}$,

each species has a velocity of the form

$$v_k = \hat{a}_i t + \hat{c}_i + \sum_{j=1, j\neq i}^{N} \mathbf{P}_{kj} \frac{1}{\lambda_{Mj}} \left(\hat{a}_j + \hat{c}_j e^{-\lambda_{Mj} t} \right) . \tag{3.2.35}$$

In the limit of $t \to \infty$ all the velocities go to the limit $v_k \to \hat{a}_i t + \hat{c}_i + \sum_{j=1, j\neq i}^{N} \mathbf{P}_{kj} \frac{1}{\lambda_{Mj}} \hat{a}_j$ and the velocity difference reads as

$$\lim_{t\to\infty} v_{k+1} - v_k = \sum_{j=1, j\neq i}^{N} \left(\mathbf{P}_{k+1j} - \mathbf{P}_{kj} \right) \frac{(\mathbf{P}^{-1}\mathcal{A})_j}{\lambda_{Mj}} , \tag{3.2.36}$$

which is zero in absence of any acceleration $\mathbf{a}$.

In the simple case where only two species are considered this equation transform into

$$\lim_{t\to\infty} v_1 - v_2 = \lambda^{-1}(a_1 - a_2). \tag{3.2.37}$$

The same limit obtained in Eq. (3.2.36) can be obtained when combining the source step (with an explicit integration) and the collision step (with the implicit update for the velocity 3.1.2).

Using the same notations as before, but in a discretized case where n indicates a time step, a full update reads as

$$\begin{aligned} \mathbf{V}^{n+s} &= \mathbf{V}^n + \Delta t \mathcal{A}^n , \\ \mathbf{V}^{n+1} &= \mathbf{T}^{-1} \mathbf{V}^{n+s} , \end{aligned} \tag{3.2.38}$$

where $\mathbf{V}^{n+s}$ are the updated velocities after the source step. Using the properties studied in Section 3.2.2.2 the velocities in the diagonal space satisfy

$$\hat{\mathbf{V}}^{n+1} = \left(\frac{1}{1 + \Delta t \lambda_{M0}} (\hat{v}_0^n + \Delta t \hat{a}_0^n), \ldots, \hat{v}_i^n + \Delta t \hat{a}_i^n, \ldots, \frac{1}{1 + \Delta t \lambda_{MN}} (\hat{v}_N^n + \Delta t \hat{a}_N^n) \right) , \tag{3.2.39}$$

where we assumed that $\lambda_{Mi} = 0$. Applying the transformation $\mathbf{V}^{n+1} = \mathbf{P}\hat{\mathbf{V}}^{n+1}$, each velocity can be written as

$$v_k^{n+1} = \hat{v}_i^n + \Delta t \hat{a}_i^n + \sum_{j=1, j\neq i}^{N} \mathbf{P}_{kj} \frac{1}{1 + \Delta t \lambda_{Mj}} (\hat{v}_j^n + \Delta t \hat{a}_j^n) , \tag{3.2.40}$$

which in the limit of $\Delta t \to \infty$ gives

$$\lim_{\Delta t \to \infty} v_{k+1}^{n+1} - v_k^{n+1} = \sum_{j=1, j \neq i}^{N} \left(\mathbf{P}_{k+1j} - \mathbf{P}_{kj}\right) \frac{\left(\mathbf{P}\mathcal{A}^n\right)_j}{\lambda_{Mj}}\,, \tag{3.2.41}$$

which is the discretized form of Eq. (3.2.36). In the simple case of considering only two species this reduces to

$$\lim_{\Delta t \to \infty} v_1^{n+1} - v_2^{n+1} = \lambda^{-1}\left(a_1^n - a_2^n\right). \tag{3.2.42}$$

3.2.4 Numerical tests

In this section, we discuss a part of the test suite presented in Benítez-Llambay et al. (2019). We use these tests to validate the accuracy, convergence properties and robustness of the method and implementation described in Sections 3.1 and 3.2.3. In all the following tests, the numerical solutions were obtained using a Courant-Friedrichs-Lewy (CFL) factor of 0.44 (Benítez-Llambay and Masset, 2016), unless a different value is specified.

3.2.4.1 Time evolution of a set of colliding species

When a set of N species evolves under the sole effect of the collision term, simple asymptotically convergent analytical solutions can be found. This simple test problem validates the correct implementation of the matrix solver and, at the same time, illustrates the convergence property described in Section 3.2.2.5.

As a first step, we show the steady-state solution of the problem, which gives insight into the fundamental property of the physical system, that is, the convergence of all the velocities towards the velocity of the center of mass. In Section 3.2.2.5, we have already shown that the implicit scheme satisfies this condition.

The steady-state momentum equation for a set of N species reduces to the matrix equation when considering only the drag force,

$$\mathbf{M}\mathbf{V}_k = 0\,. \tag{3.2.43}$$

Because the matrix $\mathbf{M}$, defined by Eq. (3.1.7), is singular (see Appendix 3.2.2.1), the system described by Eq. (3.2.43) admits a non-trivial solution. By direct calculation it can be shown that the (i, j)-element

of the echelon form of M is

$$E_{M,ij} = \delta_{ij} - \delta_{jN} \,, \tag{3.2.44}$$

This observation, combined with momentum conservation, allows us to conclude that

$$V_{1k} = \cdots = V_{Nk} = V_{\mathrm{CM},k} \,, \tag{3.2.45}$$

where $V_{\mathrm{CM},k}$ is the velocity of the center of mass, given by Eq. (3.2.22).

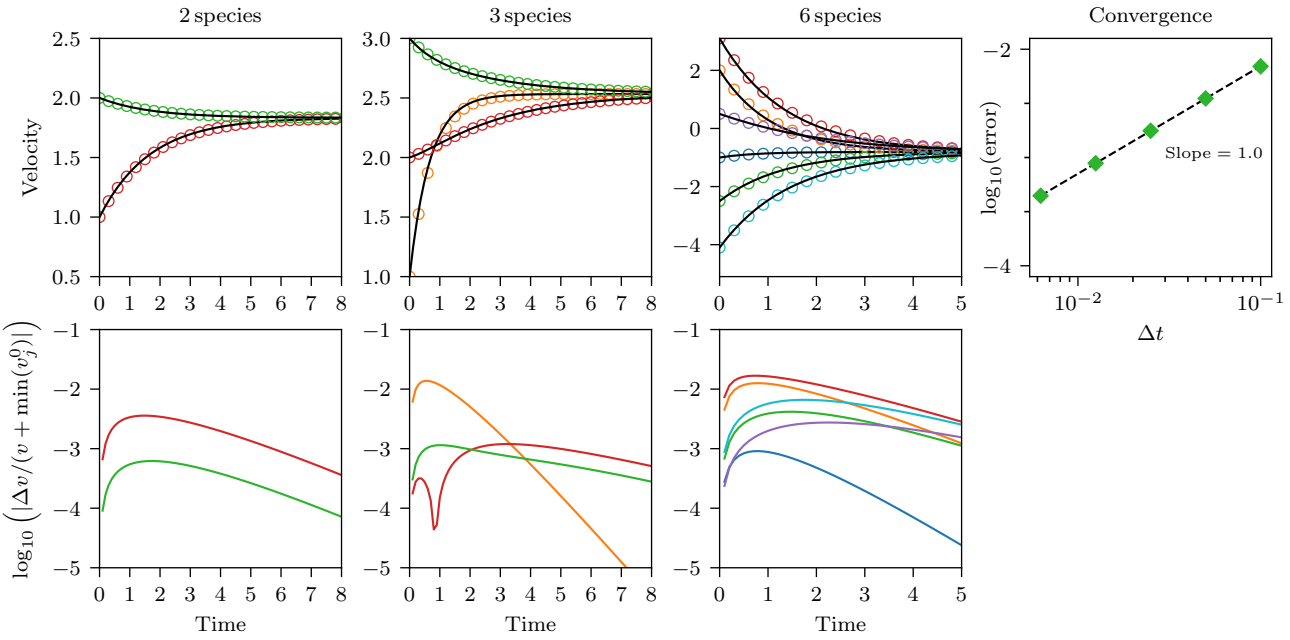

Figure 3.2.5: Figure 2 from Benítez-Llambay et al. (2019). Upper panels: Time evolution of the velocity for the various configurations described in Table 3.2.1. From left to right, we plot the evolution of two, three, and six species. The solid lines correspond to the analytical solution, given by Eq. (3.2.51). The open circles were obtained with our implementation, for which each color represents a different species. In all the panels, the velocities converge to the velocity of the center of mass of the system. Lower panels: Time evolution of the relative error between the numerical and the analytical solutions. The color code is the same one for the upper and lower panels. The time evolution of the velocities and errors are shown for the run with $\Delta t = 0.1$. In the rightmost panel, we plot, for the case with six species, the error (see Eq. (3.2.53)) as a function of the time step Δt, for five different time steps.

3.2.4.2 Evolution towards steady-state

We are not only interested in the steady-state solution of the system but also in the time evolution towards this asymptotic steady-state. The problem is independently described for any spatial component, so it is effectively a collection of 1-dimensional problems. Hence we omit the subscript k.

The temporal evolution of the system is described by the solution of

$$\frac{\partial \mathbf{V}}{\partial t} + \mathbf{M}\mathbf{V} = 0\,. \tag{3.2.46}$$

Without loss of generality, by expressing the solution of Eq. (3.2.46) as $\mathbf{V}(t) = \sum_j \tilde{\mathbf{V}}_j e^{-\lambda_j t}$, it reduces to the eigenvalue problem

$$\mathbf{M}\tilde{\mathbf{V}}_j = \lambda_j \tilde{\mathbf{V}}_j\,. \tag{3.2.47}$$

For simplicity, we define the collision rate $\alpha_{ij} \equiv \alpha_0$ for $i > j$ and $\alpha_{ij} = \rho_j/\rho_i\alpha_0$ for $i < j$, such that condition (2.1.5) is satisfied.

Defining the function

$$\zeta_j = \sum_{m=j+1}^{N} \rho_m\,, \tag{3.2.48}$$

the eigenvalues of $\mathbf{M}$ adopt the expression

$$\begin{aligned} \lambda_{j<N} &= \alpha_0 \left(j + \frac{\zeta_j}{\rho_j} \right)\,, \\ \lambda_N &= 0\,, \end{aligned} \tag{3.2.49}$$

with associated eigenvectors

$$\begin{aligned} \tilde{\mathbf{V}}_{j<N} &= \mathbf{e}_j - \frac{1}{\zeta_j} \sum_{m=j+1}^{N-1} \rho_{m-1}\mathbf{e}_m\,, \\ \tilde{\mathbf{V}}_N &= \sum_{k=1}^{N} \mathbf{e}_k\,. \end{aligned} \tag{3.2.50}$$

Thus, the solution reads

$$\begin{aligned} v_{j<N}(t) &= -\sum_{k=1}^{j-1} \frac{\rho_k c_k}{\zeta_k} e^{-\lambda_k t} + c_j e^{-\lambda_j t} + c_N\,, \\ v_N(t) &= -\sum_{k=1}^{N-1} \frac{\rho_k c_k}{\zeta_k} e^{-\lambda_k t} + c_N\,, \end{aligned} \tag{3.2.51}$$

where the coefficients c_j are

$$\begin{aligned} c_{j<N} &= v_j^0 - V_{\mathrm{CM}} + \sum_{k=1}^{j-1} \frac{\rho_k c_k}{\zeta_k}\,, \\ c_N &= V_{\mathrm{CM}}\,. \end{aligned} \tag{3.2.52}$$

3.2.4.3 Numerical solution

Table 3.2.1: Initial density, velocity, eigenvalues and coefficients needed to compute the solution of Eq. (3.2.51). In all the cases we set $\alpha_0 = 10^{-1}$.

j	ρ_j	v_j^0	λ_j	c_j
Two fluids				
1	0.2	1.0	0.6000000	-0.8300000
2	1.0	2.0	0.0000000	1.8333333
Three fluids				
1	0.2	1.0	1.5000000	-1.5333333
2	1.0	2.0	0.3800000	-0.6428571
3	1.8	3.0	0.0000000	2.5333333
Six fluids				
1	1.0	-1.0	1.3500000	-0.1925926
2	1.5	2.0	0.9333333	2.7920000
3	2.0	3.1	0.7500000	4.2727273
4	2.5	-2.5	0.6600000	-0.3777778
5	3.0	0.5	0.6166667	2.4769231
6	3.5	-4.1	0.0000000	-0.8074074

We compare the analytical solution found in Section 3.2.4.2 with the numerical solution obtained by solving the problem using the implicit scheme. We study the problem with two, three, and six different species. In order to do this, we set the initial condition on a 1D grid with 16 evenly distributed cells, over a periodic domain. We note, however, that this choice is arbitrary and, in practice, irrelevant. This is because the solution does not depend on spatial coordinates. The initial density, velocity, eigenvalues, and coefficients needed to compute both the numerical and analytical solutions for each run are summarized in Table 3.2.1. In all the cases, we set the collision rate $\alpha_0 = 10^{-1}$.

The first three panels of Figure 3.2.5 (from left to right) show the time evolution of the velocities. Each panel corresponds to a different configuration, as listed in Table 3.2.1. The lower panels Figure 3.2.5, present the relative error of the velocity for all the species, for the corresponding case on top. The time evolution of the error shows the asymptotic convergence demonstrated in Section 3.2.3.1. Regardless of the number of species, there is an excellent agreement between the analytical and numerical solutions.

3.2.4.4 Convergence with time step

For the case of six fluids, we additionally check expected first-order convergence rate in time of the implicit scheme. For this test, we performed five identical runs, in which we progressively decreased

the time step by factors of 2, starting with $\Delta t = 0.1$. The rightmost panel of Figure 3.2.5, displays the error as a function of the time step, defined as

$$\text{error}(\Delta t) = \left(\sum_{j=1}^{N} \langle v_j^{\Delta t}(t) - v_j(t) \rangle^2 \right)^{1/2} , \tag{3.2.53}$$

where $\langle\rangle$ denotes the time-average. As expected, the convergence is consistent with a first-order method, i.e., linear convergence with a slope equal to one.

3.2.4.5 Non-linear drag force

In some regimes, the collision rate might depend on the relative velocity between species, Δv. In these cases,Eqs. (3.1.1) become non-linear in the velocities. In principle, the implicit scheme described by Eq. (3.1.2) can not be used to update the velocities, since it assumes a linear velocity dependency of the drag force. However, tn the following we present simple tests of an approximation that allows us to circumvent this issue, which consists in assuming the system to be linear in Δv^{n+1}, and the collision rate, α^n, to be dependent on Δv^n. This approximation makes it possible for all the properties of the implicit scheme hold even in the non-linear drag regime. By means of a simple example, we show that this method is good enough to recover the solution of Eqs. (3.1.1) in the non-linear regime. For this test we adopt the three different collision rates presented in the Table 3.2.2.

Table 3.2.2: Collision rate α, for the different non-linear drag force laws shown in Fig 3.2.6. The coefficients γ, γ_q, γ_p, γ_m and b_m are all fixed to unity for the purpose of this test.

Linear	Quadratic	Power-law	Mixed
γ	$\gamma_q \lvert\Delta v\rvert$	$\gamma_p \lvert\Delta v\rvert^{1/p}$	$\gamma_m \sqrt{1 + b_m \lvert\Delta v\rvert^2}$

We write the analytic solutions of the non-linear drag force regime. We consider two species with initial densities and velocities, $\rho_1 = \rho_2 = 1$ and $v_1 = 20$, $v_2 = 10$, respectively, and obtain numerical solutions following Section 3.2.4.1. To this end the drag coefficient $\alpha \equiv \alpha(|\Delta v|)$, with $\Delta v = v1 - v2$. The system of equations transform into

$$\partial_t v_1 = -\alpha(|\Delta v|)(v_1 - v_2) , \tag{3.2.54}$$

$$\partial_t v_2 = -\alpha(|\Delta v|)(v_2 - v_1) , \tag{3.2.55}$$

Table 3.2.2 shows all the collision rates that we explored, where for the power-law regime we set the index $p = 2$.

Table 3.2.3: Analytical solution for the different non-linear drag force laws shown in Fig 3.2.6.

	Linear	Quadratic	Power-law	Mixed
$\frac{\Delta v}{\Delta v_0}$	$e^{-\gamma t}$	$(2\gamma_q t\lvert\Delta v_0\rvert + 1)^{-1}$	$\left(\sqrt{\lvert\Delta v_0\rvert}\gamma_2 t + 1\right)^{-2}$	$\frac{-2f(t)}{\Delta v_0^2 b_m f(t)^2 - 1}$

with $f(t) = \dfrac{e^{-2\gamma_m t}}{\sqrt{b_m \Delta v_0^2 + 1} + 1}$.

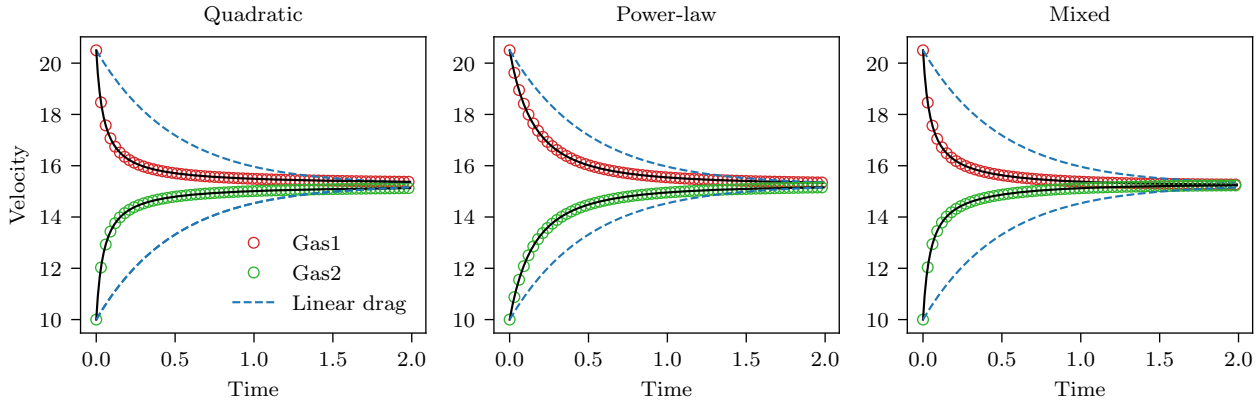

Figure 3.2.6: Figure 12 from Benítez-Llambay et al. (2019). Analytical (solid lines) and numerical (open circles) solutions for a quadratic (left panel), power law with $p = 2$ (center panel) and mixed (right panel) drag forces. The dashed line is the solution for a linear drag force.

Each panel of Figure 3.2.6 shows the analytical and numerical solutions, with solid lines and open circles, respectively. The dashed lines correspond to the solution obtained for a linear drag force. In all the non-linear drag regimes, the agreement between the analytical and numerical solutions is excellent.

3.3 Damping of a sound wave

Sound waves are a natural outcome of the fluid equations when pressure perturbations are considered. Dust fluids, however, cannot support sound waves. In systems composed of gas and dust species, sound waves can propagate – supported by the gas component – but their properties are modified due to the momentum exchange with the dust. Solutions for the case of one gas and one dust species were found by Laibe and Price (2012), who showed that sound waves are damped by the effect of the collision

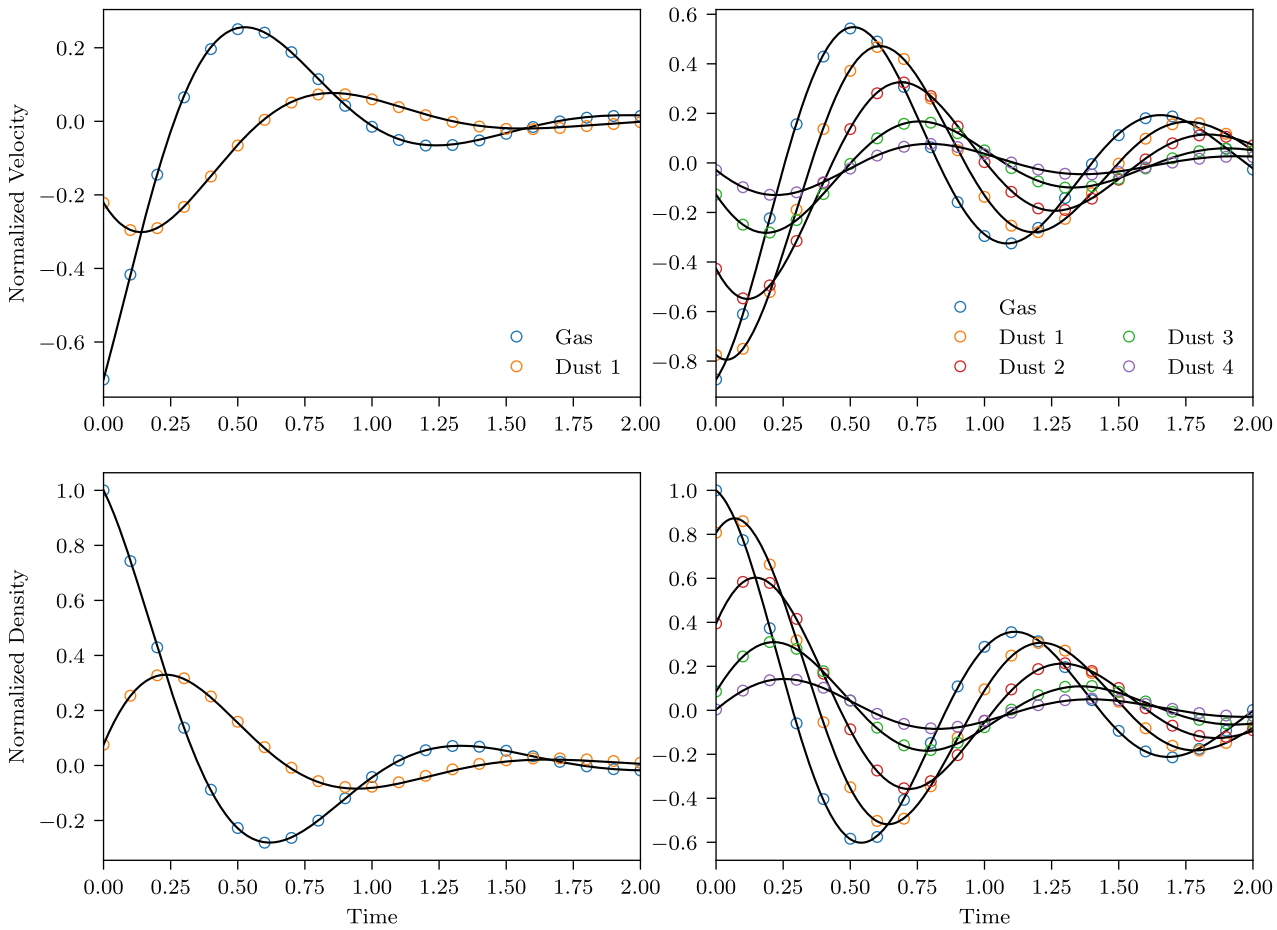

Figure 3.3.1: Figure 3 from Benítez-Llambay et al. (2019). Numerical (open circles) and analytical (solid lines) solutions of the test described in Section 3.3 for the configurations listed in Table 3.3.1. We plot the time evolution of the normalized velocity (upper panels) and density (lower panels). The results for one and four dust species are shown in the left and right panels, respectively. The blue circles correspond to the gas, while the other colors correspond to the dust species. All the solutions were obtained at $x = 0$. The normalized density and velocity are defined as $\delta\hat{\rho}/(A\rho^0)$ and $\delta\hat{v}/(Ac_\mathrm{s})$, respectively, with $A = 10^{-4}$.

between dust and gas. Solving this problem is relevant since it provides a direct – and perhaps the simplest – way to test the coupling between the implicit solver and the transport and source steps.

In the following, we derive the dispersion relation for the general problem of one gas and $N - 1$ dust species which, together with the general expression for the eigenvectors, allows us to find the full solution to the problem.

Table 3.3.1: Initial conditions for the damping of the sound wave test.

j	ρ_j	$\delta\hat{\rho}_j$	$\delta\hat{v}_j$	t_{sj}	ω
Two species					
g	1.000000	1.000000	$-0.701960 - 0.304924i$	–	$1.915896 - 4.410541i$
1	2.240000	$0.165251 - 1.247801i$	$-0.221645 + 0.368534i$	0.4	
Five species					
g	1.000000	1.000000	$-0.874365 - 0.145215i$	–	$0.912414 - 5.493800i$
1	0.100000	$0.080588 - 0.048719i$	$-0.775380 + 0.308952i$	0.100000	
2	0.233333	$0.091607 - 0.134955i$	$-0.427268 + 0.448704i$	0.215443	
3	0.366667	$0.030927 - 0.136799i$	$-0.127928 + 0.313967i$	0.464159	
4	0.500000	$0.001451 - 0.090989i$	$-0.028963 + 0.158693i$	1.000000	

3.3.1 Dispersion relation and eigenvectors

We now derive the dispersion relation for the case of one gas and $N-1$ dust species and find the general eigenvectors of the problem. For that, we assume that the gas pressure is given by $P = c_{\rm s}^2 \rho_{\rm g}$, with a constant sound speed, $c_{\rm s}$, and define the collision rate between the gas and dust species following Eq. (2.1.6), with $\alpha_j = t_{{\rm s}j}^{-1}$, where $t_{{\rm s}j}$ is the stopping time.

Assuming solutions of the form $\rho_j = \rho_j^0 + \delta\rho_j$ and $v_j = \delta v_j$, with ρ_j^0 constant, and neglecting quadratic terms in the perturbations, the continuity and momentum equations for the gas and dust species become

$$\frac{\partial \delta\rho_{\rm g}}{\partial t} + \rho_{\rm g}^0 \frac{\partial \delta v_{\rm g}}{\partial x} = 0\,, \tag{3.3.1}$$

$$\frac{\partial \delta\rho_j}{\partial t} + \rho_j^0 \frac{\partial \delta v_j}{\partial x} = 0\,, \tag{3.3.2}$$

$$\frac{\partial \delta v_{\rm g}}{\partial t} + \sum_{m=1}^{N-1} \frac{\epsilon_m^0}{t_{{\rm s}m}} (\delta v_{\rm g} - \delta v_m) + \frac{c_{\rm s}^2}{\rho_{\rm g}^0} \frac{\partial \delta\rho_{\rm g}}{\partial x} = 0\,, \tag{3.3.3}$$

$$\frac{\partial \delta v_j}{\partial t} + \frac{1}{t_{{\rm s}j}} (\delta v_j - \delta v_{\rm g}) = 0, \tag{3.3.4}$$

where $j = 1, ..., N-1$ is the index of the dust species.

We first note that the momentum equation is decoupled from the continuity equation for dust species, so the order of the problem is effectively reduced from $2N$ to $N+1$. Without loss of generality, we write any perturbation δf as $\delta f = \delta\hat{f} e^{ikx - \omega t}$, with k a real wavenumber. Thus, from Eqs. (3.3.1)-(3.3.4), we obtain the dispersion relation

$$F(\omega, \omega_{\rm s}) \equiv \omega^2 \left(1 + \sum_{m=1}^{N-1} \frac{\epsilon_m}{1 - \omega t_{{\rm s}m}} \right) + \omega_{\rm s}^2 = 0\,, \tag{3.3.5}$$

with $\omega_\mathrm{s} = kc_\mathrm{s}$. The singular values $\omega_m = t_{sm}^{-1}$ correspond to $\delta v_\mathrm{g} = 0$, $\delta\rho_\mathrm{g} = 0$, so are not considered.

Finally, the components of the associated eigenvectors are

$$\frac{\delta\hat{v}_\mathrm{g}}{c_\mathrm{s}} = -i\frac{\omega}{\omega_\mathrm{s}}\frac{\delta\hat{\rho}_\mathrm{g}}{\rho_\mathrm{g}^0}\,, \tag{3.3.6}$$

$$\frac{\delta\hat{v}_j}{c_\mathrm{s}} = -i\frac{\omega}{\omega_\mathrm{s}}\frac{1}{(1-\omega t_{\mathrm{s}j})}\frac{\delta\hat{\rho}_\mathrm{g}}{\rho_\mathrm{g}^0}\,, \tag{3.3.7}$$

$$\frac{\delta\hat{\rho}_j}{\rho_j^0} = \frac{1}{1-\omega t_{\mathrm{s}j}}\frac{\delta\hat{\rho}_\mathrm{g}}{\rho_\mathrm{g}^0}\,, \tag{3.3.8}$$

for any $\delta\hat{\rho}_\mathrm{g}$, which completes the solution of the problem.

3.3.2 Eigenvalues for the sound wave test problem

Eq. (3.3.5) can be written as a polynomial equation of degree $N+1$. In the following, we show that at least $N-1$ roots of (3.3.5) are real and positive and are thus associated with pure damping. We furthermore identify the intervals in which they can be found. This allows a simple bisection algorithm to be used to find them. We additionally explain how to use Vieta's formulae to find the final two roots which are, in general, complex. These two complex roots are the most interesting ones since they describe the propagation of damped sound waves. To solve the dispersion relation (3.3.5), we write it as the polynomial equation

$$P(\omega) = \omega^{N+1} + a_N\omega^N + \ldots + a_0 = 0\,. \tag{3.3.9}$$

The $N+1$ roots of (3.3.9) are the eigenvalues of the problem. The polynomial P has at least $N-1$ real positive roots. This is proven by first noticing that F is positive for $\omega < \min\left(t_{sm}^{-1}\right)$. Since $t_{sm} > 0$, no real root exists for $\omega < 0$. In addition, the one-sided limits of F satisfy

$$\lim_{\omega\to t_{sm}^{-1\pm}} F(\omega,\omega_\mathrm{s}) = \pm\infty\,, \tag{3.3.10}$$

i.e., the function changes sign at each side of the singular points, from which we conclude that there is at least one real positive root between two adjacent singular points, giving $N-2$ positive roots.

Furthermore, since

$$\lim_{\omega\to\infty} F(\omega,\omega_{\rm s}) = \infty\,, \tag{3.3.11}$$

there is at least one more positive root beyond the last singular point. All of these roots correspond to pure damping solutions.

An upper bound for the largest real root can be found. Defining $t_{{\rm s}N-1}^{-1}$ as the largest singular point, for $\omega \gg t_{{\rm s}N-1}^{-1}$, yields $f > 0$ if

$$1+\sum_{m=1}^{N-1}\frac{\epsilon_m}{1-\omega t_{{\rm s}m}} \simeq 1-\frac{1}{\omega}\sum_{m=1}^{N-2}\frac{\epsilon_m}{t_{{\rm s}m}}+\frac{\epsilon_{N-1}}{1-\omega t_{{\rm s}N-1}} > 0\,. \tag{3.3.12}$$

This expression is equivalent to the quadratic inequality

$$-t_{{\rm s}N-1}\omega^2+\left[1+\epsilon_{N-1}+t_{{\rm s}N-1}\sum_{m=1}^{N-2}\frac{\epsilon_m}{t_{{\rm s}m}}\right]\omega-\sum_{m=1}^{N-2}\frac{\epsilon_m}{t_{{\rm s}m}} > 0\,, \tag{3.3.13}$$

from which we find that the largest positive root of P is smaller than the largest root of Eq. (3.3.13).

Having found the $N-1$ roots of P, $\{\omega_1,\ldots,\omega_{N-1}\}$, we can use Vieta's formulae to find the remaining roots ω_N and ω_{N+1}

$$\omega_N\omega_{N+1} = (-1)^{N+1}\,a_0\prod_{j=1}^{N-1}\omega_j^{-1}\,, \tag{3.3.14}$$

$$\omega_N+\omega_{N+1} = -a_N-\sum_{j=1}^{N-1}\omega_j\,. \tag{3.3.15}$$

where a_0, a_N satisfy

$$a_0 = (-1)^{N-1}\,\omega_{\rm s}^2\prod_{j=1}^{N-1}t_{{\rm s}j}^{-1}\,, \tag{3.3.16}$$

$$a_N = -\sum_{j=1}^{N-1}t_{{\rm s}j}^{-1}\,(1+\epsilon_j)\,. \tag{3.3.17}$$

Eqs. (3.3.14) and (3.3.15) can be written as a second order polynomial equation, from which we obtain the final two roots, which are in general complex and the most interesting ones because they lead to the

propagation of the wave.

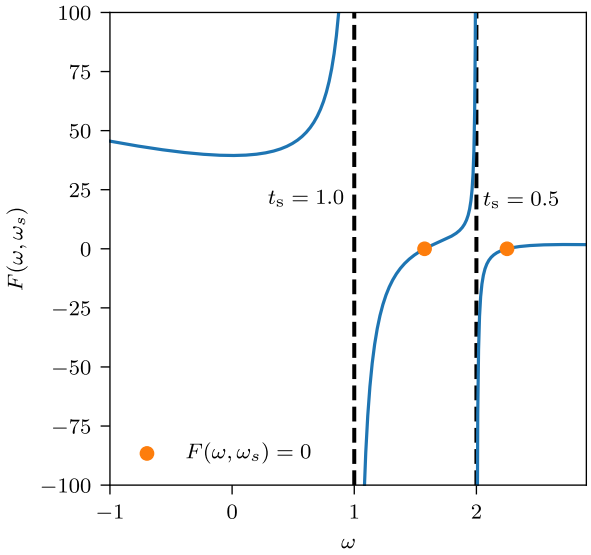

Figure 3.3.2: Example of the real roots of $F(\omega, \omega_s)$ for a case with two dust species with $t_s = 0.5$, $\epsilon_1 = 0.1$, and $t_s = 1$, $\epsilon_2 = 10$. The dashed lines shows the singularities at $\omega = 1/t_s$. Orange circles correspond to the two damping rates and $\omega_s = 2\pi$.

3.3.3 Numerical solution

Using the eigenstates as initial condition we obtain the numerical solutions for the oscillatory damped modes. From the two possible oscillatory modes, we choose only one because the other one is the complex conjugate, producing the same solution but propagating in the opposite direction. We do not consider the solutions that correspond to perfect damping because they behave as those studied in Section 3.2.4.1.

We study the cases of one gas fluid combined with one and four dust species, respectively. As initial condition we set a zero background velocity, constant background density, ρ_j^0, and perturbations, δf, of the form

$$\delta f = A \left[\mathrm{Re}\left(\delta \hat{f}\right) \cos(kx) - \mathrm{Im}\left(\delta \hat{f}\right) \sin(kx) \right] , \tag{3.3.18}$$

where A is a small amplitude needed to ensure linearity. We set its value to $10^{-4} c_s$ and $10^{-4} \rho_g^0$ for the velocity and density perturbations, respectively, and set $c_s = 1$. The background densities, perturbation amplitudes, stopping times, and complex eigenvalue for each case are listed in Table 3.3.1. We consider a domain of size $L = 1$, with spatial coordinate $x \in [0, L]$, split into 10^3 evenly spaced grid cells. We

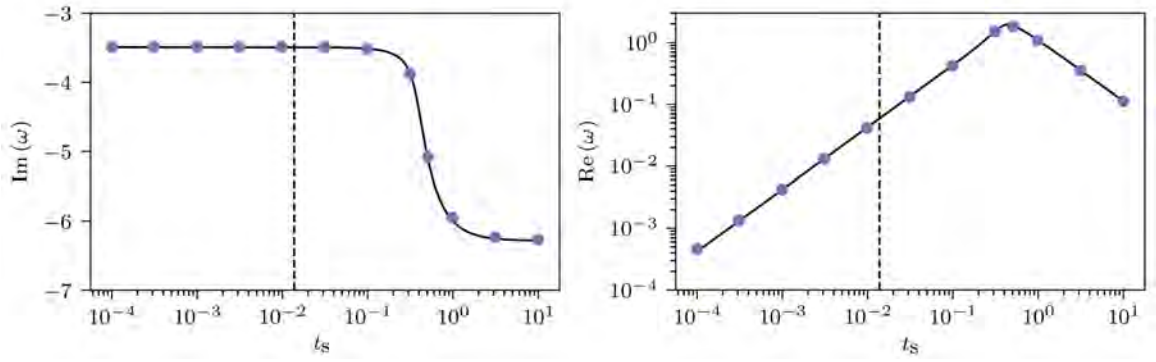

Figure 3.3.3: Figure 3 from Benítez-Llambay et al. (2019). Numerical (circles) and analytical (solid lines) imaginary and real part of the eigenvalue ω, as a function of the stopping time t_s, obtained for the two-fluid case described in Table 3.3.1. The dashed line corresponds to the time step $\Delta t = 1.375 \times 10^{-2}$, which is fixed for all the runs.

consider the wavenumber $k = 2\pi/L$ and set periodic boundary conditions.

Figure 3.3.1 shows the analytical (solid lines) and numerical (open circles) solutions, measured at $x = 0$ for the two considered configurations. The solution corresponding to different species is plotted with a different color. The first column shows the solution obtained for one gas and one dust species, while the second one shows the same for the case of five, one gas and four dust, species. In the upper and lower panels we plot the normalized velocity, defined as $\delta\hat{v}/(c_s A)$ and the normalized density, defined as $\delta\hat{\rho}/(\rho A)$, respectively. From Figure 3.3.1, it is clear that the analytical solution is successfully recovered by our implementation. This test validates the coupling of the drag force in combination with the source and transport steps for a wide range of stopping times.

To study the coupling of the implicit scheme with the transport and source steps in a more challenging situation, we test the damping of a sound wave for a range of stopping times $10^{-4} \leq t_s \leq 10$ and a fixed time step, such that we test both stiff and non-stiff regimes for the collisions. We consider the two-fluid problem described in Table 3.3.1, for different stopping times. We use a domain of size $L = 1$ and 32 cells, which sets a time step $\Delta t = 1.375 \times 10^{-2}$, given by the standard CFL condition of FARGO3D. For stopping times smaller than the time step the regime becomes more and more stiff. Note that, because of the CFL condition, the degree of stiffness depends on the resolution. We integrate the system until it reaches a final time $t = 10$. We measure the damping rate, $\mathrm{Re}(\omega)$, and the oscillatory frequency, $\mathrm{Im}(\omega)$ by fitting the numerical solutions. The upper and lower panels of Figure 3.3.3 show the analytical frequency and damping rate, respectively, together with the measurements from our simulations.

The error of the implicit scheme converges to zero asymptotically with Δt (see Section 3.2.2). Therefore,

for a fixed time step, the smaller the stopping time is, the stiffer the regime is and the faster the errors are damped. Furthermore, the excellent agreement of the oscillatory frequency permits to conclude that no phase-error is introduced by the implicit scheme, in the operator splitting approximation.

3.4 Steady-state, first-order drift solutions

In this section, we present the analytical solution of the steady-state radial drift for an arbitrary number of species, to first-order in the velocities with respect to an exact background. We then compare this analytical solution with the numerical one. The background is obtained by considering pressure gradients (which are not necessarily small) and neglecting drag forces between species. This solution generalizes that obtained by Nakagawa et al. (1986a), who presented a self-consistent first-order solution with respect to a Keplerian background for a disk, composed of gas- and one dust-species. In their approach, the background flow is obtained as the solution of the vertically integrated disk-equations when neglecting pressure and drag forces. This assumption implies that both the radial pressure gradient and the drag force are small perturbations that can be added linearly to the Keplerian velocity. However, the assumption of a small pressure gradient is not strictly necessary to find a background solution.

This generalization provides us with improved steady-state disk models which will allow us to thoroughly test our numerical method.

3.4.1 Generalized steady-state drift solutions

We consider a vertical integrated and axisymmetric disk in steady state. We assume a cylindrical coordinate system and an isothermal equation of state. The surface density, Σ, is the vertically integrated density, $\Sigma = \int_{-\infty}^{\infty} \rho(r,z)\mathrm{d}z$, and the vertically integrated pressure is $P = c_\mathrm{s}^2\Sigma$, with c_s the sound speed. The gravitational potential is $\Phi = -GM/r$, hence $\partial_r\Phi = v_\mathrm{K}^2/r$, with v_K the keplerian velocity. Furthermore, we assume a non-flared disk with constant aspect-ratio $h = c_\mathrm{s}/v_\mathrm{K}$, thus, $\partial_r P/\Sigma = c_\mathrm{s}^2/r\ (\mathrm{dlog}P/\mathrm{dlog}r) = h^2 v_\mathrm{K}^2/r\ (\mathrm{dlog}P/\mathrm{dlog}r)$. Under these assumptions (neglecting the

the magnetic contribution) Eqs. (2.1.1) read as

$$\begin{aligned}
\partial_r \left(r\Sigma_{\rm g} v_{{\rm g}r}\right) &= 0\,, \\
\partial_r \left(r\Sigma_{{\rm d},i} v_{{\rm d},ir}\right) &= 0\,, \\
v_{{\rm g}r}\partial_r v_{{\rm g}r} - \frac{v_{{\rm g}\varphi}^2}{r} &= -\frac{v_{\rm K}^2}{r}\left(1 + h^2 \frac{{\rm dlog}\ P}{{\rm dlog}\ r}\right) - \Omega_{\rm K} \sum_{j=1}^{N} \frac{\epsilon_j}{T_{{\rm s},j}} \left(v_{{\rm g}r} - v_{{\rm d},ir}\right)\,, \\
v_{{\rm g}r}\partial_r v_{{\rm g}\varphi} + \frac{v_{{\rm g}r} v_{{\rm g}\varphi}}{r} &= -\Omega_{\rm K} \sum_{j=1}^{N} \frac{\epsilon_j}{T_{{\rm s},j}} \left(v_{{\rm g}\phi} - v_{{\rm d},i\varphi}\right)\,, \\
v_{{\rm d},ir}\partial_r v_{{\rm d},ir} - \frac{v_{{\rm d},i\varphi}^2}{r} &= -\frac{v_{\rm K}^2}{r} + \frac{\Omega_{\rm K}}{T_{{\rm s},j}} \left(v_{{\rm g}r} - v_{{\rm d},ir}\right)\,, \\
v_{{\rm d},ir}\partial_r v_{{\rm d},i\varphi} + \frac{v_{{\rm d},ir} v_{{\rm d},i\varphi}}{r} &= \frac{\Omega_{\rm K}}{T_{{\rm s},j}} \left(v_{{\rm g}\varphi} - v_{{\rm d},i\varphi}\right)\,,
\end{aligned} \tag{3.4.1}$$

with $i = 1 \ldots N-1$ and $T_{\rm s}$ is the Stokes number which corresponds to the collision frequency normalized by the Keplerian frequency $\Omega_{\rm K} = v_{\rm K}/r$ (see Eq. 2.1.7).

Defining the constants

$$\eta \equiv \frac{h^2}{2}\frac{d\log P}{d\log r}\,, \quad \beta \equiv \sqrt{1+2\eta}\,, \tag{3.4.2}$$

and neglecting the drag force in the momentum equations, the exact background solution is

$$v_{{\rm g}r}^0 = 0, \quad v_{{\rm g}\phi}^0 = \beta v_{\rm K}\,, \qquad v_{{\rm d},ir}^0 = 0, \quad v_{{\rm d},i}^0 = v_{\rm K}\,, \tag{3.4.3}$$

with $i = 1 \ldots N-1$.

Given that the velocity is slightly modified by collisions one can approximate the velocity as the background solutions (3.4.3) plus a small deviation, i.e., $\mathbf{v} = \mathbf{v}^0 + \delta\mathbf{v}$.

Neglecting terms which are second-order in the perturbations, the Eqs. (3.4.1) turn into the following set of algebraic equations for the perturbed velocities

$$-2\beta\delta v_{{\rm g}\varphi} + \sum_{i=1}^{N} \frac{\epsilon_i}{T_{{\rm s}i}} \left(\delta v_{{\rm g}r} - \delta v_{{\rm d},ir}\right) = 0\,, \tag{3.4.4}$$

$$\frac{\beta}{2}\delta v_{{\rm g}r} + \sum_{i=1}^{N} \frac{\epsilon_i}{T_{{\rm s}i}} \left(\delta v_{{\rm g}\varphi} - \delta v_{{\rm d},i\varphi}\right) = \left(1-\beta\right) v_{\rm K} \sum_{i=1}^{N} \frac{\epsilon_i}{T_{{\rm s}i}}\,, \tag{3.4.5}$$

$$-2\delta v_{\mathrm{d},i\varphi} + \frac{1}{T_{\mathrm{s}i}}\left(\delta v_{\mathrm{d},ir} - \delta v_{\mathrm{g}r}\right) = 0\,, \tag{3.4.6}$$

$$\frac{1}{2}\delta v_{\mathrm{d},ir} + \frac{1}{T_{\mathrm{s}i}}\left(\delta v_{\mathrm{d},i\varphi} - \delta v_{\mathrm{g}\varphi}\right) = \frac{(\beta-1)\,v_{\mathrm{K}}}{T_{\mathrm{s}i}}\,, \tag{3.4.7}$$

for $i = 1, \ldots, N$ and where we used that $v_\varphi^2/r \simeq (v_\varphi^0)^2/r + 2\Omega_{\mathrm{K}}\beta\delta v_\varphi$ and $v_r\partial_r v_\varphi + v_r v_\varphi/r \simeq \delta v_r \beta\left(\partial_r v_{\mathrm{K}} + \Omega_{\mathrm{K}}\right)$ when neglecting quadratic terms in the perturbed velocity.

From Eqs. (3.4.6) and (3.4.7) we obtain the dust velocities in terms of the gas velocity which, in combination with Eqs.(3.4.4) and (3.4.5), allow us to find the gas velocity perturbations. Defining

$$\mathcal{S}_N \equiv \sum_{i=1}^{N} \frac{\epsilon_i}{1+T_{\mathrm{s}i}^2}\,, \quad \mathcal{Q}_N \equiv \sum_{i=1}^{N} \frac{\epsilon_i T_{\mathrm{s}i}}{1+T_{\mathrm{s}i}^2}\,, \tag{3.4.8}$$

the gas velocity perturbations read

$$\delta v_{\mathrm{g}r}(r) = -2\beta\mathcal{Q}_N\Psi\,(\beta-1)\,v_{\mathrm{K}}\,, \tag{3.4.9}$$

$$\delta v_{\mathrm{g}\varphi}(r) = -\left[\left(\mathcal{S}_N+\beta\right)\mathcal{S}_N + \mathcal{Q}_N^2\right]\Psi\,(\beta-1)\,v_{\mathrm{K}}\,, \tag{3.4.10}$$

with $\Psi \equiv \left[\left(\mathcal{S}_N+\beta\right)^2 + \mathcal{Q}_N^2\right]^{-1}$.

Finally, the expressions for the dust velocity perturbations are

$$\delta v_{\mathrm{d},ir} = \frac{2T_{\mathrm{s}i}}{1+T_{\mathrm{s}i}^2}\,(\beta-1)\,v_{\mathrm{K}} + \frac{\delta v_{\mathrm{g}r} + 2T_{\mathrm{s}i}\delta v_{\mathrm{g}\varphi}}{1+T_{\mathrm{s}i}^2}\,, \tag{3.4.11}$$

$$\delta v_{\mathrm{d},i\varphi} = \frac{1}{1+T_{\mathrm{s}i}^2}\,(\beta-1)\,v_{\mathrm{K}} + \frac{2\delta v_{\mathrm{g}\varphi} - T_{\mathrm{s}i}\delta v_{\mathrm{g}r}}{2\left(1+T_{\mathrm{s}i}^2\right)}\,. \tag{3.4.12}$$

The velocities given by Eqs. (3.4.9) and (3.4.12) are solution only if they satisfy the continuity equations. In our case we are assuming a non-flared disk[2] and the perturbed velocities are proportional to the Keplerian velocity, thus, the continuity equations

$$\partial_r\left(r\Sigma_{\mathrm{g}}^0\delta v_{\mathrm{g}r}\right) = 0\,, \tag{3.4.13}$$

$$\partial_r\left(r\Sigma_{\mathrm{d},i}^0\delta v_{\mathrm{d},ir}\right) = 0\,, \tag{3.4.14}$$

[2]Flared disks might not be solved in this formalism because momentum and continuity equation impose conditions on the radial velocity that are non consistent, in other words, the problem is over-determined.

are satisfied for power-law background surface-density profiles with exponent $\mathrm{d}\log\Sigma/\mathrm{d}\log r = -1/2$.

When considering only one dust species and $h \ll 1$, we can write $\beta \simeq 1 + \eta$ and Eqs. (3.4.9) – (3.4.12) are the solution found by Nakagawa et al. (1986a). Dipierro et al. (2018) found a similar solution for an arbitrary number of species for a viscous disk assuming a Keplerian background. This solution can be easily improved following our approach.

3.4.2 Radial drift for a particle-size distribution

In this section we present the results obtained when considering different particle-size distributions and compare with the solution obtained with only one particle size. The distributions follows from the form described in Section 2.1.2. We consider a disk with $h = 0.05$ and $\Sigma = \Sigma_0 r_{\mathrm{AU}}^{-1/2}$ with $\Sigma_0 = 1$. The units are such $GM = 1$. Because we assume a distribution of Stokes numbers rather than particle-sizes, we are implicitly assuming that the sizes vary with radius.

The first result is the radial velocity of the gas for different distributions and its comparison to the two-fluid problem. We then calculate the fraction of particles that are drifting outwards, their corresponding Stokes numbers and the fraction of the total mass of the distribution that they represent. We adopt four different slopes, $q = \{1, 2.5, 3.5, 4\}$ and three dust-to-gas dust density ratio $\epsilon = 0.01, 01, 1$. For all the distributions we fixed the minimum Stokes number to $T_{\mathrm{s,min}} = 10^{-4}$ and we continuously varying the maximum, $T_{\mathrm{s,max}}$, from 10^{-3} up to 10.

Figure 3.4.1 shows the results. The radial drift of the gas is slightly affected by the distribution compared to the two-fluid drift solution. As the slope increases the peak of the drift-velocity moves to larger Stokes numbers. Increasing the dust-to-gas density ratio also affects the maximum of the radial velocity. Distributions with $q \sim 4$ have a maximum drift at Stokes numbers larger than unity. Similarly, when $\epsilon > 0.1$ the maximum drift moves towards $T_{\mathrm{s,max}} = 10$.

3.4.3 Numerical solution

We now use the steady-state solution found in the previous section to test our implementation in the context of PPDs. For this test we initialize a large-scale 1-dimensional disk using the first-order steady-state solutions, given by Eqs. (3.4.9)-(3.4.12). The computational domain spans from $r = 1$ to $r = 100$, evenly spaced in a logarithmic grid over 1024 points. We assume an isothermal equation of

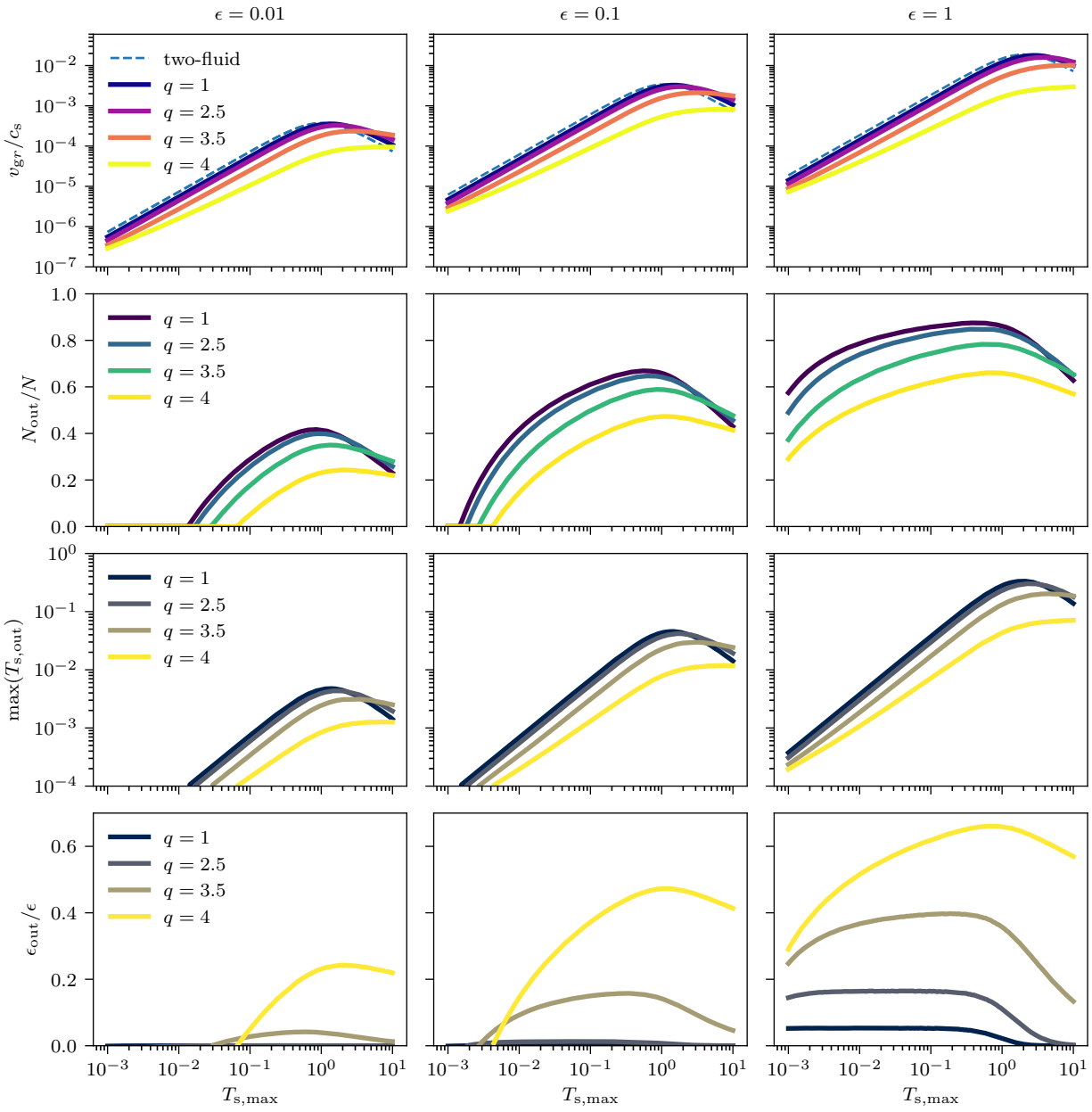

Figure 3.4.1: From top to bottom: The panels in the first-row show the radial velocity of the gas as a function of the maximum Stokes number of the distribution. The dashed line shows the radial velocity when only the species with the maximum Stokes number is considered, i.e. the two-fluid problem. The second row shows the fraction of dust-species that are moving outwards (following the gas drift) as a function of the maximum Stokes number of the distribution. The third row shows the maximum Stokes number of all the species that are drifting outwards as a function of the maximum Stokes number of the distribution. In all the panels colors correspond to different slopes of the particle-size distribution. The bottom panels show the fraction of the total dust-to-gas density ratio that is moving outwards. The values are obtained at $r = 10\text{AU}$.

state and set boundary conditions equal to the steady-state solutions for all the species. The absence of perfect numerical equilibrium at the beginning of the runs produces wave-patterns that propagate in the

disk and reach the boundaries of the mesh. To remove these spurious waves from the active domain we use small damping zones close to the boundaries (de Val-Borro et al., 2006). These buffers extend over a region such that $\Delta\Omega = 0.1$ for both the inner and outer buffers (see Benítez-Llambay et al., 2016), and the damping rate is set to one third of the local Keplerian frequency. We only damp the density and radial velocity to the value given by the initial condition.

We consider two cases with two species and two cases with four species, and vary the degree of coupling between gas and dust species. To test our implementation in more challenging regimes, we furthermore vary the aspect ratio, h, of the disk, adopting the values $h \in [0.05, 0.1, 0.15]$ for each configuration. In all the cases, we numerically integrate the 1D disks until the steady-state is reached. The initial surface density of the gas component is not relevant for these tests.

Figure 3.4.2 displays the radial velocities for all the cases studied. The results corresponding to different species and different parameters are shown in each column and row, respectively. From top to bottom, the first two rows, show the radial velocity for the two-fluid configurations and the last two rows the radial velocities for the test with four fluids. The analytical solutions, given by Eqs. (3.4.9) and (3.4.11), are plotted with solid lines. The different colors represent different species. Furthermore different symbols account for different aspects ratios. The parameters corresponding to each species are quoted inside of the panels. We observe that the agreement between the analytical and numerical solutions is excellent, and independent of the parameters and the number of species. The tests presented here validate simultaneously the first-order steady-state disk-drift solution and our numerical implementation.

We note an interesting result from the multiple fluid test. In the two fluids cases it is impossible to revert the sign of the radial velocity of the dust component due to momentum conservation, but, its magnitude depends on the dust-to-gas density ratio as well as the degree of coupling to the gas. However, this is no longer true in the more general case of multiple species. In this case, very well coupled dust can be transported outwards by the gas (see, for example, the fourth panel of the third row and the second and third panels of the fourth row). We finally comment that the same level of agreement was observed for the azimuthal velocity, which is not surprising given that the two directions are coupled.

3.4.3.1 Convergence test

We additionally performed a convergence test with resolution. This test consists in taking one particular case and measuring the error of the numerical solution when changing the resolution. For this particular

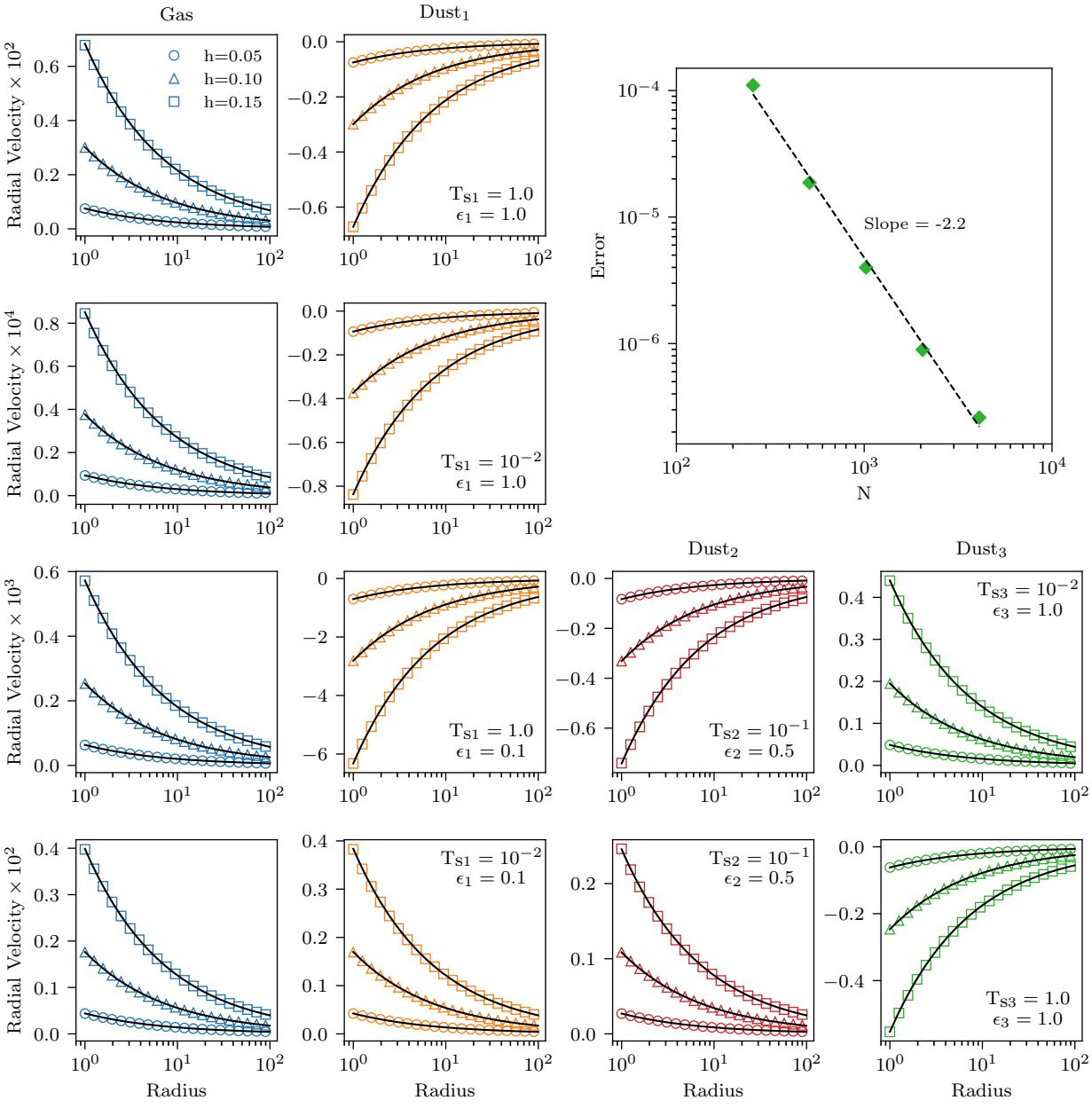

Figure 3.4.2: Figure 6 from Benítez-Llambay et al. (2019). Analytical (solid lines) and numerical (open colored symbols) solutions for the first-order dust radial drift test problem, described in Section 3.4.1. The analytical solutions are given by Eqs. (3.4.9) and (3.4.11). In the smaller panels, we plot the radial velocity for all the cases studied. Different columns correspond to different species (labeled at the top of each of the uppermost panels) while different rows correspond to runs with different parameters. For each set of parameters, we run the same test with different aspect-ratios, h, and plot the resulting radial velocity with different symbols (see the legend in the leftmost upper panel). The parameters of each run are quoted inside of the small panels. In the large panel located at the right upper corner, we additionally plot the result of the convergence test described in Section 3.4.3.1.

case, we defined the error as:

$$\text{error}(\Delta r) = \frac{1}{N}\sum_{j=1}^{N}\left\langle \frac{v_{jr}^{\Delta r} - v_{jr}}{v_{jr}} \right\rangle^2 , \tag{3.4.15}$$

with N the total number of species and $v_{jr}^{\Delta r}$ the solution obtained for different resolutions. We denote the average over the cells with $\langle\rangle$.

For this test we take the case corresponding to the fourth row of Figure 3.4.2. For this particular problem, we find that 256 cells are enough to obtain a converged solution. We then use 256 as starting number of grid points and go up to 4096, progressively increasing by factors of 2.

We plot the result of this convergence test in the large panel of Figure 3.4.2. We successfully recovered a convergence rate close to the expected order of the numerical method. For this test, the time step was allowed to vary according to the CFL condition. Thus, since the errors in space decrease rapidly, the convergence rate is dominated by the first-order error in time.

3.5 Summary and Conclusions

Numerical scheme for momentum transfer. We presented a numerical scheme to solve the multispecies momentum transfer which is valid both for the Eulerian or Lagrangian formalism. The first-order implicit scheme was designed to conserve momentum to machine precision, a quantity that must be conserved during collisions between pairs of species. In addition, we have shown that the implicit scheme is asymptotically and unconditionally stable, with the correct asymptotic limits. Since the value of the Stokes number is not directly involved when studying the properties of the implicit scheme, we stress that the algorithm works well independently of the Stokes number.

Linear and non-linear drag-forces. In the case of a linear regime, we derived analytical solutions for the velocities when an arbitrary number of species collide with the same collision rate but different density ratios. We furthermore showed that the scheme is also suitable for different non-linear regimes assuming that the collision frequency is updated in the step previous to the integration, that is $\alpha(|\Delta v|) \simeq \alpha^n$ in the step $n+1$.

Implementation in FARGO3D. We demonstrate that the operator splitting implementation converges to the correct equilibrium solution when solving the Collision step between the Source and Transport steps.

Damping of a sound wave. We derived the dispersion relation that determines the propagation of a sound wave when a gaseous fluid exchanges momentum with multiple pressureless fluids, e.g., dust species (neglecting the collisions between pressureless fluids). The benefit of having a closed form of the dispersion relation — instead of a polynomial of degree $N + 1$ — is that we could prove that only two of the $N + 1$ roots are complex and provide an efficient method to find all the damping rates. We recovered the analytical solutions with FARGO3D confirming that the implementation converges to correct equilibrium, even in stiff regimes where the Stokes number is significantly smaller (up to four orders of magnitude) than the explicit timestep imposed by the CFL condition.

Generalized first-order drift solutions. We obtained first-order, steady-state solutions for the radial drift of multiple dust species in protoplanetary disks, in which the pressure gradient is not necessarily small. Using these solutions we have shown that for particle-size distributions a significant fraction of the dust particles moves *outwards*, up to 60% for distributions with $\epsilon \sim 1$, depending on the slope. We performed simulations with FARGO3D to validate our implementation of the collision module, successfully recovering the steady-state solution considering a disk with a radial extension of $100\,\mathrm{AU}$.

4 Hall-Dominated Protoplanetary Disks

The importance of the Hall effect in protoplanetary disks has been extensively discussed in the past two decades by several authors (see e.g. Wardle, 1999; Balbus and Terquem, 2001; Sano and Stone, 2002; Salmeron and Wardle, 2003; Pandey and Wardle, 2008; Wardle and Salmeron, 2012; Bai, 2014). Detailed calculations of chemical abundances and ionization fractions including chemical reaction networks have provided an understanding of the relative importance of the Hall effect together with the Ohmic and ambipolar diffusion (e.g. Salmeron and Wardle, 2008; Bai, 2011a). Furthermore, numerical simulations provided a new picture of PPDs dynamics enhancing the importance of the Hall effect in planet forming processes (e.g. Bai, 2014; Lesur et al., 2014; Bai, 2017; Béthune et al., 2017).

In this chapter, we discuss the results presented in Krapp et al. (2018) (including tables and figures), where we addressed the existence of zonal flows and vortices induced by Hall-MHD turbulence in protoplanetary disks. We consider vertically unstratified cylindrical disk, including the Ohmic dissipation and the Hall effect. Such simplification seems adequate to model to regions close to the midplane of a typical PPD, at inner radii $r \lesssim 20\mathrm{AU}$. At these locations, the Hall effect likely dominates over Ohmic dissipation, and ambipolar diffusion (AD) is thought to be negligible.

We focus here on the discussion of two different regimes that we defined as "Weak" and "Strong" Hall-regimes. A distinction that follows from a transition that goes from a likely turbulent to a self-organized state as the Hall diffusion increases and dominates the evolution of the induction equation (Kunz and Lesur, 2013).

As a first step, we study the Maxwell and Reynolds stresses, analyzing the time evolution of the dimensionless stress, α, in the context of a globally isothermal PPDs. The results clearly show the effect of the magnetic field polarity in the turbulent flow due to the inclusion of the Hall effect. We begin the

discussion by comparing global isothermal disk simulations with the actual results by O'Keeffe and Downes (2014), obtained in the framework of multifluid MHD, and Béthune et al. (2016), which used a single-fluid Hall-MHD approach.

Secondly, we study a regime where the Hall effect likely dominates the dynamics and where the turbulent flow is prone to be organized in large scale coherent structures. This section is a followup of the previous work of Béthune et al. (2016) that allows us to test our numerical approach, which has never been used to study such a challenging regime.

Finally, after the numerical validation of our implementations in the non-linear regime, we study the effect of the self-organization on the dust dynamics, where the dust equations are solved using the implicit updated discussed in Chapter 3. This study is done assuming a radially varying disk model, with the additional inclusion of different azimuthal net flux.

4.1 Numerical considerations

In the following, we discuss boundary conditions, resolution requirements, and additional numerical techniques correctly implemented to simulate PPDs with the Hall effect. In Appendix A.1, we add a description of the numerical scheme used to solve the induction equation with the Hall term, together with the corresponding tests.

4.1.1 Cylindrical simulations of PPDs

All the simulations presented in this section are based on an unique setup. We consider a disk with a central star and assume a cylindrical gravitational potential. We solve the Eqs. (2.1.1) and (2.1.2) in a cylindrical mesh with vertical, radial and azimuthal extensions defined as L_z, L_r and L_ϕ, respectively. The simulatins were performed with FARGO3D and NIRVANA-III and the numerical methods were discussed in Sections 1.5.1 and 1.5.2.

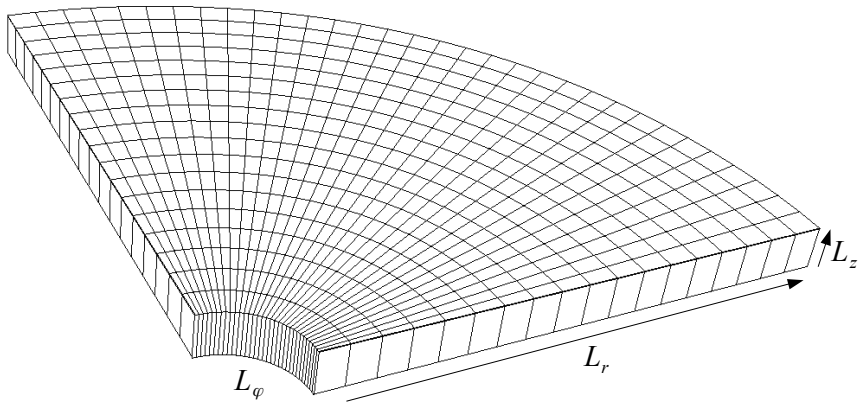

Figure 4.1.1: Example of a low resolution cylindrical mesh with only one cell in the vertical direction.

4.1.2 Boundary conditions

The numerical models presented in this Chapter are periodic in the vertical and azimuthal directions. For the radial boundary, we use reflecting conditions for both the velocity and magnetic field. We extrapolate the azimuthal velocity to the Keplerian profile, and we set the vertical velocity such that $\partial_r v_z = 0$. Furthermore, we apply reflecting boundaries to the azimuthal ($\mathbf{E}_\phi$) and vertical ($\mathbf{E}_z$) components of the electromotive force (EMF), whereas for the radial component we have $\partial_r \mathbf{E}_r = 0$. In combination, these boundary conditions conserve the magnetic and mass flux to machine precision while simultaneously preserving $\nabla \cdot \mathbf{B} = 0$. One potential disadvantage of applying reflecting boundary conditions is the accumulation of mass and vertical magnetic flux close to the radial boundaries when the MRI is fully developed. To minimize the amount of magnetic stresses at the radial boundaries, we define buffer zones (with a width of $0.2\, r_0$) where we apply Ohmic diffusion with a magnitude of $\eta_{\rm O} = 3 \times 10^{-4}$. Inside these buffer zones we define a region of size $0.05\, r_0$ where we restore the density to the initial density profile ρ. Following de Val-Borro et al. (2006), in FARGO3D the density is modified as $\rho \rightarrow (\rho\, \tau + \bar{\rho}_0 \Delta t)/(\Delta t + \tau)$, where $\tau \propto R(r)\Omega^{-1}$, with $R(r)$ a parabolic function that goes to one at the domain boundary and zero at the interior boundary of the wave-damping zone. In NIRVANA-III, we follow a similar procedure using the error function instead. In spite of reducing the accumulation of mass at the inner boundary we notice a systematic drainage of the mass density. In our simulations, we report mass losses between 2% – 10% of the total initial mass contained in the domain. The amount of mass lost increases when the saturation of the Hall MRI is reached. After that, the mass within the domain remains roughly constant, and we thus do not expect the overall findings to be severely affected.

4.1.3 Resolution requirements for MRI modes

We discuss below the resolution requirements for the linear growth of the MRI when combining Hall-MHD with Ohmic diffusion. Although we perform simulations in a global cylindrical mesh, we make the simplifying assumption that we can compute the local value of the maximum growth rate, $\gamma_{\rm m}$, for the MRI at each radius. We furthermore assume a disk with a Keplerian rotation profile and define $k_{\rm m}$ as the wavenumber with the maximum growth rate.

From linear theory, we obtain the following expression for the fastest growing wavenumber $k_{\rm m}$ (Wardle and Salmeron, 2012; Mohandas and Pessah, 2017)

$$k_{\rm m}^2 = \frac{-4\gamma_{\rm m}^2(\gamma_{\rm m}^2+\Omega^2)}{2v_A^2(2\gamma_{\rm m}^2-3\Omega^2)-(\gamma_{\rm m}^2+\Omega^2)\left[3\Omega\eta_{\rm H}-4\gamma_{\rm m}\eta_{\rm O}\right]}\,, \tag{4.1.1}$$

and the corresponding maximum growth rate, $\gamma_{\rm m}$, in terms of the Hall diffusivity as

$$\eta_{\rm H} = \frac{24\,\Omega\,\eta_{\rm O}\gamma_{\rm m}}{9\Omega^2-16\gamma_{\rm m}^2} - \frac{2\Omega v_A^2}{\gamma_{\rm m}^2+\Omega^2}\,. \tag{4.1.2}$$

If we only consider the Hall effect, equations (4.1.1) and (4.1.2) can be combined to yield

$$k_{\rm m}^2 = \frac{2\,\Omega}{\eta_{\rm H}} \equiv \frac{2\sqrt{\beta}}{L_{\rm H}H}. \tag{4.1.3}$$

where the plasma-β parameter is defined as

$$\beta = \frac{2\mu_0\rho_{\rm g}c_{\rm s}^2}{|\mathbf{B}|^2} \tag{4.1.4}$$

This result was obtained in the incompressible limit, but because of the low compressibility of our disk model, we can still establish the connection between the pressure scale height, H, and the wavenumber, $k_{\rm m}$, via Eq. (4.1.3).

We guarantee a minimum resolution for the local linear instability that in general is around seven cells at r_0. Hawley et al. (1995) suggested a minimum of five cells for codes that use finite difference schemes, such as FARGO3D and eight cells for shock capturing codes as NIRVANA-III.

4.1.4 Units

The adopted units are such that $M_\odot = 1$, $\mu_0 = 1$. The radial distance, r, is given in AU. We quote elapsed time in terms of the orbital Keplerian period, $t \equiv 2\pi\Omega_{\rm K}^{-1}(r_0)$ at the inner radius $r_0 = 1$ of the disk.

4.1.5 Artificial resistivity

The numerical scheme implemented to solve the induction equation with the Hall term is robust in terms of stability when the Hall effect is comparable to the ideal convective term and does not strongly dominate the dynamics. Stability issues might be related to the introduction of dispersive waves, namely whistler waves, which can introduce spurious oscillations at cell level that have the fastest phase velocity (Huba, 2003). We remedy this issue by applying an artificial resistivity, only in the strong Hall-dominated regime, that efficiently smooths strong gradients and removes cell-level noise without affecting the dynamics.

Empirically, we found that sharp gradients of the magnetic field become unstable, thus we apply the artificial resistivity only near a maximum (or minimum) of $\mathbf{B}$, to smeared out the gradients. The artificial resistivity is added to the Ohmic dissipation with an effective diffusion coefficient, $\eta_{\rm art}$. For instance, $\eta_{\rm art}$ is computed at the grid location $\mathbf{x}_i$ as

$$\eta_{\rm art} = \eta_{\rm art}^0 \left(\frac{\sum_s \max(\delta\mathbf{B}_x^{(s)}, \delta\mathbf{B}_y^{(s)}, \delta\mathbf{B}_z^{(s)})}{|\mathbf{B}|_{\rm ref}} \right)^{q_{\rm a}}, \tag{4.1.5}$$

where $\eta_{\rm art}^0$ has the dimension of diffusivity, and s refers to the spatial direction (i.e., x, y or z). If we take $s = y$ and consider a cell with its center at the indexed position (ϕ_i, r_j, z_k), we have

$$\begin{aligned} \delta\mathbf{B}_{x,i+1/2,j,k}^{(y)} = (|B_{x,i+1/2,j,k} &- B_{x,i+1/2,j-1,k}| + \\ |B_{x,i+1/2,j+1,k} &- B_{x,i+1/2,j,k}|)\, f(a)\,, \end{aligned} \tag{4.1.6}$$

with equivalent similar expressions for $\delta\mathbf{B}_x^{(x)}$ and $\delta\mathbf{B}_x^{(z)}$, respectively, where the differences are taken

along index i and k. Because we apply the diffusion only along a local maximum (minimum), we have

$$f(a) \equiv \begin{cases} 0 & \text{if} \quad a > 0 \\ \frac{1}{2} & \text{if} \quad a \leq 0 \end{cases} , \tag{4.1.7}$$

with $a \equiv (B_{x,i+1/2,j+1,k} - B_{x,i+1/2,j,k}) \times (B_{x,i+1/2,j,k} - B_{x,i+1/2,j-1,k})$, in the case of Eq. (4.1.6), and correspondingly for the other components.

In our numerical simulations, we find that $\eta_{\rm art0} \simeq 10^{-5}$ is sufficient to improve the stability. Besides, to enhance the contrast between regions where the artificial diffusion is needed or not, we choose an exponent of $q_{\rm a} = 2$, making the artificial dissipation more localized. A seven-point stencil with $|\mathbf{B}|_{\rm ref} \equiv (|\mathbf{B}|_{i,j,k} + |\mathbf{B}|_{i\pm1,j,k} + |\mathbf{B}|_{i,j\pm1,k} + |\mathbf{B}|_{i,j,k\pm1})/7$ proves to be convenient for the normalization. Because we apply an effective Ohmic diffusion which is the sum of the physical and artificial terms, $\eta = \eta_{\rm O} + \eta_{\rm art}$, the artificial resistivity term is also considered when evaluating the Courant-Friedrich-Lewy (CFL) condition.

As an estimate of the level of dissipation introduced by the artificial resistivity in our simulations we calculate the magnetic Reynolds number, Rm, defined as

$$\mathrm{Rm}_{\rm art} \equiv \delta v_{\rm rms}\, L/\eta_{\rm art} , \tag{4.1.8}$$

that is, taking the root mean square of the velocity perturbations, $\delta v_{\rm rms}$, as the characteristic speed. We then compute the value of $\mathrm{Rm}_{\rm art}$ setting L as the vertical cell size $L = \Delta z \lessapprox r\Delta\phi < \Delta r$, where $r\Delta\phi$ and Δr represent the azimuthal and radial cell sizes, respectively. This choice for the length scale returns the minimum possible value for $\mathrm{Rm}_{\rm art}$, providing a robust upper limit to the artificial dissipation.

In general, the artificial resistivity introduces values of $\mathrm{Rm}_{\rm art}$ which are larger than 100 for more than 80% of the active domain, ≥ 10 for 90%, and never smaller than unity. In all of our runs presented in Section 4.3, we find that around 5% of the active domain has a magnetic Reynolds number in the range $1 < \mathrm{Rm}_{\rm art} < 5$. This value drops below 3%, when zonal flows develop. In the case of the runs of Section Section 4.3.2.7, we include a background resistivity profile with a magnetic Reynolds number in a range of $10 < \mathrm{Rm} < 100$. Introducing artificial resistivity in these models affects around 6% of the active domain with $1 < \mathrm{Rm}_{\rm art} < 5$. We understand that such levels of dissipation have a minimal impact on the dynamics and do not affect our results.

4.1.6 Sub-cycling the Hall scheme step

The explicit integration of the Hall effect imposed a stability CFL condition that can be significantly smaller than that for ideal MHD. For that reason, we use a sub-cycling scheme with the aim of speeding up the integration. Both in FARGO3D and NIRVANA-III, the sub-cycling integrates the magnetic field using the scheme[1] described in Appendix A.1, with the Hall-MHD time step, producing an intermediate solution B^*. Using B^*, we integrate the remaining terms of the induction equation with the timestep constraint of the CFL condition obtained without considering the Hall effect. In the strong Hall regime, we find that the time step can be up to a hundred times smaller than the orbital advection time step. Note that we include the FARGO orbital advection scheme (Masset, 2000; Stone and Gardiner, 2010) in both codes, reducing the computational integration time and the numerical diffusion. We have performed additional convergence tests for oblique waves and the linear growth of the MRI (both local and global modes) with the sub-cycling enabled to study whether the sub-cycling affects the propagation of high-frequency waves. All these tests are described in Appendix A.2. The linear growth of the MRI does not appear to be affected by the sub-cycling in our tests. However, the convergence of the error in the oblique wave propagation test is up to 20% smaller than that recovered without the sub-cycling, with a number of sub-cycles that goes from 5 to 11. The sub-cycling of the Hall scheme decreases the computational time by a factor between three and five, depending on the adopted physical parameters.

4.1.7 Super-time-stepping

The time step is dominated by the explicit integration of the Ohmic resistivity when the sub-cycling scheme is enabled for the Hall effect. Thus, we use a super-time-stepping (STS) scheme based on the solution of Alexiades et al. (1996) and second-order Runge-Kutta-Legendre (RKL2) of Meyer et al. (2012) to further reduce the computational time. We do not include a full test of the implementation here, but we have performed runs with and without the scheme for a few specific models, recovering nearly identical results. In FARGO3D, we update the magnetic field using the STS scheme as described in Simon et al. (2013). First, we apply the Hall scheme, and then the STS before solving the ideal-MHD induction equation. The method of Alexiades et al. (1996) is first-order in time and fits well for FARGO3D, however, to maintain second-order accuracy in time in NIRVANA-III, we apply Strang splitting for the RKL2. The speed-up is within a factor of four in the case of FARGO3D for the more

[1] In NIRVANA-III, when using the Tóth et al., no sub-cycling is used owing to the un-split character of the update.

demanding simulations, where Ohmic diffusion induces a time step ten times smaller than the orbital advection step.

4.2 Weak regime and the effect of field polarity

When including the Hall effect, the dynamics of the differentially rotating disk depends on the relative orientation between the angular velocity and the background vertical magnetic field (Balbus and Terquem, 2001; Sano and Stone, 2002; Wardle and Salmeron, 2012). For a given range of Hall diffusivities, the resulting level of Maxwell stress can be amplified if both quantities are aligned, i.e., $\mathbf{B}\cdot\mathbf{\Omega} > 0$. This behavior can be traced back to the linear regime, where the additional rotation of the MRI channel solution caused by the Hall current has a destabilizing effect compared to the ideal case (Wardle and Salmeron, 2012).

4.2.1 Stress evolution for different numerical methods

Table 4.2.1: Initial conditions and mesh parameters for the results presented in Section 4.2.1.

L_H	β_z	c_s	B_{z0}	$L_z\,(N_z)$	$L_r\,(N_r)$	$L_\phi\,(N_\phi)$	η^0_art
5.5×10^{-3}	7.82×10^{2}	4.35×10^{-2}	2.2×10^{-3}	0.39 (36)	4.2 (480)	$\pi/2$ (480)	—

Domain sizes, L_r, L_ϕ, and L_z in the radial, azimuthal, and vertical direction, respectively, are listed with the number of cells given in brackets.

For the following discussion, we adopt the setup described in the Appendix B of Béthune et al. (2016), which was developed with the aim of comparing the results with the previous work by O'Keeffe and Downes (2014). The initial conditions are described in Table 4.2.1 (top row) and we run the setup using three different numerical schemes, that is,

(i) the unsplit HLL-based solver of Tóth et al.,

(ii) the split HLLD + HDS solver in NIRVANA-III,

(iii) the MOC + HDS implementation in FARGO3D.

The artificial resistivity is not included in these runs. As can be checked from Eq. (4.1.3), the fastest growing Hall-modified MRI mode, with $\lambda_\mathrm{m} \equiv 2\pi(H^2L_\mathrm{H}^2/4\beta)^{1/4}$ is resolved with approximately three

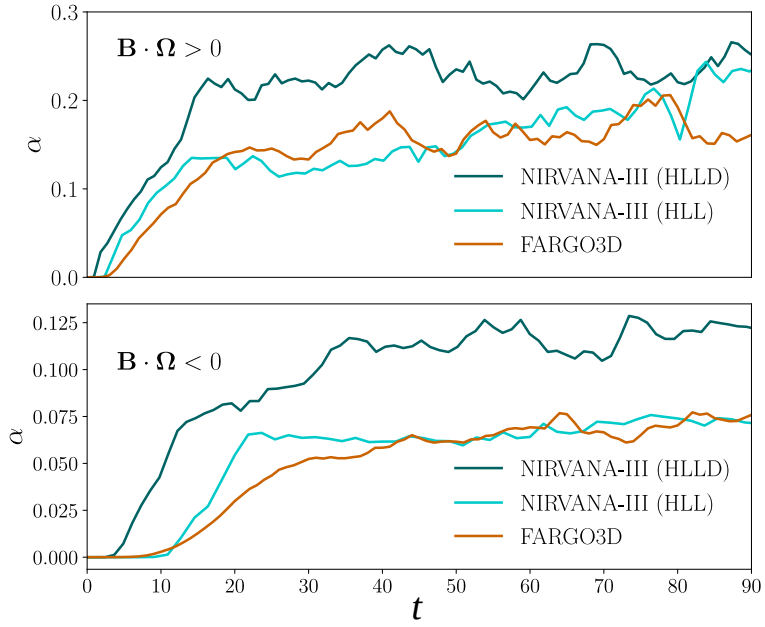

Figure 4.2.1: Figure 1 from Krapp et al. (2018). Time evolution of the dimensionless stress for the aligned (top panel) and anti-aligned configurations (bottom panel).

cells at $r = 4$. In Figure 4.2.1, we show the time evolution of the dimensionless stress, α, and we compute its time average, $\langle\alpha\rangle_{\rm T}$, between $t = 40$ and $t = 80$. The dimensionless stress, α, is defined as the sum of the (r, ϕ)-component of the Reynolds and Maxwell stresses, normalized by the gas pressure. We denote these two contributions with $\alpha_{\rm R}$ and $\alpha_{\rm M}$, respectively. We normalize the stress as $\alpha \equiv N_r^{-1} \sum_j \alpha_j$, where

$$\begin{aligned} \alpha_j &\equiv \alpha_{\rm R} + \alpha_{\rm M}\,, \\ &= \frac{\sum_{i,k}(\rho v_r \delta v_\phi)_{i,j,k}}{c_{{\rm s}j}^2 \sum_{i,k}\rho_{i,j,k}} - \frac{\sum_{i,k}(B_r B_\phi)_{i,j,k}}{c_{{\rm s}j}^2 \sum_{i,k}\rho_{i,j,k}}\,, \end{aligned} \tag{4.2.1}$$

with indices (i, j, k) as introduced in Section 4.1.5, and where δv_ϕ is the deviation from the mean azimuthal velocity, and N_r denotes the number of cells in the radial direction. Since the quantities in Eq. (4.2.1) have, in general, different staggering, they need to be interpolated to the r_j coordinate.

The results are presented in Table 4.2.2. The α-values obtained with NIRVANA-III using the HLL solver and FARGO3D only show a slight discrepancy in the average magnetic energy for the aligned configuration but otherwise agree well.

The $\langle\alpha\rangle_{\rm T}$ obtained with the MOC+HDS (for FARGO3D) and with HLL solver (for NIRVANA-III) are in

Table 4.2.2: Table 2 from Krapp et al. (2018). Measurements of the mean α-stress and magnetic energy

Hall-MHD	$\langle\alpha\rangle_{\mathrm{T}+}$	$\langle\alpha\rangle_{\mathrm{T}-}$	$\langle E_B\rangle_{\mathrm{T}+}$	$\langle E_B\rangle_{\mathrm{T}-}$
F-3D (HDS)	$0.17^{\pm 0.02}$	$0.066^{\pm 0.004}$	$0.32^{\pm 0.03}$	$0.12^{\pm 0.01}$
N-III (HLL)	$0.15^{\pm 0.02}$	$0.067^{\pm 0.005}$	$0.22^{\pm 0.02}$	$0.12^{\pm 0.01}$
N-III (HDS)	$0.23^{\pm 0.02}$	$0.12^{\pm 0.01}$	$0.30^{\pm 0.04}$	$0.17^{\pm 0.02}$
Ideal-MHD	$\langle\alpha\rangle$	$\langle E_B\rangle$		
F-3D (HDS)	$0.11^{\pm 0.01}$	$0.19^{\pm 0.02}$		
N-III (HDS)	$0.16^{\pm 0.01}$	$0.25^{\pm 0.03}$		

Averages between $t = 40 - 80$ for the different schemes. The magnetic energy, E_B, is normalized to the initial pressure, i.e., $E_B \equiv B^2/(2\rho_0\, c_{\mathrm{s}}^2)$. Brackets $\langle . \rangle_{\mathrm{T}}$ indicate time averages and the sign T$\pm$ refers to the aligned (+) and anti-aligned ($-$) configuration.

agreement with those reported by Béthune et al. (2016) but are larger than those reported by O'Keeffe and Downes (2014), where $\langle\alpha\rangle_{\mathrm{T}-} \sim 0.0092$ and $\langle\alpha\rangle_{\mathrm{T}+} \sim 0.075$ were obtained.

We moreover observe a difference between the time scales in which the MRI is found to saturate. We obtain the saturation level after $t = 20$ for $\langle\alpha\rangle_{\mathrm{T}+}$ and $t = 30$ for $\langle\alpha\rangle_{\mathrm{T}-}$. In contrast, O'Keeffe and Downes (2014) obtained that the stress saturates between 10 and 15 inner orbits. These differences might be related to the use of a different sound speed. Also, because of the single-fluid approach, our Hall diffusion coefficient only evolves with the magnetic field, whereas in the multifluid approach presented by O'Keeffe and Downes (2014), this coefficient is also updated with the densities and velocities of the charged species. Because of this, the models are likely not directly comparable.

Regarding the magnetic energy evolution, we recover a similar trend as seen by Béthune et al. (2016). The magnetic energy has the same saturation timescale as the α-parameter, and remains stable around a constant mean value between the inner orbits 30 and 90. This is another important difference with respect to O'Keeffe and Downes (2014) where they found a secular growth as a function of time.

The $\langle\alpha\rangle_{\mathrm{T}}$ values obtained with NIRVANA-III using the HLLD solver are within 30% larger compared with the ones from the other numerical schemes. We conjecture that this is simply a consequence of the higher intrinsic accuracy of the HLLD scheme[2], since the discrepancy persists for measurements of α in ideal-MHD simulations. Using the same initial conditions as in Table 4.2.2, but setting $L_{\mathrm{H}} = 0$, we found $\langle\alpha\rangle_{\mathrm{T}+} = 0.16$ with N-III, and $\langle\alpha\rangle_{\mathrm{T}+} = 0.11$ for F-3D.

[2]See Balsara and Meyer (2010) for a detailed study on the role of Riemann solvers and slope limiters in the context of MRI in the ideal MHD limit.

4.3 Strong Regime and Self-Organization

In the context of turbulent disks and considering a local, vertically unstratified model, Kunz and Lesur (2013) found that zonal flows with radial concentrations of vertical magnetic flux can develop in Hall-dominated magnetorotational turbulence.

The zonal flows are characterized by strong field amplitudes and are driven by a coherent Maxwell stress acting in concert with conservation of canonical vorticity. Recent work by Béthune et al. (2016) has confirmed the self-organization in a global cylindrical model, but still radially and vertically unstratified. The authors reported the generation of large-scale vortices and zonal flows, suggesting the possibility of dust trapping in the produced features.

Within the shearing-box framework, Lesur et al. (2014) showed that the Hall effect can induce a strong azimuthal field when vertical stratification is considered and zonal flows related to the local confinement of vertical magnetic flux can be inhibited. Bai (2015) also found zonal flows of vertical magnetic field in unstratified shearing box models; meanwhile stratified simulations show thin zonal flows that are supposedly not produced by the Hall effect.

In the following discussion we do not include vertical stratification, instead we study the impact of including a strong azimuthal net flux, which is in agreement with the outcome of stratified simulations (Bai, 2017; Béthune et al., 2017) in the context of disk accretion driven by winds.

Table 4.3.1: Initial conditions and mesh parameters for the simulations of strong Hall regime 4.3.1.

L_H	β_z	c_s	B_{z0}	$L_z\,(N_z)$	$L_r\,(N_r)$	$L_\phi\,(N_\phi)$	η^0_art
2.5×10^{-1}	2.00×10^{4}	1.00×10^{-1}	2.0×10^{-3}	0.25 (32)	4.0 (512)	$\pi/2$ (256)	5×10^{-5}

4.3.1 Self-organization in models without radial disk structure

Béthune et al. (2016) performed an extensive study of self-organization by the Hall effect using a cylindrical disk model assuming globally constant initial conditions. They concluded that a strong Hall effect is able to decrease the turbulent transport, in favor of producing large-scale azimuthal zonal flows accumulating vertical magnetic flux. Depending on the plasma-β parameter and the Hall length, these zonal flows can either evolve in the form of axisymmetric rings or vortices. Their exploration

of parameter space suggests that the general dynamics is not dramatically altered by the inclusion of Ohmic or ambipolar diffusion, nor by a non-zero toroidal magnetic flux.

Moreover, Béthune et al. (2016) discussed the possibility that the vortices generated might eventually behave as dust traps via establishing regions of super-Keplerian rotation. Their simulations, however, do not include dust directly, and we will address this topic in Section 4.3.2 in the context of radially varying models. In the following, we begin by adopting the model B3L6 of Béthune et al. (2016) as a

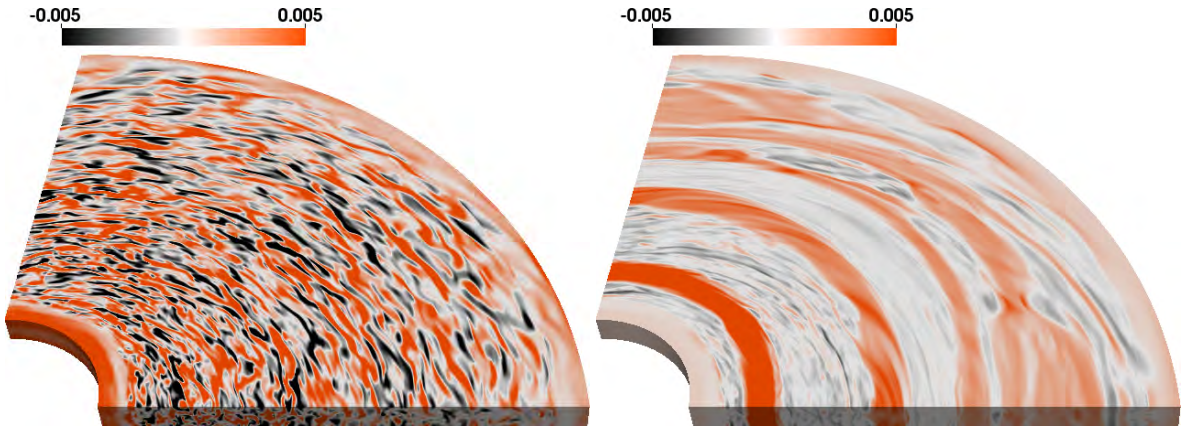

Figure 4.3.1: Figure 2 from Krapp et al. (2018). Evolution of the vertical magnetic flux in a Hall-MHD turbulence with $L_{\rm H} = 0.25$. Left panel shows the saturated MRI in an ideal MHD regime, before turning on the Hall effect. Color coding shows the vertical magnetic field.

starting reference (see Table 4.3.1). With these initial conditions, the vertical wavenumber $\lambda_{\rm m}$, yielding maximum linear growth for the Hall-MRI, is resolved with 22 cells at $r = 2$ (also see Section 4.1.3). The detailed numerical procedure for the setup is described in Section 4.1.2, above.

The left panel of Figure 4.3.1 shows the vertical magnetic field at $t = 50$, that is, before turning on the Hall effect, and in the right panel at $t = 300$, when the fluctuations have undergone an extended phase of self-organization. In our case, four bands of vertical magnetic flux are obtained, which is in good agreement with the model B3L6 described by Béthune et al. (2016).

4.3.1.1 Confinement of magnetic flux

In order to compare the level of stress and the amount of flux confined in the zonal flows, we compute the radial profile $\langle B_z \rangle$ by taking vertical and azimuthal averages, normalized by the initial value B_{z0}. We follow the same procedure for the absolute value of the Maxwell stress, $\langle B_r B_\phi \rangle$. The time-average is taken between $t = 160 - 260$ and the outcome is plotted in Figure 4.3.2, where we show the

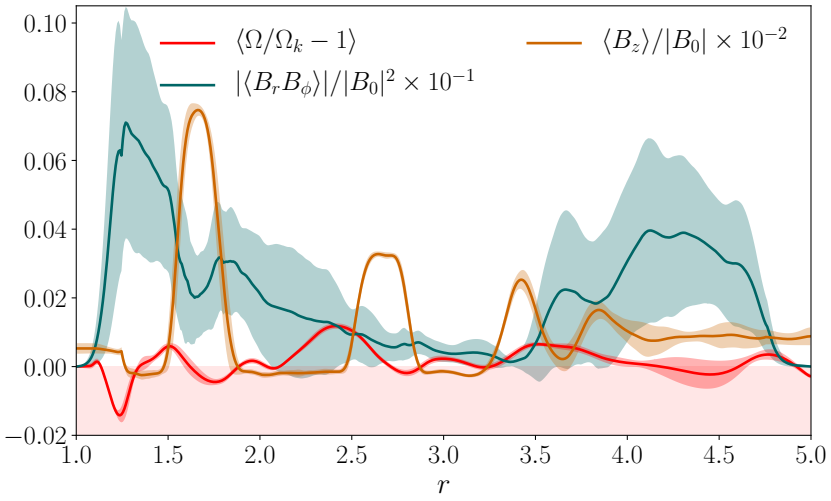

Figure 4.3.2: Figure 3 from Krapp et al. (2018). Radial profiles of the vertical-azimuthal average of the vertical field, $\langle B_z\rangle$, the Maxwell stress, $\langle B_r B_\phi\rangle$, and $\Omega/\Omega_k - 1$. The solid curve correspond to the time average between $t = 160$ and 260. Shaded areas indicate the standard deviation with respect to the time average. The light-red shaded area indicates the sub-Keplerian velocity region.

confinement of the vertical zonal flows between regions of enhanced Maxwell stress.

This mechanism of confinement was first explained by Kunz and Lesur (2013) in the context of local shearing box simulations and was studied in a cylindrical domain by Béthune et al. (2016). Using a mean-field theory, they showed that the Hall effect introduces a component proportional to the turbulent Maxwell stress in the evolution equation of the vertical magnetic field. This contribution of the Maxwell stress might induce an extra dissipation (of either sign) added to the Ohmic diffusion. Thus it can favor the accumulation of magnetic flux in regions of positive curvature of the mean Maxwell stress. After the formation of the zonal flow, the turbulent field that lies in-between starts to flow into the regions of confinement. This process generates a region of low stress and vanishing vertical flux between the azimuthal bands. On the other hand, turbulent fluctuations may survive in regions located close to the zonal flows, as is observed in Figure 4.3.2.

After around 300 orbits, the zonal flows remain quasi-stationary, and three separate zonal flows are distinguishable, with a fourth one seeming to appear close the outer boundary at $r \sim 4$. Figure 4.3.2 also shows that, on average, the Maxwell stress is larger near the radial buffer zones. Reflecting boundary conditions adopted in the radial direction (enabling conservation of the magnetic flux to machine precision) bring about the accumulation of magnetic flux close to the buffer zones, which eventually may favor the concentration of Maxwell stress as well.

4.3.1.2 Effect on the azimuthal velocity

In addition to the averages of the Maxwell stress and the vertical field, we plot in Figure 4.3.2 the vertically, azimuthally and time-averaged radial profile of $\Omega/\Omega_K - 1$ indicating deviations of the velocity field from Keplerian rotation (the light-red shaded region indicates sub-Keplerian rotation). The emerging zonal flows introduce regions of super-Keplerian rotational velocity, which may act locally to accumulate dust grains. We find in our runs that the velocity can reach a robust super-Keplerian regime, constituting an efficient dust trap, that will prospectively produce an azimuthally large-scale dust distribution. Note, however, that in the absence of a radial pressure gradient in the background flow — as assumed in the models presented in this section — the gas initially rotates at the Keplerian speed. In contrast, in a real disk, stellar irradiation heating and the density declines lead to a radial pressure profile, which will, in general, decrease with radius. In that situation, the gas disk will rotate on a slightly sub-Keplerian rotation profile, requiring a more vigorous effect to achieve regions of super-Keplerian rotation.

4.3.2 Self-organization in models with radial disk structure

In this section we study the self-organization including a radially varying disk model. Furthermore, we consider cases with different azimuthal net flux and include the dust as a pressureless fluid (see Section 3.2.3). The density and the sound speed are

$$\rho_{\rm g} = \frac{\Sigma(r)}{\sqrt{2\pi}H(r)}\,, \quad c_{\rm s} = c_{\rm s0}\, r_{\rm AU}^{-p}\,, \tag{4.3.1}$$

with a surface density, $\Sigma(r)$, and the hydrostatic scale height, $H(r)$, defined as

$$\Sigma(r) = \Sigma_0 r_{\rm AU}^{-\sigma} \quad \text{and} \quad H(r) = c_{\rm s}/\Omega_{\rm K}\,, \tag{4.3.2}$$

respectively. We initialize the vertical and azimuthal magnetic field components as

$$B_{z0} = \sqrt{\frac{2\mu_0\rho_{\rm g}c_{\rm s}^2}{\beta_z}} \quad \text{and} \quad B_{\phi 0} = \sqrt{\frac{2\mu_0\rho_{\rm g}c_{\rm s}^2}{\beta_\phi}}\,, \tag{4.3.3}$$

respectively.

The initial plasma-β parameter is set to be constant everywhere, $\Sigma_0 = 1.1 \times 10^{-4} M_\odot / r_0^2 \simeq 980\,\mathrm{g\,cm^{-2}}$ and $c_{s0} = 0.05\ r_0 \Omega_K(r_0)$. We moreover choose $\sigma = 1$ as the power-law index for the surface density profile, and $p = 1/2$ for the sound speed, yielding a constant aspect ratio of $h_0 \equiv H/r = 0.05$.

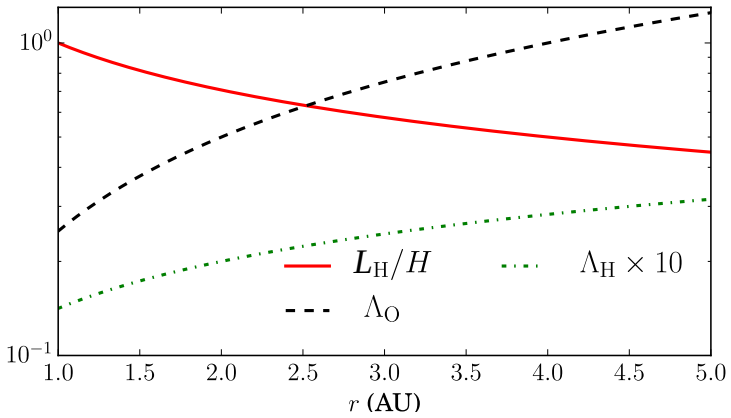

Figure 4.3.3: Figure 4 from Krapp et al. (2018). Elsasser numbers, Λ_O, and Λ_H, as well as L_H/H for $\beta_z = 10^4$ and $\beta_\phi = 0$, corresponding to model F3D-bz1.4-bp0

4.3.2.1 Hall diffusion radial profile

For the purpose of complementing the basic cylindrical model with a radial structure, we assume a radially increasing ionization fraction. In doing so, we stress the importance of maintaining consistency between the coefficients in terms of their dependence on x_e as shown in Eq. (2.2.22).

In order to compare our model with previous results, we will make use of the Hall length defined in Eq. (2.3.3), which in this simplified model is normalized by the initial density profile. We assume

$$\frac{\eta_H}{|\mathbf{B}|} = q_H \frac{h_0}{\sqrt{\rho_0}} \left(\frac{r}{r_0}\right)^{1+w} = \frac{L_H}{\sqrt{\rho_g}}\,, \tag{4.3.4}$$

where $\rho_0 = \Sigma_0/\sqrt{2\pi} H(r_0)$ and $q_H = L_H/H$ at $r = r_0$, that is,

$$q_H = \frac{L_H(r_0)}{H(r_0)}. \tag{4.3.5}$$

This defines a Hall length proportional to the aspect ratio of the disk, and a diffusion coefficient, η_H, which is a function of the initial density profile. In all our models, we use a vertical domain $L_z = 4H$, then $q_H/4 = L_H(r_0)/L_z$. With the ionization fraction following an increasing power-law of radius, that

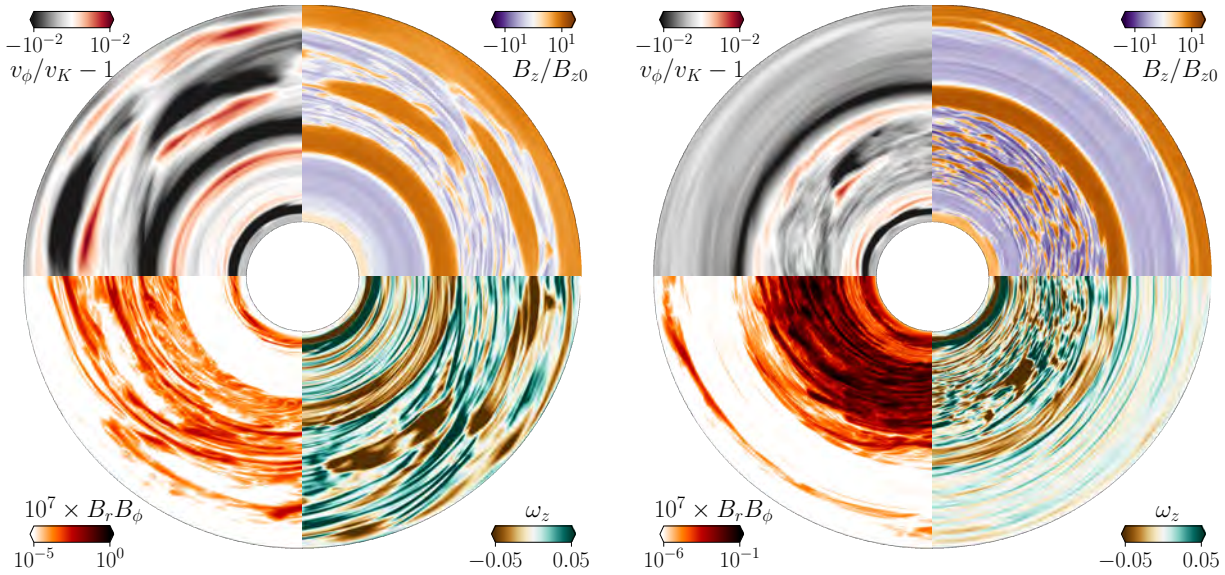

Figure 4.3.4: Figure 5 from Krapp et al. (2018). Models with $\beta_z = 10^3$ (left panel) and 10^4 (right panel) at $t = 250$, corresponding to the runs F3D-bz3-bp0 and F3D-bz4-bp0, as listed in Table 4.3.2. In a clockwise sense, starting from the top right, sectors show: i) vertical field, ii) flow vorticity, iii) Maxwell stress, and iv) deviation from Keplerian rotation.

is, $x_e \sim r^u$, with $u > 0$, we are looking for a limit on the w exponent in Eq. (4.3.4) to establish a radial profile for the Hall diffusion.

Setting $w = 0.5$ and using equation (10) from Kunz and Lesur (2013), we estimate an ionization fraction of

$$x_e \simeq 3.9 \times 10^{-12} \left(\frac{r}{r_0} \right)^{1/2} , \tag{4.3.6}$$

yielding a maximum of $x_e \sim 8.7 \times 10^{-12}$ at radius $r = 5$. We remark that we do not use a dedicated ionization model to compute x_e, but attempt to qualitatively describe radial profiles in the inner disk regions (that is, up to two scale heights from the midplane). The value obtained for the ionization fraction is in agreement with those presented by others (Bai and Goodman, 2009; Lesur et al., 2014; Keith and Wardle, 2015; Béthune et al., 2017), and it is at least one order of magnitude below the profile captured by Rodgers-Lee et al. (2016), implying that we are in a stronger Hall regime.

4.3.2.2 Simulations

The local regions of super-Keplerian velocity induced by the Hall-MHD self-organization seen in the previous section are stable in time and strong enough to halt the radial drift of the dust particles. To see

whether this trend holds for more realistic disk models, we study the conditions for dust trapping in a protoplanetary disk extended between $1-5\,\mathrm{AU}$, using the disk model defined in Section 4.3.2, focusing on results obtained with FARGO3D. The standard computational domain is $z \in [0, 4h_0]$, $r \in [1, 5]$, and $\phi \in [0, \pi/2]$, resolved with $32 \times 256 \times 512$ grid cells, respectively. We use a logarithmic spacing in the radial direction to maintain a constant radial resolution per gas pressure scale-height.

Vertical and azimuthal magnetic field components are defined via constant β_z and β_ϕ, respectively. The aspect ratio is set to $h_0 = 0.05$, and the initial angular velocity of the gas is Keplerian[3]. We add a white noise initial perturbation in the vertical and radial components of the velocity field in order to seed and grow the MRI in the ideal MHD limit. After $t = 40$ orbital periods, we switch on the Hall effect and Ohmic diffusion, and we further evolve the model until $t = 300$.

The Hall diffusion coefficient, as introduced in Section 2.2 — see Eqs. (4.3.4) and (4.3.5) — is given by

$$\eta_{\mathrm{H}}(r) = q_{\mathrm{H}} \frac{h_0}{\sqrt{\rho_0}} \left(\frac{r}{r_0}\right)^{1+w} |\mathbf{B}|\,, \tag{4.3.7}$$

with $w = 0.5$. We adopt an initial $q_{\mathrm{H}} = 1$ at $r = r_0$, but we also run models with $q_{\mathrm{H}} = 2$, and $q_{\mathrm{H}} = 4$.

The Ohmic diffusion profile is given by $\eta_{\mathrm{O}}(r) = \eta_0\, r^{-1/2}$, and we set $\eta_0 = 2 \times 10^{-6}$, which gives an initial $\Lambda_{\mathrm{O}} \lesssim 1$ throughout the radial domain. In Figure 4.3.3, we show the initial Elsasser numbers computed with $\beta_z = 10^4$ and $\beta_\phi = \infty$.

All the runs are listed in 4.3.2 with a nomenclature as follows:

FARGO3D $-$ $\beta_z = 5 \times 10^3$ $-$ $\beta_\phi = \infty$ $-$ $q_{\mathrm{H}} = 2$ $-$ azimuthal domain $= 2\pi$ $\rightarrow$ F3D-bz5.3-bp0-2-2d

FARGO3D $-$ $\beta_z = 5 \times 10^3$ $-$ $\beta_\phi = \infty$ $-$ $q_{\mathrm{H}} = 1$ $-$ azimuthal domain $= \pi/2$ $\rightarrow$ F3D-bz5.3-bp0

4.3.2.3 Self-organization for different vertical fields

We first discuss the runs with a fixed β_z and varying q_{H}, and then turn to results using three different initial β_z, while keeping q_{H} fixed.

[3]The flow adjusts to the sub-Keplerian equilibrium during the first orbit.

Table 4.3.2: Table 3 from Krapp et al. (2018). Overview of simulation runs.

	$q_{\rm H}$	β_ϕ	β_z	B_ϕ[mG]	B_z[mG]
F3D-bz1.4-bp0	1	–	10^4	0	48.1
F3D-bz1.4-bp0-2	2	–	10^4	0	48.1
F3D-bz1.4-bp0-4	4	–	10^4	0	48.1
F3D-bz5.3-bp0	1	–	5×10^3	0	68.0
F3D-bz5.3-bp0-2	2	–	5×10^3	0	68.0
F3D-bz5.3-bp0-4	4	–	5×10^3	0	68.0
F3D-bz5.3-bp5.3-2	2	5×10^3	5×10^3	68.0	68.0
F3D-bz5.3-bp50-2	2	50	5×10^3	680.	68.0
F3D-bz5.3-bp5.3-4	4	5×10^3	5×10^3	68.0	68.0
F3D-bz5.3-bp50-4	4	50	5×10^3	680.	68.0
F3D-bz1.3-bp0	1	–	10^3	0	152.1
F3D-bz5.3-bp0-fd	1	–	5×10^3	0	68.0
F3D-bz5.3-bp50-2-fd	2	50	5×10^3	680.	68.0

Values of B_ϕ and B_z are given at $r = 1$ AU. The models with 'f' have an azimuthal domain of 2π and the ones denoted with a 'd' include dust. Model labels state parameter values used, such as 'F3D-bz1.4-bp0-2', which for instance translates to: $\beta_z = 10^4$, $\beta_\phi = \infty$, $q_{\rm H} = 2$.

Fixed $\beta_z = 10^4$: This correspond to the runs F3D-bz1.4-bp0, F3D-bz1.4-bp0-2 and F3D-bz1.4-bp0-4 (see Table 4.3.2). We adopt three cases increasing the Hall diffusion by doubling $q_{\rm H}$ from $q_{\rm H} = 1$ to $q_{\rm H} = 4$. We recover zonal flows in all these configurations, but interestingly, the number of zonal flows that we observe increases as we increase $q_{\rm H}$ from one band to four bands.

Fixed $q_{\rm H} = 1$: We consider two additional models where we change the plasma-β parameter to $\beta_z = 5 \times 10^3$ and $\beta_z = 10^3$, but we fix $q_{\rm H} = 1$. We recover one zonal flow of vertical magnetic flux independently of the initial β_z, and in addition to the zonal flow, large-scale vortices show up when we decrease the β_z parameter.

These first results indicate that self-organization is robust against radially varying disk models and small variations of the Hall diffusion and the initial vertical magnetic flux only affects the number of zonal flows and vortices.

Figure 4.3.4 shows (in a clockwise sense), the vertical average of B_z/B_0 together with the vertical component of the vorticity $\omega_z \equiv (\nabla \times \mathbf{v}_{\rm g})_z$, the Maxwell stress and the deviation from the Keplerian rotation profile, $v_\phi/v_{\rm K} - 1$. The plasma-β_z parameter increases from 10^3 (left panel) to 10^4 (right panel). For the case of $\beta_z = 10^4$, a concentration of substantial Maxwell stress is located in the region between the zonal flow and the inner radius. Adjacent to the zonal flow, the Maxwell stress decreases considerably. For the case of $\beta_z = 10^3$, it is possible to recognize regions with a lower amount of

stress across the vortices. The Maxwell stress decreases as well between the zonal flows, and turbulent fluctuations persist near the regions with enhanced vertical magnetic field.

In order to confirm the ability of these models to affect the dust evolution, we show, in the same figure, the vertical average of the deviation from Keplerian rotation, $v_\phi/v_\mathrm{K} - 1$. In contrast to the setup described in section Section 4.3, the initial conditions here impose an equilibrium rotation profile with sub-Keplerian velocity. This implies that stronger local pressure gradients are needed to locally reach super-Keplerian rotation. However, for all the models, we find super-Keplerian regions with a velocity deviation of 1%, i.e., $v_\phi/v_\mathrm{K} - 1 \simeq 0.01$. These regions are stable for $t \gtrsim 100$.

4.3.2.4 Generalized flow vorticity

When considering an incompressible fluid in the absence of dissipative terms such as viscosity and Ohmic diffusion, local conservation of the magneto-vorticity, $\boldsymbol{\omega}_\mathrm{M}$, was found by Polygiannakis and Moussas (2001) (see also Pandey and Wardle (2008); Kunz and Lesur (2013)). This quantity is defined as

$$\boldsymbol{\omega}_\mathrm{M} \equiv \nabla \times \mathbf{v}_\mathrm{g} + \omega_\mathrm{H}\, \widehat{\mathbf{e}}_\mathrm{B}\,, \tag{4.3.8}$$

where $\omega_\mathrm{H} \equiv |\mathbf{B}| n_e e/\rho$ is the Hall frequency.

The local conservation of $\boldsymbol{\omega}_\mathrm{M}$ implies that a concentration of vertical flux is anti-correlated with a low vorticity region. Despite the fact that we include Ohmic diffusion, and the flow is moderately compressible, we do expect to find regions where ω_z decreases simultaneously when concentrations of the magnetic flux appear. To test this hypothesis, we compute ω_z using the vertical average of the perturbed velocity field. We plot the vorticity in the bottom right sector of the disks shown in Figure 4.3.4. By comparing the top left and bottom right sectors, respectively, one can see that negative vorticity regions coincide with the places where the vertical magnetic flux is accumulated — a trend that becomes more prominent for stronger fields, i.e., as β_z decreases.

4.3.2.5 Inclusion of a net azimuthal magnetic flux

Vertically stratified simulations show a strong azimuthal flux near the mid-plane when the Hall effect is included (e.g., Bai, 2017). To investigate the effect of the azimuthal flux in the self-organization mechanism, we run vertically unstratified simulations including an initial field $\mathbf{B} = (0, B_\phi(r), B_z(r))$.

We study the effect of a net azimuthal flux on the dynamics by first including an initial β_ϕ equal to $\beta_z = 5\times10^3$ (cf. row 7 in Table 4.3.2), and then increasing the former by a factor of a hundred, that is, $\beta_\phi = 50$ and $\beta_z = 5\times10^3$ (cf. row 8 in Table 4.3.2). As it is expected from the results of Béthune et al. (2016), the inclusion of a weak azimuthal net flux, that is, $\beta_\phi \sim \beta_z$, does not affect the global picture of self-organization, despite the presence of a slightly enhanced turbulent activity.

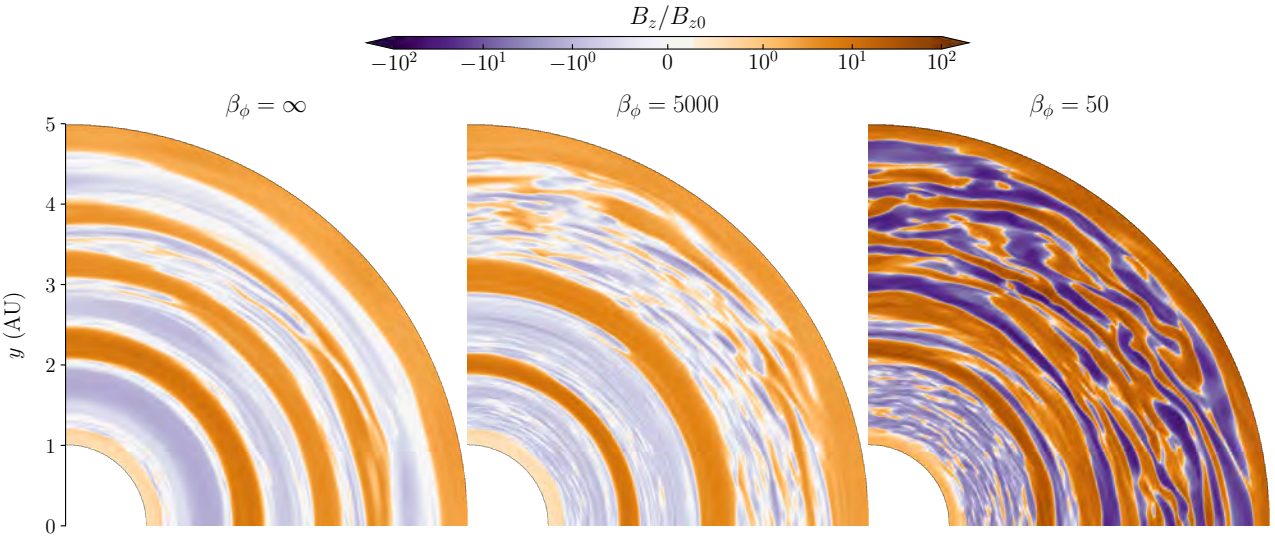

Figure 4.3.5: Figure 6 from Krapp et al. (2018). Vertical magnetic field, $\langle B_z \rangle$ at $t = 200$ for runs F3D-bz5.3-bp0-2 (left) ,F3D-bz5.3-bp5.3-2 (center) and F3D-bz5.3-bp50-2 (right), with initial values $\beta_z = 5\times10^3$ and $q_{\rm H} = 2$. Note that the color scale is *signed* logarithmic.

In Figure 4.3.5, we show the vertical magnetic field after 200 orbits for $\beta_z = 5\times10^3$, $q_{\rm H} = 2$ and different values of β_ϕ. In panels (a) and (b) of Figure 4.3.6, we plot the mean radial profile, between $t = 100 - 200$, of the vertical magnetic field and the Maxwell stress. When $\beta_\phi \simeq \beta_z$, we recover two zonal flows with adjacent regions of turbulent fluctuations. This is in agreement with the field morphology found with $\beta_\phi = \infty$, where we obtained three zonal flows. However, the disk dynamics is dramatically affected when when $\beta_\phi = 50$ is considered. Panel (b) of Figure 4.3.6 shows a prominent region of Maxwell stress in the outer disk, where large-scale turbulent perturbations dominate the dynamics. The self-organization mechanism is not clearly distinguishable despite the fact that two adjacent zonal flows are recognized. These ring-like structures are radially thinner than the zonal flows obtained with a weak azimuthal field, but are also stable in time. Furthermore, they are correlated with super-Keplerian velocity regions, so as in previous cases we obtain azimuthally large-scale regions where the radial drift of the dust is slowed down. Figure 4.3.5 conveys a clear trend, where the inclusion of a net azimuthal field prevents the self-organization, but azimuthally large-scale flux concentrations

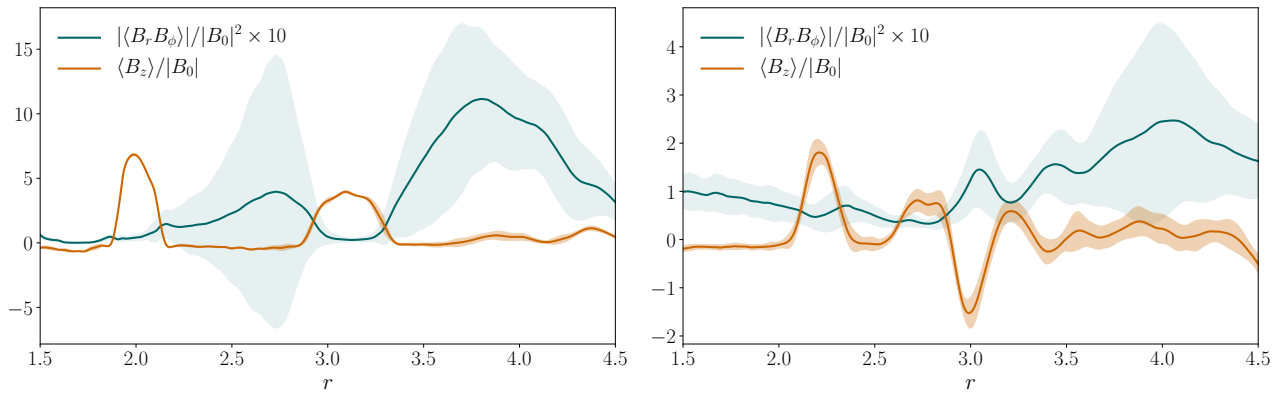

Figure 4.3.6: Figure 7 from Krapp et al. (2018). Radial profiles of $\langle B_z \rangle$ and the Maxwell stress. The shades indicate the standard deviation of the time average computed between $t = 100$ and $t = 200$.

are still possible to obtain.

We have inspected the Reynolds and Maxwell components associated with the α-parameter introduced in Eq. (4.2.1). The contribution of the Reynolds stress is below 1% of the total stress, except in the regions where the zonal flows are sustained. In these regions, the Maxwell stress decreases and the local perturbations of the magnetic field are comparable to the velocity turbulent fluctuations. When no azimuthal flux is considered, the Maxwell contribution to the α-parameter is, on average, $\sim 10^{-4}$. Over the zonal flows it drops to $\sim 10^{-6}$, whereas the Reynolds contribution has a radially constant mean of $\sim 10^{-6}$. When $\beta_\phi = 50$, the ratio between the Maxwell and Reynolds contributions is comparable to the case with zero net azimuthal flux, but the amplitude of the perturbations is higher by a factor of ~ 100 for both.

The decreased appearance of self-organized structures as a consequence of including an azimuthal field, $\mathbf{B}_\phi$, much stronger than $\mathbf{B}_z$ is in agreement with the previous work of Lesur et al. (2014). They included vertical stratification in a shearing box model, resulting in a strong azimuthal field generated by the Hall effect. Furthermore, they found that the mean azimuthal flux can be 200 times larger than the mean vertical flux, even if the initial azimuthal flux is negligible. A similar result was obtained by Béthune et al. (2017) using a spherical global disk configuration with a magnetized wind in a regime where $\beta_z = 10^2$. The authors showed that ambipolar diffusion favors the accumulation of vertical magnetic field into zonal flows. Despite the fact that the Hall effect is negligible (compared with the ambipolar diffusion), it can act against the self-organization if the wind can drive a magnetic stress in regions of strong field.

Even though we do not include vertical stratification, we observe that the inclusion of a strong azimuthal

flux can alter the dynamics, inhibiting the organization of the zonal flows between channels of strong Maxwell stress and creating a more turbulent flow. However, a sufficient strong Hall diffusion ($q_{\rm H} \gtrsim 2$) leads to azimuthally large-scale structures of the vertical magnetic field that generate super-Keplerian velocity regions which are stable for more than 100 orbits. This potentially implies that, even without a clear appearance of self-organized features, it is possible to find flow regions where the dust drift slows down or even halts.

4.3.2.6 Spectral energy distributions

In order to establish a more quantitative comparison between these cases, we compute the spectral energy distribution of the vertical and azimuthal fields between radius $r = 2\mathrm{AU}$ and $4\mathrm{AU}$ for the models F3D-bz5.3-bp0-2, -bp5.3-2 and -bp50-2.

In the left panel of Figure 4.3.7, we plot the spectral energy distribution, $m\,|\mathcal{F}(B_i)|^2$, for the azimuthal and vertical field as a function of the azimuthal mode number, m, where the smallest mode is $m = 4$. For the runs with $\beta_\phi = 5 \times 10^3$, the maximum of the distribution is located at large-scale modes – but the peak is clearly reached inside the azimuthal domain $\pi/2$ with an almost flat distribution at lower m. Increasing the azimuthal net-flux to $\beta_\phi = 50$ shows a different distribution. The maximum is reached around $m \sim 4$ for the components B_z and B_ϕ. The energy grows to larger length scales, which can be recognized in Figure 4.3.5, where large-scale field perturbations dominate the vertical field structure. This implies that a full 2π domain is needed in order to correctly capture the maximum of the energy distribution.

The 1D spectrum shown in the left panel of Figure 4.3.7 allows us to distinguish the trends of the different spectral energy distributions, but it might be affected by the specific choice of the spatial domain. To confirm the differences and obtain a clearer picture, we show in Figure 4.3.7 the spectral energy distribution for B_z as a function of radius. To this end, we divide the radial domain into 80 uniformly-spaced bins and compute the azimuthal spectrum for each annulus. The bottom panel shows the case with $\beta_\phi = 5 \times 10^3$, where it is possible to recognize the location of the two zonal flows. In these regions, the energy is mainly concentrated in low-m modes, and drops as we move outward in the disk. Perturbations are restricted to modes $m \lesssim 40$. The upper panel shows the spectral distribution for $\beta_\phi = 50$, where the energy has a more homogeneous distribution and extends to modes with $m \gtrsim 100$.

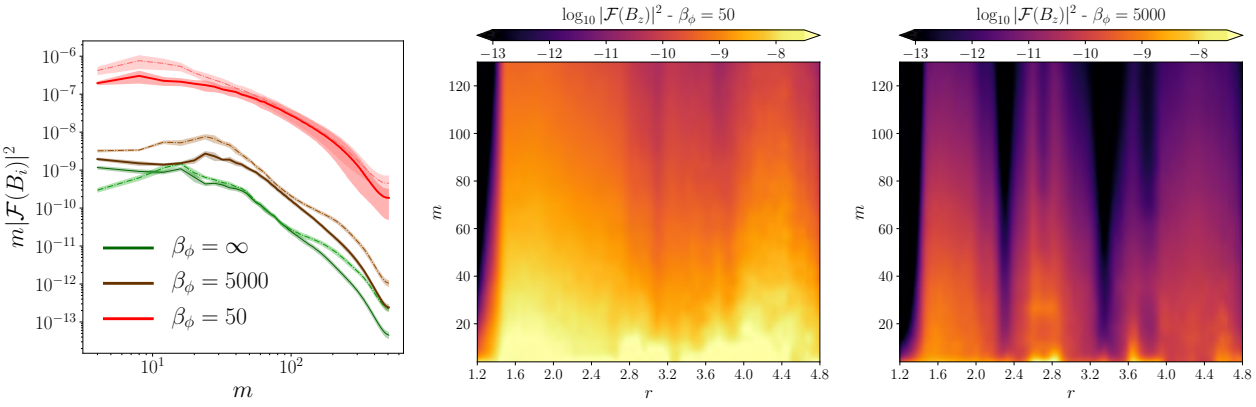

Figure 4.3.7: Figures 8 and 9 from Krapp et al. (2018). Spectral energy distribution, $m\,|\mathcal{F}(B_s)|^2$, for B_z (solid lines) and B_ϕ (dotted lines) for weak and strong azimuthal net flux (averaged between $t = 190$ and $t = 210$). Spectral energy distribution $|\mathcal{F}(B_z)|^2$, for 80 radial uniform bins, averaged between $t = 190, 210$. Top: run F3D-bz3.5-bp50 with $\beta_\phi = 50$. Bottom: run -bp5.3 with $\beta_\phi = 5000$.

4.3.2.7 Dynamics of Embedded Dust Grains

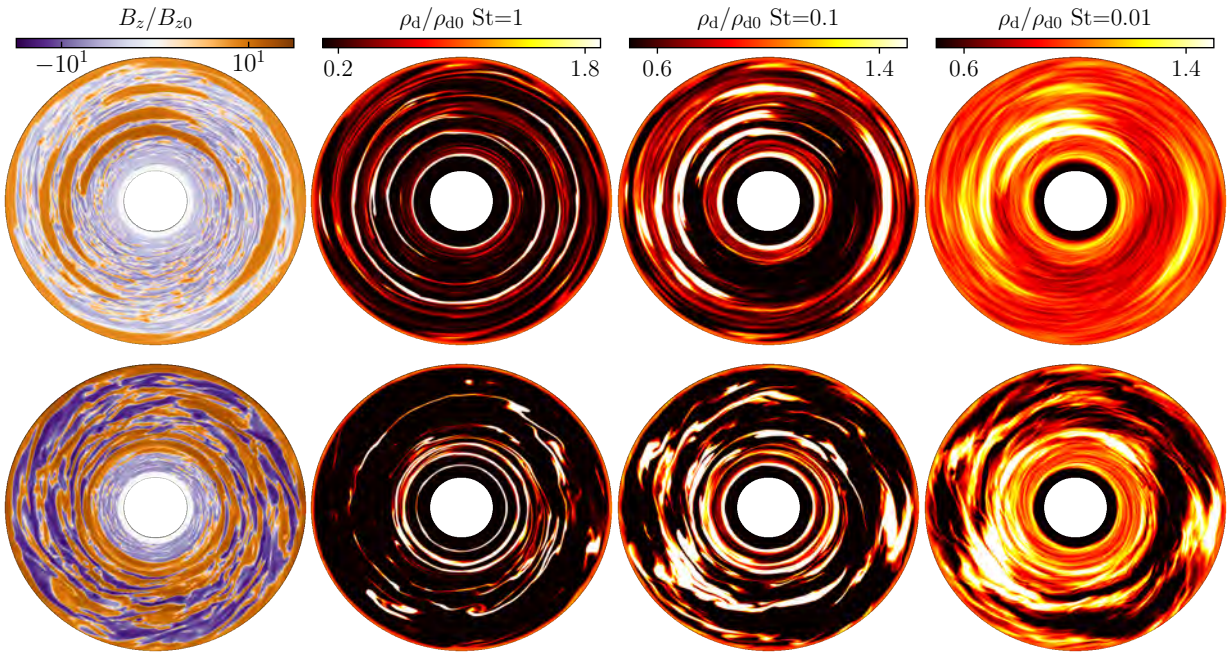

Figure 4.3.8: Figure 10 from Krapp et al. (2018). Vertical average for B_z/B_{z0} (leftmost panel) and dust density contrast ρ_d/ρ_{d0} (remaining three panels) for $t = 250$. The dust density contrast is shown in order of decreasing Stokes number (referred as St instead of T_s) of 1, 0.1, and 0.01, respectively. The upper row corresponds to model F3D-bz5.3-bp0-fd, without an azimuthal field, and the bottom row corresponds to the model F3D-bz5.3-bp50-fd, with a dominant azimuthal field.

In view of the azimuthally large-scale morphology of the flux concentrations, and accommodating for the fact that the spectral energy distribution is dominated by low azimuthal wavenumbers, we now

adopt a full-disk domain, that is, $L_\phi = 2\pi$ with 1024 uniform spaced cells. This is motivated by the possibility that the zonal bands that we observe in a disk with an azimuthal domain of $L_\phi = \pi/2$ might develop into vortices in a $L_\phi = 2\pi$ domain. This notion was already appreciated by Béthune et al. (2016) and, as we will show, it is relevant to the models that we present here.

We now turn to the models F3D-bz5.3-bp50-fd and -bp0-fd to study the dust evolution with three different Stokes number, $T_\mathrm{s} = 0.01$, 0.1 and 1 (see Eq. (2.1.8) for definition). Models F3D-bz5.3-bp0-fd and -bp50-fd-2 have the same initial conditions as F3D-bz5.3-bp0 and -bp50-2, respectively. The dust is considered as a pressureless fluid with an initial density $\rho_\mathrm{d} = 0.01\rho_\mathrm{g}$, and we, moreover, neglect its feedback onto the gas. We enable the drag force term acting on the dust at $t = 180$ inner orbits and evolve the system until we reach $t = 260$.

In Figure 4.3.8, we show the vertically-averaged dust-density contrast, $\rho_\mathrm{d}/\rho_{\mathrm{d}\,0}$, for the three different Stokes numbers. We moreover plot the vertical average of B_z/B_{z0}, for which we expect to find flux concentrations that coincide with locations of dust accumulations.

For the $L_\phi = 2\pi$ models, large-scale vortices appear, which is in contrast to the reduced $L_\phi = \pi/2$ model, where one zonal flow and two vortices were obtained (see the middle panel of Figure 4.3.4). In agreement with the model F3D-bz5.3-bp0, these vortices induce patches of strong super-Keplerian velocities. These regions all show an enhancement of the dust density for the three different Stokes numbers that we have studied here. After a period of $t = 80$ inner orbits, the different grain sizes already display different levels of local concentration, which simply reflects the segregation according to the particles' Stokes number. The dust species with $T_\mathrm{s} = 0.1$ and $T_\mathrm{s} = 0.01$ are more coupled to the gas than the species with $T_\mathrm{s} = 1$. In particular, for $T_\mathrm{s} = 0.01$, we obtain density variations smaller than 10% with respect to the gas.

The reason why we do not see similar dust concentrations in all three components, can be understood in terms of their different radial drift time scales. Let us consider a 2D equilibrium velocity dust profile (Nakagawa et al., 1986b; Takeuchi and Lin, 2002) and assume that the radial velocity of the gas can be neglected. This assumption is an approximation that not fully applies to our simulations, but nevertheless, it allows us to estimate the drift time scale τ for each Stokes number, yielding

$$\frac{\tau}{T_0} = \frac{1}{9\pi}\frac{T_\mathrm{s} + T_\mathrm{s}^{-1}}{h_0^2}\left[\left(\frac{r}{r_0}\right)^{3/2} - 1\right], \tag{4.3.9}$$

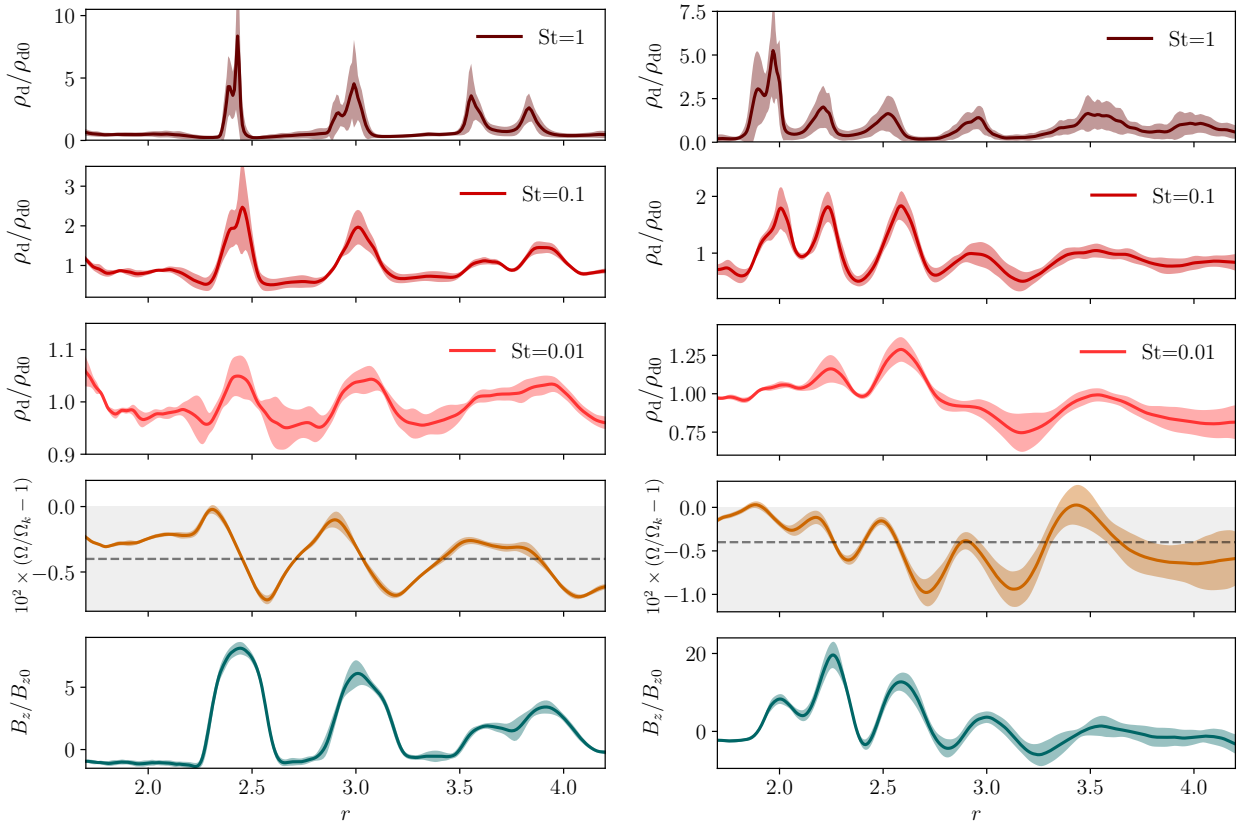

Figure 4.3.9: Figure 10 from Krapp et al. (2018). Mean radial profiles (averaged between $t = 190-260$) for models F3D-bz5.3-bp0-fd, with zero azimuthal flux (left panel), and F3D-bz5.3-bp50-fd, with a strong azimuthal flux (right panel). Dashed lines indicate the (sub-Keplerian) equilibrium velocity profile.

where $T_0 = 2\pi/\Omega_0$. If we consider a trap located at $r = 3$, the drift time scale is $\tau/T_0 \simeq 118$ inner orbits for unity Stokes number – meanwhile, for $T_s = 0.01$, it is around $\tau/T_0 \simeq 6\times10^3$, so we need to integrate for 6000 orbits for $T_s = 0.01$ in order to cover the same fraction of the drift timescale as that of the species with $T_s = 1$.

Figure 4.3.9 shows azimuthally averaged radial profiles of the dust-density ratios $\rho_d/\rho_{d\,0}$, along with the deviation, $\Omega/\Omega_K - 1$, from Keplerian rotation, and the vertical magnetic field enhancement, B_z/B_{z0}. Despite not being axisymmetric, the vortical structures are sufficiently large in their azimuthal extent that averaging the velocity deviation in the toroidal direction will enhance regions were the dust accumulations are stable in time. Taking azimuthal averages moreover brings out regions where the average velocity field becomes almost super-Keplerian over significant intervals of time – even though the super-Keplerian rotation of the vortices does get washed-out by taking the mean. This allows us to identify the radial locations of strong magnetic flux concentrations and recognize that these are the regions of dust enhancement. For Stokes number $T_s = 1$, in some locations, the density contrast reaches

a peak of $\rho_{\rm d}/\rho_{\rm d\,0} \simeq 10$. For longer times, it might reach even higher values, and the feedback onto the gas can no longer be neglected.

In agreement with the discussion in section Section 4.3.2.5, the inclusion of a strong azimuthal field induces large-scale concentrations of the vertical magnetic field, which in this particular case can be axisymmetric. These regions are generally stable in time and induce super-Keplerian flows. The profiles shown in the right panel of Figure 4.3.9 highlight the coincidence of these locations with the dust enhancements.

4.4 Summary and Conclusions

Weak Hall regime: The inclusion of the Hall effect with different magnetic field polarity significantly affects the non-linear evolution of the turbulent flow. In our configuration, the case with $\mathbf{B}$ parallel to Ω shows an average α-value that is larger with respect to the anti-parallel case. Furthermore, our findings agree with the previous results from Béthune et al. (2016) in the simulations performed with both NIRVANA-III (with HLL) and FARGO3D, which validates the numerical implementation of the Hall effect in both codes.

Self-organization: Comparison with previous work. Adopting a different numerical approach, we have reproduced a similar setup for a disk with no initial radial structure, as is described in Béthune et al. (2016) (see B3L6). We found four regions where vertical magnetic flux is confined, which is in excellent agreement with the mentioned previous work. This result validates the numerical implementation in FARGO3D in a strong Hall regime with the inclusion of artificial Ohmic resistivity.

Self-organization with azimuthal net flux. We simulated disks models with different azimuthal and vertical net flux. For a plasma-β parameter in the range $\beta_z = 10^4 - 10^3$, our results show minor differences between cases with zero azimuthal net flux and cases where the azimuthal flux is comparable to the vertical flux. When the initial model has a strong azimuthal net flux, i.e., $\beta_\phi \simeq 10^{-2} \times \beta_z$, it is still possible to obtain azimuthally large-scale concentrations of vertical magnetic flux. However, the picture of field confinement between regions of enhanced Maxwell stress is no longer identified in these simulations. Besides, when the azimuthal component of the magnetic field strongly dominates the

dynamics, the self-organized zonal flows are harder to recover, which is in agreement with previous results from Lesur et al. (2014) and Béthune et al. (2017).

Self-organization and disk azimuthal domain: Simulations, with azimuthal domain reduced to $L_\phi = \pi/2$, show axisymmetric zonal flows and vortices; however, we are only able to recognize large-scale vortical features if the domain is $L_\phi = 2\pi$. We studied the spectral energy distribution considering different azimuthal domains and found that the maximum of energy increases as we move towards shorter azimuthal wavenumber, $m \simeq 4$. We furthermore compared the spectral energy distributions of the models with different azimuthal net flux but in an azimuthal domain of $\pi/2$. When $\beta_\phi = 5 \times 10^3$, the distribution shows a maximum followed by a flat profile at the lower azimuthal modes. Increasing β_ϕ leads to a spectrum that has a peak at intermediate azimuthal wavenumbers.

Self-organization and magneto-vorticity: Our findings confirm that the zonal flows (and vortices) are confined between regions of strong Maxwell stress — in agreement with the mechanism described by Kunz and Lesur (2013). Because of the low flow compressibility and the inclusion of small Ohmic dissipation, the vortices and zonal flows are anti-correlated with low vorticity regions, which is expected when the magneto-vorticity is locally conserved.

Self-organization and dust evolution: By including the evolution of pressureless dust fluids in the ensuing Hall-MHD turbulence, we demonstrate that quasi-axisymmetric dust enhancements can be obtained for the range of Stokes numbers explored – even in the absence of prominent flow features, such as the result of Hall-effect induced self-organization. There appears to be a difference in character regarding the precise nature of the ensuing dust traps, however. In models without azimuthal net flux, dust enhancements are typically located at the position of vortices themselves, which agrees well with the notion of vortices being able to trap dust (Klahr and Henning, 1997). In contrast to this, in models with significant azimuthal magnetic flux ($\beta_\phi \simeq 50$), the dust accumulations appear to coincide with local concentrations of the vertical magnetic flux.

Dust evolution for different Stokes numbers: For particles with Stokes number $T_\mathrm{s} = 1$, peaks in the dust concentration with $\rho_d/\rho_{d0} \simeq 20$ are reached during the integration time of a few hundred inner orbits that we have adopted here, implying that the feedback onto the gas might have to be considered

when pursuing longer integration times. The drift time scale of the $T_{\rm s} = 0.1$ and $T_{\rm s} = 0.01$ particles can be estimated to be between one and two orders of magnitude higher than that for $T_{\rm s} = 1$. As a result, lower dust enhancement factors were obtained for these two dust species, which we, at least partially, attribute to the insufficient evolution time covered by our current simulations.

5 Multispecies Streaming Instability

The aerodynamic coupling between solids and gas in a differentially rotating disk leads to the so-called streaming instability (Youdin and Goodman, 2005). Depending on the dust-to-gas density ratio and the collision frequency, the instability can grow on relatively short time scales, comparable to a few tenths of orbits of the PPD. Higher dust concentrations and larger particle-sizes show the fastest growth (Youdin and Goodman, 2005; Youdin and Johansen, 2007). The primary outcome of the non-linear evolution is the formation of clumps or filaments where conditions are favorable for gravitational collapse (Johansen and Youdin, 2007; Simon et al., 2016). Thus, this instability is thought to play a central role in the early stages of planet formation by enabling the efficient bypass of several barriers hindering the formation of planetesimals.

In this chapter, we offer an extended discussion about the linear and the non-linear phase of the streaming instability. We adopt a different derivation than the one presented by Youdin and Goodman (2005), by considering a compressible regime where the background drift induced by the gas pressure gradient is obtained, defining an external force. Besides, our equations are not at the center-of-mass reference frame, and we consider an arbitrary number of dust species.

In Section 5.1.1, we present the steady-state analytical solutions for the drift velocity of multiple dust species, generalizing the obtained by Nakagawa et al. (1986a). We derive analytical closed expressions for the background velocities, an important difference concerning the solutions found by Bai and Stone (2010a). In Section 5.1.2 we present the linearized equations and in Section 5.1.3 we present numerical results that validate both our analytical framework and the numerical approach discussed in Chapter 3. In Section 5.2, we study the linear phase of the streaming instability and show how the inclusion of multiple species impose secular timescales for the linear growth. Finally, in Section 5.3, we show

the non-linear evolution of the two-fluid streaming instability, successfully recovering the dynamics previously obtained by other authors using Lagrangian particles. Most of the following discussions, tables and figures, were published in Benítez-Llambay et al. (2019) and Krapp et al. (2019).

5.1 Streaming instability

To obtain the linear growth rate of the streaming-instability, we solve the 2.5D linearized axisymmetric shearing-box equations for gas and one dust species. The fluid equations linearization is usually done around the steady-state drift solution obtained by Nakagawa et al. (1986a). However, in order to study the instability for an arbitrary number of dust species, generalized background solutions are needed. These are similar to the approximated solutions obtained for the global disk (see Section 3.4.1), but in this case are analytical. Furthermore, the solution is exact because velocities are not first-order expanded as in the global case. We derive and write them explicitly in Section 5.1.1.

When the background density is assumed constant in the shearing-box approximation, a self-consistent sub-Keplerian background velocity for the gas cannot be obtained. However, to study the instability in this formalism, we add a constant external force mimicking the effect of a constant pressure gradient within the box (see e.g. Bai and Stone, 2010b).

The equations leading to the streaming instability, when N dust species are considered, are

$$\partial_t \rho_{\rm g} + \nabla \cdot (\rho_{\rm g} \mathbf{v}_{\rm g}) = 0\,, \tag{5.1.1}$$

$$\partial_t \rho_j + \nabla \cdot (\rho_j \mathbf{v}_j) = 0\,, \tag{5.1.2}$$

$$\begin{aligned}\partial_t \mathbf{v}_{\rm g} + \mathbf{v}_{\rm g} \cdot \nabla \mathbf{v}_{\rm g} = &- \frac{\nabla P}{\rho_{\rm g}} + \chi_0 \Omega_0 \mathbf{e}_x + 2q\Omega_0^2 x \mathbf{e}_x \\ &- 2\boldsymbol{\Omega}_0 \times \mathbf{v}_{\rm g} - \Omega_0 \sum_{k=1}^{N} \frac{\epsilon_k \boldsymbol{\Delta}_k}{T_{{\rm s}k}}\,,\end{aligned} \tag{5.1.3}$$

$$\partial_t \mathbf{v}_j + \mathbf{v}_j \cdot \nabla \mathbf{v}_j = 2q\Omega_0^2 x \mathbf{e}_x - 2\boldsymbol{\Omega}_0 \times \mathbf{v}_j + \Omega_0 \frac{\boldsymbol{\Delta}_j}{T_{{\rm s}j}}\,, \tag{5.1.4}$$

for $j = 1, \ldots, N$, with q the shear parameter. The term $\chi_0 \Omega_0$ is the constant radial acceleration that

mimics the pressure gradient within the box, with χ_0 an arbitrary constant speed. It is usually chosen to reproduce the drift speed of dust in protoplanetary disks, i.e., $\chi_0 = 2h_0^2 v_{\rm K0}$, with $h_0 = c_{\rm s0}/v_{\rm K0}$ and $c_{\rm s0}$ the constant sound speed. The unit vector along the radial direction is denoted as $\mathbf{e}_x$. The pressure is related to the density as $P = c_{\rm s0}^2 \rho_{\rm g}$. The other terms depend on the dust-to-gas mass ratio $\epsilon_i \equiv \rho_i/\rho_{\rm g}$, the Stokes number $T_{{\rm s}i}$ and, the relative velocity vector between species $\mathbf{\Delta}_i = \mathbf{v}_{\rm g} - \mathbf{v}_i$, where $\mathbf{v}_{\rm g}$ and $\mathbf{v}_i$ are the gas and dust velocity vectors, respectively.

5.1.1 Steady-state solution

In this section, we derive analytical solutions of the Eqs. (5.1.4) considering an arbitrary number of species and a constant background density- Thus, the pressure gradient does not affect the background and the drift is imposed by the external force. To satisfy the continuity equation with a constant background density, the background velocity $v_x \equiv v_x^0$ must also be a constant. Assuming that $v_y = -q\Omega_0 x + v_y^0$, the axisymmetric steady-state (with no vertical gradients) system of equations reads as,

$$
\begin{aligned}
0 &= \chi_0 + 2v_{{\rm g}y}^0 - \sum_{j=1}^{N} \frac{\epsilon_j}{T_{{\rm s}j}} (v_{{\rm g}x}^0 - v_{{\rm d}jx}^0)\,, \\
0 &= 2v_{{\rm d}jy}^0 + \frac{1}{T_{{\rm s}j}} (v_{{\rm g}x}^0 - v_{{\rm d}jx}^0)\,, \qquad \text{for } j = 1, \ldots, N\,, \\
0 &= (q-2) v_{{\rm g}x}^0 - \sum_{j=1}^{N} \frac{\epsilon_j}{T_{{\rm s}j}} (v_{{\rm g}y}^0 - v_{{\rm d}jy}^0)\,, \\
0 &= (q-2) v_{{\rm d}jx}^0 + \frac{1}{T_{{\rm s}j}} (v_{{\rm g}y}^0 - v_{{\rm d}jy}^0) \quad \text{for } j = 1, \ldots, N\,.
\end{aligned}
\tag{5.1.5}
$$

where $\partial_x v_y = -q\Omega_0$ because v_x^0 is a constant, that is, v_y^0 is also constant.

Taking only the momentum equations in the x and y direction for the species l we obtain

$$
\begin{bmatrix} 1 & -2T_{{\rm s}l} \\ -(q-2)T_{{\rm s}l} & 1 \end{bmatrix} \begin{bmatrix} v_{{\rm d}lx}^0 \\ v_{{\rm d}ly}^0 \end{bmatrix} = \begin{bmatrix} v_{{\rm g}x}^0 \\ v_{{\rm g}y}^0 \end{bmatrix}\,, \tag{5.1.6}
$$

which can be inverted to the form:

$$
\frac{1}{D_l} \begin{bmatrix} 1 & 2T_{{\rm s}l} \\ (q-2)T_{{\rm s}l} & 1 \end{bmatrix} \begin{bmatrix} v_{{\rm g}x}^0 \\ v_{{\rm g}y}^0 \end{bmatrix} = \begin{bmatrix} v_{{\rm d}lx}^0 \\ v_{{\rm d}ly}^0 \end{bmatrix}\,, \tag{5.1.7}
$$

where $D_l = 1 - 2(q-2)T_{sl}^2$. Which is reduced to $D_l = 1 + T_{sl}^2$ for a keplerian disk, i.e. $q = 3/2$. Solving the velocity for the species l and replacing the solution into the equations for the gas species we have

$$\begin{aligned} -\chi_0 = \quad 2v_{gy}^0 \quad &- \sum_j \frac{\epsilon_j}{T_{sj}} \left(v_{gx}^0 - \frac{1}{D_j} \left(v_{gx}^0 + 2T_{sj} v_{gy}^0 \right) \right) , \\ 0 = (q-2)v_{gx}^0 &- \sum_j \frac{\epsilon_j}{T_{sj}} \left(v_{gy}^0 - \frac{1}{D_j} \left(v_{gy}^0 + (q-2)T_{sj} v_{gx}^0 \right) \right) , \end{aligned} \tag{5.1.8}$$

which gives a linear system for v_{gx}^0 and v_{gy}^0 of the form

$$\begin{bmatrix} -\sum_j \frac{\epsilon_j}{T_{sj}} \frac{1-D_j}{D_j} & 2\left(\sum_j \frac{\epsilon_j}{D_j} + 1\right) \\ (q-2)\left(\sum_j \frac{\epsilon_j}{D_j} + 1\right) & -\sum_j \frac{\epsilon_j}{T_{sj}} \frac{1-D_j}{D_j} \end{bmatrix} \begin{bmatrix} v_{gx}^0 \\ v_{gy}^0 \end{bmatrix} = \begin{bmatrix} -\chi_0 \\ 0 \end{bmatrix} \tag{5.1.9}$$

Defining

$$\mathcal{A}_N = \tilde{\kappa}^2 \sum_{i=1}^{N} \frac{\epsilon_i T_{si}}{1 + \tilde{\kappa}^2 T_{si}^2}, \qquad \mathcal{B}_N = 1 + \sum_{i=1}^{N} \frac{\epsilon_i}{1 + \tilde{\kappa}^2 T_{si}^2}, \tag{5.1.10}$$

and $\tilde{\kappa}^2 = \kappa^2 \Omega_0^{-2}$, where $\kappa^2 = 2\,(2-q)\,\Omega_0^2$, is the square of the epicyclic frequency the Eq. (5.1.9) reads

$$\begin{bmatrix} -\mathcal{A}_N & 2\mathcal{B}_N \\ -\tilde{\kappa}^2 \mathcal{B}_N/2 & -\mathcal{A}_N \end{bmatrix} \begin{bmatrix} v_{gx}^0 \\ v_{gy}^0 \end{bmatrix} = \begin{bmatrix} -\chi_0 \\ 0 \end{bmatrix} , \tag{5.1.11}$$

and the steady-state solution of Eqs. (5.1.1)-(5.1.4) is

$$v_{gx}^0 = \mathcal{A}_N \chi_0 \psi \,, \qquad v_{gy}^0 = -\frac{\tilde{\kappa}^2}{2} \mathcal{B}_N \chi_0 \psi \,, \tag{5.1.12}$$

with $\psi = \left(\mathcal{A}_N^2 + \tilde{\kappa}^2 \mathcal{B}_N^2\right)^{-1}$.

For the i-th dust species, its velocity can be written in terms of the velocity of the gas as

$$v_{ix}^0 = \frac{v_{gx}^0 + 2T_{si} v_{gy}^0}{1 + \tilde{\kappa}^2 T_{si}^2} \,, \qquad v_{iy}^0 = \frac{v_{gy}^0 - (2-q) T_{si} v_{gx}^0}{1 + \tilde{\kappa}^2 T_{si}^2} \,. \tag{5.1.13}$$

The vertical velocities are $v_{gz}^0 = v_{iz}^0 = 0$ and the densities are constant for all the species. We note that, for the case $q = 3/2$ (i.e., Keplerian shear), Eqs. (5.1.12)-(5.1.13) are, as expected, equivalent to the expansion of Eqs. (3.4.9)-(3.4.12) for $h_0 \ll 1$.

5.1.2 Linear regime - eigenvalues and eigenvectors

In this section, we linearize Eqs. (5.1.1)-(5.1.4) around the background solution (5.1.12)-(5.1.13) to provide a framework for studying the stability of a given axisymmetric mode $\mathbf{k} = (k_x, 0, k_z)$.

Without loss of generality we assume perturbations of the form $\delta f = \mathrm{Re}\left(\delta \hat{f} e^{i(k_x x + k_z z) - \omega t}\right)$.

Defining the dimensionless densities $\delta\tilde{\rho} = \delta\hat{\rho}/\rho_{\mathrm{g}}^0$, $\epsilon_k^0 = \rho_k^0/\rho_{\mathrm{g}}^0$, velocities $\tilde{v} = \hat{v}/(h_0^2 v_{\mathrm{K0}})$, wavenumber $K = k h_0^2 v_{\mathrm{K0}}/\Omega_0$, eigenvalue $\tilde{\omega} = \omega/\Omega_0$, and relative velocities $\Delta_{kx}^0 = \tilde{v}_{\mathrm{g}x}^0 - \tilde{v}_{kx}^0$, $\Delta_{ky}^0 = \tilde{v}_{\mathrm{g}y}^0 - \tilde{v}_{ky}^0$, the axisymmetric equations describing the linear evolution of the system are

$$
\begin{aligned}
iK_x\tilde{v}_{\mathrm{g}x}^0\delta\tilde{\rho}_{\mathrm{g}} + iK_x\delta\tilde{v}_{\mathrm{g}x} + iK_z\delta\tilde{v}_{\mathrm{g}z} &= \tilde{\omega}\delta\tilde{\rho}_{\mathrm{g}} \\
\left(iK_x h_0^{-2} - \sum_{k=1}^{N}\frac{\epsilon_k^0\Delta_{kx}^0}{T_{\mathrm{s}k}}\right)\delta\tilde{\rho}_{\mathrm{g}} + \left(iK_x\tilde{v}_{\mathrm{g}x}^0 + \sum_{k=1}^{N}\frac{\epsilon_k^0}{T_{\mathrm{s}k}}\right)\delta\tilde{v}_{\mathrm{g}x} - 2\delta\tilde{v}_{\mathrm{g}y} + \sum_{k=1}^{N}\frac{\Delta_{kx}^0}{T_{\mathrm{s}k}}\delta\tilde{\rho}_k - \sum_{k=1}^{N}\frac{\epsilon_k^0}{T_{\mathrm{s}k}}\delta\tilde{v}_{kx} &= \tilde{\omega}\delta\tilde{v}_{\mathrm{g}x} \\
-\left(\sum_{k=1}^{N}\frac{\epsilon_k^0\Delta_{ky}^0}{T_{\mathrm{s}k}}\right)\delta\tilde{\rho}_{\mathrm{g}} + (2-q)\,\delta\tilde{v}_{\mathrm{g}x} + \left(iK_x\tilde{v}_{\mathrm{g}x}^0 + \sum_{k=1}^{N}\frac{\epsilon_k^0}{T_{\mathrm{s}k}}\right)\delta\tilde{v}_{\mathrm{g}y} + \sum_{k=1}^{N}\frac{\Delta_{ky}^0}{T_{\mathrm{s}k}}\delta\tilde{\rho}_k - \sum_{k=1}^{N}\frac{\epsilon_k^0}{T_{\mathrm{s}k}}\delta\tilde{v}_{ky} &= \tilde{\omega}\delta\tilde{v}_{\mathrm{g}y} \\
iK_z h_0^{-2}\delta\tilde{\rho}_{\mathrm{g}} + \left(iK_x\tilde{v}_{\mathrm{g}x}^0 + \sum_{k=1}^{N}\frac{\epsilon_k^0}{T_{\mathrm{s}k}}\right)\delta\tilde{v}_{\mathrm{g}z} - \sum_{k=1}^{N}\frac{\epsilon_k^0}{T_{\mathrm{s}k}}\delta\tilde{v}_{kz} &= \tilde{\omega}\delta\tilde{v}_{\mathrm{g}z} \\
iK_x\tilde{v}_{jx}^0\delta\tilde{\rho}_j + iK_x\epsilon_j^0\delta\tilde{v}_{jx} + iK_z\epsilon_j^0\delta\tilde{v}_{jz} &= \tilde{\omega}\delta\tilde{\rho}_j \\
-\frac{1}{T_{\mathrm{s}j}}\delta\tilde{v}_{\mathrm{g}x} + \left(iK_x\tilde{v}_{jx}^0 + \frac{1}{T_{\mathrm{s}j}}\right)\delta\tilde{v}_{jx} - 2\delta\tilde{v}_{jy} &= \tilde{\omega}\delta\tilde{v}_{jx} \\
-\frac{1}{T_{\mathrm{s}j}}\delta\tilde{v}_{\mathrm{g}y} + (2-q)\,\delta\tilde{v}_{jx} + \left(iK_x\tilde{v}_{jx}^0 + \frac{1}{T_{\mathrm{s}j}}\right)\delta\tilde{v}_{jy} &= \tilde{\omega}\delta\tilde{v}_{jy} \\
-\frac{1}{T_{\mathrm{s}j}}\delta\tilde{v}_{\mathrm{g}z} + \left(iK_x\tilde{v}_{jx}^0 + \frac{1}{T_{\mathrm{s}j}}\right)\delta\tilde{v}_{jz} &= \tilde{\omega}\delta\tilde{v}_{jz}
\end{aligned}
\tag{5.1.14}
$$

A general expression for the dispersion relation and its eigenvectors can be easily obtained and written in closed form (similar to what it was done in Section 3.3). However, due to the complexity of these expressions, we avoid writing them here. Instead, for solving the eigenvalue problem we use the function `eig` of NumPy (Walt et al., 2011), which uses LAPACK routines for complex non-symmetric matrices (Anderson et al., 1999).

In Table 5.1.1 we present the parameters, the eigenvalues and the eigenvectors for the three different cases, called LinA, LinB, and Lin3. The first two cases correspond to one gas and one dust species, and have already been studied (e.g. Youdin and Johansen, 2007; Balsara et al., 2009; Bai and Stone, 2010b).

Table 5.1.1: Table 4 from Benítez-Llambay et al. (2019). Eigenvalues, eigenvectors and parameters for the runs LinA, LinB and Lin3

	LinA	LinB	Lin3
Parameters			
K	30	6	50
T_{s1}	0.1	0.1	0.0425
ϵ_1	3.0	0.2	1.0
T_{s2}	–	–	0.1
ϵ_2	–	–	0.5
Eigenvalue			
ω/Ω_0	$-0.4190091323 + 0.3480181522i$	$-0.0154862262 - 0.4998787515i$	$-0.3027262829 + 0.3242790653i$
Eigenvector			
$\delta\tilde{\rho}_g$	$+0.0000074637 + 0.0000070677i$	$-0.0000337227 - 0.0003456248i$	$+0.0000061052 + 0.0000080743i$
$\delta\tilde{v}_{gx}$	$-0.0563787907 + 0.0120535455i$	$-0.0870451125 - 1.3851731095i$	$-0.1587288108 + 0.0213251096i$
$\delta\tilde{v}_{gy}$	$+0.0445570113 + 0.0197224299i$	$+1.3839936168 - 0.0937424679i$	$+0.1327989476 + 0.0674232641i$
$\delta\tilde{v}_{gz}$	$+0.0563784989 - 0.0120536242i$	$+0.0870497444 + 1.3852113520i$	$+0.1587286212 - 0.0213252588i$
$\delta\tilde{v}_{1x}$	$-0.0466198076 + 0.0124333223i$	$+0.2314730923 - 1.3715260043i$	$-0.1461274403 + 0.0234873672i$
$\delta\tilde{v}_{1y}$	$+0.0435211557 + 0.0213517453i$	$+1.3696536978 + 0.0196879160i$	$+0.1325843682 + 0.0691301709i$
$\delta\tilde{v}_{1z}$	$+0.0546507401 - 0.0077776652i$	$+0.0416164539 + 1.3844311928i$	$+0.1571142133 - 0.0174328415i$
$\delta\tilde{\rho}_2$	–	–	$+0.1522281314 + 0.1836379253i$
$\delta\tilde{v}_{2x}$	–	–	$-0.1335593453 + 0.0025396632i$
$\delta\tilde{v}_{2y}$	–	–	$+0.1092222067 + 0.0952973332i$
$\delta\tilde{v}_{2z}$	–	–	$+0.1485545469 + 0.0200753935i$

The dimensionless velocity amplitudes and wavenumber are defined as $\delta\tilde{v} = \delta v/(h_0^2 v_{K0})$ and $K = kh_0^2 v_{K0}/\Omega_0$, respectively. The dust-density perturbation $\delta\tilde{\rho}_1 = 1$ for all the runs.

The third one contains one gas and two dust species.

We report a small difference with respect to the eigenvalues obtained by Youdin and Johansen (2007). We tracked down the difference to two terms in the linearized equations:

$$-\delta\tilde{\rho}_g \sum_{k=1}^{N} \frac{\epsilon_k^0 \Delta_{kx}^0}{T_{sk}}, \quad \text{and} \quad -\delta\tilde{\rho}_g \sum_{k=1}^{N} \frac{\epsilon_k^0 \Delta_{ky}^0}{T_{sk}}. \tag{5.1.15}$$

Neglecting these terms modifies the fourth digit of the eigenvalues, and allows us to recover the values reported by Youdin and Johansen (2007).

5.1.3 Linear regime - numerical solution

In this section, we study the numerical solution of the fully non-linear set of equations in the shearing-box approximation. Simulations are performed with the shearing-box module of FARGO3D where dust equations are solve using the scheme discussed in Chapter 3. We then compare the results with those obtained from the linearized problem described in the previous section.

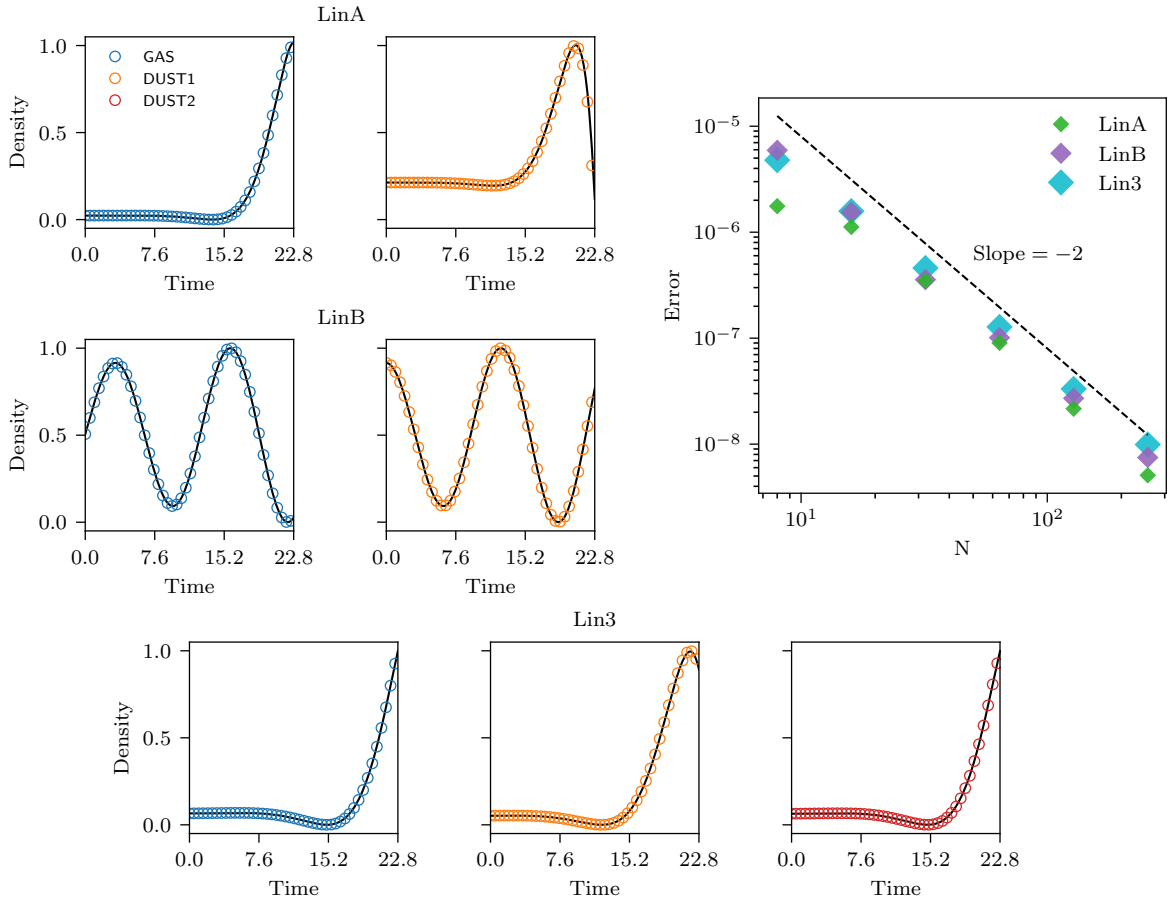

Figure 5.1.1: Figure 7 from Benítez-Llambay et al. (2019). Analytical (solid lines) and numerical (open circles) solutions of the linear streaming instability, for the runs LinA (top), LinB (center) and Lin3 (bottom), obtained with 128^2 grid points. From left to right, we plot the gas and dust densities. We additionally plot the result of the convergence test, described in Section 5.1.3.1. The agreement between the analytical and numerical solutions is excellent. The slope recovered from the convergence test is consistent with the expected convergence rate for all the cases, showing small deviations for very low resolutions.

The results presented in this section allow us to validate our framework and numerical methods to further study the streaming instability including multiple species as well as the non-linear evolution, as we will discuss in Sections 5.2 and 5.3.

To numerically recover the solutions we set $h_0 = 0.05$ and $v_{\rm K0} = 1$, and add the constant external force χ_0 to the gas component along the x direction. The shear parameter q is set to $3/2$. We only consider wavenumbers $k_x = k_z = k$, so we employ a square axisymmetric shearing-box with $x, y \in [-L/2, L/2]$ and $L = 2\pi/k$. The grid is evenly spaced over 256 cells in each direction. We set periodic and shear-periodic boundary conditions in the z and x directions, respectively. The initial condition is given by the steady-state background solution Eqs. (5.1.12) – (5.1.13), and we set the background densities to

$\rho_i^0 = \epsilon_i \rho_{\rm g}^0$, with $\rho_{\rm g}^0 = 1.0$.

Because of truncation errors, the numerical equilibrium does not match to machine precision that given by Eqs. (5.1.12)-(5.1.13). However, after initializing each run, the system rapidly relaxes towards an exact numerical equilibrium. Thus, to improve our measurements, we wait for a time $t_0 = 1.2\Omega_0^{-1}$ until obtaining the numerical equilibrium. Then we excite the unstable mode. We note that to speed-up the calculations, the relaxation step can be done in a 1D grid. We fix the CFL factor to 0.3 for all the runs. The linear mode is excited by adding to the steady-state background the small perturbation δf, defined

Table 5.1.2: Table 5 from Benítez-Llambay et al. (2019). Measured growth rates for different number of cells for the runs LinA, LinB and Lin3.

N	LinA		LinB		Lin3	
8	-0.325	$\pm 3.3 \times 10^{-2}$	$+0.030$	$\pm 1.2 \times 10^{-3}$	-0.222	$\pm 8.5 \times 10^{-2}$
16	-0.3961	$\pm 1.7 \times 10^{-3}$	-0.00821	$\pm 2.9 \times 10^{-4}$	-0.271	$\pm 4.9 \times 10^{-2}$
32	-0.41311	$\pm 5.2 \times 10^{-4}$	-0.014468	$\pm 7.3 \times 10^{-5}$	-0.291	$\pm 1.3 \times 10^{-2}$
64	-0.41762	$\pm 1.5 \times 10^{-4}$	-0.015349	$\pm 2.2 \times 10^{-5}$	-0.3000	$\pm 2.4 \times 10^{-3}$
128	-0.418583	$\pm 8.0 \times 10^{-5}$	-0.0154688	$\pm 6.5 \times 10^{-6}$	-0.30248	$\pm 1.4 \times 10^{-4}$
256	-0.418900	$\pm 5.4 \times 10^{-5}$	-0.0154839	$\pm 2.0 \times 10^{-6}$	-0.302672	$\pm 5.1 \times 10^{-5}$

The values correspond to the average of the growth rates obtained by fitting the time evolution of each component of the eigenvector. The errors correspond to the standard deviation of this average.

as:

$$\delta f = A \left[\mathrm{Re}\left(\delta \hat{f}\right) \cos(k_x x + k_z z) \; - \mathrm{Im}\left(\delta \hat{f}\right) \sin(k_x x + k_z z) \right], \tag{5.1.16}$$

where $\delta \hat{f}$ is the complex amplitude of the corresponding component of the unstable eigenvector (see Table 5.1.1) and A is a small amplitude that ensures linearity. Its value is set to $A = 10^{-5}$.

In Figure 5.1.1, we plot the time evolution of the normalized density perturbations for each of the three different cases, measured from time t_0 at the location $x = z = -L/2$ (this is an arbitrary choice). In the plot we adopt a normalization that sets the density perturbation between zero and one. In each panel, we plot with open circles, the values obtained numerically with our implementation, while the solid lines are the analytical ones. The color represents different species, blue being the gas and, orange and red, the dust species. The first two rows of Figure 5.1.1 correspond to the tests LinA and LinB, respectively. The third one corresponds to the three species Lin3 test. In all of the runs, the agreement between the analytical and numerical solutions is excellent. We additionally comment that the same level of agreement is observed for the velocities of the gas and the dust species.

In Table 5.1.2, we present the result of the measured growth rates for the tests LinA, LinB and Lin3, for

different resolutions. The growth rate for each mode was obtained first by fitting each component of the eigenvector and then averaging the results of the fits. For the tests LinA and Lin3, the instability can be recovered with 8 cells. However, for the mode LinB, at least 16 cells are required to obtain an unstable behavior. The errors correspond to the standard deviation of the average.

5.1.3.1 Linear regime - Convergence test

To test the convergence rate of these test problems, we perform a series of runs decreasing the resolutions by factors of two, starting with 256^2 cells down to 8^2 cells.

We measure the convergence rate for the three configurations described in the previous section by computing the error, defined as

$$\text{error} = \left(\sum_{i=1}^{m} \left\langle \left(\delta f_i^{\Delta}(t) - \delta f_i(t) \right)^2 \right\rangle \right)^{1/2}, \tag{5.1.17}$$

where m is the number of components of the eigenvector, δf^{Δ} the numerical solution, δf_i is the analytical one, and $\langle\,\rangle$ the time average between $t = t_0$ and $t = t_0 + 7\Omega_0^{-1}$.

The rightmost large panel of Figure 5.1.1, shows the result of the convergence test for the three different cases. We additionally plot (dashed line) the expected second-order accuracy slope. The lowest resolution cases slightly depart from it. However, an excellent convergence rate is observed for $N > 32^2$ grid points. The convergence properties for all the modes analyzed demonstrate the validity of our implementation in agreement with the results presented in Chapter 3. It is remarkable that, even with low resolution, our implementation is able to recover the linear growth rate with an acceptable level of accuracy.

We report that we have observed the mode LinB to be prone to develop noise at cell level which, eventually, contaminates the computational domain. By disabling the drag term, we have concluded that this noise is something entirely related to the gas component. This issue was significantly reduced by enabling a predictor using a half transport-step before the source step, allowing us to recover excellent second-order accurate linear solutions (see Chapter 3 Section 3.2.3).

5.2 Streaming Instability for a Particle-Size Distribution

The linear phase of the Streaming Instability has been extensively studied including only one-dust species (see e.g. Johansen and Youdin, 2007; Balsara et al., 2009; Kowalik et al., 2013; Chen and Lin, 2018; Riols and Lesur, 2018). However, the dust component of PPDs may be characterized by a non-trivial particle-size distribution (e.g., Birnstiel et al., 2012). In this section, we describe and summarize the results obtained in Krapp et al. (2019), where we presented the first study of the linear phase of the multispecies streaming instability. Our systematic exploration of parameter space allowed us to provide the growth rate of the most unstable mode as a function of the dust-to-gas density ratio, particle-size range, and number of dust species considered for describing a particle-size distribution a we defined in Section 2.1.2.

5.2.1 Linear Modes in Fourier Space

The equations describing the dynamics of a gas coupled to N dust species via drag forces in the framework of the shearing box, together with the analytical steady-state background solution, have been presented in Section 5.1.1. Moreover, the linearized axisymmetric continuity and momentum equations of $4(N+1)$ species where derived in Section 5.1.2 and validated in Section 5.1.3, where we successfully recovered the linear growth of the streaming instability predicted by our analytical calculations. In this section we study the stability of a given eigenmode that evolves in space and time according to $\mathrm{Re}[\delta\hat{f}(k_x,k_z)\,e^{i(k_x x+k_z z)-\omega t}]$. Here, $\delta\hat{f}(k_x,k_z)$ are the $4(N+1)$-dimensional (complex) eigenvectors in Fourier space, spanned by the wavenumbers (k_x,k_z), associated with the (complex) eigenvalue $\omega(k_x,k_z)$. In the context of the streaming instability, it is customary to work with dimensionless wavenumbers $K = H_0^2 k/R_0$, where H_0 is the disk sale-height at the fiducial radius R_0, where the shearing box is centered, and to use the Keplerian angular frequency, $\Omega_0 \equiv \Omega_\mathrm{K}(R_0)$, to scale the eigenvalues.

The early evolution of the instability is governed by the unstable modes – i.e., those with $\mathrm{Re}(\omega) < 0$ – with maximum growth rate σ, given by

$$\sigma = \max\{|\mathrm{Re}(\omega)| : \mathrm{Re}(\omega) < 0\}. \tag{5.2.1}$$

In order to identify these modes, we consider the space spanned by the set (K_x, K_z) when each normalized wavenumber takes values in the range $[10^{-1}, 10^{3}]$. Our fiducial grid is evenly spaced in logarithmic scale and contains 260 cells in each direction. Given a particle-size distribution, the dynamical evolution of a specific mode is completely determined by the spectrum of $4(N+1)$ complex eigenvalues ω.

The density of each dust species is obtained adopting a particle-size distribution as defined in Section 2.1.2 with $q = 3.5$ and a logarithmic spacing in Stokes number. This adopted discrete approximation of the underlying continuous distribution should in principle lead to a dynamical model that converges as the number of dust species considered increases. Therefore, it is of particular interest to understand the sensitivity of linear phase of the streaming instability with respect to the number of dust species, N, used to describe the dust-size distribution.

5.2.2 Fastest Growing Modes – Two Test Cases

The goal of this section is to introduce the two significant findings of our study which correspond to (i) the secular growth of the multispecies streaming instability and, (ii) the decay of the growth rate with the number of species. We will only consider two discrete particle-size distributions both with $\epsilon = 1$, but spanning two different overlapping ranges of Stokes numbers: $\Delta T_{\rm s}^{\rm I} = [10^{-4}\,, 10^{-1}]$ and $\Delta T_{\rm s}^{\rm II} = [10^{-4}\,, 1]$.

We compute the growth rate using $N \in \{16, 128, 512\}$ dust species. These considerations lead to six different eigenvalue problems that are solved to find the fastest growing modes as a function of (K_x, K_z). The results corresponding to $\Delta T_{\rm s}^{\rm I}$ and $\Delta T_{\rm s}^{\rm II}$, for each of the adopted N-values, are shown in the upper and lower panels of Figure 5.2.1, respectively. For $\Delta T_{\rm s}^{\rm I}$, the upper panels show a maximum growth rate that converges with increasing dust species to $\sigma \simeq 1.6 \times 10^{-2}\Omega_0$ (see Figure 5.2.2). For this distribution, the set of modes that grow fastest converge to a confined region close to the center of the explored domain in (K_x, K_z). In contrast, for $\Delta T_{\rm s}^{\rm II}$ the maximum growth rate decreases monotonically from $\sigma \simeq 6.7 \times 10^{-2}\Omega_0$ for 16 species to $\sigma \simeq 0.33 \times 10^{-2}\Omega_0$ for 512 species (see also Figure 5.2.2).

The sensitivity of the results obtained for the fastest growth rate with respect to the number of species N can be better appreciated in the leftmost panel in Figure 5.2.2, which shows the growth rates of the most unstable modes for the two distributions with $\Delta T_{\rm s}^{\rm I}$ (orange line) and $\Delta T_{\rm s}^{\rm II}$ (blue line), when the

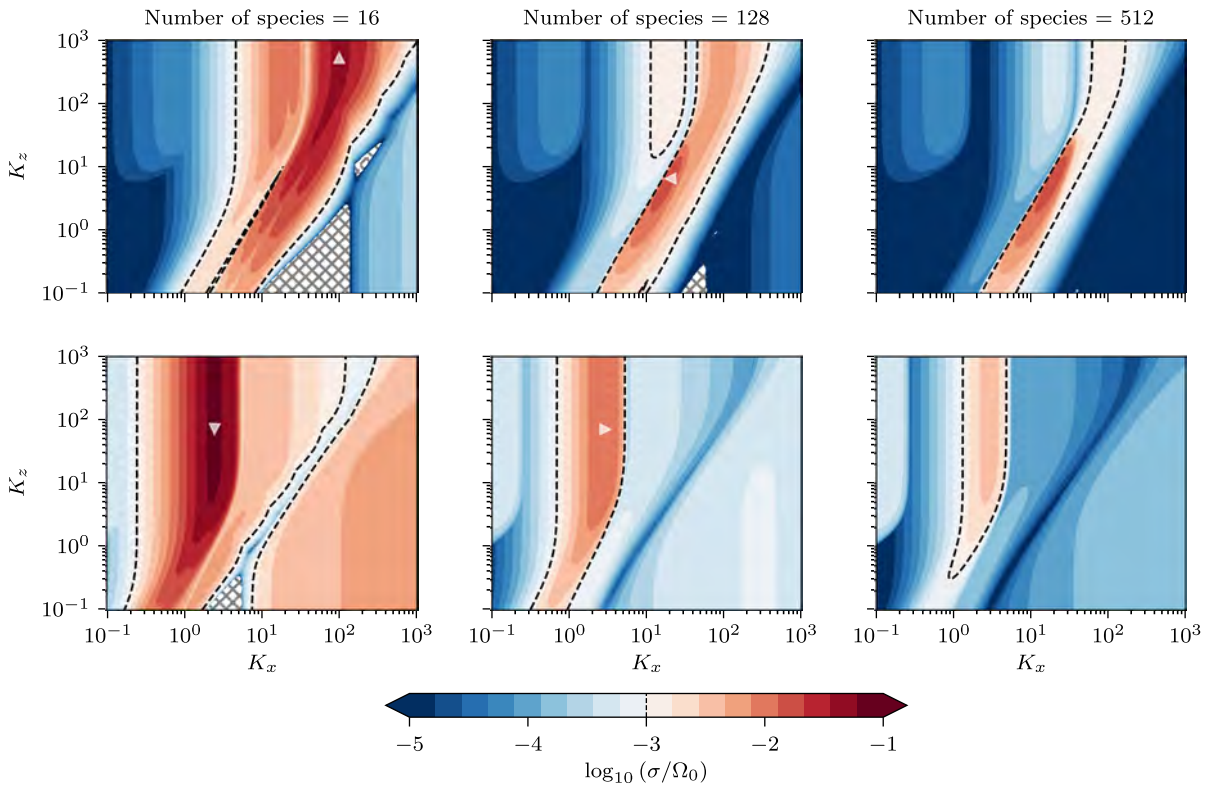

Figure 5.2.1: Figure 1 from Krapp et al. (2019). Color map displaying the growth rate σ of the most unstable mode for the multi-species streaming instability as a function of the wavenumbers K_x and K_z. Results are shown for two number-density distributions with power-law of index $q = -3.5$ in the particle-size/Stokes number and equal dust-to-gas mass ratio, $\epsilon = 1$, for Stokes numbers logarithmically spaced in $\Delta T_{\rm s}^{\rm I} = [10^{-4}\,, 10^{-1}]$ (upper panels) and $\Delta T_{\rm s}^{\rm II} = [10^{-4}\,, 1]$ (lower panels) and for an increasing number of dust species $N = 16, 128, 512$. Dashed lines denoting $\sigma = 10^{-3}\Omega_0$, mark the turning point of the divergent color palette. Hatched regions are stable. White triangles correspond to the fastest growing modes whose temporal evolution we checked independently using the code FARGO3D (see Fig. 5.2.2).

number of dust species doubles from $N = 2$ to $N = 2048$. For the case $\Delta T_{\rm s}^{\rm I}$ the maximum growth rate converges when using 64 dust species. This is not the case for $\Delta T_{\rm s}^{\rm II}$, for which the maximum growth rate decreases below $\sigma < 10^{-3}\Omega_0$. However, in a region around $K_x = 10^{-1}$, the growth rate converges to $\sim 5 \times 10^{-4}\Omega_0$ for $N \geq 64$. This value sets the time scale of the linear instability for $N > 2048$ species.

In order to shed some light on the strikingly different behaviour exhibited by $\Delta T^{\rm I}$ and $\Delta T^{\rm II}$, we show in Figure 5.2.3 high resolution maps in (K_x, K_z) zooming-in the neighborhood of the fastest growing modes. The left and right panels show the maximum growth rate for 64 and 128 species, respectively. The upper and lower panels correspond to $\Delta T_{\rm s}^{\rm I}$ and $\Delta T_{\rm s}^{\rm II}$ (orange and blue curves in Figure 5.2.2),

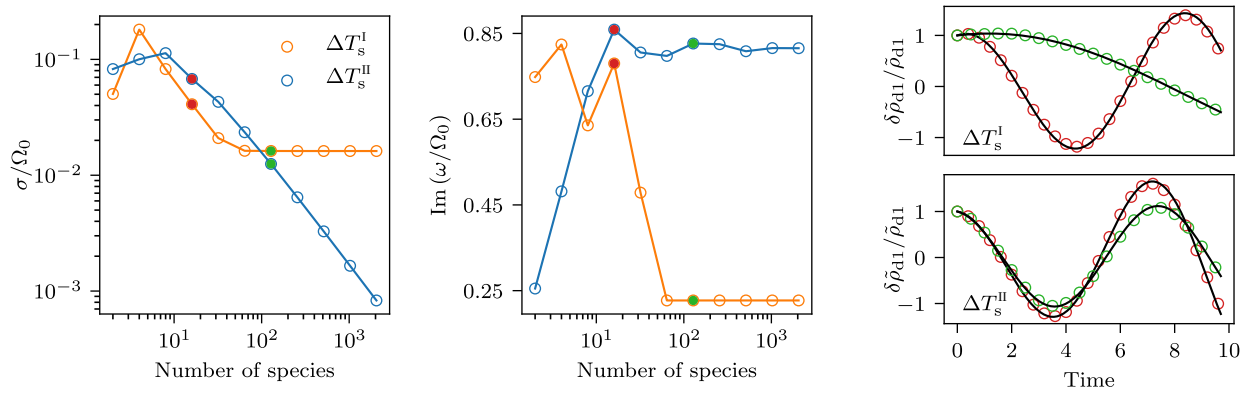

Figure 5.2.2: Figure 2 from Krapp et al. (2019). Real (left panel) and imaginary (middle panel) parts for the eigenvalues corresponding to the most unstable modes for the particle distributions with dust-to-gas mass ratio $\epsilon = 1$ and Stokes numbers in the intervals $\Delta T_s^I = [10^{-4}, 10^{-1}]$ (orange) and $\Delta T_s^{II} = [10^{-4}, 1]$ (blue) as a function of particle species number N. The two rightmost panels show the time evolution of the density fluctuation of dust species 1, $\delta\rho_1$, for the most unstable eigenmode. Red and green unfilled circles show the solutions obtained with FARGO3D for 16 and 128 dust-species, respectively, using 32 cells per wavelength. The solid black lines correspond to the solutions of the linear mode analysis described in Section 5.2.1.

respectively. These maps reveal a pattern with a number of fringes that increases linearly with N, as they split unstable regions for which the growth rates also decay also linearly with N. If these fringes merge, i.e., their separation is smaller than their width, the growth rates converge. It is worth stressing that the imaginary parts corresponding to the most unstable eigenvalues (shown in the middle panel of Figure 5.2.2) do converge as N increases in both cases. Because only the real part of the eigenvalue varies with the number of species, the decay seems to be an intrinsic property of the instability rather than systematic errors introduced in our method.

The decay observed in the growth rate of the most unstable modes when N increases in the case ΔT_s^{II} is in stark contrast with the behavior observed for ΔT_s^I. This warrants a systematic exploration of parameter space including also the dust-to-gas mass ratio. Before embarking on this, and given the complexity of the equations involved in the linear mode analysis describing the multi-species streaming instability, we provide an independent check of our solutions below.

5.2.3 Verification of the Linear Mode Analysis

We test the time evolution of the most unstable modes following the procedure described in Section 5.1.3. We consider four representative cases from Figure 5.2.2 (red and green filled circles) and use the corresponding eigenvectors to initialize four numerical simulations. The rightmost panels of Figure 5.2.2

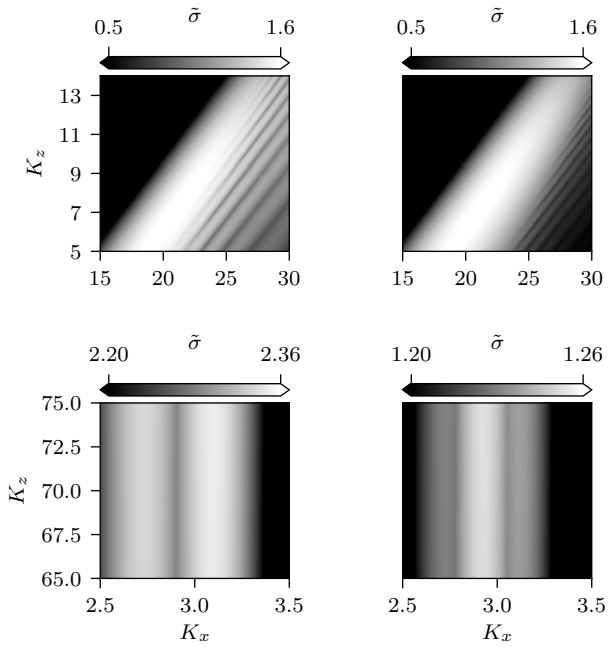

Figure 5.2.3: Figure 3 from Krapp et al. (2019). High-resolution maps of the normalized growth rate $\tilde{\sigma} = 10^2\sigma/\Omega_0$. Zoom-in domains surrounding the fastest growing modes for the distributions with Stokes numbers in $\Delta T_{\rm s}^{\rm I} = [10^{-4}\,, 10^{-1}]$ and $\Delta T_{\rm s}^{\rm II} = [10^{-4}\,, 1]$ (upper and lower panels, respectively) for $N = 64$ and 128 species (left and right panels, respectively).

show the time evolution for one of the components (the dust density for species 1, $\delta\rho_1$) for each of these four modes. The solutions obtained with FARGO3D are shown with red and green unfilled circles for 16 and 128 dust-species, respectively. The black solid lines are the solutions obtained from our linear mode analysis described in Section 5.2.1. A detailed comparison between the analytical and numerical solutions of the density and velocity components of all the species is presented in Appendix A.3. The excellent agreement between the time evolution of the selected eigenmodes provides additional support to our linear calculations. This critically reduces the possibility of potential issues in several steps of our analysis including the derivation of the background equilibrium, the linearization of the perturbed system, and the method used to find the eigenvalues and eigenvectors.

5.2.4 Systematic Parameter Space Exploration

We seek the growth rate of the most unstable mode given a particle-size distribution characterized by the dust-to-gas mass ratio, ϵ, a range of Stokes numbers, $\Delta T_{\rm s} = [T_{\rm s,min}, T_{\rm s,max}]$, and the total number of species N. We consider four different mass ratios, $\epsilon = \{0.01, 0.1, 0.5, 1\}$ and two sets of intervals in Stokes numbers for which either the minimum is fixed and the maximum varies,

i.e., $\Delta T_{\mathrm{s,min}} = [10^{-4}, T_{\mathrm{s,max}}]$ with $T_{\mathrm{s,max}} \in \{10^{-3}, 10^{-2}, 10^{-1}, 1\}$, or the maximum is fixed and the minimum varies, i.e., $\Delta T_{\mathrm{s,max}} = [T_{\mathrm{s,min}}, 1]$ with $T_{\mathrm{s,min}} = \{10^{-1}, 10^{-2}, 10^{-3}, 10^{-4}\}$. For each of these intervals in Stokes numbers, we consider an increasing number of dust-species by doubling N from 2 to 2048 while keeping the dust-to-gas mass ratio characterizing the distribution constant. This procedure leads to $4 \times (4 \times 2 - 1) \times 11 = 308$ independent discrete distributions.

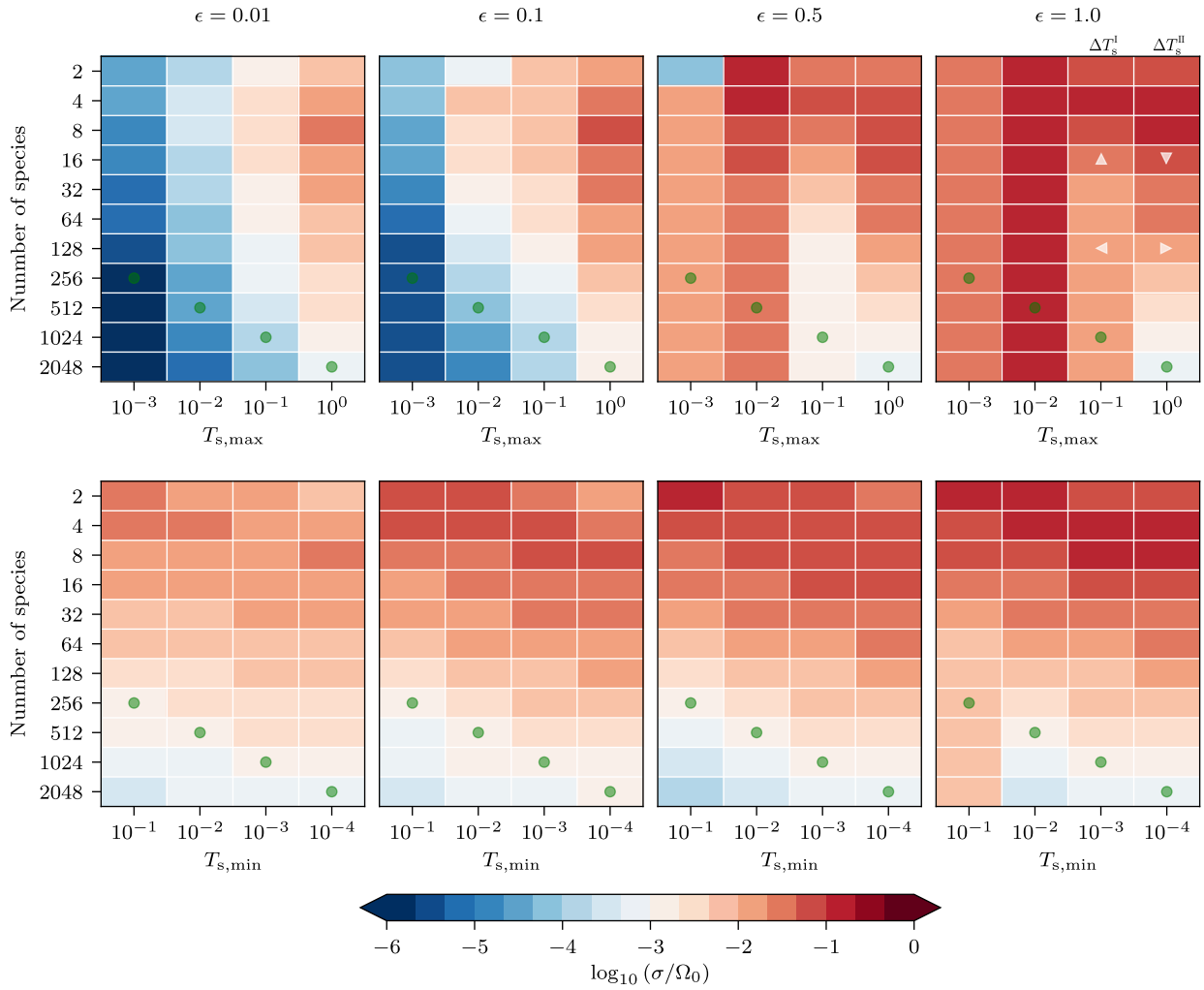

Figure 5.2.4: Figure 4 from Krapp et al. (2019). Maximum growth rate for the multi-species streaming instability as a function of the number of the dust-species N for different ranges of Stokes numbers and (fixed) dust-to-gas mass ratio, from left to right each block corresponds to $\epsilon = \{0.01, 0.1, 0.5, 1\}$. The upper panels show the results when considering a fixed $T_{\mathrm{s,min}} = 10^{-4}$ and varying $T_{\mathrm{s,max}}$. The lower panels show the results when considering a fixed $T_{\mathrm{s,max}} = 1$ and varying $T_{\mathrm{s,min}}$. The green circles, in each panel, show examples of distributions that have the same number of species per decade in Stokes number. White triangles are used to indicate the correspondence with the distributions used to compute the growth rate maps in Figure 5.2.1.

The maximum growth rates for each of the distributions defined above are shown in Figure 5.2.4. Each panel corresponds to a different dust-to-gas mass ratio ϵ. The rows and columns correspond to a given

N and $\Delta T_{\rm s}$, respectively. Each cell is color-coded according to the logarithm of the maximum growth rate obtained in (K_x, K_z)-space, following the method described in Section 5.2.1.

The most relevant outcomes are (i) the growth rate of the most unstable modes corresponding to the majority of the distributions with low dust-to-gas mass ratios $\epsilon \lesssim 0.1$ have not converged and decreases below $10^{-3}\Omega_0$, independently of $T_{\rm s,max}$. In particular, when $T_{\rm s,min} = 10^{-4}$ is fixed, (Figure 5.2.4, upper panels), the upper bound for the growth rate decreases from $\sigma = 10^{-3}\Omega_0$ to $\sigma = 10^{-5}\Omega_0$ as $T_{\rm s,max}$ decreases. (ii) The range of Stokes numbers for which convergence of the growth rate with the number of species is reached increases with ϵ when $T_{\rm s,min} = 10^{-4}$. (iii) When fixing $T_{\rm s,max} = 1$ (Figure 5.2.4, lower panels) convergence of the growth rate, with $N = 2048$, is achieved for none of the cases considered but one. The only exception is the case that corresponds to $\epsilon = 1$ and $T_{\rm s,min} = 10^{-1}$, for which the most unstable mode has a growth rate $\sigma \simeq 6 \times 10^{-3}\Omega_0$. In all other cases, the growth rate decreases below $10^{-3}\Omega_0$, independently of the dust-to-gas mass ratio, ϵ.

5.2.5 Outcome and implications of the parameter exploration

We have provided the first systematic study of the linear growth of the multispecies streaming instability. We found two different types of behaviors. On the one hand, there are distributions for which convergence of the growth rates is reached by considering between a handful and a couple of hundred dust species. In the majority of cases we considered, however, we were only able to find upper limits to the growth rates, which are, in many cases, well below the values obtained when only one dust species is involved. This result is better appreciated in Figure 5.2.5, where we show the maximum growth rates for the classical (gas and one dust-species) streaming instability (leftmost panel) together with those obtained for the distributions with 2048 species studied in Section 5.2.4 (center and rightmost panels).

Critical Dust-to-gas Mass Ratio Our study suggests that particle-size distributions with $\epsilon \geq 0.5$ allow the multispecies streaming instability to grow on timescales shorter than $10^3\Omega_0^{-1}$ (see Figure 5.2.5). This, however, depends on the range of Stokes numbers defining the distribution. For example, if $T_{\rm s,max} = 1$ the growth rates are smaller than $10^{-3}\Omega_0$, even for large dust-to-gas mass ratios (i.e., $\epsilon = 1$). When $\epsilon = 0.5$ and $T_{\rm s,min} = 10^{-4}$ the maximum growth rate converges to $\sigma \simeq 10^{-3}\Omega_0$ for $T_{\rm s,max} = 10^{-1}$, and the instability can grow faster for particle-size distributions with $T_{\rm s,max} \leq 10^{-2}$. It can also grow faster if the dust-to-gas mass ratio increases to $\epsilon \simeq 1$ for those ranges of Stokes

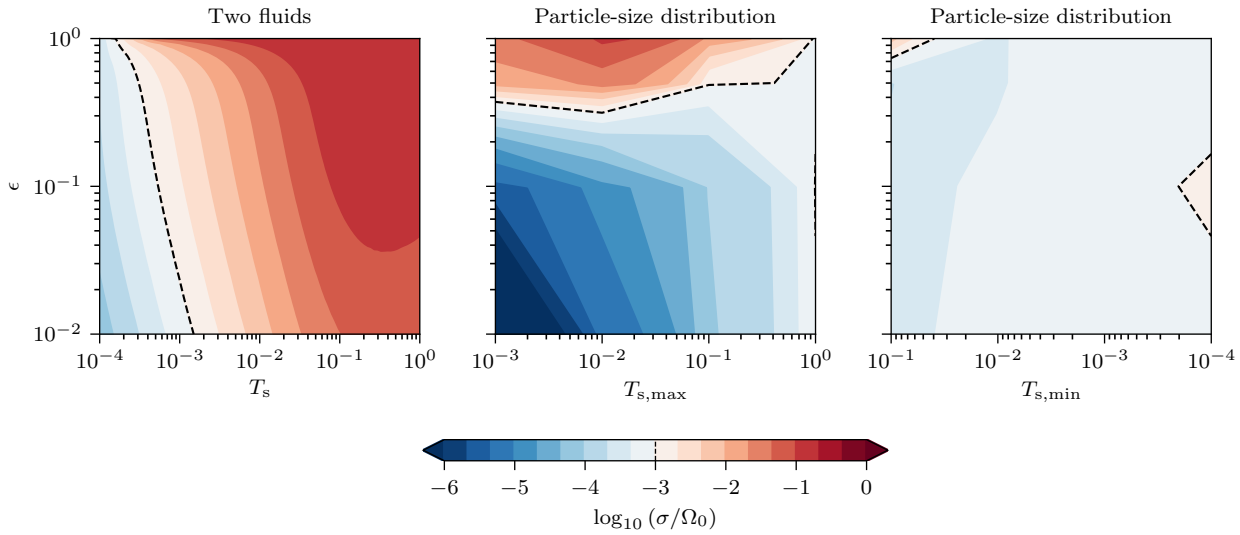

Figure 5.2.5: The left panel shows the maximum growth rate corresponding to the classical streaming instability involving only one dust-species. The center and rightmost panel show the maximum growth rate obtained for distributions with 2048 species when fixing $T_{s,min} = 10^{-4}$ and $T_{s,max} = 1$, respectively. The dashed line corresponds to $\sigma = 10^{-3}\Omega_0$ in all panels.

numbers. We additionally found that, if the total mass of the distribution decreases below $\epsilon = 0.5$, the instability develops on timescales of the order of $10^5\Omega_0^{-1}$, or even longer, depending on the range of Stokes numbers spanned by the particle distribution.

Simulations of Multi-Species Streaming Instability The successful recovery of known solutions is a key benchmark for any numerical code. Previous numerical studies of the non-linear evolution of the streaming instability with one dust species have been reported to recover, for example, its linear phase (see e.g. Johansen and Youdin, 2007; Balsara et al., 2009; Kowalik et al., 2013; Chen and Lin, 2018; Riols and Lesur, 2018; Benítez-Llambay et al., 2019). Even though the linear results have been derived using an Eulerian formalism, it has been shown that numerical codes evolving Lagrangian particles agree very well during the early phases of the streaming instability (Youdin and Johansen, 2007). This suggests that our findings will also hold in the Lagrangian framework. It is possible that a significant decay of the growth rate has not yet been observed in multiple dust-species simulations because of the relatively low number of species that have been used so far (see e.g. Bai and Stone, 2010b; Schaffer et al., 2018).

Single-dust Species Models of Streaming Instability We report the emergence of an unstable region for $K_x \gg 1$ and $K_z \geq 0$, which has not been observed before (see Youdin and Goodman, 2005; Youdin

and Johansen, 2007). A good example is provided by the two distributions studied in Figure 5.2.1. While a comprehensive study of this new unstable region is beyond the scope of this work, we found that the necessary condition for it to appear is the presence of at least two dust-species with opposite background drift-directions. This observation suggests that it may not be possible to capture the full dynamics of multi-species streaming instabilities using single dust-species models (e.g., Laibe and Price, 2014; Lin and Youdin, 2017).

5.2.6 Growth Rate Decay and Connection with Resonant Drag Instabilities

A systematic result of the parameter exploration is the decay of the growth rate with the increasing number of species. In this section we will discuss whether this observed decay is correlated with the decreasing mass of the individual species. The starting point will be to compare the growth rate of the distribution to the growth rate obtained when considering a single dust species with a dust-to-gas mass ratio $\epsilon_1 \sim \epsilon/N$ corresponding to the species with Stokes number that in isolation leads to fastest growth. Besides, we will address the potential connection between the resonant drag instability (RDI) theory Squire and Hopkins (2018) and our results.

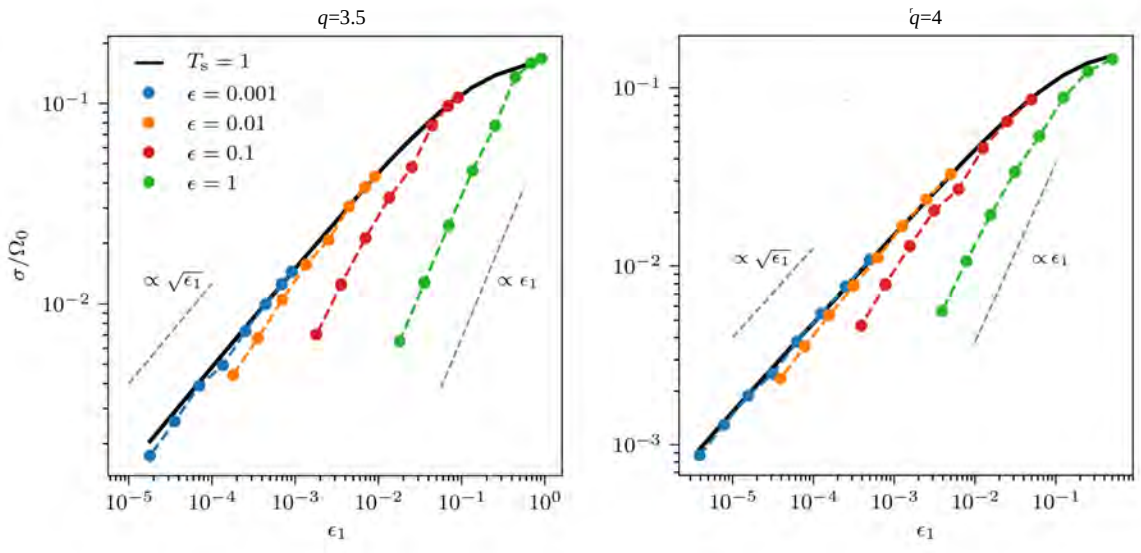

Figure 5.2.6: Maximum growth rate as a function of the dust-to-gas mass ratio $\epsilon_1 \sim \epsilon/N$ of the species with Stokes number that leads to fastest growth when considered in isolation, $T_s = 1$ in this case (solid black curve). The dashed colored curves correspond to distributions with different dust-to-gas mass ratios (each filled circle is obtained, from right to left, by doubling the number of species N from 2 to 256). The left panel shows the results for a distribution with $q = 3.5$ while the values in the right panels were obtained with a slope $q = 4$.

We consider two distribution in a range of Stokes number $[10^{-4}, 1]$ that differ in the adopted slopes, $q = 3.5$ and $q = 4$, respectively. Figure 5.2.6 shows the results of the comparison. The black solid line correspond to the growth rate of two-fluid problem obtained considering an species with $T_{\rm s} = 1$ and a dust-to-gas density ratio ϵ_1, obtained from the distribution.

We found that for $\epsilon < 10^{-2}$ the maximum growth rate of the distribution is in good agreement with the value obtained when considering in isolation the species with largest Stokes number. However, as the total mass of the distribution considered is increased, a significant difference between these growth rates exists. This is due to two effects that are difficult to disentangle; *i*) the background drift-velocity for each individual dust-species is modified because it is sensitive to the total mass of the particle-size distribution and not just the mass per bin (see Section 5.1.1) and *ii*) as the ensuing gas perturbation increases, the coupling between species increases and interference among them may not be negligible.

It seems that in the regime where $\epsilon < 10^{-2}$, the resonant drag instability (RDI) framework (Squire and Hopkins, 2018) can help to provide insight into the behavior of the multispecies streaming instability. At sufficiently low dust-to-gas mass ratios the maximum growth rate is expected to decay as $\sqrt{\epsilon_1} \sim \sqrt{\epsilon/N}$. This is indeed obtained for distributions with dust-to-gas mass ratios smaller than $\epsilon = 0.01$ (see Figure 5.2.6).

The connection between the multiple species streaming instability and the RDI can be better appreciated in Figure 5.2.7, where we show the stability maps (equivalent to the maps in Figure 5.2.1) for two distributions. Each distribution has eight species with a dust-to-gas mass ratio of $\epsilon = 10^{-5}$ (upper panel) and $\epsilon = 1$ (lower panel). The left panels in each of these figures show the maps of the growth rate for the multi-fluid system. On top of the maps, we over plot with dashed lines each of the normalized resonant wavenumbers, $(K_{x,i}, 0, K_{z,i})$, solution of the equation (see Squire and Hopkins, 2018, Eq. 30)

$$K_{x,i}(\tilde{v}^0_{{\rm g}x} - \tilde{v}^0_{{\rm d}x,i}) = \frac{K_{z,i}}{\sqrt{K^2_{x,i} + K^2_{z,i}}}\Omega_0\,, \qquad \text{with } i = 1, \ldots, 8\,, \tag{5.2.2}$$

where K_z, K_x, Ω_0, $\tilde{v}^0_{{\rm g}x}$ and $\tilde{v}^0_{{\rm d}x,i}$ where defined in Section 5.1.3.

Right panels of Figure 5.2.7 show a 1-dimensional cut of the left panels at those vertical wavenumbers where the local maxima of the multi-species system are found (solid black line) together with the corresponding results obtained for the single dust-species configurations (dashed colored lines).

In the limit of very low mass, the multi-species streaming instability can be well described as the

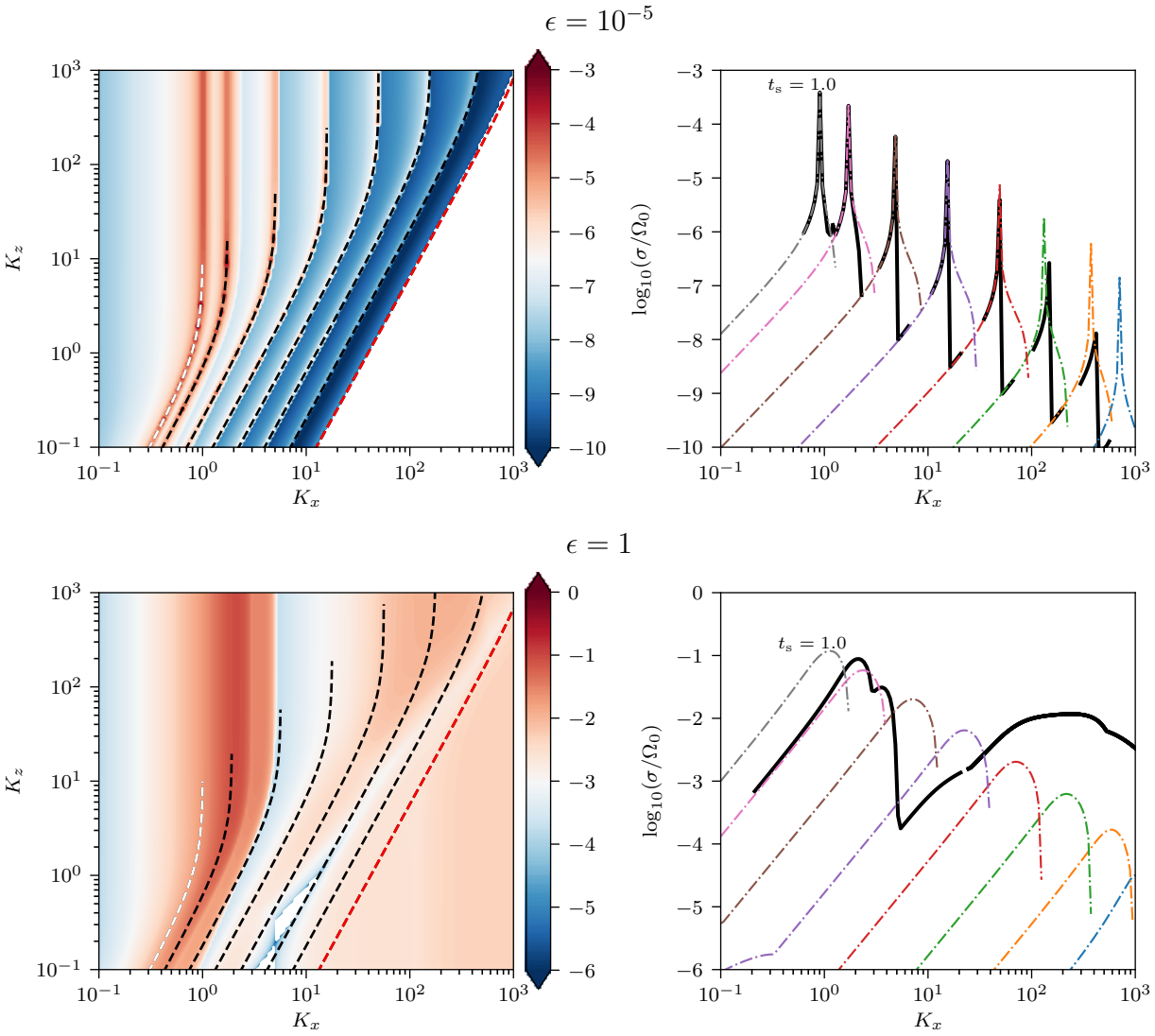

Figure 5.2.7: Left panels: Growth rate map in the K-plane for a particle-size distribution considering only eight dust-species. Dashed lines show the resonant wavenumber obtained from the two-fluid resonant drag instability theory, applied to each dust-species. The white dashed line corresponds to $T_s = 1$ (largest Stokes number of the distribution) while the resonant modes with smaller Stokes number is drawn with a red dashed line. Right panels: the black line represents a cut of the left panel at those vertical wavenumbers where the local maxima are found. The growth-rates at the same K_z but for each of the eight single dust-species considered in isolation are shown with dashed colored lines.

superposition of N different two-fluid instabilities occurring in a seemingly independent way, where the growth rate is dominated by the larger Stokes number (white dashed line in Figure 5.2.7). Furthermore, the growth rate (and the locus of the fastest modes in the K-plane) for each of these two-fluid instabilities can be well described with the RDI framework. This observation implies that, since the mass-per-bin decreases with the number of species under consideration, the growth rate of the multi-fluid instability will decrease as $\sigma \sim \sqrt{\epsilon_1}$, with ϵ_1 the mass of the bin with largest stokes number. In this case,

the convergence of the growth rate as the number of species increases is, for obvious reasons, not guaranteed.

As the mass of the distribution increases, the naive superposition of two-fluid instabilities does not work anymore. However, even for such a large mass, it is interesting to note that one could arbitrarily increase the number of species to obtain a mass-per-bin arbitrarily small, where the RDI theory could be, in principle, applied to each mass bin. Nevertheless, this is not strictly true because the background velocities do depend on the total mass of the distribution but not on the individual mass-per-bin. Furthermore, as shown in Figure 5.2.6, for the dust-to-gas mass ratio $\epsilon > 0.01$ the growth rate associated with particle distributions decreases proportionally to the number of species (or mass-per-bin), which might be due to the non-trivial feedback between several subdominant species.

5.3 Non-linear evolution of the Streaming Instability

As we concluded in the previous section, if dust-to-gas mass ratios are larger than $\epsilon > 0.5$ or segregation mechanisms induce a monodisperse population of dust, the streaming instability might be a natural outcome of the aerodynamic coupling between gas and dust. Understanding the non-linear evolution of the streaming instability and its consequences still represent a challenge, and numerical simulations seems good candidates to tackle the problem. Motivated by the reduced number of simulations where dust is treated as a pressureless fluid and the benefits of our numerical implementation (see Chapter 3 for a discussion), we dedicate this section to study previous results where the dust was simulated using Lagrangian particles. We discuss the advantages of our approach, together with the major discrepancies.

We consider the runs AB and BA described by Johansen and Youdin (2007) and Bai and Stone (2010b). We focus our attention on the convergence with resolution, the cumulative dust density distribution and the time evolution of the maximum density. These tests give us, in particular, the opportunity to assess whether the Eulerian approach for the dust species is able to reproduce similar features as those obtained by Bai and Stone (2010b) using Lagrangian particles.

For each test, we set a square shearing-box of size $L = lh_0H_0$, with $h_0 = 0.05$, $H_0 = h_0R_0$, and the fiducial radius $R_0 = 1$. The shear parameter q is, as above, $3/2$ (i.e., Keplerian rotation). For the test AB (BA), we set the dust-to-gas mass ratio $\epsilon_1 = 1$ ($\epsilon_1 = 0.2$), the Stokes number $T_{s1} = 0.1$ ($T_{s1} = 1.0$),

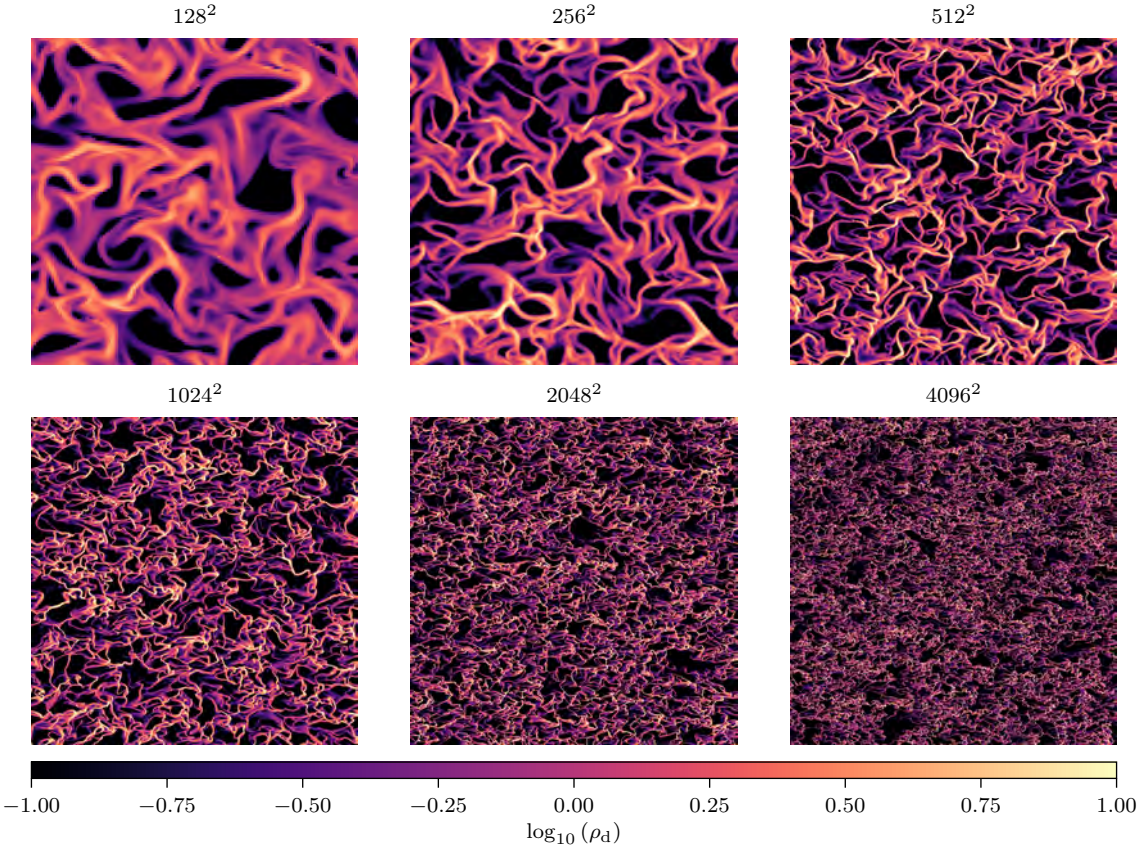

Figure 5.3.1: Figure 8 from Benítez-Llambay et al. (2019) Dust density maps for the test AB. Each panel is labeled by the total number of cells of the box. This mode is dominated by over-dense filaments and voids. The larger the resolution, the smaller and denser the filaments become. Convergence with resolution is far from being observed for the resolutions studied. The panels corresponding to 256^2 and 1024^2 cells can be compared with Figure 5 of Bai and Stone (2010b), where a good qualitative agreement is observed.

and the parameter $l = 2$ ($l = 40$). The total integration time is set to $40\Omega_0^{-1}$ ($800\Omega_0^{-1}$), which allows the saturated turbulent state to be reached (Bai and Stone, 2010b). We seed the instability with white noise in the three velocity components of the two species, with an amplitude $A = 10^{-2} h_0 v_{\rm K0}$.

To test convergence with resolution, for a fixed box size, we vary the number of grid cells by a factor of four. For the test BA, we set the nominal box with 64^2 cells – a resolution of roughly $32/H_0$ – and obtain results when varying the number of cells up to 2048^2 – a resolution of $1024/H_0$. For the test AB, since a box with 64^2 cells does not allow the instability to growth, we start with 128^2 cells – a resolution of $1280/H_0$ – and increase it up to 4096^2 cells – a resolution of $40960/H_0$. We note that, when using 64^2 cells for the run AB, Bai and Stone (2010b) were able to recover an unstable evolution, which is probably due to the higher order of the Athena code. For the run AB, and the lowest resolution (128^2 grid cells), we report a saturation time $\simeq 12\Omega_0^{-1}$, a value higly dependent on resolution. On the

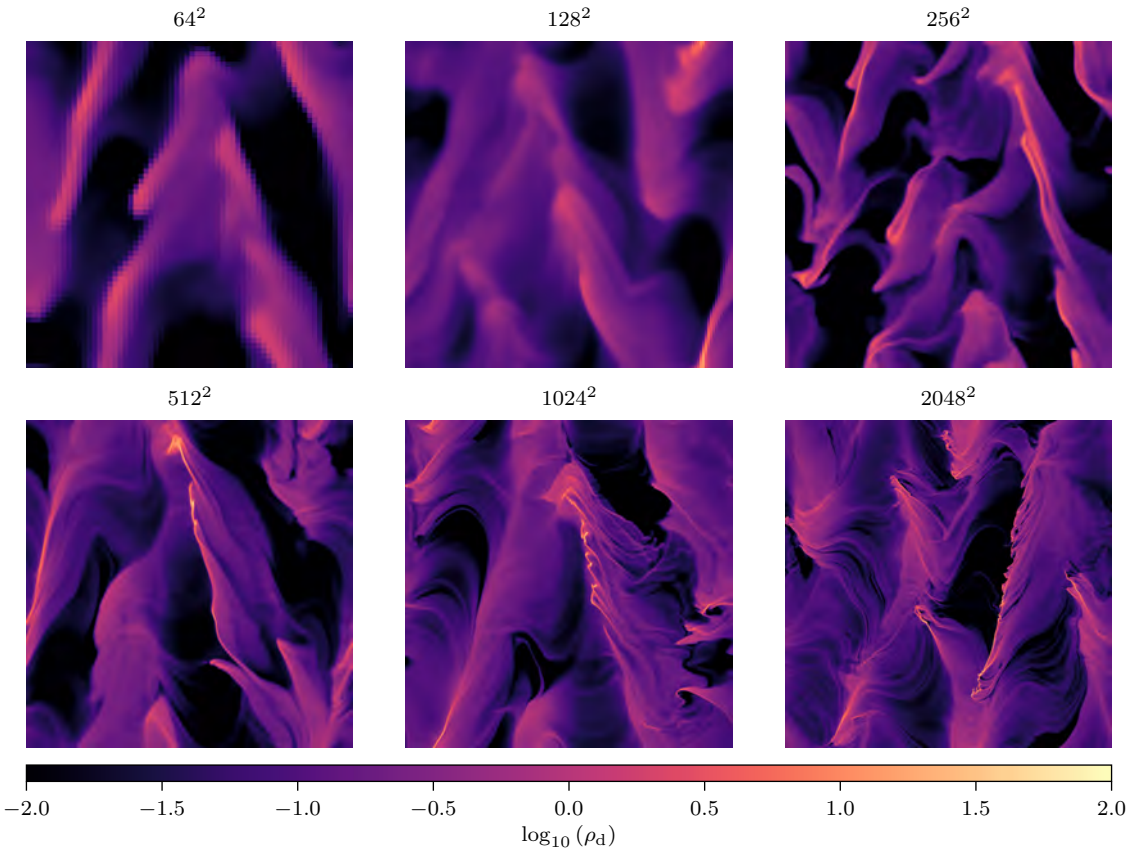

Figure 5.3.2: Figure 9 from Benítez-Llambay et al. (2019). Dust density maps for the test BA. Each panel is labeled by the total number of cells of the box. While the number of details increases with the number of cells, convergence with resolution is observed for number of cells $> 512^2$. The panels corresponding to 256^2 and 1024^2 cells can be compared with Figure 5 of Bai and Stone (2010b), where a good qualitative agreement is observed.

other hand, for the case BA, and the lowest resolution (64^2 grid cells), it saturates after $\simeq 150\Omega_0^{-1}$. This value is not very dependent on resolution.

In Figs. 5.3.1 and 5.3.2, we show snapshots of the dust density when the instability is saturated, at times $20\Omega_0^{-1}$ and $400\Omega_0^{-1}$, for the runs AB and BA, respectively. Figure 5.3.1 shows that, for the test AB, smaller and denser structures develop when the resolution increases, where no sign of convergence with resolution is observed. This effect, while still present, is not so strong for the low resolution runs in the test BA (Figure 5.3.2). Naively, this can be understood by analyzing the dispersion relation of the instability (see e.g. Youdin and Johansen, 2007). In the absence of any dissipative process, such as viscosity or diffusion, the smaller scales ($k_z \to \infty$) grow at a rate given by the maximum growth rate. Thus, density concentrations are prone to grow in very localized regions, a trend that can be clearly recognized in Figure 5.3.1 for the case AB. We refer to this as a naive explanation because it is not clear that the same occurs for the case BA, even when considering that the dispersion relation is not very

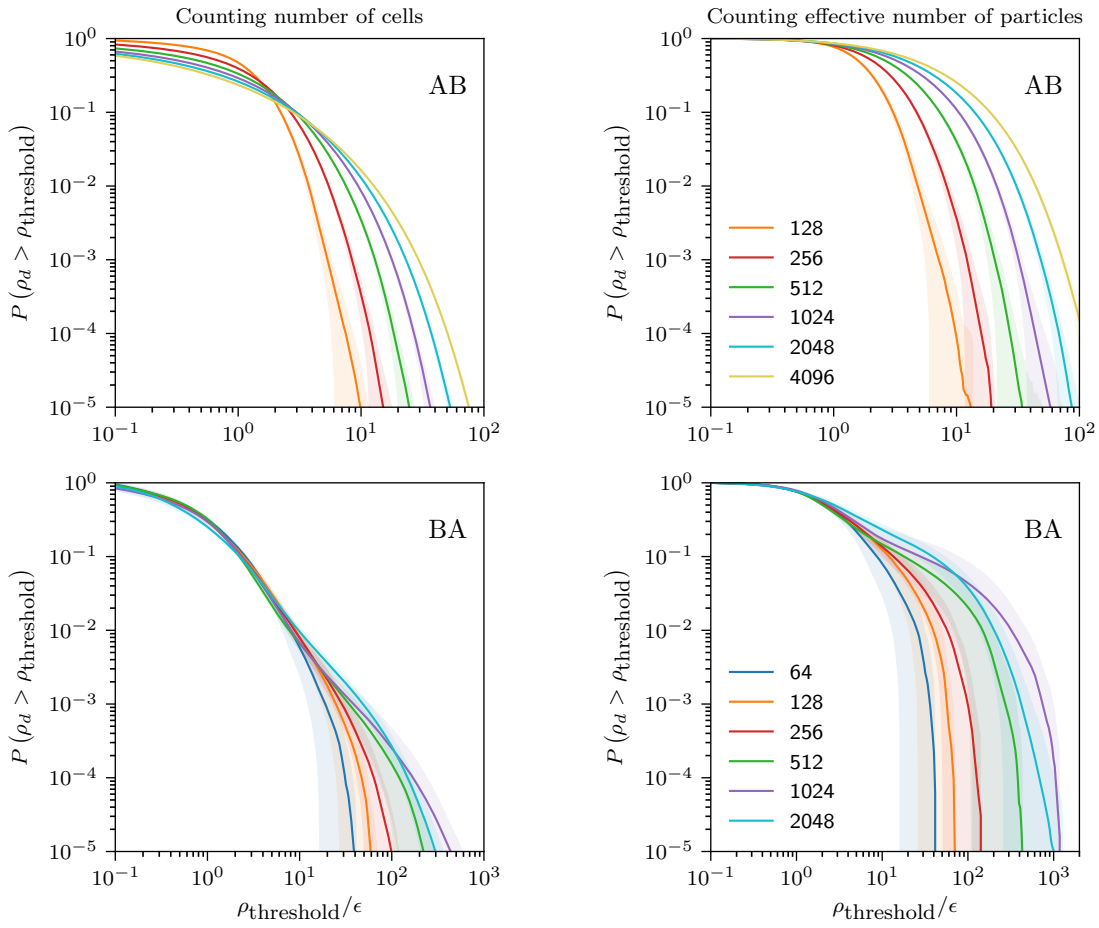

Figure 5.3.3: Figure 10 from Benítez-Llambay et al. (2019). Cumulative dust density distributions for the models AB (top) and BA (bottom). Solid lines correspond to the time-averaged cumulatives. Shaded regions correspond to the standard deviation. The different colors represent each of the cases shown in Figure 5.3.1 and 5.3.2. The left and right panels show the distributions obtained by counting cells and density, respectively. The distributions are normalized such that they integrate to one (left panels) or the probability of the lowest density-threshold is equal to one (right panels). The upper panel shows that, for the mode AB, the maximum density increases linearly with the resolution, a clear evidence of lack of convergence. Contrary to this case, the bottom panel shows that, for a number of cells $> 512^2$, the mode BA converges for all the density values. These results are independent of the statistical method used to compute the distributions. The right panels can be directly compared with Figure 6 of Bai and Stone (2010b).

different from that obtained for the case AB. Further studies are necessary to understand the real source of the discrepancy in the convergence properties between these two cases.

The panels that correspond to 256^2 and 1024^2 cells can be compared with those presented in Figure 5 of Bai and Stone (2010b). The level of qualitative agreement between the dust density obtained using a particle approach (Bai and Stone, 2010b) and our fluid approach is remarkable. We note that, in the non-linear turbulent regime, the instability could, in principle, be dominated by crossing trajectories, thus

invalidating our approach. However, the overall agreement obtained from this qualitative comparison suggests that the dynamics of the instability, in the non-linear regime, could be treated using a fluid approach.

To better quantify the convergence properties for both the AB and BA tests, following Youdin and Johansen (2007) and Bai and Stone (2010b), we study the cumulative dust-density distribution. We calculate it by following two different procedures, one by the counting number of cells with density above some threshold value, $\rho_{\text{threshold}}$, and another one by adding up the density of cells with density above $\rho_{\text{threshold}}$. The latter is similar to counting (the effective) number of particles, as done by Youdin and Johansen (2007) and Bai and Stone (2010b). We split the dust density in 300 logarithmic bins, between $\log_{10}(\rho_a\epsilon)$ and $\log_{10}(\rho_b\epsilon)$, where $\rho_b = 10^2$ for the case AB, while $\rho_b = 2 \times 10^3$ for BA, and $\rho_a = 10^{-1}$ in both cases. To obtain a representative cumulative function of the saturated regime, we compute it for different times, between $t = 30\Omega_0^{-1}$ and $t = 600\Omega_0^{-1}$ for the cases AB and BA, respectively, until the final integration time, and we finally average them. We also compute the standard deviation, which provides valuable information about the fluctuations of the density in the saturated phase.

In Figure 5.3.3 we plot the time averaged cumulative distributions for the dust density, corresponding to the cases AB (upper panels) and BA (lower panels). In each panel, and with different colors, we plot the cumulative function corresponding to the data shown in the panels of Figure 5.3.1 and 5.3.2. Shaded regions show the standard deviation. The left and right panels show the results obtained by counting the number of cells and by summing the density of the cells, respectively. In the left panels, the distributions are normalized such that they integrate to one. For comparative purposes with Bai and Stone (2010b), the curves in the right panels are normalized such that the probability of the minimum density bin is one.

For both cases, AB and BA, the dispersion is very small and does not depend on the method used to calculate the cumulative distribution. In particular, for the run BA, a strong degree of convergence, down to probabilities of the order $P(\rho_{\text{d}} > \rho_{\text{threshold}}) \sim 10^{-3}$ is observed for all the resolutions. We report that, for $P = 10^{-5}$, the obtained probabilities correspond to values of $\rho_{\text{threshold}}/\epsilon$ that are roughly one order of magnitude below the values presented by Bai and Stone (2010b) when counting number of cells. However, counting (the effective) number of particles, by adding up densities, removes this discrepancy. Contrary to what is observed for the case AB, the mode BA seems converged for a number

of cells larger than 512^2.

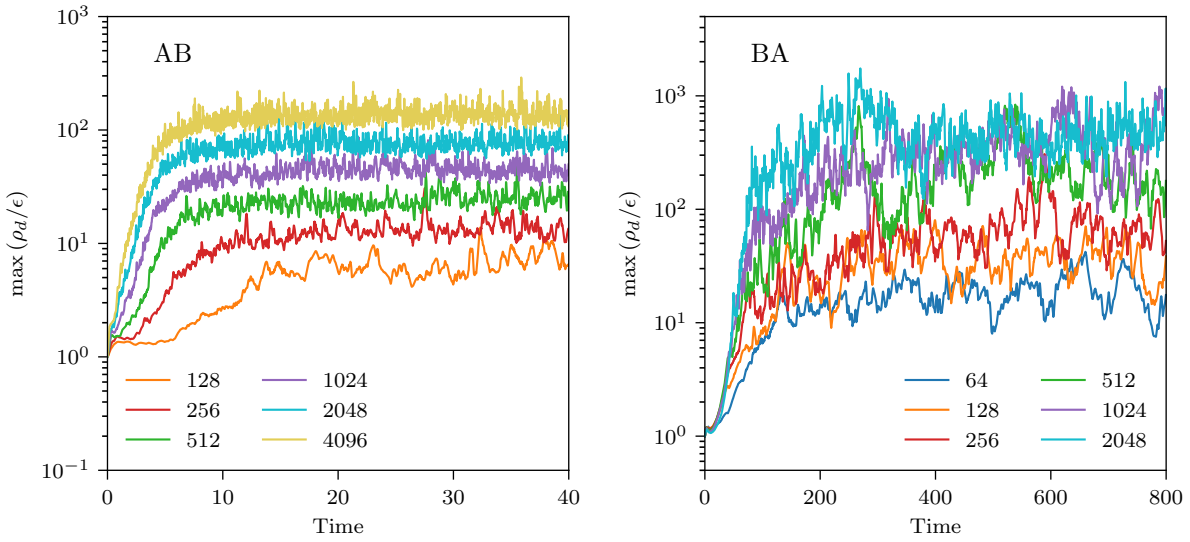

Figure 5.3.4: Figure 11 from Benítez-Llambay et al. (2019). Maximum dust density over time for the modes AB (left panel) and BA (right panel). As shown in Figure 5.3.3, the maximum density for the case AB increases linearly with resolution. The left panel also shows that the time for saturation is directly correlated with the resolution. Contrary to this case, the mode BA presents much better convergence properties with resolution. The right panel shows that, for low resolution, the initial growth rate directly correlates with resolution. However, for number of cells $> 512^2$, convergence in the growth rate is observed. The same degree of convergence is observed for the maximum dust density over the time interval considered, where both the maximum and fluctuations are comparable.

The method used to calculate the cumulative distributions does not modify the degree of convergence found for each run, AB and BA. However, the shape of the distributions is method-dependent. When counting cells, lower densities contribute more significantly in shaping the cumulative distribution, while when counting (the effective) number of particles, denser regions contribute more. While the maximum-density values differ from those obtained by Bai and Stone (2010b) for the run AB, the overall shape of the distributions agrees better when adding up densities.

The run AB shows a direct correlation between the saturation time scale and the resolution, i.e., the higher the resolution, the faster the instability saturates. Furthermore, we find the maximum density to be proportional to the number of cells, a clear evidence of lack of convergence. The previous analysis is supported by Figure 5.3.4, where we plot the maximum dust density as a function of time for each case and resolution. As described above, we show again that the run BA is much better behaved in terms of convergence. While the maximum density also increases with resolution for the low resolution cases, it converges when using more than 512^2 cells.

The differences found when comparing our results with those obtained using Lagrangian particles, in particular the lack of convergence for the run AB, warrant a detailed comparison between these two approaches.

5.4 Summary and Conclusions

Framework for linear theory. We derived the steady-state analytical solutions in a shearing-box approximation using an external force to mimic the pressure gradient within the disk. We linearized the equations assuming axisymmetric perturbations to study the time evolution of unstable modes. The obtained analytical solutions were recovered numerically by solving the full non-linear fluid equations with FARGO3D considering 1, 2, 16, and 128 dust species. These results validate both our numerical implementation discussed in Chapter 3 and our analytical framework.

Linear streaming instability for a particle size-distribution. We presented the first systematic study of the linear phase of the streaming instability, including multiple dust species. We considered power-law particle-size distributions with different ranges of Stokes numbers and dust-to-gas density ratios. The growth rate for the distribution with $\epsilon \gtrsim 0.5$ are similar to those obtained for the two-fluid problem, except for the distribution with small Stokes numbers, i.e., $T_{\mathrm{s,max}} < 10^{-2}$, where the instability grows on timescales much faster in comparison with the two-fluid case. Convergence of the linear phase is reached for system with less than 100 species. Contrary to these cases, when $\epsilon < 0.5$ the timescale of the instability significantly decreases to values comparable to those of secular instabilities. Furthermore, convergence with the number of species is not found (up to 2048 species) and only upper bound for the growth rate are reported.

Connection with the resonant drag instability theory. We found that for distribution with $\epsilon \lesssim 10^{-2}$ the instability is dominated by the species with the larger Stokes number. Furthermore, the growth rate decays with the number of species, used to represent the distribution, as $\sigma \sim 1/\sqrt{N}$. This is in agreement with the decay predicted by Squire and Hopkins (2018) for one dust species where $\sigma \sim \sqrt{\epsilon_1}$. We showed as well that, for low dust-to-gas ratios, the locus of the resonant drag modes of each species (in the K-space) agree with the local maxima of the growth rate. Thus, if $\epsilon \lesssim 10^{-2}$, the multi-species streaming instability can be well described as the superposition of N different two-fluid instabilities

occurring in a seemingly independent way, where the growth rate is dominated by the larger Stokes number.

Implication of our findings in Planetesimal Formation. We anticipate that the multi-species streaming instability could still be an efficient mechanism to enable planetesimal formation if dust-particles are filtered/segregated according to their size and accumulated somewhere in the disk. This will naturally produce regions with large concentrations of dust with distributions characterized by specific particle-sizes. For instance, vertical sedimentation affected by the presence of winds (e.g Riols and Lesur, 2018) or turbulence sustained by the vertical shear instability (e.g., Lin, 2019) have proven to remove tiny grains from the mid-plane of PPDs, favoring the local predominance of larger grains. Some other potential mechanisms for such filtering/segregation are vortices (e.g., Barge and Sommeria, 1995; Meheut et al., 2012; Raettig et al., 2015; Ragusa et al., 2017), zonal flows (e.g., Johansen et al., 2009; Dittrich et al., 2013; Béthune et al., 2016; Krapp et al., 2018), planet-induced pressure bumps (e.g. Zhu et al., 2012; Pinilla et al., 2012; Weber et al., 2018), and planetary torques (Benítez-Llambay and Pessah, 2018; Chen and Lin, 2018).

Non linear streaming instability. A qualitative comparison between Bai and Stone (2010b) and this work has shown that the agreement between particles and the pressureless fluid approximation for dust is excellent. An important caveat is the lack of convergence with resolution appreciated when studying the cumulative particle density distribution and maximum density for the case AB where the Stokes number $T_{\rm s} = 0.1$, $\epsilon = 1$ and a domain size $L = 2h_0^2 R_0$. However, the opposite occurs for the case BA, where $T_{\rm s} = 1.0$, $\epsilon = 0.2$ and $L = 40h_0^2 R_0$, and the results are in excellent agreement with those reported by Bai and Stone (2010b). Whether this discrepancy is due to the use of a fluid approach for the dust, the different Stokes numbers, domain sizes or the proper evolution of the instability in the absence of any dissipation will require further studies comparing both approximations.

6 Conclusions and Future Perspectives

In the following, we discuss the most relevant outcomes, caveats, and future perspectives of this thesis. In addition to our results, we would like to stress that, as a consequence of this work, a new public version of the code FARGO3D[1] is available, providing a robust, state-of-the-art set of numerical tools to study dust dynamics together with non-ideal magnetohydrodynamics in protoplanetary disks.

Multi-fluid framework We presented an asymptotically and unconditionally stable numerical method to solve the momentum transfer between multiple species, independent of an Eulerian or Lagrangian formalism. The scheme conserves momentum to machine precision, and its implementation in an operator splitting fashion converges to the correct solution. The robustness of the implicit scheme presented in this work and its versatility for adding an arbitrary number of species, are critical to investigate a wide range of phenomena in dusty protoplanetary disks. Hence, the implementation can be taken as a fundamental basis to include dust evolution, planetesimal dynamics and, ultimately the processes that lead to planet formation. We emphasize, however, that before using this implementation in an Eulerian formalism, it is necessary to assess whether the pressureless fluid approximation is expected to provide a good description of the prevalent dust dynamics in a given particular problem. Generally, if the dynamics of the problem is not dominated by crossing trajectories – which are transformed into shocks by the fluid approach – our method should represent a good approximation. In such a regime, the inclusion of an effective pressure mimicking the velocity dispersion of the particles may prevent the formation of strong shocks and help obtaining a better representation of the real dynamics of dust.

[1] https://fargo3d.bitbucket.io/

Hall-MHD and dust segregation Self-organization induced by the Hall effect may be a natural outcome of the non-linear evolution of turbulent regions of protoplanetary disks, even when strong azimuthal magnetic fields dominate the dynamics. The quasi-axisymmetric induced vortices stall the radial drift of the dust species providing an efficient mechanism to circumvent the so-called "drift-barrier".

Because the non-ideal MHD coefficient diffusion strongly depends on the ionization fraction, a self-consistent ionization evolution model with a proper thermodynamics is crucial to understand under which conditions self-organization operates. Thus, future progress in this problem will be to assess our results including Hall and Ohmic diffusion coefficients based on equilibrium ionization chemistry models. In addition, in the context of wind-driven accretion models with vertical stratification in PPDs, zonal flows induced by the Hall effect were not yet recovered. In contrast, it was found that ambipolar diffusion dominates the large scale evolution of the magnetic field. However, whether localized turbulence in the inner disk can be a self-consistent outcome in global disk models still remains as an open question. Finally, we conclude that the robustness of the numerical methods implemented in FARGO3D and NIRVANA-III to solve the Hall effect opens new possibilities to study non-ideal MHD effects in more challenging scenarios.

Streaming Instability A properly resolved particle-size distribution can significantly affect the linear phase of the streaming instability. Depending on the dust-size distribution and dust-to-gas mass ratio, the multi-species instability may only grow on timescales much larger than those expected from the classical (gas and one dust-species) case when approaching the continuum limit. Taken at face value, our results imply that the scope of the streaming instability may be narrowed down profoundly. Nevertheless, processes leading to particle segregation and/or concentration may create favorable conditions for the instability to develop. Because transport and collisional processes continuously affect the evolution of grains, the dynamically varying particle sizes will warrant the inclusion of time-dependent distributions. This issue can be circumvented if an equilibrium is reached in sufficiently short timescales in localized regions. In addition to the inclusion of non-trivial particle-size distributions, an assessment of the non-linear dynamics — that properly recovers the linear phase predicted by theory — is necessary to determine the effect of considering multiple species in the saturation regime of the streaming instability. However, such an assessment of the non-linear dynamics requires numerical simulations, and our method may not be entirely appropriate due to the lack of convergence with resolution found in one

particular setup. Thus, after recovering the linear growth, the next mandatory step is a convergence test of the non-linear phase studying, for instance, the time evolution of the maximum density and Reynolds stress during the saturation regime.

Connection to observables

In this work, we have explored diverse aspects of the dynamics of protoplanetary disks with specific emphasis on the momentum transfer between different components. Although we presented and discussed rather specific scenarios, our results and the tools that we developed can be utilized in a much broader context. For example, recent state-of-the-art continuum observations of PPDs have demanded a theoretical and numerical framework to link the observed structures to ongoing dynamical processes. For this, a clean and efficient treatment of multispecies momentum transfer is mandatory. Our results on the self-organization induced by the Hall effect could also have some significance in this respect. Once interferometric (sub)millimeter telescopes such as ALMA can observe the innermost part of PPDs at an adequate resolution, the possible occurrence of rings and vortices like structure could be linked to the presence of magnetic field by our work. However, this will require the production of synthetic images based on radiative transfer models using the outputs of the Hall-MHD simulations. The action of the streaming instability, on the other hand, is hard to observe, even with modern telescopes. The potential observable relying on this instability is mostly the size-distribution of Kuiper belt objects within the Solar System. These objects are believed to be the remains of early planetesimal formation, as a consequence of the gravitational collapse of over-dense dust clumps. This idea has been proposed by recent works studying the non-linear phase of the streaming instability. We have to emphasize once more that the models employed so far may well be unrealistically efficient by regarding only one particular dust size. From our results it is clear that the most urgent challenge is to overcome the linear growth of the instability when including disperse particle-size distribution. For this, better constraints on the typical dust size distribution and maximum grain size are crucial information.

A Appendix

A.1 Implementation of the Hall numerical scheme

The Hall-MHD scheme that we use in NIRVANA-III (with the HLLD solver) and in FARGO3D is based on the Hall diffusion scheme (HDS) of O'Sullivan and Downes (2007) and follows the same procedure as described in appendix A of Bai (2014). The scheme is based an on operator splitting of the Hall electric field $\mathbf{E}_{\rm H} \equiv \eta_{\rm H}\mathbf{J} \times \widehat{\mathbf{e}}_{\rm B}$. We begin by computing the $E_{{\rm H}x}$ component at the position $(i, j+\frac{1}{2}, k+\frac{1}{2})$

$$\mathbf{E}_{{\rm H}x} = \frac{\eta_{\rm H}}{|\mathbf{B}|}(J^*_y B^*_z - J^*_z B^*_y)\,, \tag{A.1.1}$$

where the superscript $*$ means that the components of the current and the magnetic field have to be interpolated to the $\mathbf{E}_{{\rm H}x}$ position. We then update B_y and B_z for a full time step using a CT step, but only with the component $\mathbf{E}_{{\rm H}x}$, that is,

$$B^{n+1}_{y,i,j+\frac{1}{2},k} = B^{n}_{y,i,j+\frac{1}{2},k} + \frac{\Delta t}{S_{XZ}}\left(E_{{\rm H}x,i,j+\frac{1}{2},k+\frac{1}{2}}\Delta X_{i,j+\frac{1}{2},k+\frac{1}{2}} - E_{{\rm H}x,i,j+\frac{1}{2},k-\frac{1}{2}}\Delta X_{i,j+\frac{1}{2},k-\frac{1}{2}}\right)\,, \tag{A.1.2}$$

$$B^{n+1}_{z,i,j,k+\frac{1}{2}} = B^{n}_{z,i,j,k+\frac{1}{2}} - \frac{\Delta t}{S_{XY}}\left(E_{{\rm H}x,i,j+\frac{1}{2},k+\frac{1}{2}}\Delta X_{i,j+\frac{1}{2},k+\frac{1}{2}} - E_{{\rm H}x,i,j-\frac{1}{2},k+\frac{1}{2}}\Delta X_{i,j-\frac{1}{2},k+\frac{1}{2}}\right)\,, \tag{A.1.3}$$

where S_{XZ} and S_{XY} denote the area of the cell faces at which the magnetic fields $B_{y,i,j+\frac{1}{2},k}$ and $B_{z,i,j,k+\frac{1}{2}}$ are defined at, respectively. With the updated values B^{n+1}_y and B^{n+1}_z, we compute $E_{{\rm H}y}$ and do the update of B^{n+1}_x and B^{n+1}_z using the equivalent of equations A.1.2 and A.1.3. In the same manner we compute $E_{{\rm H}z}$ with the new updated magnetic field components. In FARGO3D, with the computed

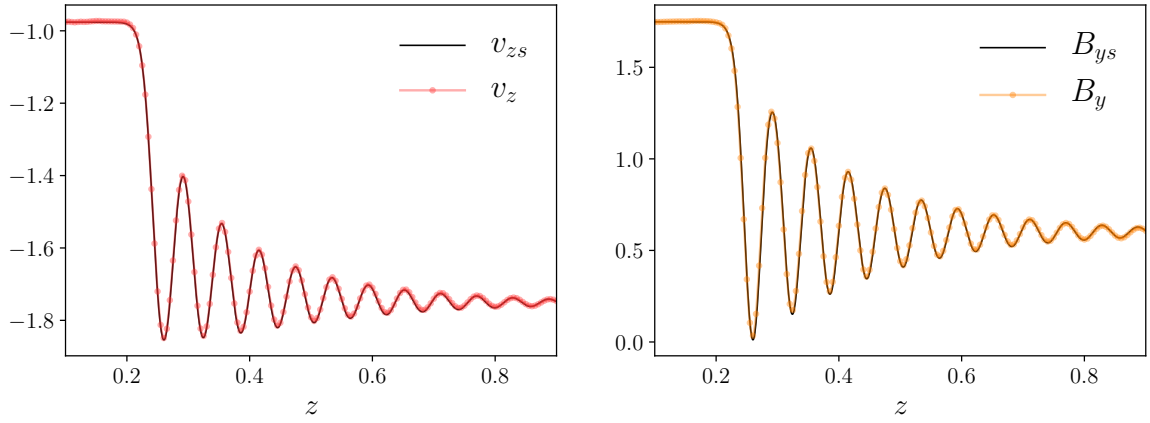

Figure A.2.1: Figure 12 from Krapp et al. (2018). Solutions of the shock test problem of the fluid velocity (left panel) and magnetic field (right panel). Black solid lines show the analytic steady-state shock solution, while data points are obtained from the numerical solution at $t = 2.7$, when the system has relaxed.

$\mathbf{E}_\mathrm{H}$ we do an update of $B^n \to B^{n+1}$ using the sum of all the electric fields., that is,

$$\mathbf{E}_\mathrm{T} = \mathbf{E}_\mathrm{I} + \mathbf{E}_\mathrm{H} + \mathbf{E}_\mathrm{O} + \mathbf{E}_\mathrm{A}\,, \tag{A.1.4}$$

while in NIRVANA-III, the update is simply operator-split, which means that the state of the magnetic field before the Hall-specific update does not have to be stored. The described update naturally lends itself to sub-stepping (see Section 4.1.6) in both codes.

The Tóth et al. scheme that is used with HLL fluxes in NIRVANA-III closely follows the implementation by Lesur et al. (2014) in the PLUTO code. We found that, as an empirical requirement for stability when interpolating the face-centered electric fields to the cell edges, the (more accurate) up-winded Gardiner and Stone (2008) interpolation has to be sacrificed in favor of plain arithmetic averages (also G. Lesur, priv. comm.). While arithmetic averaging is unstable in the context of the more accurate HLLD (Flock et al., 2010), it is tolerable with the intrinsically more diffusive HLL solver.

A.2 Testing the Hall module

A.2.1 Shock test

As a baseline non-linear test, we perform the shock tube test problem described in O'Sullivan and Downes (2006). The shock propagates under the combined effect of ambipolar and Ohmic diffusion, along with the Hall effect. Because the original problem is formulated for three-fluid MHD, in order to obtain the correct diffusivity coefficients, we have to solve a multifluid system of equations (see O'Sullivan and Downes, 2006). Using the multifluid version of FARGO3D, we update the densities of the two charged species via a continuity equation and we solve their velocities, $\mathbf{v}_\mathrm{i}$, assuming steady-state in the momentum equation. This yields

$$\mathbf{E} + (\mathbf{v}_\mathrm{i} - \mathbf{v}_\mathrm{g}) \times \mathbf{B} - \frac{\rho_\mathrm{g}\,\mathrm{K_i}}{\alpha_\mathbf{i}}(\mathbf{v}_\mathrm{i} - \mathbf{v}_\mathrm{g}) = \mathbf{0}\,, \tag{A.2.1}$$

where $\mathbf{v}_\mathrm{g}$ denotes the velocity of the neutrals, and α_i is the charge-to-mass ratio of the species. Assuming constant coefficients, $\mathrm{K_i}$, the velocity of each of the charged species can be obtained via

$$(\mathbf{v}_\mathrm{i} - \mathbf{v}_\mathrm{g})\,\left(|\mathbf{B}|^2 + \xi^2\right) = \frac{(\mathbf{E}\cdot\mathbf{B})}{\xi}\mathbf{B} + \xi\,\mathbf{E} + \mathbf{E}\times\mathbf{B}\,, \tag{A.2.2}$$

where $\xi = \rho_\mathrm{g}\,\mathrm{K_i}/\alpha_\mathrm{i}$ and $\mathbf{E}$ was defined in Eq. (2.1.3) in Section 2.1. In our case, the diffusion coefficients are $\eta_\mathrm{A} \equiv r_\mathrm{A}$, $\eta_\mathrm{H} \equiv r_\mathrm{H}$ and $\eta_\mathrm{O} \equiv r_\mathrm{O}$, where r_A, r_H and r_O are computed using equations (10) and (11) in O'Sullivan and Downes (2006). The initial conditions are such that the left and right states are given by respectively. The sound speed is $c_\mathrm{s} = 0.1$ and $B_z = 1.0$ for both states, while

Table A.2.1: Left ans right states for the Hall-MHD problem

ρ_L	$v_{z\mathrm{L}}$	$v_{y\mathrm{L}}$	$B_{y\mathrm{L}}$	$\rho_{1\mathrm{L}}$	$\rho_{2\mathrm{L}}$
1.7942	-0.9759	-0.6561	1.74885	8.9712×10^{-8}	1.7942×10^{-3}
ρ_R	$v_{z\mathrm{R}}$	$v_{y\mathrm{R}}$	$B_{y\mathrm{R}}$	$\rho_{1\mathrm{R}}$	$\rho_{2\mathrm{R}}$
1.0	-1.751	0.0	0.6	5×10^{-8}	1×10^{-3}

$v_x = B_x = 0.0$. The coefficients for the charged species are

$$\alpha_1 = -2\times10^9\,,\ \alpha_2 = 1\times10^5\,,\ \mathrm{K_1} = 4\times10^2\,,\ \mathrm{K_2} = 2.5\times10^6\,. \tag{A.2.3}$$

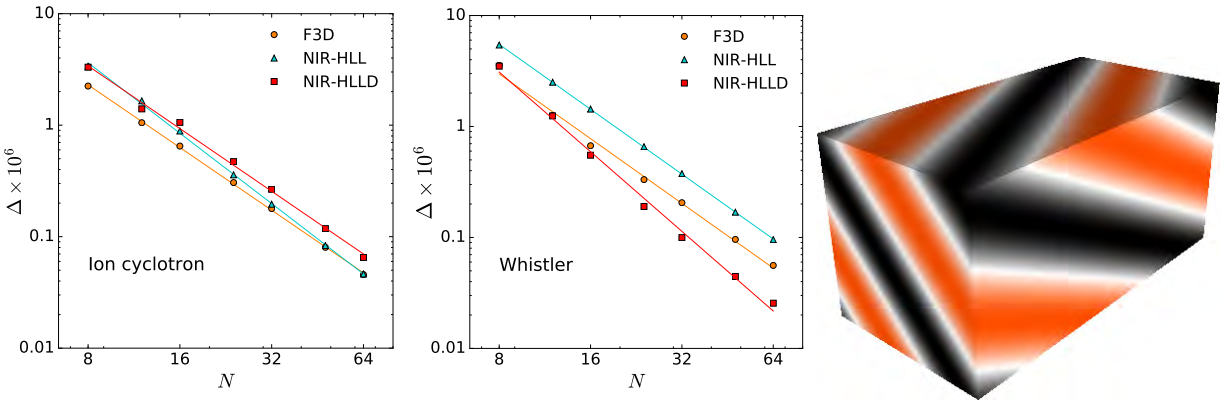

Figure A.2.2: Figure 13 from Krapp et al. (2018). Linear wave convergence test for an oblique circular-polarized Alfvén wave. *Left and center panel:* Truncation error, where solid lines mark least square fits to the function Δ, defined via $\Delta^2 \equiv \sum_s (\delta q_s)^2$, where δq_s is the L-1 error of the s-component of the magnetic field. *Right panel:* illustration of the oblique wave mode.

The shock propagates along the z direction in a domain of unit size, using 500 and 1000 cells, respectively. The initial discontinuity is located at $z = 0.25$, and the boundary conditions are fixed at the initial state. Figure A.2.1 shows the numerical solution at $t = 2.7$. The L1 error for a grid resolution of $\Delta z = 2\times10^{-2}$ is $e_1 = 3.66\times10^{-2}$ and with a resolution of $\Delta z = 1\times10^{-3}$, it is $e_1 = 9.8\times10^{-3}$, giving the scaling $e_1 \sim \Delta z^{1.9}$ which is close to the expected second-order convergence.

A.2.2 Linear Wave Convergence

In this section, we consider the linearized Hall-MHD equations of an incompressible fluid with only the Lorentz Force in the momentum equation. Let us assume a background magnetic field $\mathbf{B}_0 = B_0\hat{x}_1$ subject to the fluctuations $\delta\mathbf{B} = (0, \delta B_2, \delta B_3)$ and a perturbed velocity field $\delta\mathbf{v} = (0, \delta v_2, \delta v_3)$. All perturbations have the form $\delta f = \delta f_0 \exp[i\,(\omega t - \mathbf{k}\cdot\mathbf{x})]$ along the direction x_1, that is, $\mathbf{k} = \pm k\hat{x}_1$. It can be shown that

$$\delta v_{2,3} = -\frac{\mathbf{k}\cdot\mathbf{B}_0}{\mu_0\rho_0\omega}\,\delta B_{2,3}\,, \tag{A.2.4}$$

where $\delta B_{2,3}$ is the non-trivial solution of the system $A\,\delta B = 0$, with A being the matrix

$$A \;=\; \begin{bmatrix} i\,(-\omega^2 + v_A^2 k^2) & -\omega\,\eta_{\rm H} k^2 \\ \omega\,\eta_{\rm H} k^2 & i\,(-\omega^2 + v_A^2 k^2) \end{bmatrix}\,, \tag{A.2.5}$$

and where $v_A = B_0/\sqrt{\mu_0\rho_0}$ is the Alfvén speed, and $\eta_{\rm H}$ is considered constant and normalized by B_0. The system has four independent solutions, which correspond to two circular polarized waves

propagating along $\pm x_1$. For non-zero $\eta_{\rm H}$, these waves are commonly know as the whistler mode and the ion-cyclotron mode, respectively. Characteristically, these are dispersive waves, that is, the phase velocity, ω/k, depends on the wavenumber. More precisely,

$$\frac{\omega}{k} = \frac{\eta_{\rm H}}{2}(\mathbf{k}\cdot\widehat{\mathbf{e}}_{\rm B}) \pm \left[\frac{1}{4}(k\eta_{\rm H})^2 + v_A^2\right]^{\frac{1}{2}}, \tag{A.2.6}$$

with $\widehat{\mathbf{e}}_{\rm B}$ the unit vector in the direction of $\mathbf{B}_0$.

In order test the newly developed Hall-MHD modules, we perform a convergence study of an oblique wave propagation following a similar ansatz as the one presented in Gardiner and Stone (2008) for circularly polarized waves in the ideal-MHD regime. We define a Cartesian periodic box with dimensions $(3, 1.5, 1.5)$, resolved by $(2N, N, N)$ grid cells in x, y, and z, respectively. The propagation is along the oblique coordinate $x1 = k_x x + k_y y + k_z z$, with

$$k_x = 2\pi\cos(\alpha)\cos(\beta)\,, \quad k_y = 2\pi\cos(\alpha)\sin(\beta)\,, \quad \text{and} \quad k_z = 2\pi\cos(\alpha)\,. \tag{A.2.7}$$

We moreover set $\alpha = 2/3$ and $\beta = 2/\sqrt{5}$, in order to fit one wavelength $\lambda = 1$ inside the box. The initial velocity field is $\vec{v} = (0, 10^{-6}\cos(2\pi x_1), 10^{-6}\sin(2\pi x_1))$ and the initial magnetic field is computed via a vector potential in such a way that $\mathbf{B}$ satisfies Eq. (A.2.4) with a background field $\mathbf{B}_0 = 1.0\hat{x}_1$. The gas is treated as isothermal where $P_0 = c_{\rm s}^2\rho_0$, with an initial density $\rho_0 = 1.0$ and gas pressure $P_0 = 1.0$. The Hall diffusion is set to $\eta_{\rm H} = 0.1$.

We compute the L1-error for the centered components of the magnetic field as defined in Equation (70) by Gardiner and Stone (2008), and we plot the results for different resolutions in Figure A.2.2. For the Whistler mode NIRVANA-III returns an error $e_1 \sim \Delta_z^{2.3}$ and $e_1 \sim \Delta_z^{1.94}$, with the HLLD and HLL solvers, respectively. This scaling is different for the Ion cyclotron mode, where $e_1 \sim \Delta_z^{1.87}$ with HLLD solver and $e_1 \sim \Delta_z^{2.1}$ with the HLL scheme. In the case of FARGO3D, the error goes as $e_1 \sim \Delta z^{1.94}$ for the Whistler mode and $e_1 \sim \Delta z^{1.87}$ for the ion cyclotron mode. All the results are reasonably close to the expected second order convergence of the implemented schemes.

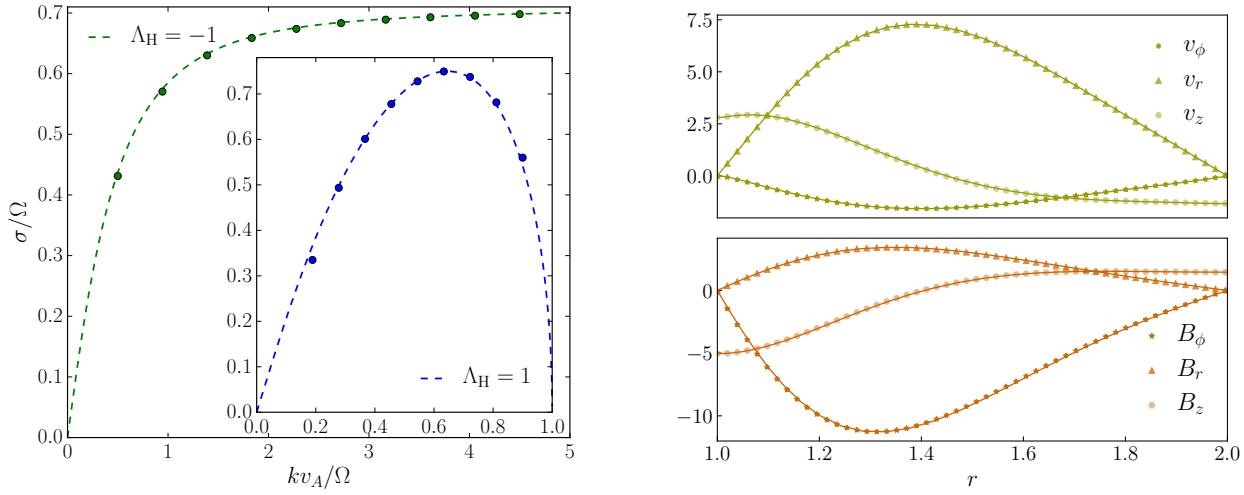

Figure A.2.3: Figure 14 from Krapp et al. (2018). *Left panel:* Analytic (dashed lines) and numerical (points) growth rates of the linear, local MRI. *Right panel:* Analytic (lines) and numerical (symbols) eigenvectors of linear, global cylindrical MRI modes. The velocities are normalized by a factor 10^{-6} and the magnetic field components by a factor 10^{-5}. Both results were obtained with FARGO3D.

A.2.3 Linear MRI growth — local modes

We now study the growth rate of linear MRI modes under the Hall effect. We use an axisymmetric, two-dimensional cylindrical domain with a grid of 64×64 cells, where the radial domain is fixed to $r \in [0.8, 1.2]$. We adopt a strategy where we initialize simulations such that the vertical box size matches the wavelength of a given individual mode. In this way, we run one simulation for each mode in a box with $L_z = \lambda \equiv 2\pi/k_z$, maintaining the same effective resolution for all the modes.

We use a similar initial condition as Sano and Stone (2002), where the plasma-β parameter is set to $\beta = 800$, $\rho_0 = 1.0$, $c_s = 0.1$, and we apply a Keplerian background velocity field. We then add perturbations to the azimuthal and radial velocities of the form $v_0 \cos(kz)$ and $v_0 \sin(kz)$, respectively, where $v_0 = 10^{-6} c_s$. The Hall diffusivity coefficient, η_H, is defined in such a way that the Elsasser numbers are $\Lambda_H = 1$ when $\mathbf{B}\cdot\mathbf{\Omega} > 0$ and $\Lambda_H = -1$ when $\mathbf{B}\cdot\mathbf{\Omega} < 0$. We integrate for two orbits at $r = 1$, and we measure the growth rate between $t = 1.5 - 1.9$ orbits at the same radius. By means of an exponential fit to the maximum value of the radial magnetic field at $r = 1$, we obtain the numerical solutions shown in the left panel of Figure A.2.3, which agrees with the analytic solution to within 3% for the critical mode and 0.02% for the maximum growth rate. We attribute deviations to the discrepancy between the local Cartesian approximation and the cylindrical computational setup.

A.2.4 Linear MRI growth — global modes

The eigenvectors that we show are the solutions of the linear Hall-MRI equation in a cylindrical coordinate system assuming axisymmetric perturbations. The perturbed MHD system of equations is linear but not fully algebraic. Thus, to compute the semi-analytic solutions we use a spectral code that expands the radial velocity and magnetic field using Chebyshev polynomials. The numerical setup is initialized using random white noise in the velocity field of the order $10^{-8}c_{\rm s}$ in a global isothermal disk. We adopt a box of size $(L_r, L_z) = [1, 1]$ with 256×256 cells, with periodic boundaries in the vertical and azimuthal directions. The radial boundary conditions we apply are $v_r = b_r = b_\phi = \partial_r b_z = \partial_r v_z = 0$. The disk is assumed to rotate with a Keplerian profile, and the initial conditions are

$$\beta = 31250\,, \quad \rho = 1.0\,, \quad c_{\rm s} = 0.25\,, \quad \eta_{\rm O} = 0.003\,, \quad \text{and} \quad L_{\rm H} = 1.0\,, \tag{A.2.8}$$

In the right panel of Figure A.2.3, we plot the eigenvectors obtained after 37 orbits. We compute as well the growth rate of the modes via a linear fit of $\log(B_r(t))$. We obtained a growth rate $\gamma = 0.0989$ with F-3D, $\gamma = 0.0989$ ($\gamma = 0.0988$) with N-III HLLD (HLL). All the values are in excellent agreement with the expected analytic value of $\gamma_0 = 0.0989$ (also cf. Béthune et al., 2016).

A.3 Streaming instability for a particle-size distribution

Table A.3.1: Wavenumbers for the multispecies streaming instability test.

Distribution	Number of dust species	K_x	K_z	σ/Ω_0	$\mathrm{Im}(\omega)$
$\Delta T_{\rm s}^{\rm I}$	16	99.11491118	527.2392351	0.04099431	0.77997688
	128	20.00590956	6.41135474	0.01619400	0.22712983
$\Delta T_{\rm s}^{\rm II}$	16	2.45449069	70.0	0.06775048	−0.85886862
	128	2.93211816	70.0	0.01249546	−0.82647018

The range of Stokes number is spanned in $\left[10^{-4}, 10^{-1}\right]$ and $\left[10^{-4}, 1\right]$ for $\Delta T_{\rm s}^{\rm I}$ and $\Delta T_{\rm s}^{\rm II}$, respectively. Both distributions has $q = 3.5$ and $\epsilon = 1$.

In this section we present the solutions used to validate our methods discussed in Section 5.2.3. The test consisted in recovering the time evolution of the eigenvector with 16 and 128 dust species and for two different distribution. Thus, the eigenvector has 16(128) dust densities and velocities plus the gas density and velocity. The cases selected are shown with green and red circles in Figure 5.2.2 and

with withe triangles in Figures 5.2.1 and 5.2.4. The corresponding values of the radial and vertical wavenumber, growth rate and oscillatory frequency are listed in Table A.3.1. We initialize the steady state solution for each species (see Eqs. 5.1.12 and 5.1.13). After $t = 1.2\Omega_0^{-1}$ we excite the eigenvector which evolves until $t = 11\Omega_0^{-1}$.

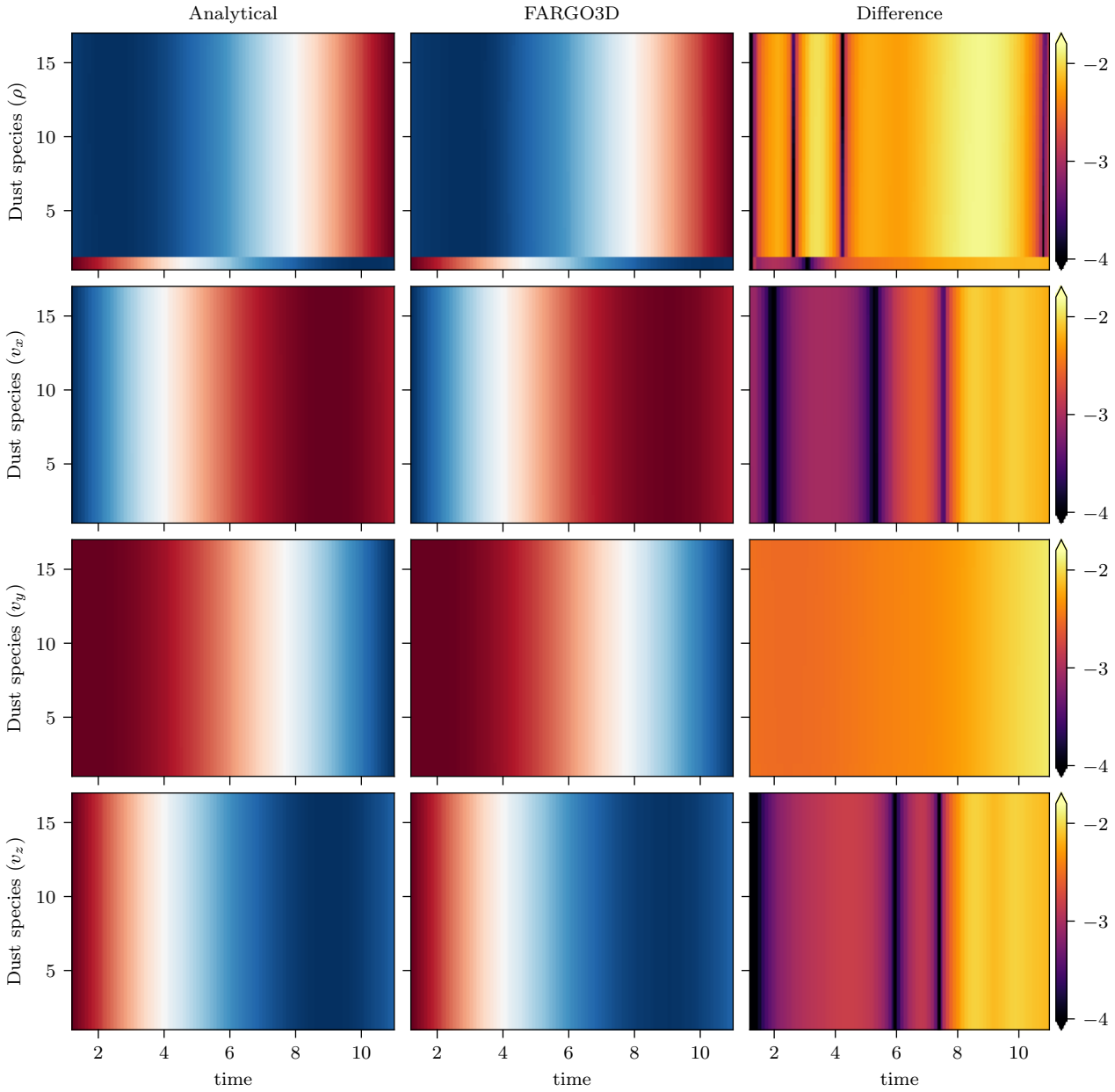

Figure A.3.1: Eigenvector components for the distribution refereed as ΔT_s^I with 16 species. Left panel and middle panels show the analytical and numerical solutions, respectively. The right panel shows the difference in logarithmic scale. The rows of the panels correspond to the time evolution of each of the species. The analytical and numerical solutions are normalized between zero and one, so we omit the colorbar.

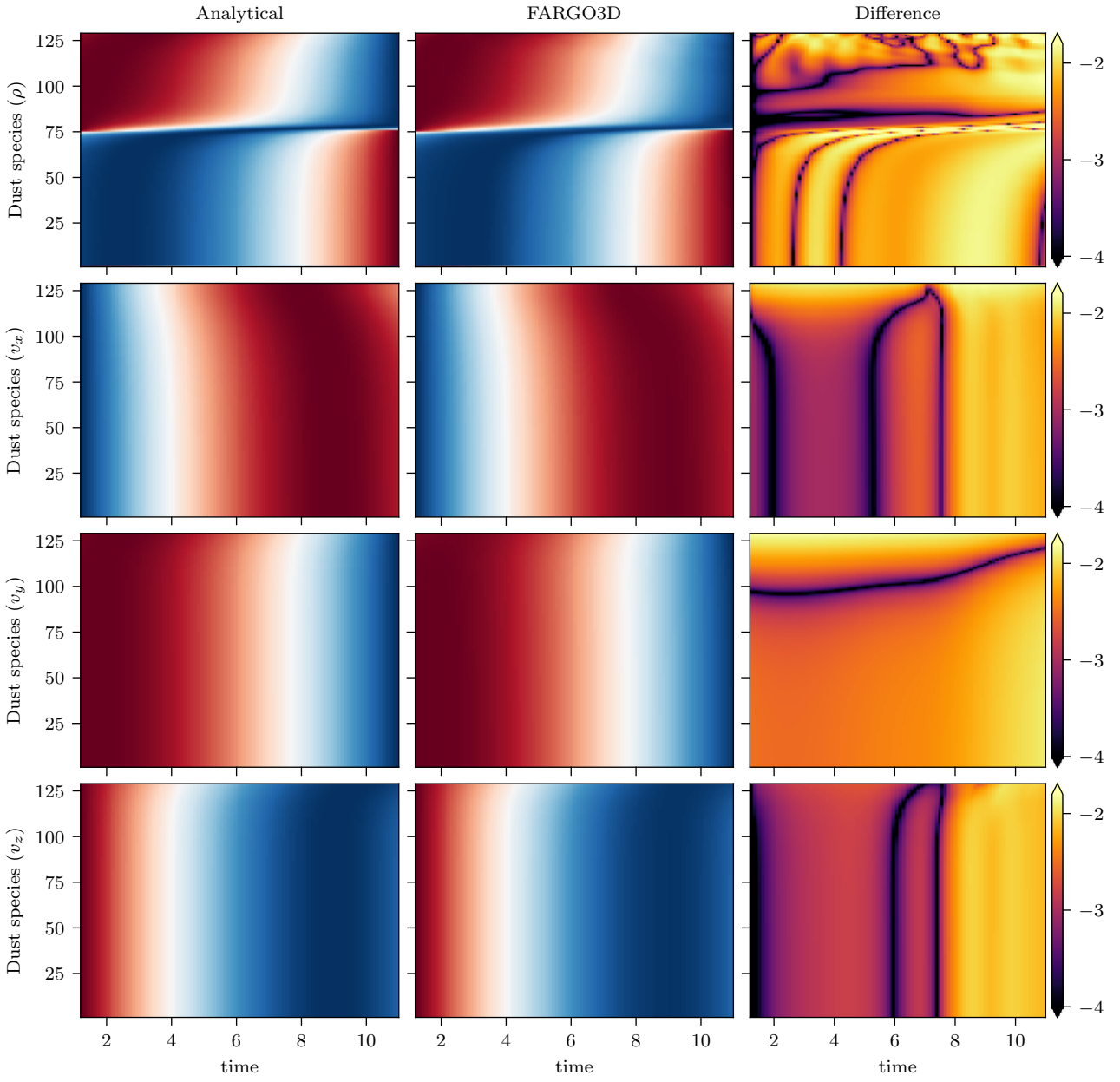

Figure A.3.2: Eigenvector components for the distribution refereed as $\Delta T_{\mathrm{s}}^{\mathrm{I}}$ with 128 species. Left panel and middle panels show the analytical and numerical solutions, respectively. The right panel shows the difference in logarithmic scale. The rows of the panels correspond to the time evolution of each of the species. The analytical and numerical solutions are normalized between zero and one, so we omit the colorbar.

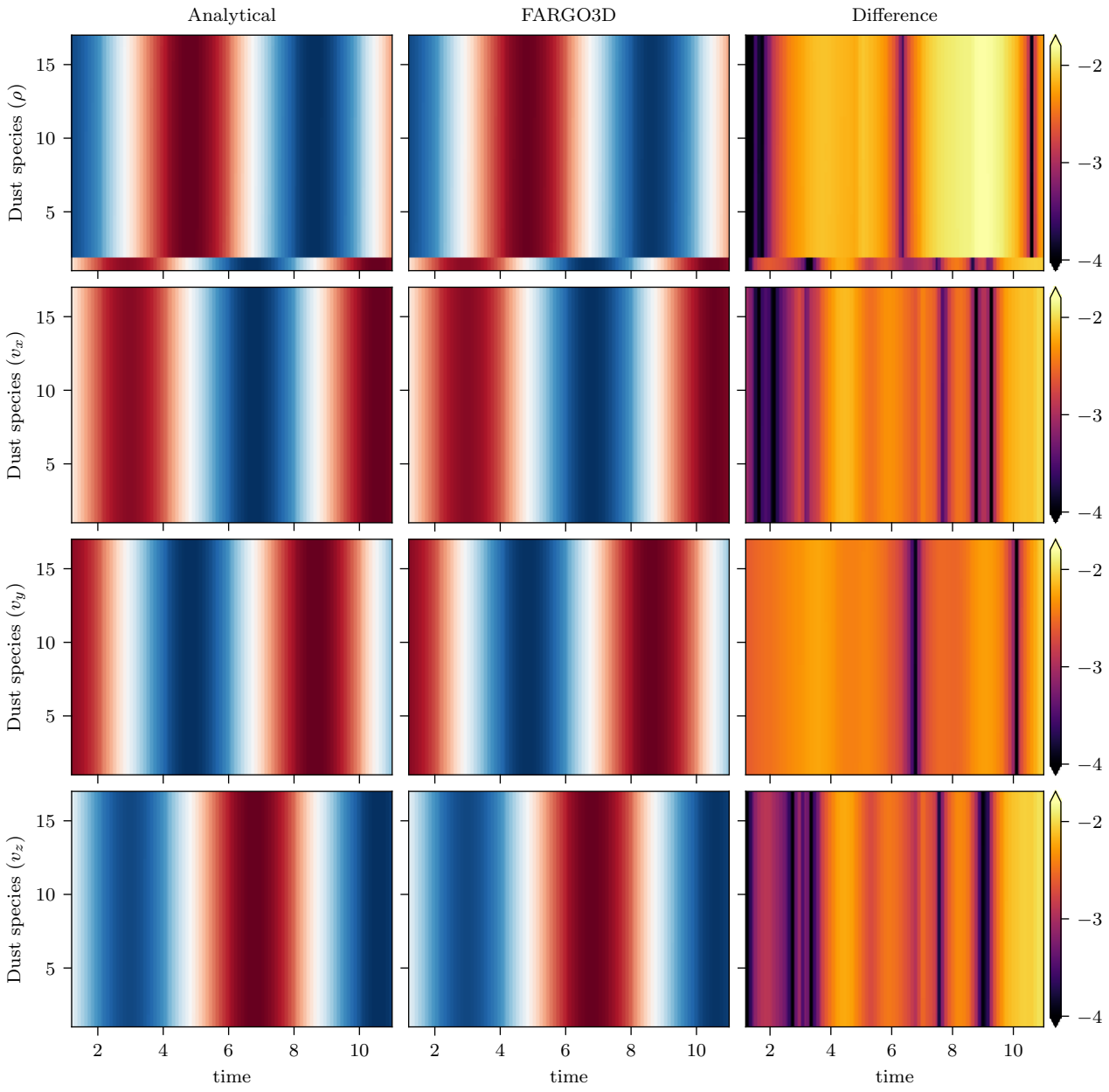

Figure A.3.3: Eigenvector components for the distribution refereed as $\Delta T_{\mathrm{s}}^{\mathrm{II}}$ with 16 species. Left panel and middle panels show the analytical and numerical solutions, respectively. The right panel shows the difference in logarithmic scale. The rows of the panels correspond to the time evolution of each of the species. The analytical and numerical solutions are normalized between zero and one, so we omit the colorbar.

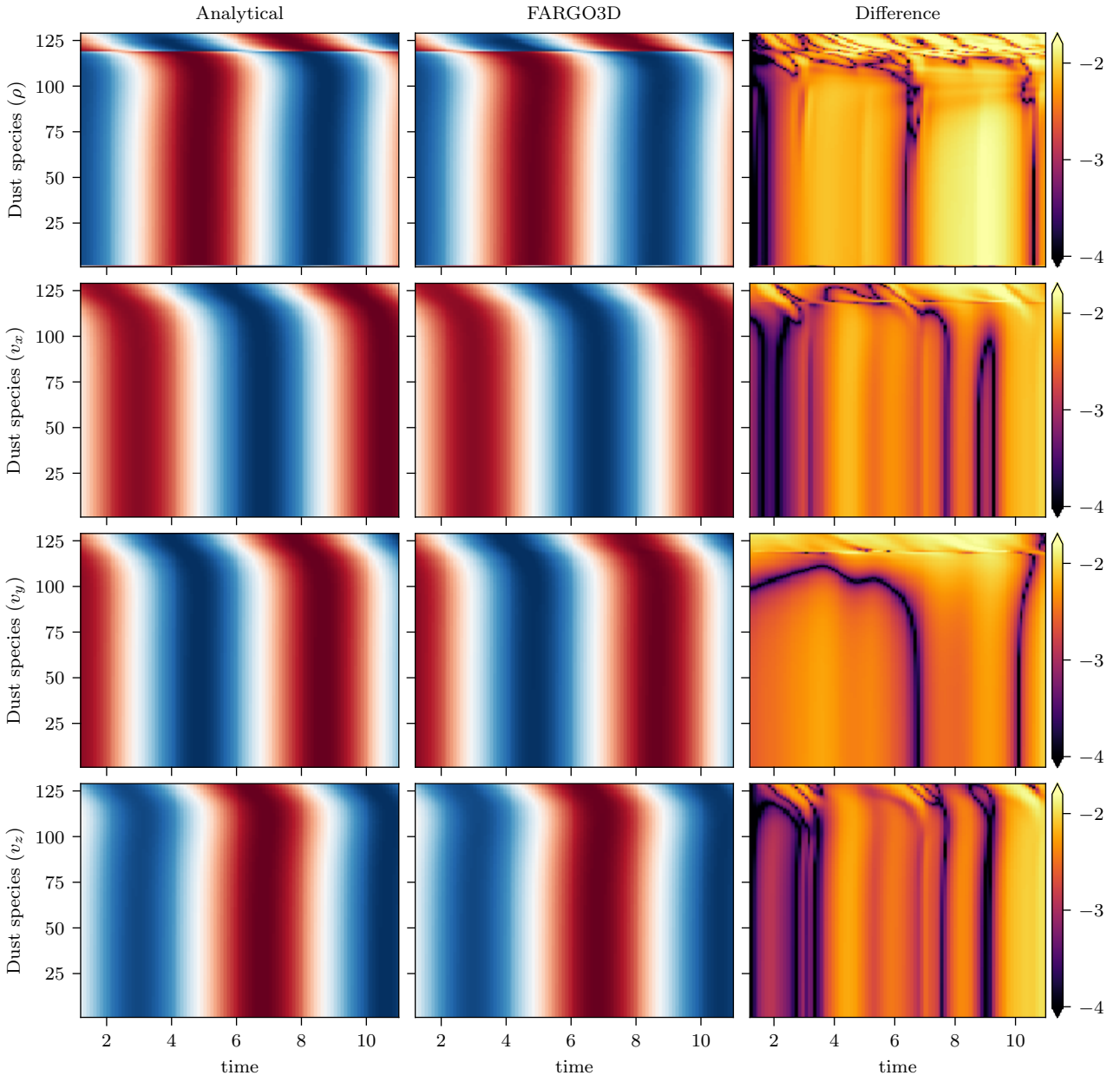

Figure A.3.4: Eigenvector components for the distribution refereed as $\Delta T_{\mathrm{s}}^{\mathrm{II}}$ with 128 species. Left panel and middle panels show the analytical and numerical solutions, respectively. The right panel shows the difference in logarithmic scale. The rows of the panels correspond to the time evolution of each of the species. The analytical and numerical solutions are normalized between zero and one, so we omit the colorbar.

Bibliography

Alexander, R., Pascucci, I., Andrews, S., Armitage, P., and Cieza, L. (2014). The Dispersal of Protoplanetary Disks. Protostars and Planets VI, pages 475–496.

Alexander, R. D., Clarke, C. J., and Pringle, J. E. (2006). Photoevaporation of protoplanetary discs - II. Evolutionary models and observable properties. MNRAS, 369(1):229–239.

Alexiades, V., Amiez, G., and Gremaud, P.-A. (1996). Super-time-stepping acceleration of explicit schemes for parabolic problems. Comm. in Num. Methods in Engineering, 12(1):31–42.

ALMA Partnership, Brogan, C. L., Pérez, L. M., Hunter, T. R., Dent, W. R. F., Hales, A. S., Hills, R. E., Corder, S., Fomalont, E. B., and Vlahakis, C. (2015). The 2014 ALMA Long Baseline Campaign: First Results from High Angular Resolution Observations toward the HL Tau Region. ApJ, 808(1):L3.

Anderson, E., Bai, Z., Bischof, C., Blackford, S., Demmel, J., Dongarra, J., Du Croz, J., Greenbaum, A., Hammarling, S., McKenney, A., and Sorensen, D. (1999). LAPACK Users' Guide. Society for Industrial and Applied Mathematics, Philadelphia, PA, third edition.

Andrews, S. M., Huang, J., Pérez, L. M., Isella, A., Dullemond, C. P., Kurtovic, N. T., Guzmán, V. V., Carpenter, J. M., Wilner, D. J., and Zhang, S. (2018). The Disk Substructures at High Angular Resolution Project (DSHARP). I. Motivation, Sample, Calibration, and Overview. ApJ, 869(2):L41.

Andrews, S. M., Wilner, D. J., Zhu, Z., Birnstiel, T., Carpenter, J. M., Pérez, L. M., Bai, X.-N., Öberg, K. I., Hughes, A. M., Isella, A., and Ricci, L. (2016). RINGED SUBSTRUCTURE AND a GAP AT 1 au IN THE NEAREST PROTOPLANETARY DISK. The Astrophysical Journal, 820(2):L40.

Ansdell, M., Williams, J. P., van der Marel, N., Carpenter, J. M., Guidi, G., Hogerheijde, M., Mathews, G. S., Manara, C. F., Miotello, A., and Natta, A. (2016). ALMA Survey of Lupus Protoplanetary Disks. I. Dust and Gas Masses. ApJ, 828(1):46.

Arce, H. G., Shepherd, D., Gueth, F., Lee, C.-F., Bachiller, R., Rosen, A., and Beuther, H. (2007). Molecular Outflows in Low- and High-Mass Star-forming Regions. Protostars and Planets V, pages 245–260.

Armitage, P. J. (2011). Dynamics of Protoplanetary Disks. ARA&A, 49(1):195–236.

Armitage, P. J. (2015). Physical processes in protoplanetary disks. arXiv e-prints, page arXiv:1509.06382.

Bai, X.-N. (2011a). Magnetorotational-instability-driven Accretion in Protoplanetary Disks. ApJ, 739:50.

Bai, X.-N. (2011b). The Role of Tiny Grains on the Accretion Process in Protoplanetary Disks. ApJ, 739(1):51.

Bai, X.-N. (2014). Hall-effect-Controlled Gas Dynamics in Protoplanetary Disks. I. Wind Solutions at the Inner Disk. ApJ, 791:137.

Bai, X.-N. (2015). Hall Effect Controlled Gas Dynamics in Protoplanetary Disks. II. Full 3D Simulations toward the Outer Disk. ApJ, 798:84.

Bai, X.-N. (2017). Global Simulations of the Inner Regions of Protoplanetary Disks with Comprehensive Disk Microphysics. ApJ, 845:75.

Bai, X.-N. and Goodman, J. (2009). Heat and Dust in Active Layers of Protostellar Disks. ApJ, 701(1):737–755.

Bai, X.-N. and Stone, J. M. (2010a). Dynamics of Solids in the Midplane of Protoplanetary Disks: Implications for Planetesimal Formation. ApJ, 722:1437–1459.

Bai, X.-N. and Stone, J. M. (2010b). Particle-gas Dynamics with Athena: Method and Convergence. ApJS, 190:297–310.

Bai, X.-N. and Stone, J. M. (2013). Wind-driven Accretion in Protoplanetary Disks. I. Suppression of the Magnetorotational Instability and Launching of the Magnetocentrifugal Wind. ApJ, 769:76.

Bai, X.-N., Ye, J., Goodman, J., and Yuan, F. (2016). Magneto-thermal Disk Winds from Protoplanetary Disks. ApJ, 818:152.

Balbus, S. A. and Hawley, J. F. (1991). A powerful local shear instability in weakly magnetized disks. I - Linear analysis. II - Nonlinear evolution. ApJ, 376:214–233.

Balbus, S. A. and Hawley, J. F. (1998). Instability, turbulence, and enhanced transport in accretion disks. Rev. Mod. Phys., 70:1–53.

Balbus, S. A. and Terquem, C. (2001). Linear Analysis of the Hall Effect in Protostellar Disks. ApJ, 552(1):235–247.

Balsara, D. S. and Meyer, C. (2010). Evaluating the Magnetorotational Instability's Dependence on Numerical Algorithms and Resolution. ArXiv e-prints.

Balsara, D. S., Tilley, D. A., Rettig, T., and Brittain, S. D. (2009). Dust settling in magnetorotationally driven turbulent discs - I. Numerical methods and evidence for a vigorous streaming instability. MNRAS, 397:24–43.

Barge, P. and Sommeria, J. (1995). Did planet formation begin inside persistent gaseous vortices? A&A, 295:L1–L4.

Benilov, M. S. (1997). A kinetic derivation of multifluid equations for multispecies nonequilibrium mixtures of reacting gases. Physics of Plasmas, 4(3):521–528.

Benítez-Llambay, P., Krapp, L., and Pessah, M. E. (2019). Asymptotically Stable Numerical Method for Multispecies Momentum Transfer: Gas and Multifluid Dust Test Suite and Implementation in FARGO3D. ApJS, 241:25.

Benítez-Llambay, P. and Masset, F. S. (2016). FARGO3D: A New GPU-oriented MHD Code. ApJS, 223:11.

Benítez-Llambay, P. and Pessah, M. E. (2018). Torques Induced by Scattered Pebble-flow in Protoplanetary Disks. ApJL, 855:L28.

Benítez-Llambay, P., Ramos, X. S., Beaugé, C., and Masset, F. S. (2016). Long-term and large-scale hydrodynamical simulations of migrating planets. ApJ, 826:13.

Berman, A. and Plemmons, R. J. (1979). Nonnegative matrices in the mathematical sciences. Academic Press New York.

Béthune, W., Lesur, G., and Ferreira, J. (2016). Self-organisation in protoplanetary discs. Global, non-stratified Hall-MHD simulations. A&A, 589:A87.

Béthune, W., Lesur, G., and Ferreira, J. (2017). Global simulations of protoplanetary disks with net magnetic flux. I. Non-ideal MHD case. A&A, 600:A75.

Birnstiel, T., Fang, M., and Johansen, A. (2016). Dust Evolution and the Formation of Planetesimals. SSRv, 205:41–75.

Birnstiel, T., Klahr, H., and Ercolano, B. (2012). A simple model for the evolution of the dust population in protoplanetary disks. A&A, 539:A148.

Bjerkeli, P., van der Wiel, M. H. D., Harsono, D., Ramsey, J. P., and Jørgensen, J. K. (2016). Resolved images of a protostellar outflow driven by an extended disk wind. Nature, 540:406–409.

Blandford, R. D. and Payne, D. G. (1982). Hydromagnetic flows from accretion disks and the production of radio jets. MNRAS, 199:883–903.

Blum, J. (2018). Dust Evolution in Protoplanetary Discs and the Formation of Planetesimals. What Have We Learned from Laboratory Experiments? SSRv, 214(2):52.

Booth, R. A., Sijacki, D., and Clarke, C. J. (2015). Smoothed particle hydrodynamics simulations of gas and dust mixtures. Monthly Notices of the Royal Astronomical Society, 452(4):3932–3947.

Braginskii, S. I. (1965). Transport Processes in a Plasma. Reviews of Plasma Physics, 1:205.

Chen, J.-W. and Lin, M.-K. (2018). Dusty disc-planet interaction with dust-free simulations. MNRAS, 478:2737–2752.

Chernoff, D. F. and Shapiro, S. L. (1987). Globular Cluster Evolution in the Galaxy: A Global View. ApJ, 322:113.

Cowling, T. G. (1956). The dissipation of magnetic energy in an ionized gas. MNRAS, 116:114.

Cuzzi, J. N., Dobrovolskis, A. R., and Champney, J. M. (1993). Particle-Gas Dynamics in the Midplane of a Protoplanetary Nebula. Icarus, 106(1):102–134.

de Val-Borro, M., Edgar, R., Artymowicz, P., Ciecielag, P., Cresswell, P., D'Angelo, G., Delgado-Donate, E., Dirksen, G., Fromang, S., Gawryszczak, A., Klahr, H., Kley, W., Lyra, W., Masset, F., Mellema, G., Nelson, R., Paardekooper, S.-J., Peplinski, A., Pierens, A., Plewa, T., Rice, K., Schäfer, C., and Speith, R. (2006). A comparative study of disc-planet interaction. MNRAS, 370:529–558.

de Val-Borro, M., Edgar, R. G., Artymowicz, P., Ciecielag, P., Cresswell, P., D'Angelo, G., Delgado-Donate, E. J., Dirksen, G., Fromang, S., Gawryszczak, A., Klahr, H., Kley, W., Lyra, W., Masset, F., Mellema, G., Nelson, R. P., Paardekooper, S.-J., Peplinski, A., Pierens, A., Plewa, T., Rice, K., Schäfer, C., and Speith, R. (2006). A comparative study of disc-planet interaction. MNRAS, 370:529–558.

Dipierro, G., Laibe, G., Alexander, R., and Hutchison, M. (2018). Gas and multispecies dust dynamics in viscous protoplanetary discs: the importance of the dust back-reaction. MNRAS, 479:4187–4206.

Dittrich, K., Klahr, H., and Johansen, A. (2013). Gravoturbulent Planetesimal Formation: The Positive Effect of Long-lived Zonal Flows. ApJ, 763:117.

Dohnanyi, J. S. (1969). Collisional Model of Asteroids and Their Debris. J. Geophys. Res., 74:2531–2554.

Draine, B. T. (1986). Multicomponent, reacting MHD flows. MNRAS, 220:133–148.

Draine, B. T. and Salpeter, E. E. (1979). On the physics of dust grains in hot gas. ApJ, 231:77–94.

Epstein, P. S. (1924). On the resistance experienced by spheres in their motion through gases. Phys. Rev., 23:710–733.

Ercolano, B. and Glassgold, A. E. (2013). X-ray ionization rates in protoplanetary discs. Monthly Notices of the Royal Astronomical Society, 436(4):3446–3450.

Evans, C. R. and Hawley, J. F. (1988). Simulation of magnetohydrodynamic flows - A constrained transport method. ApJ, 332:659–677.

Falle, S. A. E. G. (2003). A numerical scheme for multifluid magnetohydrodynamics. MNRAS, 344(4):1210–1218.

Flock, M., Dzyurkevich, N., Klahr, H., and Mignone, A. (2010). High-order Godunov schemes for global 3D MHD simulations of accretion disks. I. Testing the linear growth of the magneto-rotational instability. A&A, 516:A26.

Flock, M., Dzyurkevich, N., Klahr, H., Turner, N. J., and Henning, T. (2011). Turbulence and Steady Flows in Three-dimensional Global Stratified Magnetohydrodynamic Simulations of Accretion Disks. ApJ, 735(2):122.

Fromang, S., Terquem, C., and Balbus, S. A. (2002). The ionization fraction in α models of protoplanetary discs. MNRAS, 329:18–28.

Garaud, P., Barrière-Fouchet, L., and Lin, D. N. C. (2004). Individual and Average Behavior of Particles in a Protoplanetary Nebula. ApJ, 603:292–306.

Gardiner, T. A. and Stone, J. M. (2008). An unsplit Godunov method for ideal MHD via constrained transport in three dimensions. Journal of Computational Physics, 227:4123–4141.

Geršgorin, S. (1931). Über die Abgrenzung der Eigenwerte einer Matrix. Bulletin de l'Académie des Sciences de l'URSS. Classe des sciences mathématiques et na, 6:749–754.

Gressel, O., Turner, N. J., Nelson, R. P., and McNally, C. P. (2015). Global Simulations of Protoplanetary Disks With Ohmic Resistivity and Ambipolar Diffusion. ApJ, 801:84.

Hartmann, L., Calvet, N., Gullbring, E., and D'Alessio, P. (1998). Accretion and the evolution of t tauri disks. The Astrophysical Journal, 495(1):385–400.

Hawley, J. F., Gammie, C. F., and Balbus, S. A. (1995). Local Three-dimensional Magnetohydrodynamic Simulations of Accretion Disks. ApJ, 440:742.

Hayashi, C. (1981). Structure of the solar nebula, growth and decay of magnetic fields and effects of magnetic and turbulent viscosities on the nebula. Progress of Theoretical Physics Supplement, 70:35–53.

Huba, J. D. (2003). Hall Magnetohydrodynamics - A Tutorial. In Büchner, J., Dum, C., and Scholer, M., editors, Space Plasma Simulation, volume 615 of Lecture Notes in Physics, Berlin Springer Verlag, pages 166–192.

Igea, J. and Glassgold, A. E. (1999). X-Ray Ionization of the Disks of Young Stellar Objects. ApJ, 518:848–858.

Ilgner, M. and Nelson, R. P. (2006). On the ionisation fraction in protoplanetary disks. I. Comparing different reaction networks. A&A, 445:205–222.

Johansen, A. and Youdin, A. (2007). Protoplanetary Disk Turbulence Driven by the Streaming Instability: Nonlinear Saturation and Particle Concentration. ApJ, 662:627–641.

Johansen, A. and Youdin, A. (2007). Protoplanetary disk turbulence driven by the streaming instability: Nonlinear saturation and particle concentration. The Astrophysical Journal, 662(1):627.

Johansen, A., Youdin, A., and Klahr, H. (2009). Zonal Flows and Long-lived Axisymmetric Pressure Bumps in Magnetorotational Turbulence. ApJ, 697:1269–1289.

Keith, S. L. and Wardle, M. (2015). Magnetic fields in gaps surrounding giant protoplanets. MNRAS, 451:1104–1116.

Klahr, H. and Hubbard, A. (2014). CONVECTIVE OVERSTABILITY IN RADIALLY STRATIFIED ACCRETION DISKS UNDER THERMAL RELAXATION. The Astrophysical Journal, 788(1):21.

Klahr, H. H. and Henning, T. (1997). Particle-Trapping Eddies in Protoplanetary Accretion Disks. Icarus, 128:213–229.

Kounkel, M., Hartmann, L., Loinard, L., Ortiz-León, G. N., Mioduszewski, A. J., Rodríguez, L. F., Dzib, S. A., Torres, R. M., Pech, G., Galli, P. A. B., Rivera, J. L., Boden, A. F., II, N. J. E., Briceño, C., and Tobin, J. J. (2017). THE GOULD's BELT DISTANCES SURVEY (GOBELINS). II. DISTANCES AND STRUCTURE TOWARD THE ORION MOLECULAR CLOUDS. The Astrophysical Journal, 834(2):142.

Kowalik, K., Hanasz, M., Wóltański, D., and Gawryszczak, A. (2013). Streaming instability in the quasi-global protoplanetary discs. MNRAS, 434:1460–1468.

Krapp, L., Benítez-Llambay, P., Gressel, O., and Pessah, M. E. (2019). Streaming Instability for Particle-size Distributions. ApJ, 878(2):L30.

Krapp, L., Gressel, O., Benítez-Llambay, P., Downes, T. P., Mohandas, G., and Pessah, M. E. (2018). Dust Segregation in Hall-dominated Turbulent Protoplanetary Disks. ApJ, 865:105.

Kunz, M. W. and Lesur, G. (2013). Magnetic self-organization in Hall-dominated magnetorotational turbulence. MNRAS, 434:2295–2312.

Laibe, G. and Price, D. J. (2012). Dusty gas with smoothed particle hydrodynamics - I. Algorithm and test suite. MNRAS, 420:2345–2364.

Laibe, G. and Price, D. J. (2014). Dusty gas with one fluid. MNRAS, 440:2136–2146.

Lesur, G., Kunz, M. W., and Fromang, S. (2014). Thanatology in protoplanetary discs. The combined influence of Ohmic, Hall, and ambipolar diffusion on dead zones. A&A, 566:A56.

Lesur, G. and Papaloizou, J. C. B. (2010). The subcritical baroclinic instability in local accretion disc models. A&A, 513:A60.

Lin, M.-K. (2019). Dust settling against hydrodynamic turbulence in protoplanetary discs. MNRAS, 485:5221–5234.

Lin, M.-K. and Youdin, A. N. (2017). A Thermodynamic View of Dusty Protoplanetary Disks. ApJ, 849:129.

Lissauer, J. J. (1993). Planet formation. ARA&A, 31:129–174.

Londrillo, P. and del Zanna, L. (2004). On the divergence-free condition in Godunov-type schemes for ideal magnetohydrodynamics: the upwind constrained transport method. Journal of Computational Physics, 195:17–48.

Lynden-Bell, D. (1996). Magnetic collimation by accretion discs of quasars and stars. MNRAS, 279:389–401.

Lynden-Bell, D. and Pringle, J. E. (1974). The evolution of viscous discs and the origin of the nebular variables. MNRAS, 168:603–637.

Marcus, P. S., Pei, S., Jiang, C.-H., Barranco, J. A., Hassanzadeh, P., and Lecoanet, D. (2015). ZOMBIE VORTEX INSTABILITY. i. a PURELY HYDRODYNAMIC INSTABILITY TO RESURRECT THE DEAD ZONES OF PROTOPLANETARY DISKS. The Astrophysical Journal, 808(1):87.

Masset, F. (2000). FARGO: A fast eulerian transport algorithm for differentially rotating disks. A&AS, 141:165–173.

Mathis, J. S., Rumpl, W., and Nordsieck, K. H. (1977). The size distribution of interstellar grains. ApJ, 217:425–433.

Mayor, M. and Queloz, D. (1995). A Jupiter-mass companion to a solar-type star. Nature, 378:355–359.

McCall, B. J., Huneycutt, A. J., Saykally, R. J., Geballe, T. R., Djuric, N., Dunn, G. H., Semaniak, J., Novotny, O., Al-Khalili, A., Ehlerding, A., Hellberg, F., Kalhori, S., Neau, A., Thomas, R., Österdahl,

F., and Larsson, M. (2003). An enhanced cosmic-ray flux towards ζ Persei inferred from a laboratory study of the H_3^+-e^- recombination rate. Nature, 422:500–502.

Meheut, H., Meliani, Z., Varniere, P., and Benz, W. (2012). Dust-trapping Rossby vortices in protoplanetary disks. A&A, 545:A134.

Meyer, C. D., Balsara, D. S., and Aslam, T. D. (2012). A second-order accurate Super TimeStepping formulation for anisotropic thermal conduction. MNRAS, 422:2102–2115.

Mignone, A., Flock, M., Stute, M., Kolb, S. M., and Muscianisi, G. (2012). A conservative orbital advection scheme for simulations of magnetized shear flows with the PLUTO code. A&A, 545:A152.

Mohandas, G. and Pessah, M. E. (2017). Spectral Analysis of Non-ideal MRI Modes: The Effect of Hall Diffusion. ApJ, 838:48.

Nakagawa, Y., Sekiya, M., and Hayashi, C. (1986a). Settling and growth of dust particles in a laminar phase of a low-mass solar nebula. Icarus, 67:375–390.

Nakagawa, Y., Sekiya, M., and Hayashi, C. (1986b). Settling and growth of dust particles in a laminar phase of a low-mass solar nebula. Icarus, 67:375–390.

Nakano, T. and Umebayashi, T. (1986a). Dissipation of magnetic fields in very dense interstellar clouds. I - Formulation and conditions for efficient dissipation. MNRAS, 218:663–684.

Nakano, T. and Umebayashi, T. (1986b). Dissipation of magnetic fields in very dense interstellar clouds. II - Final phases of star formation and the magnetic flux of a newborn star. MNRAS, 221:319–338.

Nelson, R. P., Gressel, O., and Umurhan, O. M. (2013). Linear and non-linear evolution of the vertical shear instability in accretion discs. Monthly Notices of the Royal Astronomical Society, 435(3):2610–2632.

Norman, C. and Heyvaerts, J. (1985). Anomalous magnetic field diffusion during star formation. A&A, 147(2):247–256.

O'Keeffe, W. and Downes, T. P. (2014). Multifluid simulations of the magnetorotational instability in protostellar discs. MNRAS, 441:571–581.

O'Sullivan, S. and Downes, T. P. (2006). Numerical Modeling of Weakly Ionized Plasmas. In Zank,

G. P. and Pogorelov, N. V., editors, Numerical Modeling of Space Plasma Flows, volume 359 of Astronomical Society of the Pacific Conference Series, page 178.

O'Sullivan, S. and Downes, T. P. (2007). A three-dimensional numerical method for modelling weakly ionized plasmas. MNRAS, 376:1648–1658.

Pandey, B. P. and Wardle, M. (2008). Hall magnetohydrodynamics of partially ionized plasmas. MNRAS, 385:2269–2278.

Perez-Becker, D. and Chiang, E. (2011). SURFACE LAYER ACCRETION IN CONVENTIONAL AND TRANSITIONAL DISKS DRIVEN BY FAR-ULTRAVIOLET IONIZATION. The Astrophysical Journal, 735(1):8.

Perron, O. (1907). Zur theorie der matrices. Mathematische Annalen, 64:248–263.

Pinilla, P., Birnstiel, T., Ricci, L., Dullemond, C. P., Uribe, A. L., Testi, L., and Natta, A. (2012). Trapping dust particles in the outer regions of protoplanetary disks. A&A, 538:A114.

Pinte, C., Dent, W. R. F., Ménard, F., Hales, A., Hill, T., Cortes, P., and de Gregorio-Monsalvo, I. (2016). Dust and Gas in the Disk of HL Tauri: Surface Density, Dust Settling, and Dust-to-gas Ratio. ApJ, 816:25.

Polygiannakis, J. M. and Moussas, X. (2001). A review of magneto-vorticity induction in hall-mhd plasmas. Plasma Physics and Controlled Fusion, 43(2):195.

Press, W. H., Teukolsky, S. A., Vetterling, W. T., and Flannery, B. P. (2007). Numerical Recipes 3rd Edition: The Art of Scientific Computing. Cambridge University Press, New York, NY, USA, 3 edition.

Raettig, N., Klahr, H., and Lyra, W. (2015). Particle Trapping and Streaming Instability in Vortices in Protoplanetary Disks. ApJ, 804:35.

Ragusa, E., Dipierro, G., Lodato, G., Laibe, G., and Price, D. J. (2017). On the origin of horseshoes in transitional discs. MNRAS, 464:1449–1455.

Riols, A. and Lesur, G. (2018). Dust settling and rings in the outer regions of protoplanetary discs subject to ambipolar diffusion. A&A, 617:A117.

Rodgers-Lee, D., Ray, T. P., and Downes, T. P. (2016). Global multifluid simulations of the magnetorotational instability in radially stratified protoplanetary discs. MNRAS, 463:134–145.

Safronov, V. (1972). Evolution of the protoplanetary cloud and formation of the earth and planets. Translated from Russian. Jerusalem (Israel): Israel Program for Scientific Translations, Keter Publishing House, 212 p.

Salmeron, R. and Wardle, M. (2003). Magnetorotational instability in stratified, weakly ionized accretion discs. MNRAS, 345:992–1008.

Salmeron, R. and Wardle, M. (2008). Magnetorotational instability in protoplanetary discs: the effect of dust grains. MNRAS, 388:1223–1238.

Sano, T. and Stone, J. M. (2002). The Effect of the Hall Term on the Nonlinear Evolution of the Magnetorotational Instability. I. Local Axisymmetric Simulations. ApJ, 570:314–328.

Schaffer, N., Yang, C.-C., and Johansen, A. (2018). Streaming instability of multiple particle species in protoplanetary disks. A&A, 618:A75.

Schneider, J., Dedieu, C., Le Sidaner, P., Savalle, R., and Zolotukhin, I. (2011). Defining and cataloging exoplanets: the exoplanet.eu database. A&A, 532:A79.

Sicilia-Aguilar, A., Hartmann, L., Calvet, N., Megeath, S. T., Muzerolle, J., Allen, L., D'Alessio, P., Merin, B., Stauffer, J., Young, E., and Lada, C. (2006). Disk evolution in cep OB2: Results from theSpitzer space telescope. The Astrophysical Journal, 638(2):897–919.

Simon, J. B., Armitage, P. J., Li, R., and Youdin, A. N. (2016). The Mass and Size Distribution of Planetesimals Formed by the Streaming Instability. I. The Role of Self-gravity. ApJ, 822(1):55.

Simon, J. B., Bai, X.-N., Stone, J. M., Armitage, P. J., and Beckwith, K. (2013). Turbulence in the Outer Regions of Protoplanetary Disks. I. Weak Accretion with No Vertical Magnetic Flux. ApJ, 764:66.

Simon, J. B., Lesur, G., Kunz, M. W., and Armitage, P. J. (2015). Magnetically driven accretion in protoplanetary discs. MNRAS, 454:1117–1131.

Squire, J. and Hopkins, P. F. (2018). Resonant drag instabilities in protoplanetary discs: the streaming instability and new, faster growing instabilities. MNRAS, 477:5011–5040.

Stone, J., Gardiner, T., Teuben, P., Hawley, J., and Simon, J. (2008). Athena: A new code for astrophysical mhd. ApJS, 178:137–177.

Stone, J. M. (1997). The Wardle Instability in Interstellar Shocks. I. Nonlinear Dynamical Evolution. ApJ, 487:271–282.

Stone, J. M. and Gardiner, T. A. (2010). Implementation of the Shearing Box Approximation in Athena. ApJS, 189:142–155.

Stone, J. M. and Norman, M. L. (1992). ZEUS-2D: A Radiation Magnetohydrodynamics Code for Astrophysical Flows in Two Space Dimensions. II. The Magnetohydrodynamic Algorithms and Tests. ApJS, 80:791.

Stoyanovskaya, O. P., Vorobyov, E. I., and Snytnikov, V. N. (2018). Analysis of numerical algorithms for computing rapid momentum transfers between the gas and dust in simulations of circumstellar disks. Astronomy Reports, 62:455–468.

Takeuchi, T. and Lin, D. N. C. (2002). Radial Flow of Dust Particles in Accretion Disks. ApJ, 581(2):1344–1355.

Testi, L., Birnstiel, T., Ricci, L., Andrews, S., Blum, J., Carpenter, J., Dominik, C., Isella, A., Natta, A., Williams, J. P., and Wilner, D. J. (2014). Dust evolution in protoplanetary disks. Protostars and Planets VI, pages 339–361.

Torres, R. M., Loinard, L., Mioduszewski, A. J., Boden, A. F., Franco-Hernández, R., Vlemmings, W. H. T., and Rodríguez, L. F. (2012). VLBA DETERMINATION OF THE DISTANCE TO NEARBY STAR-FORMING REGIONS. v. DYNAMICAL MASS, DISTANCE, AND RADIO STRUCTURE OF v773 tau a. The Astrophysical Journal, 747(1):18.

Tóth, G., Ma, Y., and Gombosi, T. I. (2008). Hall magnetohydrodynamics on block-adaptive grids. Journal of Computational Physics, 227:6967–6984.

Turner, N. J., Carballido, A., and Sano, T. (2010). Dust Transport in Protostellar Disks Through Turbulence and Settling. ApJ, 708:188–201.

Turner, N. J. and Drake, J. F. (2009). Energetic Protons, Radionuclides, and Magnetic Activity in Protostellar Disks. ApJ, 703:2152–2159.

Umebayashi, T. and Nakano, T. (1981). Fluxes of Energetic Particles and the Ionization Rate in Very Dense Interstellar Clouds. PASJ, 33:617.

van Leer, B. (1977). Towards the Ultimate Conservative Difference Scheme. IV. A New Approach to Numerical Convection. Journal of Computational Physics, 23:276.

Vorobyov, E. I., Akimkin, V., Stoyanovskaya, O., Pavlyuchenkov, Y., and Liu, H. B. (2018). Early evolution of viscous and self-gravitating circumstellar disks with a dust component. A&A, 614:A98.

Walt, S. v. d., Colbert, S. C., and Varoquaux, G. (2011). The numpy array: A structure for efficient numerical computation. Computing in Science and Engg., 13(2):22–30.

Wang, L., Bai, X.-N., and Goodman, J. (2019). Global Simulations of Protoplanetary Disk Outflows with Coupled Non-ideal Magnetohydrodynamics and Consistent Thermochemistry. ApJ, 874:90.

Wardle, M. (1999). The Balbus-Hawley instability in weakly ionized discs. MNRAS, 307(4):849–856.

Wardle, M. (2007). Magnetic fields in protoplanetary disks. Ap&SS, 311(1-3):35–45.

Wardle, M. and Salmeron, R. (2012). Hall diffusion and the magnetorotational instability in protoplanetary discs. MNRAS, 422:2737–2755.

Weber, P., Benítez-Llambay, P., Gressel, O., Krapp, L., and Pessah, M. (2018). Characterizing the variable dust permeability of planet-induced gaps. ApJ, 854:153.

Weidenschilling, S. J. (1977). Aerodynamics of solid bodies in the solar nebula. MNRAS, 180:57–70.

Whipple, F. L. (1972a). On certain aerodynamic processes for asteroids and comets. In Elvius, A., editor, From Plasma to Planet, page 211.

Whipple, F. L. (1972b). On certain aerodynamic processes for asteroids and comets. In Elvius, A., editor, From Plasma to Planet, page 211.

Williams, J. P. and Cieza, L. A. (2011). Protoplanetary Disks and Their Evolution. ARA&A, 49(1):67–117.

Windmark, F., Birnstiel, T., Ormel, C. W., and Dullemond, C. P. (2012). Breaking through: The effects of a velocity distribution on barriers to dust growth. A&A, 544:L16.

Youdin, A. and Johansen, A. (2007). Protoplanetary disk turbulence driven by the streaming instability: Linear evolution and numerical methods. ApJ, 662:613–626.

Youdin, A. N. and Goodman, J. (2005). Streaming instabilities in protoplanetary disks. ApJ, 620:459–469.

Zhu, Z., Nelson, R. P., Dong, R., Espaillat, C., and Hartmann, L. (2012). Dust filtration by planet-induced gap edges: Implications for transitional disks. ApJ, 755:6.

Ziegler, U. (2004). A central-constrained transport scheme for ideal magnetohydrodynamics. JCoPh, 196:393–416.

Ziegler, U. (2011). A semi-discrete central scheme for magnetohydrodynamics on orthogonal curvilinear grids. JCoPh, 230:1035–1063.

Ziegler, U. (2016). A chemical reaction network solver for the astrophysics code NIRVANA. A&A, 586:A82.